NNT : 2016SACLX010

Thèse de doctorat de l'Université Paris-Saclay préparée à l'École Polytechnique

École doctorale n°573
INTERFACES
Spécialité de doctorat : Physique

par

Maksim Markov

Prédiction de la conductivité thermique et stratégie de réduction du transport de la chaleur dans le bismuth : étude *ab initio*.

Thèse présentée et soutenue à l'École Polytechnique, le 11 Mars 2016.

Composition du Jury :

Dr.	Sylvie Hébert	Présidente du jury Laboratoire CRISMAT UMR6508 CNRS et ENSICAEN
Prof.	Alan J. H. McGaughey	Rapporteur Université Carnegie Mellon
Prof.	Sebastian Volz	Rapporteur École Centrale de Paris
Prof.	Antoine Georges	Examinateur Centre de Physique Théorique, École Polytechnique
Prof.	Francesco Mauri	Examinateur Université de Rome "La Sapienzà", IMPMC Université Paris VI, CNRS
Dr.	Jelena Sjakste	Co-directrice de thèse École Polytechnique
Dr.	Nathalie Vast	Co-directrice de thèse École Polytechnique

NNT : 2016SACLX010

Doctoral thesis
University Paris-Saclay
prepared at École Polytechnique

Graduate school n°573
INTERFACES
Speciality : Physics
by

Maksim Markov

Prediction of thermal conductivity and strategies for heat transport reduction in bismuth : an *ab initio* study.

Thesis presented and defended at École Polytechnique on March 11, 2016.

Examining committee :

Dr.	Sylvie Hébert	Chairwoman Laboratory CRISMAT UMR6508 CNRS and ENSICAEN
Prof.	Alan J. H. McGaughey	Referee Carnegie Mellon University
Prof.	Sebastian Volz	Referee École Centrale of Paris
Prof.	Antoine Georges	Examiner Center for Theoretical Physics, École Polytechnique
Prof.	Francesco Mauri	Examiner University of Rome "La Sapienzà", IMPMC University Paris VI, CNRS
Dr.	Jelena Sjakste	Co-supervisor École Polytechnique
Dr.	Nathalie Vast	Co-supervisor École Polytechnique

Acknowledgements

First and foremost, I would like to express my sincere gratitude to my advisors, Dr. Jelena Sjakste and Dr. Nathalie Vast, for giving me an opportunity to do this work as well as for their continuous support of my PhD study and related research, for their patience, motivation, and immense knowledge. During these years I learned a lot about modern condensed matter physics and about computer simulations as a powerful and a highly efficient tool to solve physical problems. My advisors have provided enormous amounts of scientific guidance, invaluable advice and a critical scientific outlook. I am also thankful for encouraging me to attend numerous trainings, conferences, workshops and tutorials.

I would like to thank Prof. Kees van der Beek, the director of the Laboratoire des Solides Irradiés of the École Polytechnique, for having welcomed me at LSI. I thank Prof. Alan J. H. McGaughey and Prof. Sebastian Volz to have accepted to review the manuscript and to participate in the jury of this thesis; Prof. Antoine Georges, for having accepted to chair the jury; Dr. Sylvie Hébert and Prof. Francesco Mauri to have accepted to be members of the jury of this thesis.

I am very grateful to my collaborators Prof. Francesco Mauri, Prof. Michele Lazzeri, Dr. Giorgia Fugallo, Dr. Lorenzo Paulatto for giving me an opportunity to use the D3Q code and the thermal conductivity code. I deeply appreciate your advises, comments and valuable scientific discussions that helped me a lot while working on the project and on the paper.

I would like to thank all old and new members of the group "Théorie de la Science des Matériaux" including Michèle Raynaud, Gaston Kané, Giuliana Barbarino, Iurii Timrov, Antoine Jay, Liang Liang, Zhangxuan Fan, Oleksandr Motornyi, Sabuhi Badalov, Yi Liu, Aminata Doucoure. In particular, I am very thankful for his friendship to Olivier Hardouin Duparc with whom I shared the office all these years. Thank you for all numerous conversations about science, history, literature and especially for your tolerance to my mistakes in French. I would like to thank our system administrator, Andrea Cucca, for keeping the IT system working well and for his help with all kinds of computer issues as well as Andrea Sartirana for his help with LLR-LSI cluster. I am very grateful to all LSI members who created a great scientific environment at the lab.

I would like to thank and dedicate this thesis to my parents, Lidia and Nikolay, whose love, caring and trust supported me throughout my whole life. I am grateful to my brother, Vladimir, who has always been a role model for me and greatly inspired me to study physics. I would like to thank my wife, Olga, for her endless love and support, and enormous patience during my PhD.

Finally, I acknowledge the financial support from École Polytechnique (DRE grant).

Résumé

Cette thèse de doctorat porte sur l'étude théorique de la conductivité thermique du réseau dans le bismuth semi-métallique et sur les stratégies favorables pour la réduire. Les propriétés thermiques du bismuth sont extrêmement intéressantes grâce à sa conductivité thermique très basse qui rend ce matériau approprié pour les applications de gestion thermique. De plus, étant un matériau archétypique pour les thermoélectriques modernes, tels que les alliages à base du bismuth (BiSb) et les composés du bismuth (Bi_2Te_3), le bismuth est une excellente substance modèle pour étudier la thermoélectricité. Potentiellement, les matériaux thermoélectriques pourraient être utilisés dans l'industrie pour la conversion d'énergie thermoélectrique ou pour la dissipation de la chaleur en microélectronique.

Le présent travail est basé sur les progrès significatifs réalisés récemment dans notre laboratoire dans la description des propriétés électroniques et vibrationnelles du bismuth, et la détermination de la grandeur du couplage électron-phonon à la fois expérimentalement et théoriquement [1, 2, 3, 4]. Les résultats sont devenus un point de départ de ce travail et m'ont permis d'étudier les propriétés de transport thermique dans le bismuth.

En collaboration avec L. Paulatto (IMPMC), G. Fugallo (École Polytechnique), F. Mauri (IMPMC) et M. Lazzeri (IMPMC), j'ai utilisé des méthodes avancées de résolution de l'équation de transport de Boltzmann pour les phonons [5], et de calcul *ab initio* des éléments de matrice de l'interaction phonon-phonon [6]. J'ai calculé la dépendance en température de la conductivité thermique du réseau dans le matériau en volume en excellent accord avec les rares expériences disponibles [7]. De plus, une description microscopique très précise de transport de la chaleur a été réalisée et la contribution des porteurs de charge électrique à la conductivité thermique totale a été déterminée.

En outre, j'ai démontré que la nano-structuration et la photo-excitation sont des moyens très efficaces dans le bismuth pour contrôler la diffusion des phonons qui portent la chaleur, respectivement par interaction avec les bords de l'échantillon et par interaction phonon-phonon. En contrôlant l'équilibre entre ces deux derniers effets, j'ai prédit de façon exhaustive l'effet de réduction pour différentes températures et tailles de nano-structures, pour des mono- et poly-cristaux, semi-conducteurs ou semi-métalliques [7].

Les méthodes que j'utilise ne contiennent aucun paramètre ajustable et ainsi donnent un aperçu direct sur les mécanismes microscopiques qui déterminent les propriétés de transport et les propriétés anharmoniques des matériaux. Cela m'a permis d'analyser l'élargissement anharmonique, qui est inversement proportionnel à la durée de vie des phonons, le long des directions de haute symétrie dans la zone de Brillouin, et de montrer quels sont les principaux canaux de diffusion (collision/fission) des phonons qui régissent le transport thermique dans le bismuth. De plus, l'atténuation des ondes sonores a été prédite et mes résultats pourraient être utilisés pour concevoir de futures expériences. Enfin, l'approximation des grandes longueurs d'ondes [long-wave approximation (LWA)], largement utilisé dans la littérature, a été validée pour le bismuth et ses limites ont été déterminées.

Abstract

This Ph.D. thesis has been devoted to the theoretical study of the lattice thermal conductivity (LTC) in bismuth and of the possible strategies for its reduction. Thermal properties of Bi are extremely interesting because of its low thermal conductivity that makes this material suitable for the thermal management applications. Moreover, being an archetype material for typical thermoelectrics such as bismuth-based alloys (BiSb) and compounds (Bi_2Te_3), bismuth is an excellent model substance for the study of thermoelectricity. The thermoelectric materials could be potentially used in industry, for example, for the thermoelectric energy conversion or for the thermal dissipation in microelectronics.

The present work stands on the significant progress achieved recently in our laboratory in the description of electronic and vibrational properties of bismuth, and in the determination of the magnitude of the electron-phonon coupling, both experimentally and theoretically [1, 2, 3, 4]. These results have become a starting point of my Ph.D. work and have allowed me to study the thermal transport properties in bismuth.

In collaboration with L. Paulatto (IMPMC), G. Fugallo (Ecole Polytechnique), F. Mauri (IMPMC) and M. Lazzeri (IMPMC) I have employed the recently developed advanced methods of the solution of the Boltzmann transport equation (BTE) for the phonon system [5] and of *ab initio* calculations of the phonon-phonon matrix elements [6]. I have obtained the temperature dependence of the bulk LTC which is in excellent agreement with the rare experiments and have predicted the LTC at temperatures at which it has not been measured [7]. A very accurate microscopic description of heat transport has been achieved and the charge-carrier contribution to the total thermal conductivity has been determined.

I have demonstrated that nanostructuring and photoexcitation are very efficient routes to control respectively phonon-boundary scattering and phonon-phonon interaction in bismuth. By controlling the interplay between these two scattering processes, I have predicted in an exhaustive way the effect of size reduction for various temperatures and nanostructure shapes, both single- and polycrystalline ones, and both semiconducting and semi metallic [7].

The methods I use contain no empirical fitting parameters and give a direct insight into the microscopic mechanisms determining the transport and anharmonic properties of the materials. This allows me to analyze the anharmonic broadening that is inversely proportional to the phonon lifetime, for the various phonon modes along the high symmetry directions in the Brillouin zone and show what are the major scattering channels for coalescence/decays of phonons that govern the thermal transport in Bi. Moreover, the attenuation of sound waves has been predicted and could be used as a guide for future experiments. Finally, the long-wave approximation (LWA), widely used in the literature, has been validated for bismuth and its limitations studied.

Contents

Introduction

Bismuth is an important material in the history of thermoelectricity. It has been first used in the pioneer experiments of T.J. Seebeck in thermocouples and has remained the best electron-based thermoelectric material for a long time. Nowadays, the attention of scientists has mainly moved to compounds based on bismuth, such as Bi_2Te_3, and to alloys with antimony, Bi-Sb. However, bismuth is still competitive with respect to other materials for thermoelectric applications, especially in its nanostructured form that is expected to have superior thermoelectric properties with respect to bulk bismuth. Indeed, since bismuth is a chemically pure material, it is technologically easy to produce comparing with the alloys and compounds. Moreover, the cost of bismuth is very low in comparison with tellurium[1] that makes it advantageous from the economical point of view.

Bismuth has a very high Seebeck coefficient that amounts to $S \approx -110\ \mu\mathrm{VK}^{-1}$ in the trigonal direction at $T = 200$ K [8] that is more than 10 times higher than values in typical metals [9]. In a magnetic field, the Seebeck coefficient is increased even more, reaching the value of $S \approx -200\ \mu\mathrm{VK}^{-1}$ for $B > 3$ T [10]. Such high values of the Seebeck coefficient, make bismuth a good candidate for applications like temperature sensors based on thermocouples with an electric output signal, or like thermal converters in which an electrical signal is measured by converting it into heat. Moreover, due to its giant magnetoresistance bismuth can be used as a magnetoresistive thermometer or magnetorestive sensor [11].

The Seebeck coefficient is defined by the entropy per charge carriers [12]. In metals the Seebeck coefficient results from a very sensitive balance of energy current by charge carriers in a small shell near the Fermi energy [13], and is proportional to the ratio $S \sim \frac{k_B T}{\varepsilon_F}$ [12]. Since in metals the carriers are degenerate, $k_B T \ll \varepsilon_F$, the Seebeck coefficient is small. The situation is different in the case of bismuth, where for $T > 60$ K one finds $\varepsilon_F \sim k_B T$ and the full Fermi-Dirac statistics must be used [14], resulting in high values of the Seebeck coefficient. However, in semimetals like bismuth, there are two types of charge carriers, electrons and holes, at the same time. They contribute to the Seebeck coefficient with opposite signs partially compensating each other. The electrons at L points have very small effective masses and, thus, high mobilities resulting in the dominant electronic contribution and negative sign of the total Seebeck coefficient which is quite high.

In intrinsic semiconductors and insulators the total entropy spreads over only a few charge carriers. For the case of two bands separated by an energy gap Δ, the Seebeck

[1] The price of Bi is about 9$ per kg while the price of Te is 110$ per kg. Data from http://www.metalprices.com/ on January 2016.

coefficient is $S \sim \frac{\Delta}{k_B T}$ [12] and in the non-degenerate regime, $k_B T \ll \Delta$, the Seebeck coefficient has very high values. However, the large gap Δ will spoil the electrical conductivity σ.

The optimal values of the power factor $P_F = S^2\sigma$ lie in the region of concentrations at the interface between the narrow-gap semiconductors and semimetals. However, in bismuth the concentration of charge carriers, electrons and holes, is very low $n = p = 2.7 \cdot 10^{18}$ cm^{-3} at T = 300 K [14]. It is partially compensated by high mobilities, but the resulting electrical conductivity is still about two orders of magnitude lower than in metals [14].

Bismuth has the lowest thermal conductivity among all metals except mercury [15] which is explained mainly by its high atomic mass[2]. However, in bismuth there is no one single mechanism determining the thermal conductivity. Apart from the lattice part, there are also monopolar contributions from electrons and holes, as well as the bipolar contribution which exists in semimetals due to the presence of an equal number of electrons and holes, that move together in the same direction transporting energy without carrying any net charge [16]. The separation of the lattice and non-lattice contributions is hard from the experimental point of view. Thus, the first objective of this thesis is to provide reliable quantitative data about the lattice thermal conductivity in the two crystallographic directions of bulk bismuth.

Since the works of L. D. Hicks and M. S. Dresselhaus, nanostructuring is known to be a promising route to enhance the thermoelectric properties of materials [17, 18]. First, due to the confinement effect, nanostructuring increases the asymmetry of the density of states on the two sides of the Fermi level, leading to the increase of the Seebeck coefficient. Moreover, nanostructuring is a well-known way to reduce the lattice thermal conductivity by limiting the longest phonon mean free paths. However, compared to intensive studies in relatively simple materials such as Si and Si-Ge alloys, systematic studies are scarce in bismuth. Most of the studies are experimental. Measurements made in thin films [19, 20, 21] and nanowires [22, 15, 23, 24, 25, 26] have yielded widely scattered values, preventing a deep understanding of the mechanisms at play in nanostructures [15]. Thus, a theoretical determination of the nanostructuring effect on the lattice thermal conductivity is the second objective of this thesis.

The methods I use in this thesis are *ab initio* plus the Boltzmann Transport Equation. At the beginning of this work, this approach had been applied to graphene, graphite and diamond by G. Fugallo, L. Paulatto and collaborators at IMPMC (Université Paris VI) [6, 5]. I had to develop my own tool to analyze the data for bismuth. In particular, I have performed the analysis of the lattice thermal conductivity contributions in the Brillouin zone, the analysis of anharmonic broadening along the high symmetry directions and the analysis of anharmonic matrix elements. Moreover, in this work I will test some common approximations existing in the literature such as the long-wave approximation.

During my PhD, a paper from my competitors in the Massachusetts Institute of Technology (MIT) has been published [25], that confirmed my unpublished data of the *ab initio* lattice thermal conductivity between 50 K and 300 K and showed a discrepancy with experiments that will be explained in Chapter 4. Then I have developed the analy-

[2]Bismuth is the heaviest non-radioactive element in the periodic table.

sis tool to understand the discrepancy. This enabled me to understand the mechanisms governing the magnitude of the lattice thermal conductivity on the microscopic level and particularly the large effect of acoustic-optical anharmonic interaction.

Finally, I have also implemented the Casimir model for wires and thin films for a three-dimensional and anisotropic material.

In this work, calculations in a high performance computing environment have been performed. 585 thousands hours of CPU time approximately have been spent in total. In particular, I have spent about 300 thousands hours of CPU time in Grand Équipement National de Calcul Intensif (GENCI) and about 285 thousands hours at the local LSI-LLR cluster.

The thesis consists of two parts. First, in Part I, I consider the general computational and theoretical framework necessary to perform thermal transport calculations shown in Part II. I also review the physical properties of bismuth with which my results will be compared in Part II. Then, Part II gathers all of the results of thermal transport calculations in bulk bismuth and its nanostructures as well as the analyzes of these calculations. An Appendix completes the manuscript.

Part I contains 2 chapters.

In Chapter 1, I will formulate the problem of heat conduction in solids. I will define the system of equations governing thermal transport. I will present the methods to solve this system. In particular, I will focus my attention on the limitations of the formalism which I will use in Part II.

In Chapter 2, I will explain why bismuth still remains competitive as a material for thermoelectric applications. I will discuss the thermoelectric figure of merit of Bi as well as its ingredients. I will show that the experimental methods used to extract the lattice part of the thermal conductivity in Bi are non-direct and have considerable limitations which are the motivation for the theoretical study presented in this thesis. This information will be required for the discussion of my results in Chapter 4. I will also discuss nanostructuring of bismuth as a promising route to enhance its thermoelectric efficiency and to improve its thermal insulating properties.

Part II contains 4 chapters of results.

In Chapter 3, I will discuss vibrational properties of bismuth and I will show the crucial role of spin-orbit coupling in the phonon dispersion of bismuth. I will present the results of the calculation of the lattice thermal conductivity and I will show a crucial role of the the acoustic-optical phonon interaction on its magnitude. I will perform a detailed analysis of the heat transfer mechanisms in bismuth.

In Chapter 4, I will analyze the results of my calculations of the lattice thermal conductivity with respect to the experimental data discussed in Chapter 2. I will discuss the anisotropy of the thermal conductivity. Finally, I will evaluate the non-lattice (charge carrier) contribution to the thermal conductivity found as a difference between the measured total thermal conductivity and my calculation of the lattice part.

In Chapter 5, I will discuss the possible mechanisms of the thermal conductivity reduction in bismuth. I will study the effect of acoustic-optical phonon interaction and its possible realization in photoexcited bismuth. I will study the lattice thermal conductivity

reduction in nanostructures of different geometries, thin films, nanowires and polycrystalline grains, compare my results with available experiments and predict the reduction factors for thin films and grains of different sizes.

In Chapter 6, I will discuss the anharmonic properties of phonons in bismuth. I will perform a detailed analysis of scattering processes contributing to the anharmonicity of both acoustic and optical phonons, as well as the role of acoustic-optical phonon interaction on it. I will discuss the sound attenuation in bismuth and predict the results that can be measured in future experiments. Then, I will analyze the phonon-phonon anharmonic matrix elements and I will examine the applicability of the long-wave approximation.

Finally, I will draw the general conclusions and perspectives.

Part I

Background: the state of the art

Chapter 1

Heat transport

In this Chapter I present the computational framework for the calculations of heat transport in bulk materials and nanostructures, and discuss its limitations. First, in Section 1.1, I consider the definition of thermal conductivity *via* Fourier's law and discuss the scope of its application. In Section 1.2, I present the microscopic statistical equation, namely the Boltzmann Transport Equation (BTE), that governs the statistical behavior of out-of-equilibrium thermodynamic system when the gradient of temperature is imposed. Then, I discuss the contribution to the total scattering rate due to the different sources of scattering such as phonon-phonon scattering, boundary scattering and isotopic scattering. In Section 1.4, I present the methods to solve the linearized BTE: the relaxation time approximation (RTA), as well as the exact methods such as iterative and variational approaches. Finally, in Section 1.5, I discuss the calculation of the three-phonons anharmonic coefficients that determine phonon lifetimes and thus is a crucial ingredient in phonon transport theory. The general review of thermal transport theory and methods essentially follows Ref. [27, 5, 6].

1.1 Thermal conductivity

1.1.1 Thermoelectricity: figure of merit ZT

The thermoelectric phenomena refer to the two well-known reciprocal physical effects consisting in the direct conversion of a temperature difference into an electric voltage (the Seebeck effect) and *vice versa* (the Peltier effect [1]) [28]. These thermoelectric effects have a number of promising applications including power generation and refrigeration [29, 30, 31, 32]. The thermoelectric properties are some of the material characteristics and the potential use of a material for thermoelectric applications is determined by its thermoelectric efficiency.

The efficiency of a thermoelectric material is defined by the dimensionless figure of merit ZT [28]

$$ZT = \frac{S^2\sigma}{\kappa}T = \frac{P_F}{\kappa}T \tag{1.1}$$

[1] Thomson effect can be considered as a continuous version of the Peltier effect

where T is the absolute temperature, σ is the electrical conductivity, κ is the total thermal conductivity and S is the Seebeck coefficient or thermopower. By definition, the Seebeck coefficient is a coefficient of proportionality between the temperature difference ΔT and the corresponding voltage difference ΔV

$$S = -\frac{\Delta V}{\Delta T} \tag{1.2}$$

Together, the square of the Seebeck coefficient S^2 and the electrical conductivity σ, are often denoted as the power factor $P_F = S^2\sigma$ [33, 34]. In essence, the figure of merit ZT is a measure of the competition between electronic transport (defined by the power factor P_F) and thermal transport (defined by the total thermal conductivity κ) [33]. As can be seen from formula 1.1, the enhancement of the figure of merit is a very challenging task since it requires the optimization of three quantities at the same time.

The prime objective of this thesis is the investigation of the thermal conductivity κ that governs the heat transport in materials. From Eq. 1.1 one can see that the reduction of thermal conductivity enables us to improve thermoelectric properties of material as well as to improve its thermal insulation properties. In general, the thermal conductivity κ contains the contribution due to the lattice vibrations κ_L and the contribution due to the charge carriers κ_E such as monopolar contribution of electrons, holes and bipolar contribution due to the electron-hole pairs (see Section 2.4). The total thermal conductivity can be found as the sum of all contributions

$$\kappa = \kappa_L + \kappa_E \tag{1.3}$$

Further discussion in this Chapter will concern only the lattice part of thermal conductivity if the reverse is not stated.

1.1.2 Thermal conductivity: Fourier's law.

Fourier's law is an empirical relationship which defines the thermal conductivity κ as

$$\mathbf{J} = -\kappa \cdot \boldsymbol{\nabla} T \tag{1.4}$$

where $\mathbf{J}$ is the heat flux that is the amount of energy that flows through a unit area per unit time, $\boldsymbol{\nabla} T$ is the gradient of temperature in the direction of heat flow. Thermal conductivity is a strictly positive quantity that requires the heat flux and the gradient of temperature to have opposite signs. Otherwise, the heat propagates from lower to higher temperature that is prohibited by the second law of thermodynamics.

If heat is carried by phonons, the heat flux in the direction of temperature gradient can be expressed as follows [5]

$$\mathbf{J} = \frac{1}{N_{\mathbf{q}} V} \sum_{\nu} \hbar\omega_{\nu} \mathbf{c}_{\nu} n_{\nu} \tag{1.5}$$

where $\hbar\omega_{\nu}$ is the energy of phonon mode ν with vector $\mathbf{q}$ (uniformly sampled with $N_{\mathbf{q}}$ points in the Brillouin zone) and branch index j, V is the volume of the unit cell, $\mathbf{c}_{\nu} =$

$\nabla_{\mathbf{q}}\omega_\nu$ is the phonon group velocity in the direction of heat propagation and n_ν is the out-of-equilibrium phonon distribution established after the imposition of the gradient of temperature. To determine the resulting heat flux $\mathbf{J}$ and, thus, to obtain the thermal conductivity from Eq. 1.4, one needs to know the out-of-equilibrium phonon distribution n_ν, the determination of which requires an additional equation: the Boltzmann Transport Equation (BTE).

1.1.3 Limitation of Fourier's law: second sound.

In the absence of density and pressure gradients, the continuity equation for heat transport can be written as [35]

$$C\frac{\partial T}{\partial t} + \boldsymbol{\nabla}\cdot\mathbf{J} = 0 \tag{1.6}$$

where C is the heat capacity per unit volume. Putting Eq. 1.4 into Eq. 1.6, one gets a well-known partial differential equation of parabolic type that describes the distribution of heat in a given region over time

$$\frac{\partial T}{\partial t} = D\Delta T \tag{1.7}$$

where $\Delta = \frac{\partial^2}{\partial x^2} + \frac{\partial^2}{\partial y^2} + \frac{\partial^2}{\partial z^2}$ is the Laplace operator and $D = \frac{\kappa}{C}$ is the thermal diffusivity. Equation 1.7 is called the heat (or diffusion) equation. The solution of heat equation 1.7 with the initial value

$$T(\boldsymbol{r}, t=0) = T_0(\boldsymbol{r}), \qquad \boldsymbol{r}\in\mathbb{R}^3 \tag{1.8}$$

is given by

$$T(\boldsymbol{r},t) = \frac{1}{(4\pi Dt)^{3/2}}\int_{\mathbb{R}^3} T_0(\boldsymbol{r'})\exp\left(-\frac{|\boldsymbol{r}-\boldsymbol{r'}|^2}{4Dt}\right)d^3r' \tag{1.9}$$

Equation 1.9 shows that even if the initial temperature distribution $T_0(\boldsymbol{r'})$ is localized in space, the solution $T(\boldsymbol{r},t)$ at any time $t>0$ will be spread out over the entire space $\mathbb{R}^3$. In other words, thermal pulse has an **infinite** speed of propagation [36, 37, 38] and I discuss this point in the next paragraph.

Analogy with the harmonic oscillator.

An important partial differential equation describing the propagation of signal with a **finite** velocity v is the wave equation

$$\frac{\partial^2 T}{\partial t^2} = v^2\Delta T \tag{1.10}$$

that after the Fourier transform becomes

$$\frac{d^2 T_{\mathbf{q}}}{dt^2} + \omega_0^2 T_{\mathbf{q}} = 0 \tag{1.11}$$

where $\omega_0^2 = v^2k^2$ and $T_{\mathbf{q}} = \int T(\mathbf{r},t)\exp(-i\mathbf{q}\cdot\mathbf{r})d\mathbf{q}$. Equation 1.11 has a direct analogy with a simple harmonic oscillator vibrating with frequency ω_0 where the role of temperature T is replaced by displacement x

$$\frac{d^2x}{dt^2} + \omega_0^2 x = 0 \tag{1.12}$$

where $\omega_0^2 = \frac{\alpha}{m}$. The second term of equation 1.12 results from the force determined by Hooke's law $F = -\alpha x$ with a positive spring constant α that is balanced by $F = m\frac{d^2x}{dt^2}$ (first term in 1.12) in the second Newton law.

The heat equation 1.7 after the Fourier transform becomes

$$\frac{dT_{\mathbf{q}}}{dt} + DT_{\mathbf{q}} = 0 \tag{1.13}$$

It has no analogy with a harmonic oscillator since there is no second order derivative $\frac{d^2T_{\mathbf{q}}}{dt^2}$ corresponding to $F = ma$. However, the first term $\frac{dT_{\mathbf{q}}}{dt}$ in equation 1.13 resembles a viscous force $F = -\beta\frac{dx}{dt}$ with β being a viscous damping coefficient. One can include this term into the second Newton law and get the following equation for the damped harmonic oscillator

$$\frac{d^2x}{dt^2} + 2\zeta\frac{dx}{dt} + \omega_0^2 x = 0 \tag{1.14}$$

where $\zeta = \frac{\beta}{2m}$ is a damping parameter. The solution of this equation 1.14 in case of small friction $\zeta < \omega_0$ is

$$x(t) = A\exp(-\zeta t)\sin\left(\sqrt{\omega_0^2 - \zeta^2} - \phi\right) \tag{1.15}$$

where A is a constant and ϕ is an initial phase. As one can see from equation 1.15, $x(t)$ is decaying in time with the characteristic time inversely proportional to a damping parameter ζ.

Application of Vernotte's correction to Fourier's law.

One can arrive at equation similar to 1.14 instead of the heat equation 1.7 if, following Vernotte [36], one assumes that Fourier's law 1.4 is violated and introduces an extra term in its left hand side

$$\tau_{ss}\frac{\partial \mathbf{J}}{\partial t} + \mathbf{J} = -\kappa\boldsymbol{\nabla}T \tag{1.16}$$

The physical sense of τ_{ss} will become clear later. Combining Eq. 1.16 and Eq. 1.6, one gets the final equation

$$\tau_{ss}\frac{\partial^2 T}{\partial t^2} + \frac{\partial T}{\partial t} - D\Delta T = 0 \tag{1.17}$$

which becomes

$$\frac{d^2T_{\mathbf{q}}}{dt^2} + \frac{1}{\tau_{ss}}\frac{dT_{\mathbf{q}}}{dt} + \frac{D}{\tau_{ss}}k^2T_{\mathbf{q}} = 0 \tag{1.18}$$

after the Fourier transform. Drawing an analogy with Eq. 1.14, one can write $2\zeta = \frac{1}{\tau_{ss}}$ and $\omega_0^2 = \frac{D}{\tau_{ss}}k^2$. As we have seen, the parameter ζ describes the damping of harmonic

oscillator and is inversely proportional to the characteristic relaxation time of damping thermal wave that is now defined by τ_{ss}. Then, using the expression for ω_0^2 obtained for wave equation 1.11, one can define the velocity for the propagation of a thermal pulse as $v_{ss} = \sqrt{\frac{D}{\tau_{ss}}}$. Now, if the second-order derivative term is absent in Eq. 1.17 (*i.e.* $\tau_{ss} = 0$), the propagation velocity is infinitely large as it has been concluded from the heat equation 1.7 .

Second sound.

Equation 1.17 predicts the propagation of heat pulse in form of a damped temperature wave, instead of the diffusion propagation predicted by Fourier's law in equation 1.7 [35]. This temperature wave is called *second sound* similar to first sound when density or pressure is used instead of temperature in equation. 1.17 [39].

However, the diffusive propagation of heat predicted by Fourier's law is usually a good approximation over a wide temperature range in solids. This is due to the important role of resistive Umklapp processes that do not conserve the crystal momentum and are activated at high temperatures. In contrast, the non-diffusive hydrodynamic transport described by equation 1.17 appears for situations involving very short times, extreme thermal gradients and cryogenic temperatures [40]. At low temperatures, normal processes conserving the total crystal momentum become dominant and the heat flow is similar to the hydrodynamic flow of gas. This phenomenon has been observed experimentally in NaF [41], in Bi [42] and solid helium [43]. Moreover, recent theoretical studies reveals that the conditions under which second sound can be observed are fulfilled in 2D materials at temperatures as high as room temperature and above [44, 45].

In further discussion in this Chapter I will rely on Fourier's law as a definition of the thermal conductivity.

1.2 The Boltzmann Transport Equation and phonon scattering processes.

1.2.1 Introduction

The lattice Boltzmann transport equation (BTE) has been first formulated by R. Peierls in 1929 [46]. It states that, when in the presence of a stationary temperature gradient, the steady state heat flow (*i.e.* $\frac{\partial n}{\partial t} = 0$) is established, the phonon diffusion due to the gradient of temperature is balanced by the scattering rate due to all kinds of scattering processes in which phonons are involved [47, 27, 5].

$$\mathbf{c}_\nu \cdot \boldsymbol{\nabla} T \left(\frac{\partial n_\nu}{\partial T} \right) = \left. \frac{\partial n_\nu}{\partial t} \right|_{scatt} \tag{1.19}$$

I keep the symbolic notation $\left. \frac{\partial n_\nu}{\partial t} \right|_{scatt}$ even for the time independent steady state process as described in textbooks [27, 48]. I consider the situation when external (electric or magnetic) fields are absent. The difficulty with the Boltzmann transport equation is the

complexity of the scattering term $\frac{\partial n_\nu}{\partial t}\Big|_{scatt}$ which includes the transition rates from all other states. These transition rates, in turn, depend on the occupation number of those states [27].

The different sources of scattering contribute independently to the scattering term $\frac{\partial n_\nu}{\partial t}\Big|_{scatt}$ and, thus one can express the latter as

$$\frac{\partial n_\nu}{\partial t}\bigg|_{scatt} = \frac{\partial n_\nu}{\partial t}\bigg|_{ph-ph} + \frac{\partial n_\nu}{\partial t}\bigg|_{be} + \frac{\partial n_\nu}{\partial t}\bigg|_{iso} + ... \tag{1.20}$$

where the first term represents the intrinsic phonon-phonon scattering, the second term is due to the scattering of phonons by sample boundaries, the third term is due to the isotopic (also called impurity) scattering. In the next paragraphs I discuss in detail the probability scattering rates due to the mentioned scattering mechanisms. Any other sources of scattering can be included in Eq. 1.20 in the same way if the analytical form of the scattering term is known.

1.2.2 Phonon-phonon scattering

The intrinsic phonon-phonon scattering is the prime mechanism determining heat propagation by lattice vibrations in crystals. In principle, processes involving three, four or even more phonons are possible. However, in this work I will consider only the three-phonon processes that are enough to determine phonon lifetimes and their mean free paths. The fourth order terms have no imaginary part and, thus, do not contribute to the phonon lifetime[2] [49, 50, 51].

The scattering rate describing the transition from the initial phonon state $|i\rangle$ to the final phonon state $|f\rangle$ due to phonon-phonon interaction is given by Fermi's Golden Rule [27]

$$P^{ph-ph}_{|i\rangle\to|f\rangle} = \frac{2\pi}{\hbar}\,|\langle i|V_3|f\rangle|^2 \cdot \delta(E_i - E_f) \tag{1.21}$$

where $V_3 = \frac{1}{3!}\sum_{ss's''} \frac{\partial^3 V}{\partial u^{s,\alpha}_{\mathbf{R}}\partial u^{s',\alpha'}_{\mathbf{R}'}\partial u^{s'',\alpha''}_{\mathbf{R}''}} u^{s,\alpha}_{\mathbf{R}} u^{s',\alpha'}_{\mathbf{R}'} u^{s'',\alpha''}_{\mathbf{R}''}$ is the cubic term in Taylor expansion of the potential energy V of the system with respect to atomic displacements $\{u^{s,\alpha}_{\mathbf{R}}, u^{s',\alpha'}_{\mathbf{R}'}, u^{s'',\alpha''}_{\mathbf{R}''}\}$. Atoms are labeled by indices s, s' and s'' in the unit cells with the lattice vectors $\mathbf{R}$, $\mathbf{R}'$ and $\mathbf{R}''$; α, α' and α'' are the Cartesian indices of the displacement vector components, $\delta(E_i - E_f)$ is the joint density of states ensuring the energy and momentum conservation rules.

Generally, two types of three-phonon process are possible, that are coalescence and decay processes. These processes are schematically illustrated in Figs. 1.1 (a) and (b). The respective energy and momentum conservation rules for coalescence (plus) and decay (minus) are

$$\hbar\omega_\nu \pm \hbar\omega_{\nu'} = \hbar\omega_{\nu''} \tag{1.22}$$

$$\mathbf{q} \pm \mathbf{q}' = \mathbf{q}'' + \mathbf{G} \tag{1.23}$$

[2] In perturbation theory the effect of cubic anharmonicity to second order and the effect of quartic anharmonicity to first order is taken into account.

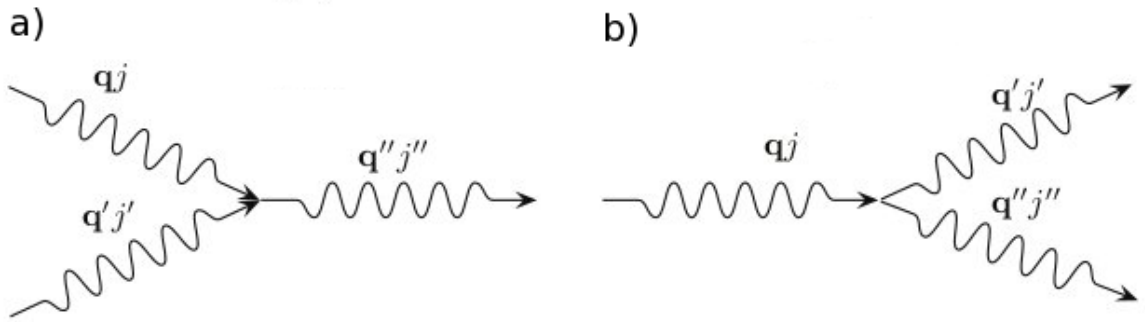

Figure 1.1: Schematic illustration of three-phonon scattering processes. **a)** Coalescence of incoming phonon $|\mathbf{q}, j\rangle$ with another incoming phonon $|\mathbf{q}', j'\rangle$ resulting in the creation of a single outcoming phonon $|\mathbf{q}'', j''\rangle$. **b)** Spontaneous decay of a single phonon mode $|\mathbf{q}, j\rangle$ into two outcoming phonon modes $|\mathbf{q}', j'\rangle$ and $|\mathbf{q}'', j''\rangle$. The figure is extracted from Ref. [5].

where $\mathbf{G}$ is a reciprocal lattice vector. A process in which the total phonon momentum is conserved, $\mathbf{G} = \mathbf{0}$, is called Normal or N-process [27]. Otherwise, when $\mathbf{G} \neq \mathbf{0}$, the process is called Umklapp or U-process indicating that the phonon "flop over" in the process [27].

Explicitly treating the matrix elements $\langle i|V_3|f\rangle$ in eq. (1.21), one can obtain the following expressions for the probability rate of coalescence $P^{\nu''}_{\nu,\nu'}$ and for the probability rate of decay $P^{\nu',\nu''}_{\nu}$ [27, 5, 6]

$$P^{\nu''}_{\nu,\nu'} = \frac{2\pi}{N_q\hbar^2}\sum_{\mathbf{G}}\frac{|V^{(3)}(\nu,\nu',-\nu'')|^2}{\omega_\nu\omega_{\nu'}\omega_{\nu''}}n_\nu n_{\nu'}(n_{\nu''}+1)\delta_{\mathbf{q}+\mathbf{q}'-\mathbf{q}'',\mathbf{G}}\delta(\hbar\omega_\nu+\hbar\omega_{\nu'}-\hbar\omega_{\nu''}) \quad (1.24)$$

$$P^{\nu',\nu''}_{\nu} = \frac{2\pi}{N_q\hbar^2}\sum_{\mathbf{G}}\frac{|V^{(3)}(\nu,-\nu',-\nu'')|^2}{\omega_\nu\omega_{\nu'}\omega_{\nu''}}n_\nu(n_{\nu'}+1)(n_{\nu''}+1)\delta_{\mathbf{q}-\mathbf{q}'-\mathbf{q}'',\mathbf{G}}\delta(\hbar\omega_\nu-\hbar\omega_{\nu'}-\hbar\omega_{\nu''}) \quad (1.25)$$

where the third order derivative of the total energy $V^{(3)}(\nu,\nu',\nu'')$ is defined as

$$V^{(3)}(\nu,\nu',\nu'') = \frac{1}{N}\frac{\partial^3 V}{\partial X_\nu \partial X_{\nu'}\partial X_{\nu''}} \quad (1.26)$$

with the quantity X_ν defined in this manuscript as[3]

$$\frac{\partial}{\partial X_\nu} = \sum_{s,\alpha}\sqrt{\frac{\hbar}{2M_s}}z^{s,\alpha}_\nu\frac{\partial}{\partial u^{s,\alpha}_{\mathbf{q}}} \quad (1.27)$$

[3]In Refs. [5, 6] X_ν is defined as adimensional quantity $\frac{\partial}{\partial X_\nu} = \sum_{s,\alpha}\sqrt{\frac{\hbar}{2M_s\omega_\nu}}z^{s,\alpha}_\nu\frac{\partial}{\partial u^{s,\alpha}_{\mathbf{q}}}$. In this manuscript I carry frequency ω_ν outside of the definition of X_ν to facilitate the relation with the long-wave approximation in Sections 1.5.1 and 6.7.

where $z_\nu^{s,\alpha}$ being the orthogonal phonon eigenmodes of the harmonic dynamical matrix, normalized in the unit cell, M_s is the atomic mass and $u_{\mathbf{q}}^{s,\alpha}$ is the Fourier transform of the atomic displacement $u_{\mathbf{R}}^{s,\alpha}$

$$u_{\mathbf{q}}^{s,\alpha} = \frac{1}{N}\sum_{\mathbf{R}} u_{\mathbf{R}}^{s,\alpha} e^{-i\mathbf{q}\cdot\mathbf{R}} \tag{1.28}$$

where the sum is performed on the lattice vectors $\{\mathbf{R}\}$ and N is the number of cells involved in the summation [6].

1.2.3 Boundary scattering.

At low temperatures the phonon-phonon scattering processes may be frozen and ineffective because of the low phonon occupation, leading to very large mean free paths exceeding the length of the specimen [27]. In this case, the sample boundaries act as highly efficient scattering regions, and limit the apparent mean free path of the carriers [27]. The probability scattering rate for boundary scattering of phonons is then given by Casimir's model [5, 52]

$$P_\nu^{be} = \frac{|\mathbf{c}_\nu^b|}{L^{Cas}F} n_\nu(n_\nu + 1) \tag{1.29}$$

where L^{Cas} is the Casimir length of the sample, F characterizes the sample roughness [27] and $|\mathbf{c}_\nu^b|$ is the modulus of the phonon group velocity vector which has components in the direction(s) in which the phonon transport is limited by the sample boundaries.

Casimir's model is also applied to nanostructures with sizes in the nanometer range, resulting in an efficient scattering by the sample boundaries even at high temperatures [48].

1.2.4 Isotope scattering.

Another scattering mechanism which could contribute to the thermal resistance of crystals is the elastic scattering of phonons by isotopic impurities. For a crystal containing a fraction f_s of isotopes of type s with a difference of mass ΔM_s with respect to the average isotopic mass $M_{avg} = \sum_s f_s M_s$, assuming that the isotopes are distributed randomly, one can use the following expression of the scattering probability rate [5, 53, 54, 55, 56, 57]

$$P_{\nu,\nu'}^{isot} = \frac{\pi}{2N_q}\omega_\nu\omega_{\nu'}\left[n_\nu(n_{\nu'}+1)\right]\sum_s f_s\left(\frac{\Delta M_s}{M_{avg}}\right)^2\left|\sum_\alpha z_\nu^{s\alpha *}\cdot z_{\nu'}^{s\alpha}\right|^2\delta(\omega_\nu - \omega_{\nu'}) \tag{1.30}$$

Large isotope effects have been found for several systems such as diamond [5, 58], graphene [59], gallium nitride (GaN) [60], cubic boron nitride (c-BN) [61], boron antimonide (BSb) [61], beryllium telluride (BeTe) [61] and germanium carbide (GeC) [61].

The scattering rate (1.30) has also been used to predict the spectral phonon relaxation times and the thermal conductivity of doped materials and even alloys [62].

1.2.5 Other sources of scattering.

As has already been mentioned, other scattering mechanisms might be present in material such as, for instance, the scattering of phonons by electrons in light materials or the scattering of phonons by dislocations. They are not considered in this work.

1.3 Boltzmann Transport Equation

1.3.1 Full Boltzmann Transport Equation

Now, when the scattering probabilities are derived, one can write down the resulting total scattering rate $\frac{\partial n_\nu}{\partial t}\Big|_{scatt}$ which balances the diffusion term in the Boltzmann Transport Equation (1.19). The total scattering rate of a particular phonon mode ν due to intrinsic (elastic) three-phonon scattering with two other phonons ν' and ν'' is a sum over all possible three-phonon processes [27]

$$\frac{\partial n_\nu}{\partial t}\bigg|_{ph-ph} = \sum_{\nu',\nu''} \left[(P^{\nu,\nu'}_{\nu''} - P^{\nu''}_{\nu,\nu'}) + \frac{1}{2}(P^{\nu}_{\nu',\nu''} - P^{\nu',\nu''}_{\nu}) \right] \tag{1.31}$$

where the probability $P^{\nu''}_{\nu,\nu'}$ and $P^{\nu',\nu''}_{\nu}$ are given by (1.24) and (1.25) respectively. Here the factor $\frac{1}{2}$ comes from the fact that we count $|\nu\rangle \to |\nu'\rangle + |\nu''\rangle$ and $|\nu'\rangle + |\nu''\rangle \to |\nu\rangle$ processes twice when summing over all possible ν' and ν'' in eq. (1.31) [63].

The total scattering rate due to the elastic scattering of phonon with isotopic impurities is given by [5]

$$\frac{\partial n_\nu}{\partial t}\bigg|_{iso} = \sum_{\nu'} P^{iso}_{\nu,\nu'} \tag{1.32}$$

where the probability $P^{iso}_{\nu,\nu'}$ from eq. (1.30). Finally, the third term in equation (1.20) represents the scattering of phonon ν with boundary

$$\frac{\partial n_\nu}{\partial t}\bigg|_{iso} = P^{be}_{\nu} \tag{1.33}$$

where P^{be} is the probability of boundary scattering from eq. (1.29).

Finally, the Boltzmann Transport Equation can be written as

$$\mathbf{c}_\nu \cdot \nabla T \left(\frac{\partial n_\nu}{\partial T} \right) = \sum_{\nu',\nu''} \left[(P^{\nu,\nu'}_{\nu''} - P^{\nu''}_{\nu,\nu'}) + \frac{1}{2}(P^{\nu}_{\nu',\nu''} - P^{\nu',\nu''}_{\nu}) \right] + \sum_{\nu'} P^{iso}_{\nu,\nu'} + P^{be}_{\nu} \tag{1.34}$$

1.3.2 Linearization of the Boltzmann Transport Equation

The obtained Boltzmann Transport Equation (1.34) can be linearized, if one assumes the deviation f_ν of phonon exact distribution n_ν from the equilibrium Bose-Einstein distribution $n^0_\nu = (e^{\hbar\omega_\nu/k_BT} - 1)^{-1}$ to be small. Moreover, I assume that the temperature

gradient is established in x direction. Then, replacing $\left(\frac{\partial n_\nu}{\partial T}\right) = \left(\frac{\partial n^0_\nu}{\partial T}\right)$ and writing the non-equilibrium phonon distribution as

$$n_\nu = n^0_\nu - \left(\frac{\partial n^0_\nu}{\partial \hbar\omega_\nu}\right)\frac{\partial T}{\partial x}\cdot f_\nu \tag{1.35}$$

we arrive at the linearized Boltzmann Transport Equation

$$-c_\nu\left(\frac{\partial n^0_\nu}{\partial T}\right) = \sum_{\nu,\nu'}\left[P^{\nu''}_{\nu,\nu'}(f_\nu + f_{\nu'} - f_{\nu''}) + \frac{1}{2}P^{\nu',\nu''}_{\nu}(f_\nu - f_{\nu'} - f_{\nu''})\right] + \\ + \sum_{\nu'} P^{iso}_{\nu,\nu'}(f_\nu - f_{\nu'}) + P^{be}_\nu f_\nu \tag{1.36}$$

where c_ν is the group velocity projection on the direction of heat propagation in crystal. The resulting equation is linear and can be written in the matrix form following [5]

$$\mathbf{A}\cdot\mathbf{f} = \mathbf{b} \tag{1.37}$$

where $\mathbf{A}$ is a scattering matrix defined as

$$A_{\nu,\nu'} = \underbrace{\left[\sum_{\nu'',\nu'''}\left(P^{\nu''}_{\nu,\nu'''} + \frac{P^{\nu''',\nu''}_{\nu}}{2}\right) + \sum_{\nu''}P^{iso}_{\nu,\nu''} + P^{be}_\nu\right]\delta_{\nu,\nu'}}_{\mathbf{A^{out}}} \underbrace{-\sum_{\nu''}(P^{\nu'}_{\nu,\nu''} - P^{\nu,\nu'}_{\nu''} + P^{\nu',\nu''}_{\nu}) + P^{iso}_{\nu,\nu'}}_{\mathbf{A^{in}}} \tag{1.38}$$

and $\mathbf{b}$ is a vector consisting of the known quantities

$$b_{\nu'} = -c_{\nu'}\hbar\omega_{\nu'}n^0_{\nu'}(n^0_{\nu'}+1) \tag{1.39}$$

As can be seen from (1.38), the scattering matrix $\mathbf{A}$ can be separated into two parts, $\mathbf{A^{out}}$ and $\mathbf{A^{in}}$, where the former is diagonal [5]. This diagonal term, in turn, can be written in the following form

$$A^{out}_{\nu,\nu'} = \frac{n^0_\nu(n^0_\nu+1)}{\tau^R_\nu}\delta_{\nu,\nu'} \tag{1.40}$$

where τ^R_ν denotes the total relaxation time of phonon mode ν defined via Matthiessen's rule

$$\frac{1}{\tau^R_\nu} = \frac{1}{\tau^{ph-ph}_\nu} + \frac{1}{\tau^{be}_\nu} + \frac{1}{\tau^{iso}_\nu} \tag{1.41}$$

where the inverse relaxation time due to phonon-phonon interaction is given by

$$\frac{1}{\tau^{ph-ph}_\nu} = \frac{\Gamma_\nu}{\hbar} = \frac{\pi}{\hbar^2 N_0}\sum_{\nu'}\frac{\left|V^{(3)}(\nu,\nu',\nu'')\right|^2}{\omega_\nu\omega_{\nu'}\omega_{\nu''}}\Big[2(n^0_{\nu'} - n^0_{\nu''})\delta(\hbar\omega_\nu + \hbar\omega_{\nu'} - \hbar\omega_{\nu''})\delta_{\mathbf{q}+\mathbf{q}'-\mathbf{q}'',\mathbf{G}} + \\ + (1 + n^0_{\nu'} + n^0_{\nu''})\delta(\hbar\omega_\nu - \hbar\omega_{\nu'} - \hbar\omega_{\nu''})\delta_{\mathbf{q}-\mathbf{q}'-\mathbf{q}'',\mathbf{G}}\Big] \tag{1.42}$$

and the relaxation time due to the boundary effects is

$$\frac{1}{\tau_\nu^{be}} = \frac{|\mathbf{c}_\nu^{\mathbf{b}}|}{LF} \tag{1.43}$$

and, finally, the relaxation time due to the isotopic scattering is

$$\frac{1}{\tau_\nu^{iso}} = \frac{\pi}{2N_q}\omega_\nu^2 \sum_{\nu'} \delta(\hbar\omega_\nu - \hbar\omega_{\nu'}) \sum_s f_s \left(\frac{\Delta M_s}{M_{avg}}\right)^2 \left|\sum_\alpha z_\nu^{s\alpha *} \cdot z_{\nu'}^{s\alpha}\right|^2 \tag{1.44}$$

1.3.3 Expression of the thermal conductivity.

To obtain the lattice thermal conductivity one needs to explicitly write down the phonon heat flux (1.5) in Fourier's law (1.4), that results in the following equality

$$-\kappa\nabla T = \frac{1}{N_{\mathbf{q}}V}\sum_\nu \hbar\omega_\nu \mathbf{c}_\nu n_\nu \tag{1.45}$$

Then, the linearized Boltzmann Transport Equation can be formally solved by inversion of the scattering matrix, *i.e.* $\mathbf{f} = \mathbf{A}^{-1}\mathbf{b}$, that gives the first-order deviation f_ν of phonon exact distribution n_ν from the equilibrium Bose-Einstein distribution.

By substituting the linearized out-of-equilibrium phonon distribution (1.35) into (1.45) and taking into account the fact that the equilibrium flux is zero, $\mathbf{J_0} = \sum_\nu \hbar\omega_\nu \mathbf{c}_\nu n_\nu^0 = 0$, we arrive at the following expression for the lattice thermal conductivity

$$\kappa = -\frac{\hbar}{N_{\mathbf{q}}Vk_BT}\sum_\nu \omega_\nu n_\nu^0(n_\nu^0+1)\mathbf{c}_\nu^{heat}\boldsymbol{f}_\nu \tag{1.46}$$

that can be formally written as

$$\kappa = \lambda \mathbf{b}\cdot\mathbf{f} \tag{1.47}$$

with coefficient $\lambda = \frac{1}{N_{\mathbf{q}}Vk_BT}$. I will use equation 1.46 in my calculations.

1.4 Solution of the Boltzmann Transport Equation

1.4.1 Single mode relaxation time approximation

Let us assume that the diagonal part $\mathbf{A^{out}}$ of the scattering matrix gives a good estimation for the whole scattering matrix, such that $\mathbf{A} = \mathbf{A^{out}}$. This approximation is called the Relaxation Time Approximation (RTA) or the Single Mode Approximation (SMA). Then, the formal solution of the BTE can be written as

$$\mathbf{f^{RTA}} = (\mathbf{A^{out}})^{-1}\cdot\mathbf{b} \tag{1.48}$$

Substituting (1.48) into (1.47), one gets

$$\kappa^{RTA} = \lambda\mathbf{b}\cdot(\mathbf{A^{out}})^{-1}\cdot\mathbf{b} \tag{1.49}$$

Taking into account (1.39) and (1.40)

$$\kappa^{RTA} = \frac{\hbar^2}{N_{\mathbf{q}} V k_B T} \sum c_\nu^2 \omega_\nu^2 n_\nu^0 (n_\nu^0 + 1) \tau_\nu^R \tag{1.50}$$

Such an approximation is exact if the repopulation loses memory of the initial phonon distribution and if it is proportional to the equilibrium population of ν. It remains a good approximation if the repopulation is isotropic [5]. I note that in SMA (RTA) the Matthiessen rule 1.41 defines the full relaxation time of each phonon mode. This is not the case in the exact solution.

1.4.2 Exact solution: the iterative approach

To exactly solve the BTE, one must consider the whole scattering matrix $\mathbf{A} = \mathbf{A}^{out} + \mathbf{A}^{in}$

$$\mathbf{f} = \left(\mathbf{A^{out}} + \mathbf{A^{in}}\right)^{-1} \cdot \mathbf{b} \tag{1.51}$$

Considering $\mathbf{A}^{in}$ as a correction to $\mathbf{A}^{out}$, one can expand the right side of eq. (1.51) into geometrical series and obtain the following iterative solution [54] of the linearized BTE

$$\mathbf{f_i} = \sum_{j=0}^{i} \left(-(\mathbf{A^{out}})^{-1}\mathbf{A^{in}}\right)^j (\mathbf{A^{out}})^{-1}\mathbf{b} \tag{1.52}$$

Then, if the iterative solution $\mathbf{f_i}$ is known, the lattice thermal conductivity can be found from equation (1.47)

$$\kappa^{IT}(\mathbf{f_i}) = \lambda \mathbf{b} \cdot \mathbf{f_i} \tag{1.53}$$

It should be noted that the convergence can be achieved only if $(\mathbf{A^{out}})^{-1}\mathbf{A^{in}} < 1$.

1.4.3 Exact solution: the variational approach

Another more computationally efficient way to solve the linearized BTE is to employ a variational principle [27]. Since the scattering matrix $\mathbf{A}$ is symmetric, positive and semi-definite [5], one can minimize the following quadratic form

$$F(\mathbf{f}) = \frac{1}{2}\mathbf{f} \cdot \mathbf{Af} - \mathbf{b} \cdot \mathbf{f} \tag{1.54}$$

Indeed, the first variational derivative of functional $F(\mathbf{f})$ is equal to

$$\frac{\delta F(\mathbf{f})}{\delta \mathbf{f}} = \mathbf{Af} - \mathbf{b} \tag{1.55}$$

that gives exactly the Boltzmann Transport Equation for a minimal vector $\mathbf{f}^{min}$

$$\mathbf{Af^{min}} = \mathbf{b} \tag{1.56}$$

Then, the second variational derivative gives the scattering matrix that is positive

$$\frac{\delta^2 F(\mathbf{f})}{\delta \mathbf{f}^2} = \mathbf{A} > 0 \tag{1.57}$$

Alternatively, one can maximize the functional of thermal conductivity

$$\kappa^V(\mathbf{f}) = -2\lambda F(\mathbf{f}) \tag{1.58}$$

The resulting vector $\mathbf{f}^{min}$ that minimizes functional $F(\mathbf{f})$ in (1.54) gives the lattice thermal conductivity $\kappa(\mathbf{f}^{min}) = -2\lambda F(\mathbf{f}^{min})$. All other solutions $\mathbf{f}$ will result in lower values of the lattice thermal conductivity [5].

1.4.4 Conclusions

In this manuscript, most of the results have been obtained with the variational solution of the BTE described in Section 1.4.3. In Chapter 3, I also compare the exact solution with the one obtained with the Single Mode Approximation (SMA) of Section 1.4.1. Part of the analysis has been performed with the help of the results obtained with the iterative approach of Section 1.4.2. Both exact solutions, the variational solution and the iterative one, gives the same value of the lattice thermal conductivity in my calculations.

1.5 Phonon-phonon interaction

As we have seen in Section 1.2.2, the key ingredients to model the intrinsic phonon-phonon scattering are the anharmonic matrix elements. These matrix elements govern the phonon lifetimes (eq. (6.1)) and scattering rates (eqs. (1.24) and (1.25)), that determine the phonon transport in materials. In the following, I consider the existing approximations and computational methods to obtain the anharmonic matrix elements.

1.5.1 The long-wave approximation (LWA)

From the elastic theory, one can obtain for the long-wave acoustic phonons the following approximate expression for the anharmonic matrix elements [64, 65, 66]

$$V^{(3)}(\mathbf{q}, \mathbf{q}', \mathbf{q}'') = \sum_{\alpha\beta\mu\nu\zeta\xi} S_{\alpha\beta,\mu\nu,\zeta\xi} \times \mathbf{q}_\alpha \mathbf{q}'_\gamma \mathbf{q}''_\mu \times \mathbf{e}_\beta \mathbf{e}_\delta \mathbf{e}_\nu \tag{1.59}$$

where $\mathbf{q}_\alpha$ is a phonon wave-vector, $\mathbf{e}_\beta$ is the phonon polarization, $S_{\alpha\beta,\mu\nu,\zeta\xi}$ is a combination of the second and third-order elastic constants

$$S_{\alpha\beta,\mu\nu,\zeta\xi} = C_{\alpha\beta,\mu\nu,\zeta\xi} + \delta_{\alpha\mu} C_{\beta\nu,\zeta\xi} + \delta_{\alpha\zeta} C_{\mu\nu,\beta\xi} + \delta_{\mu\zeta} C_{\alpha\beta,\nu\xi} \tag{1.60}$$

and the Greek indices run over $\{x, y, z\}$.

However, to exactly calculate the anharmonic matrix elements (or anharmonic force constants) one must use advanced computational methods such as the supercell approach or the reciprocal space method that are described next.

1.5.2 The supercell approach: a real space method.

Both harmonic and anharmonic force constants can be extracted by the direct real space method. In this method a small displacement of an atom placed in a supercell is performed. This displacement produces the forces acting on the surrounding atoms. The ratio between the components of the induced force and the components of the imposed small displacement gives the harmonic force constants. The third and higher order anharmonic force constants, in turn, can be calculated from finite differences of forces.

However, since the real space method to extract the anharmonic force constants requires a supercell that contains several primitive unit cells, it is computationally very expensive. In general, one can reduce the number of force constants by applying the symmetries of the force constants that are deduced from the rotational and translational invariances of the system as well as from the symmetries of the crystal itself. This method has been recently implemented as a part of an open source code ShengBTE [67] and is described in detail, for instance, in Refs. [68] and [69].

1.5.3 The "2n+1" theorem: a reciprocal space method

The second-order interatomic force constants interpolated with the Fourier transform to the reciprocal space are called the dynamical matrices. These dynamical matrices can be obtained by using the density functional perturbation theory (DFPT) within the linear response formalism [70]. In this approach the small periodic displacements of atoms $\boldsymbol{u}_{\mathbf{q}}$ produce a perturbing potential and the resulting electron-density linear response of a system, determining the dynamical matrices, is calculated.

The anharmonic force constants interpolated with the Fourier transform to the reciprocal space are called the anharmonic matrix elements. In general, these matrix elements are given by the derivatives of the system total energy which, in turn, can be calculated by using the "$2n+1$" theorem. This theorem states that the knowledge of the derivatives of the wave functions up to order n allows one to calculate the derivatives of the energy up to order "$2n+1$" [70]. Thus, to calculate the third order derivatives of total energy, one needs to compute only the first order derivatives of the ground-state density and wave functions. As a positive consequence, this method does not require any expensive supercell calculations. Moreover, the responses to perturbations of different wavelengths are decoupled [70]. Recently, this method has been implemented by L. Paulatto *et al.* [6] and will be used further in this work.

1.6 Limitations of the formalism.

The lattice thermal conductivity of equation 1.46 relies on Fourier's law that, as we have seen in Section 1.1.3, is not appropriate for the description of second sound. However, using the BTE one can study the conditions for the hydrodynamic flow of phonons that is necessary for the existence of second sound. Namely, one must have

$$\Gamma^U < \Gamma^B < \Gamma^N \tag{1.61}$$

where Γ is phonon linewidth for Normal (N), Umklapp (U) and Boundary (B) scattering processes solely. In my formalism, the BTE yields only the stationary state for the non-equilibrium distribution function. The use of molecular dynamics is a possible solution to study the transition non-steady state and observe the propagation of heat pulse in form of second sound. Such simulations have not been done in this work.

1.7 Summary and outlook

In this Chapter I have briefly reviewed the general theory of thermal transport with emphasis on approaches used in this work for the thermal conductivity calculations. First, I have defined the thermal conductivity with empirical Fourier's law and I have discussed its possible violation resulting in the heat propagation in form of damped temperature wave instead of the usual diffusive propagation predicted by Fourier's law. Then, I have presented the Boltzmann Transport Equation that provides the out-of-equilibrium phonon distribution necessary for the determination of thermal conductivity. I have discussed in detail the scattering term that balances the diffusion. I have presented the analytical expressions of contributions to the total scattering rate due to phonon-phonon scattering, boundary scattering and isotopic scattering. Then, I reviewed the methods to solve the BTE such as RTA, iterative and variational approaches. Finally, I have reviewed the methods of calculation of three-phonon anharmonic coefficients that govern the magnitude of internal phonon-phonon scattering and define phonon lifetimes.

The next Chapter will be devoted to the brief up-to-date review of thermal and thermoelectric properties of bismuth and its compounds. I will also discuss some particular phenomena existing in bismuth at low temperatures such as phonon drag and second sound. Moreover, I will also shortly discuss the thermal conductivity of bismuth nanostructures and thin films.

Chapter 2

Material: bismuth.

This Chapter provides the description of the physical properties of bismuth with which my results will be compared. It is devoted to the brief review of thermal and thermoelectric properties of bismuth. First, in Section 2.1, I discuss an important historical role of bismuth as a material used in the first experiments with thermocouples that led to the discovery of thermoelectricity. Then, I consider the archetype role of bismuth for modern thermoelectric materials, such as bismuth telluride and the bismuth-antimony alloy, that are already used in technological applications nowadays. In Section 2.2, I show why pure bismuth still remains competitive for thermoelectricity and discuss in detail the ingredients that determine the figure of merit ZT: the Seebeck coefficient, the electrical conductivity and the thermal conductivity. In particular, I focus my attention on the remarkable thermal insulating properties of bismuth and discuss the difficulties in the experimental determination of the mechanisms governing thermal conduction in this material. I also briefly consider some interesting effects, such as the second sound and the phonon drag, observed in bismuth at low temperatures. In conclusion, in Section 2.5, I discuss bismuth nanostructures and bismuth thin films as promising candidates for thermoelectricity and outstanding thermal insulators.

2.1 Archetype material for thermoelectrics.

2.1.1 Seebeck effect on Bi/Sb thermocouple

Bismuth played an important role in the history of thermoelectricity. In 1821, a German physicist Thomas Johann Seebeck discovered the effect that bears his name on a bismuth-antimony thermocouple that is a circuit made from two dissimilar metals with junctions [71]. He found that a compass magnet is deflected when the junctions are put into the heat reservoirs of different temperatures. A schematic picture of the experiment is shown in Fig. 2.1. First, this effect has been mistakenly attributed to magnetic phenomenon. However, later Seebeck understood that the reason is the presence of an electric current flowing in the circuit. The discovered effect has been entitled in honor of T.J. Seebeck.

Seebeck's finding was only the first step in a series of exciting discoveries of thermo-

electric (Peltier, Thompson) and magnetothermoelectric (Nernst, Ettingshausen) effects. The importance of thermoelectric phenomena has been realized later in view of the possible applications to energy conversion and refrigeration. However, to widely use thermoelectricity in industry, one needs to enhance the thermoelectric efficiency. As has been mentioned in Chapter 1, this task is quite challenging since it requires the optimization of three independent quantities at the same time: the Seebeck coefficient S, the electrical conductivity σ and the thermal conductivity κ. Nowadays, the advanced methods on the interface of physics, chemistry and engineering are applied to solve this critical and important problem, in conjunction with the modeling of transport properties.

Today, bismuth still remains a competitive thermoelectric material due to its high Seebeck coefficient and low thermal conductivity. However, the electrical conductivity of bismuth is very low. Meanwhile, it was demonstrated that bismuth would be an outstanding material for n-type thermoelements, whenever the positive holes as minority carriers were absent [72].

Nowadays the attention of scientists is also attracted by the materials based on bismuth such as Bi_2Te_3 and the Bi-Sb alloy that will be discussed in the next paragraphs.

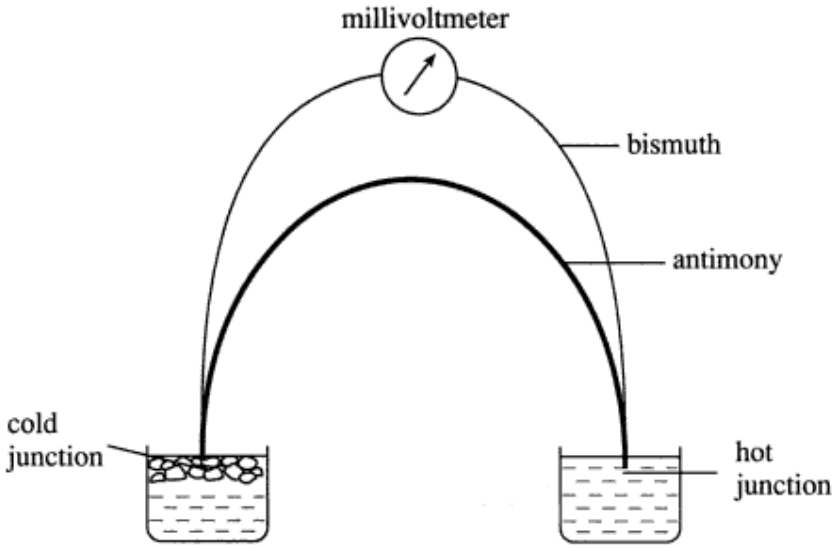

Figure 2.1: A schematic picture of a thermocouple based on bismuth and antimony metallic wires with two junctions put in the reservoirs at different temperatures. Due to the Seebeck effect, the established temperature difference leads to an electric current flowing in the circuit that can be detected by the attached voltmeter. The picture has been extracted from Ref. [73].

2.1.2 Bismuth compound: Bi_2Te_3

Bulk bismuth telluride is a narrow gap semiconductor with a high mean atomic weight [74]. In 1954 H.J. Goldsmid and R.W. Douglas first reported that bismuth telluride, Bi_2Te_3, is an efficient thermoelectric material [74]. In their experiment, they constructed a thermocouple by using melt-grown Bi_2Te_3, which turned out to have an excess of Bi atoms, leading to a p-type conduction, in conjunction with pure (n-type) bismuth. Later, n-type material based on Bi_2Te_3 doped with iodine donor impurities has been produced [75].

Generally, the inclusion of donor (Bi_2Se_3) and acceptor (Sb_2Te_3) impurities has proved to lead to much higher values of ZT for n-type and p-type Bi_2Te_3 [76]. To get the highest value of ZT, one needs to optimize the stoichometry of an alloy. However, it has been firmly established that ZT at ambient temperature has a maximum value of 1.0 for large-grained p-type $(Bi\text{-}Sb)_2Te_3$ and is almost as high as 0.9 for aligned n-type $Bi_2(Se\text{-}Te)_3$ [76]. Significant advances can be achieved by nanostructuring. Recently, the values $ZT = 1.41$ for nanostructured p-type $Bi_{0.5}Sb_{1.5}Te_3$ and $ZT = 1.19$ for nanostructured n-type $Bi_2Te_{2.82}Se_{0.18}$ have been reported [76].

The superior thermoelectric properties of Bi_2Te_3 are reinforced by the low values of the thermal conductivity that are due to the high mean atomic weight of this alloy and to a strong impurity (isotopic) scattering. The lattice thermal conductivity at T = 300 K for different concentrations of Sb_2Te_3 and Bi_2Se_3 are shown in Fig. 2.2. As one can see, the minimum values $\kappa_L \approx 0.45$ $Wm^{-1}K^{-1}$ for $x \approx 62\%$ of Sb_2Te_3 and $\kappa_L \approx 0.90$ $Wm^{-1}K^{-1}$ for $x \approx 25\%$ of Bi_2Se_3 have been measured in experiments [77]. These values are lower than $\kappa_L \approx 1.3$ $Wm^{-1}K^{-1}$ in pure Bi_2Te_3 [77].

Bismuth telluride is the material that is already used in a variety of thermoelectric applications such as thermoelectric coolers and thermoelectric generators [30].

2.1.3 Bismuth alloys: Bi-Sb

Another potentially important thermoelectric material is the alloy of bismuth and antimony[1] [72]. Addition of Sb acts as a neutral dopant, and thus the concentrations of electrons and holes are equal in both Bi and in the Bi-Sb alloy [80]. However, the band structure of Bi-Sb alloy changes as a function of Sb concentration. Its evolution is schematically shown in Fig. 2.3 [79]. As one can see, in pure bismuth there is an overlap between the highest valence band at T point and the lowest conduction band L_s at L point resulting in the semimetallic structure of Bi. With the increase of Sb concentration, the valence band at T point goes down very fast opening the band gap at a Sb concentration of $x = 7\%$. Thus, the Bi-Sb alloy becomes semiconducting and remains so until the valence band at the H point has the same energy as the conduction band at L, forming a semimetallic state for a $x = 22\%$ Sb concentration [78, 79]. A maximum positive gap in the semiconducting state of about 30 meV has been observed at Sb concentrations $15 < x < 17\%$ [72, 79]. The presence of the energy gap in semiconducting Bi-Sb alloys results in the enhancement of the Seebeck coefficient [80].

The differences in the atomic properties[2] of Bi and Sb lead to the formation of local

[1] Similarly to Bi, Sb is also a group V semimetal with the same A7 rhombohedral structure.

[2] The atomic masses of Bi and Sb differ by a factor of 1.71: $M_{Bi} \approx 209$, $M_{Sb} \approx 122$

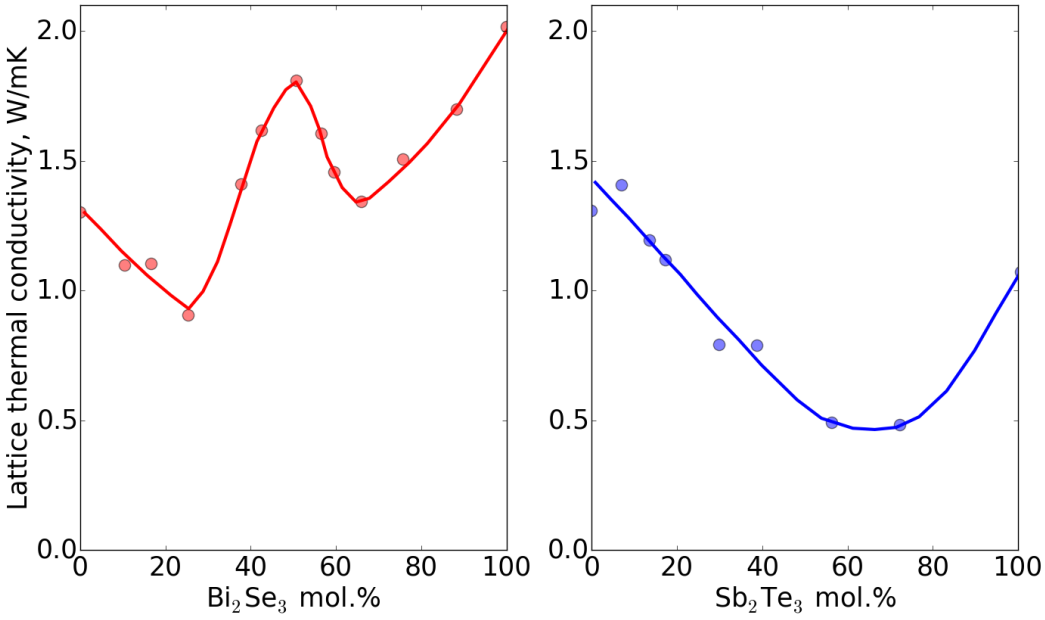

Figure 2.2: Lattice thermal conductivity of Bi_2Te_3 at T = 300 K as a function of Bi_2Se_3 (left panel) and Sb_2Te_3 (right panel) concentrations. The points and lines denote the measured values and interpolations reproduced after Ref. [77]. The anoumalous sharp rise in κ in the range of 25-50 % of Bi_2Te_3 concentrations might be explained by the superlattice formation in experiment [75].

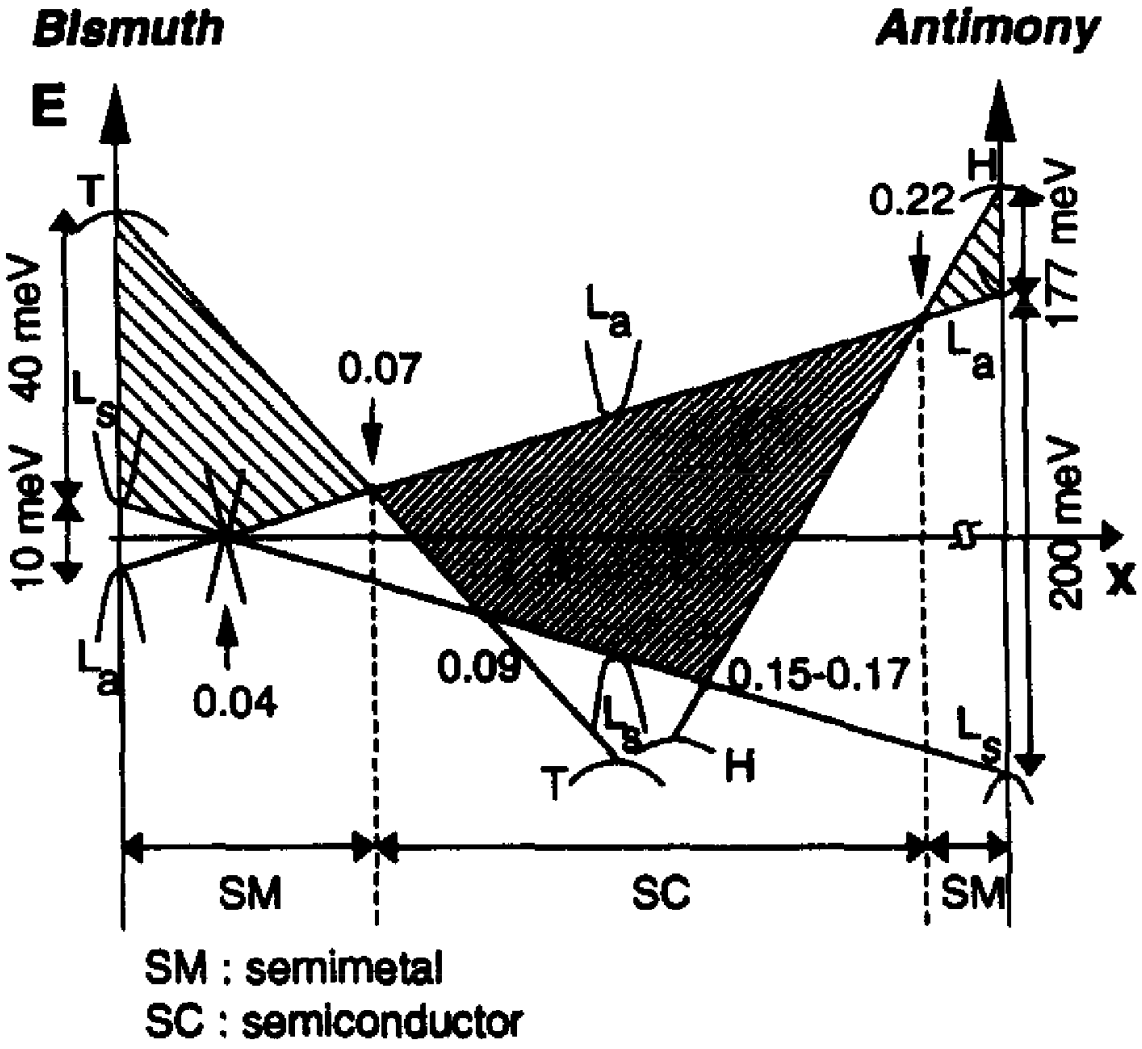

Figure 2.3: Schematic illustration of the band edge configuration of $Bi_{1-x}Sb_x$ alloys as a function of Sb concentration x at $T = 0$ K. The band edges at T and L high-symmetry points in the Brillouin zone and the point H of the hole extremum experimentally observed in Ref [78] are denoted by the corresponding letters. The semiconducting state is observed in the range of Sb concentrations $7\% < x < 22\%$. The picture is extracted from Ref. [79].

defects at antimony-atom sites in the crystal lattice of Bi-Sb alloy, which causes the intense scattering (similar to isotopic scattering) of phonons by these defects [81]. The magnitude of this scattering can be enhanced with the number of defects (the Sb concentration) in an alloy. This results in the reduced lattice thermal conductivity[3], which also helps to increase the thermoelectric figure of merit [81, 48].

However, the energy band gap in semiconducting Bi-Sb alloys is too small to be used in thermoelectric applications at ordinary temperatures. For instance, at ambient temperature the figure of merit is $ZT = 0.20$ in the binary direction and $ZT = 0.31$ in the trigonal direction at Sb concentration of 12% close to the gap maximum [83]. Nevertheless, Bi-Sb alloy significantly improves its thermoelectric properties at lower temperatures. For the same alloy with 12% Sb concentration at T = 120 K, the figure of merit is increased to $ZT = 0.25$ in the binary direction and $ZT = 0.51$ in the trigonal direction [83].

Despite of all the advantages of Bi-Sb alloys, like higher Seebeck coefficient and lower thermal conductivity with respect to pure Bi, it should be mentioned that the homogeneous single crystal Bi-Sb alloys are exceedingly difficult to produce technologically [80, 84].

2.1.4 Conclusion.

In conclusion, there is presently a high research activity in the development of new materials based on bismuth and in the study of their thermoelectric properties [76, 72]. These studies show that the highest ZT values can be achieved in nanostructured and doped materials of optimized stoichiometry.

2.2 Thermoelectric properties of bismuth

Bismuth is a semimetal with remarkable and highly anisotropic transport properties such as long carrier mean free paths, small effective masses at L point [4] and long electron wavelengths [15, 85]. It is close to be a good thermoelectric material because of the asymmetry between electron and hole densities of states, which make the thermopower S high [12], and also because of the high mean atomic weight resulting in the low intrinsic lattice thermal conductivity [15]. However, the presence of two types of carriers, electrons and holes, at the same time and approximately equal (and low) concentrations is not advantageous for the electrical conductivity that is about two orders of magnitude lower than in metals [14]. Moreover, it results in the additional bipolar contribution which is estimated to give respectively about 29% and 12.5% of the total thermal conductivity in the binary direction and trigonal directions at ambient temperature [8] (see Section 2.4).

The thermoelectric figure of merit in two principal directions, along the trigonal axis (green solid line) and along the binary axis perpendicular to the trigonal one (blue solid line), is shown in Fig. 2.4. As one can see, ZT is almost 6.5 times higher if the current flows in the trigonal direction, rather than in the binary direction [8]. Below I consider

[3] In Bi-Sb alloy at $T > 20$ K there is also an important contribution to thermal conductivity due to the charged carriers [81]. This component has been found to be major in the region of temperatures $77 < T < 300$ K [82].

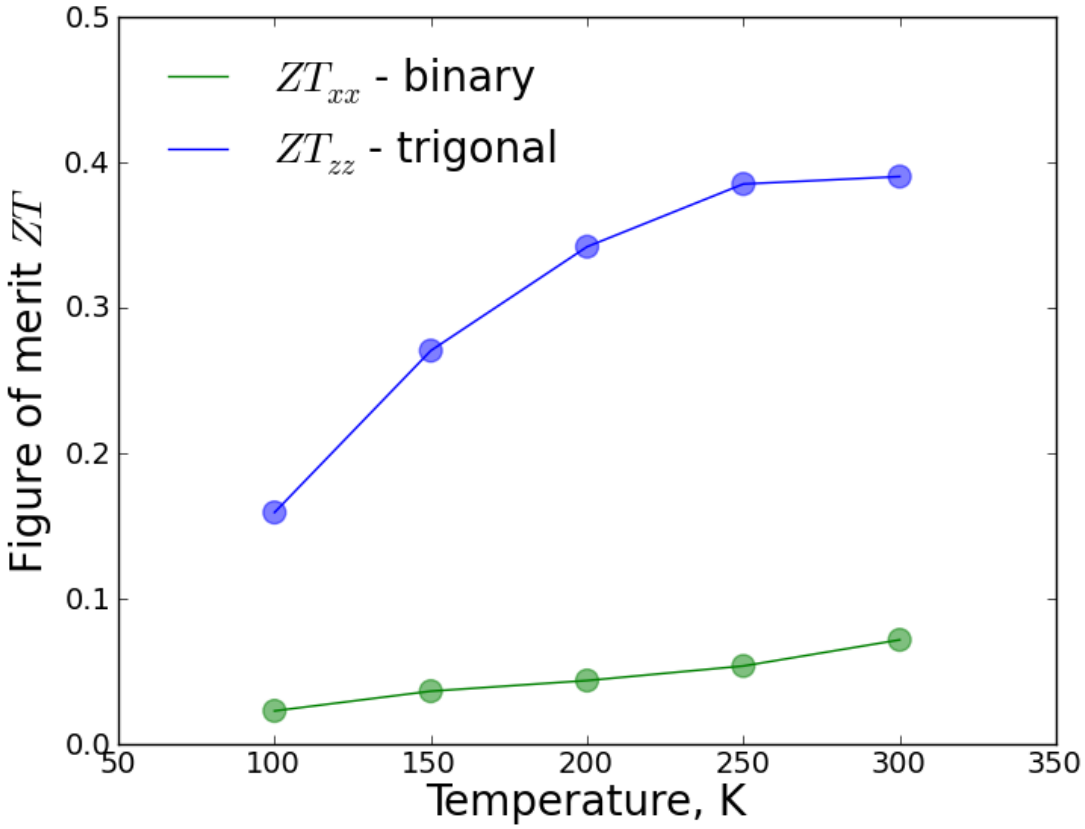

Figure 2.4: Temperature variation of the thermoelectric figure of merit ZT of bismuth in the binary and trigonal directions. Reproduced after Ref. [14].

all three ingredients determining the thermoelectric figure of merit separately and show that this giant anisotropy results from the Seebeck coefficient S and from the thermal conductivity κ.

2.3 Electronic properties of bismuth: electrical conductivity and Seebeck coefficient

2.3.1 Electrical conductivity.

Bismuth has a very low density of charge carriers, electrons and holes, $n = p = 2.7 \cdot 10^{18}$ cm^{-3} at T = 300 K that is more than four times less than values in typical metals $n \sim 10^{23}$ cm^{-3} [86]. The density decreases even more with the decrease of temperature reaching the value of $n = p = 3.0 \cdot 10^{17}$ cm^{-3} at liquid helium temperature. Thus, one can expect to get very low values of the electrical conductivity as well. However, as one can see in Fig. 2.5 the electrical conductivity of bismuth has a value of $\sigma \approx 10^6$ Sm^{-1} that is only two orders of magnitude lower than in metals $\sigma_{metal} \sim 10^8$ Sm^{-1}. It is explained by the very small effective masses of carriers in bismuth ($m^* \sim 0.001 m_e$) with respect to the free electron mass m_e. It results in the high carrier mobilities that compensate a low density of charge carriers and leads to values of the electrical conductivity higher than those expected from the densities of charged carriers [14].

One can also see in Fig. 2.5 that the electrical conductivity is almost isotropic and grows as T^{-1} with the decrease of temperature. At ultra-low temperatures the regime changes to T^{-2} growth and reaches the value of $\sigma \approx 5 \cdot 10^8$ Sm^{-1} [14].

2.3.2 Seebeck coefficient

The Seebeck coefficient S, or thermopower, enters the thermoelectric figure of merit as S^2. It has been defined in Eq.1.2 as the ratio between the thermoelectric voltage and the gradient of temperature. Generally, the diffusion and the phonon dragging of charge carriers are the two major mechanisms governing the Seebeck coefficient [14]. The resulting Seebeck coefficient contains the diffusion and phonon drag contributions, S_{diff} and S_{drag}, and the phonon drag contribution is estimated as

$$S_{drag} = S - S_{diff} \tag{2.1}$$

where S is the total Seebeck coefficient measured in experiment. The diffusion term in metals can be found with the Mott formula

$$S_{diff} = \frac{\pi^2 k_B^2}{3e\varepsilon_f} T \left. \frac{\partial \ln \sigma(\varepsilon)}{\partial \ln \varepsilon} \right|_{\varepsilon=\varepsilon_F} PAge29, titleofparagraph2.4.6 \tag{2.2}$$

where the energy-dependent electrical conductivity $\sigma(\varepsilon)$ is defined in

$$\sigma = \int \sigma(\varepsilon) \left(-\frac{\partial f(\varepsilon)}{\partial \varepsilon} \right) d\varepsilon \tag{2.3}$$

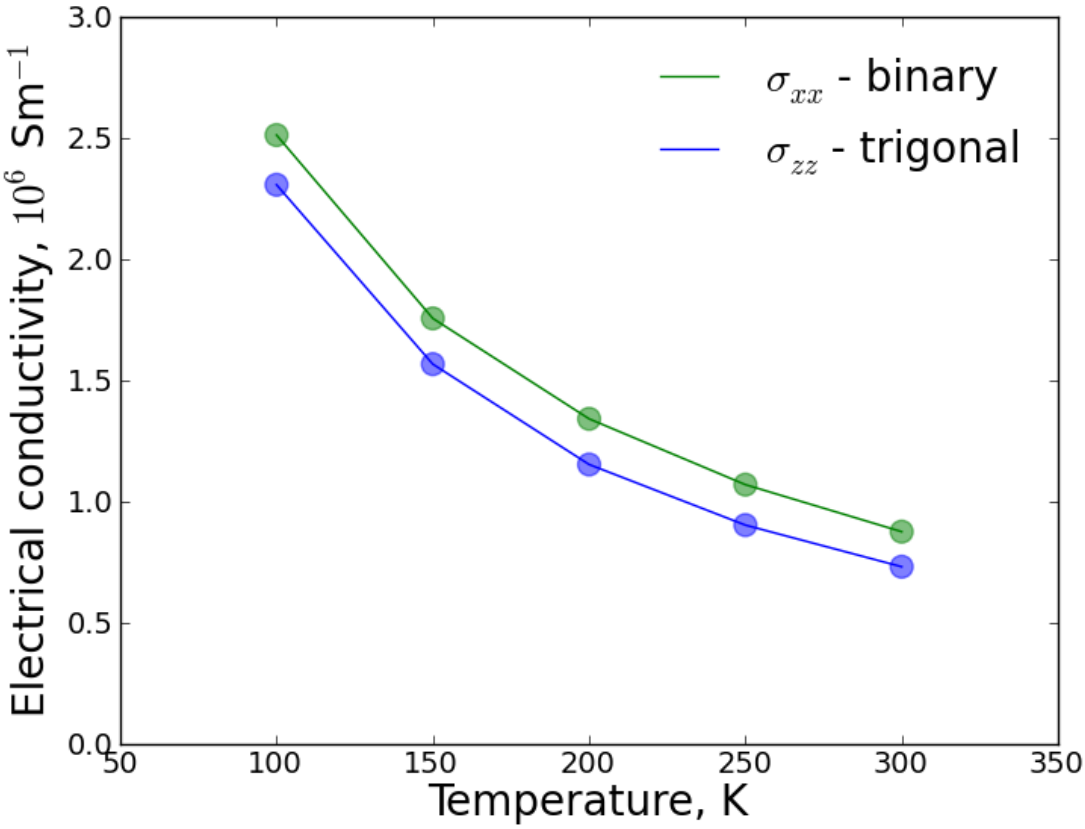

Figure 2.5: Temperature variation of electrical conductivity σ of bismuth in the binary (green curve) and trigonal (blue curve) directions. Reproduced after Ref. [8].

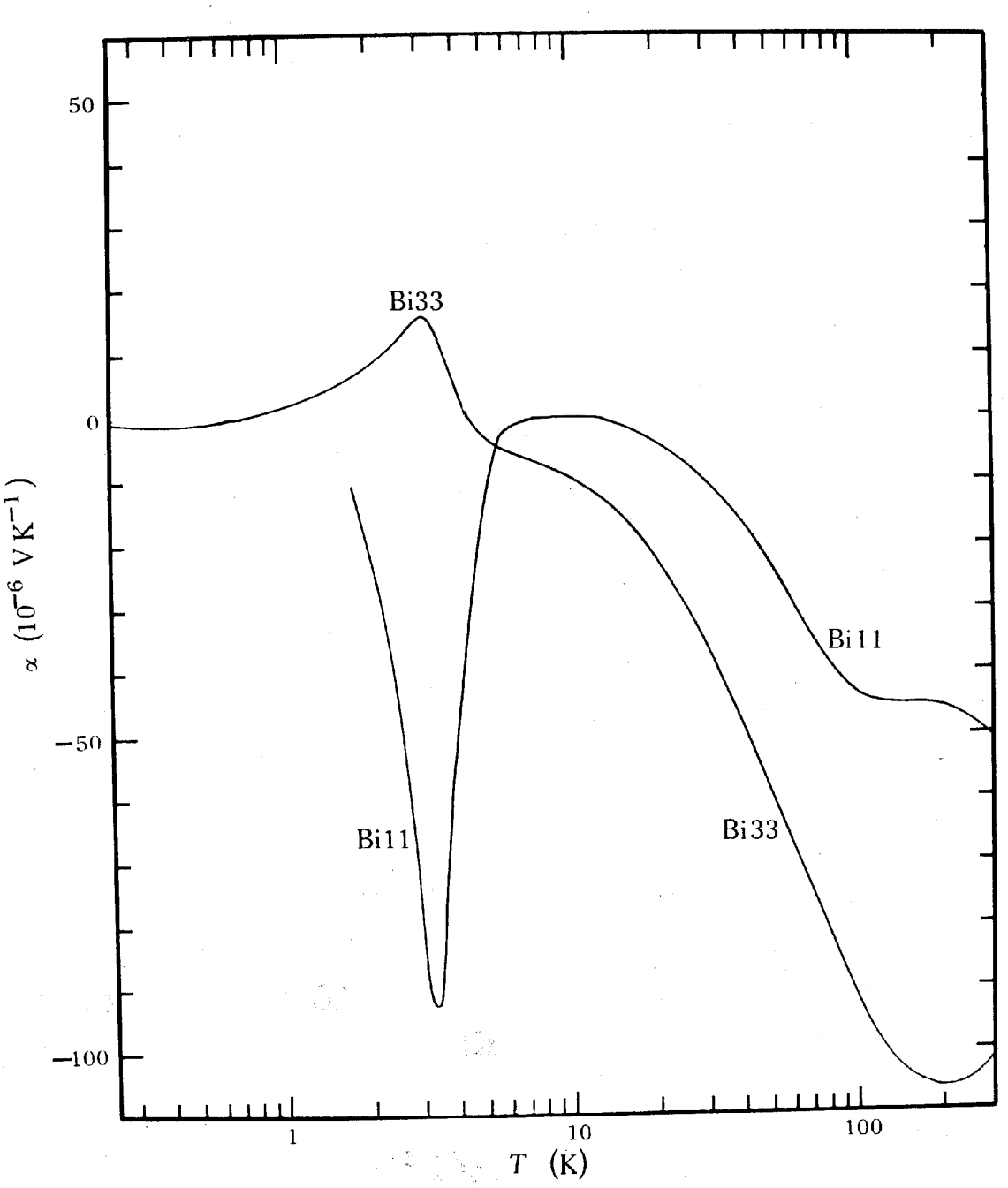

Figure 2.6: Temperature variation of the absolute Seebeck coefficient S of bismuth in the binary (Bi11) and trigonal (Bi33) directions. Reproduced after Ref. [14].

with $f(\varepsilon)$ being the equilibrium Fermi-Dirac distribution function. The diffusion part S_{diff} in Eq. 2.2 varies linearly with temperature and usually dominates at high temperatures [14]. It results from a very sensitive balance of energy current by charge carriers in a small shell right below and above the Fermi energy ε_F and is favored by the asymmetry of the electronic bands near the Fermi level [12, 13]. Diffusion takes place from hot to cold regions and is counterbalanced by the thermoelectric electromotive force (e.m.f.) ΔV in Eq. 1.2.

Semiconductors usually have the Seebeck coefficient $S \sim 10^{-3}$ VK^{-1} that is much higher than $S \sim 10^{-6}$ VK^{-1} in pure metals [14]. Semimetals like bismuth, in turn, possess intermediate values of the Seebeck coefficient $S \sim 10^{-4} - 10^{-5}$ VK^{-1} that is limited by the presence of two types of charge carriers at the same time. Indeed, if two types of carriers coexist, the absolute Seebeck coefficient S can be expressed as

$$S = \frac{\sigma_e S_e + \sigma_h S_h}{\sigma_e + \sigma_h} \tag{2.4}$$

where S_e and S_h are the partial Seebeck coefficients of electrons and holes, and σ_e and σ_h are the partial electrical conductivities of electrons and holes. The two contributions in the denominator have different signs and partially compensate each other.

The temperature variation of the absolute Seebeck coefficient of bismuth along the binary and trigonal directions is shown in Fig. 2.6. As one can see, the Seebeck coefficient is negative everywhere except of the small region below $T < 3$ K in the trigonal direction, demonstrating that the electronic part S_e is dominant. The absolute Seebeck coefficient is highly anisotropic and, in the high temperature region, shows maximum values of $S \approx -110 \times 10^{-6}$ VK^{-1} at $T \approx 200$ K in the trigonal direction and $S \approx -50 \times 10^{-6}$ VK^{-1} at $T \approx 300$ K in the binary direction. This high temperature behavior has been explained by Gallo *et al.* [8] by accounting only for the diffusion contribution of electrons and holes to the Seebeck coefficient.

2.3.3 Phonon drag

At low temperatures the Seebeck coefficient in the binary direction has a sharp and narrow peak with the maximum value of $S \approx -100 \times 10^{-6}$ VK^{-1} at $T \approx 3$ K. This peak has been attributed to the guide role of phonon drag mechanism which accounts for the drift of electrons dragged by the phonon flow [14, 87, 88]. The phonon drag process has a two-step character [89]. First, the non-equilibrium thermal phonons transfer an additional momentum to low-energy phonons via Normal phonon-phonon collisions. The transfer is especially intense at low temperatures, when Normal phonon collisions dominate over resistive Umklapp collisions. Then, the low-energy phonons transfer the momentum to electrons via electron-phonon interaction. The important role of low energy phonons is explained by the fact that they have a small enough wavevector to obey the conservation rules while interacting with electrons. In contrast, the phonon momentum of high energy thermal phonons substantially exceeds the characteristic momentum of electrons [89].

The phonon drag effect might also result in an enhancement of the electrical conductivity [14]. In principle, phonons should be less affected by electrons because of the

hight atomic masses comparing with electrons. However, to the best of my knowledge, there were no attempts to evaluate the effect of electron-phonon interaction on the lattice thermal conductivity in the phonon drag temperature region.

2.4 Thermal conductivity of bismuth.

Bismuth has the lowest thermal conductivity among all metals except mercury. This low thermal conductivity is explained mainly by its high atomic mass [15]. The thermal conductivity of bismuth is highly anisotropic and strongly varies with temperature, as shown in Fig. 2.7. As one can see, the thermal conductivity is lower in the trigonal direction than in the plane perpendicular to it. For example, at ambient temperature $\kappa_{tot} = 11.4$ WK^{-1}m^{-1} [8] in the binary direction and $\kappa_{tot} = 8.0$ WK^{-1}m^{-1} in the trigonal direction [90].

2.4.1 Heat transport mechanisms in bismuth.

Contrastingly to metals and insulators where electrons and phonons respectively are the only heat carriers, in bismuth there is no one single mechanism governing the heat transport at all temperatures [14]. The relative importance of different heat carriers changes with temperature and, thus, one needs to separate the lattice and non-lattice contributions. One of the objectives of this thesis is to provide *ab initio* data for the lattice part which will help separating the contributions and complement the experimental data where they are not available.

Material	**Lattice**	**Electrons, holes**	**Bipolar**
Insulator	All temperatures	-	-
Semiconductor	All temperatures	Usually weak	-
Metal	-	All temperatures	-
Bismuth	2-20 K	Below 1K, above 20K	Above 50 K
Antimony	Low temperatures	All temperatures	Weak
Arsenic	Low temperatures	All temperatures	-

Table 2.1: Summary of the major heat transport mechanisms existing in materials including the group V elements such as As, Sb and Bi. The table has been extracted from Ref [14].

Table 2.1 summarizes how most of the known heat transport mechanisms contribute to the total thermal conductivity of the materials [16]. As one can see, in bismuth at ultra-low temperatures below 2 K and temperatures from 20 K to 50 K the major role is played by the monopolar contributions of electrons and holes. At temperatures higher than 50 K a significant role is played by the bipolar thermodiffusion. When electron-hole pairs are created at the hot end of the sample, they flow down the temperature gradient and recombine at the cold end. This gives rise to the additional transport ionization energy [92]. Between 2 K and 20 K the heat is primarily transferred by phonons.

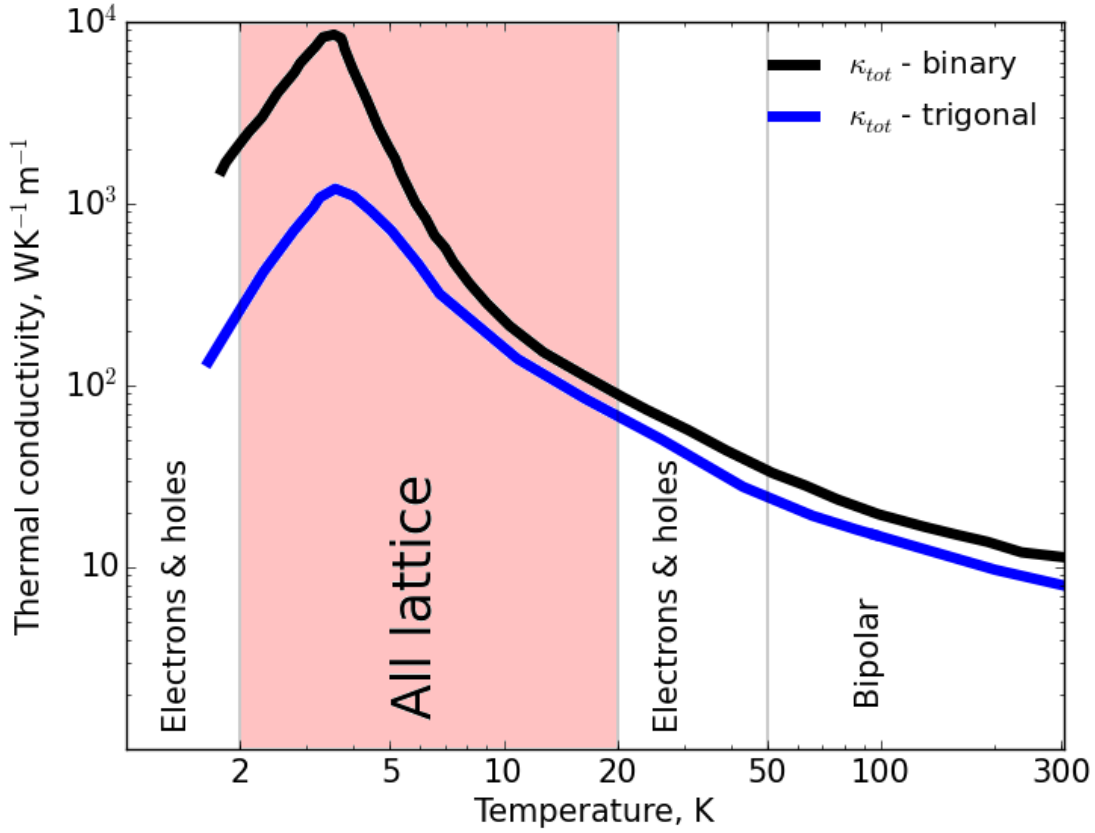

Figure 2.7: Total thermal conductivity measured in the binary (black curve) [14] and trigonal [91, 90] (blue curve) directions. The pink region denotes the temperature range where the lattice thermal conduction is found to be the single dominant mechanism of heat transport [14]. According to Ref. [14], other mechanisms are also indicated by vertical legends in the temperature regions were they are found to play a significant role.

2.4.2 Evaluation the non-lattice thermal conductivity.

The lattice thermal conductivity has been first evaluated by C. Gallo *et al.* [8] as a difference between the measured total thermal conductivity and the non-lattice part calculated analytically. The latter can be found as a sum of the ordinary monopolar contributions of electrons and holes, κ_e and κ_h, and an extra bipolar term κ_{eh} which exists in semimetals due to the presence of an equal amount of electrons and holes that move together in the same direction, transporting energy without carrying any net charge [16]

$$\kappa_E = \kappa_e + \kappa_h + \kappa_{eh} \tag{2.5}$$

The monopolar terms for electrons κ_e and holes κ_h can be estimated by means of the empirical Wiedmann-Franz law

$$\kappa_i = L_i T \sigma_i \tag{2.6}$$

where L_i is the Lorenz number and σ_i is the electrical conductivity due to electrons, $i = e$, and holes, $i = h$. The Lorenz number is known for metals $L_0 = 2.44 \times 10^{-8}$ $\mathrm{V^2K^{-2}}$ and supposes that the charge carriers are highly degenerate [14]. However, this condition does not hold in bismuth at high temperatures and instead the monopolar contributions to thermal conductivity can be expressed in a way analogous to semiconductors [14]

$$\kappa_i = T \left(\frac{k}{e}\right)^2 \gamma(\xi_e) \tag{2.7}$$

where

$$\gamma(\xi) = \frac{(s+\frac{7}{2})F_{s+\frac{5}{2}}(\xi)}{(s+\frac{3}{2})F_{s+\frac{1}{2}}(\xi)} \left[\frac{(s+\frac{5}{2})F_{s+\frac{3}{2}}(\xi)}{(s+\frac{3}{2})F_{s+\frac{1}{2}}(\xi)}\right]^2 \tag{2.8}$$

with $F_j(\xi) = \int_0^\infty \frac{x^j dx}{e^{x-\xi}+1}$ being the Fermi-Dirac integral and $\xi_i = E_f^i/k_B T$ are the adimensional Fermi energies of electrons and holes measured from the edges of their respective bands [93, 8]. The derivation of Eq. 2.5 relies on the assumption of the quadratic dispersion law $E(k) \sim k^2$ and assumes the power law for the charge carrier relaxation time $\tau_e = \tau_{e0} E^s$ with $s = -1/2$ for the dominant intravalley acoustic lattice scattering.

The bipolar contribution in Eq. 2.5 can be expressed as [93, 8]

$$\kappa_{eh} = T \frac{\sigma_e \sigma_h}{\sigma_e + \sigma_h} (S_e - S_h)^2 \tag{2.9}$$

κ_{eh} is particularly important when the mobilities of electrons and holes are comparable [16]. As one can see, the derivation of C. Gallo heavily relies on the description of the details of the band structure, which in principle can lead to inaccurate results, as I will show in Section 4.2.

2.4.3 Measurements under a strong magnetic field.

Another attempt to separate the lattice and non-lattice (charge carrier) contributions to thermal conductivity by means of a strong magnetic field has been applied by C. Uher

et al [16]. This method relies only minimally on an accurate theoretical description of the electronic properties of bismuth and thus avoids the drawbacks of Gallo's theoretical analysis. Application of a magnetic field does not change the lattice thermal conductivity, while the remaining non-lattice part is now associated with the non-vanishing Nernst and Ettingshausen coefficients and can be expressed as [16]

$$\kappa_{ii}^{E}(\mathbf{B}) = \bar{\kappa}_{ii}^{E}(\mathbf{B}) - T\alpha_{si}(-\mathbf{B})\sigma_{sl}(\mathbf{B})\alpha_{li}(\mathbf{B}) \tag{2.10}$$

where i denotes a crystallographic direction (1 - binary, 2 - bisectrix, 3 - trigonal), $\bar{\kappa}_{ii}^{E}(\mathbf{B})$ is a part of the charge carrier thermal conductivity vanishing when $B \to \infty$, $\alpha_{si}(\mathbf{B})$ is the thermomagnetic tensor, $\sigma_{sl}(\mathbf{B})$ is the galvanomagnetic tensor. These tensors, in turn, can be expressed in terms of partial Seebeck coefficients and charge carrier (electron and hole) mobilities.

By measuring the thermal conductivity $\kappa_{\perp}(\mathbf{B}) = \kappa_{11}(\mathbf{B})$ with the magnetic field along the bisectrix and trigonal axis, B_2 and B_3, and using the theoretical ratio $\frac{\kappa_{11}^{E}(B_2\to\infty)}{\kappa_{11}^{E}(B_3\to\infty)}$ for the remaining electronic part of the thermal conductivity, the lattice part of thermal conductivity can be determined [16]

$$\kappa_{\perp}^{L} = \kappa_{\perp}(B_3 \to \infty) - \frac{\kappa_{\perp}(B_2 \to \infty) - \kappa_{\perp}(B_3 \to \infty)}{\frac{\kappa_{11}^{E}(B_2\to\infty)}{\kappa_{11}^{E}(B_3\to\infty)} - 1} \tag{2.11}$$

When the temperature becomes sufficiently low, the second term in equation 2.11 vanishes and the lattice thermal conductivity is well approximated by the high magnetic field limit of the total thermal conductivity. As a limitation, the method requires the classical field conditions $\mu_i B_i \gg 1$, which restricts its application to low temperatures, since the mobilities in bismuth becomes small at high temperatures. The lattice thermal conductivity has been extracted only in the binary direction below 150 K [16].

2.4.4 Comparison of the experimental results.

To compare the results of the two approaches described above, I plot the measured lattice thermal conductivity in Fig. 2.8 (blue and red curves) and the total thermal conductivity (black curve) in the binary direction. As one can see, the results of Gallo (red curve) are considerably lower providing the value $\kappa_L \approx 6$ WK^{-1}m^{-1} at T $\approx$ 150 K, while Uher gets $\kappa_L \approx 10$ WK^{-1}m^{-1} that is more than 60% higher. However, the measurement of Uher does not rely on the electronic properties of bismuth, that are approximated by simple models in the estimation of Gallo, and, thus, are more preferable as I will show in Section 4.2. However, the recent study of Ref. [94] shows, that phonons might be sensitive to the presence of the magnetic field even in a diamagnetic material such as in InSb where the lattice thermal conductivity has been found to be decreased by 12%. Thus, the theoretical calculations should be performed to provide the reliable data of the lattice thermal conductivity that is an objective of this thesis.

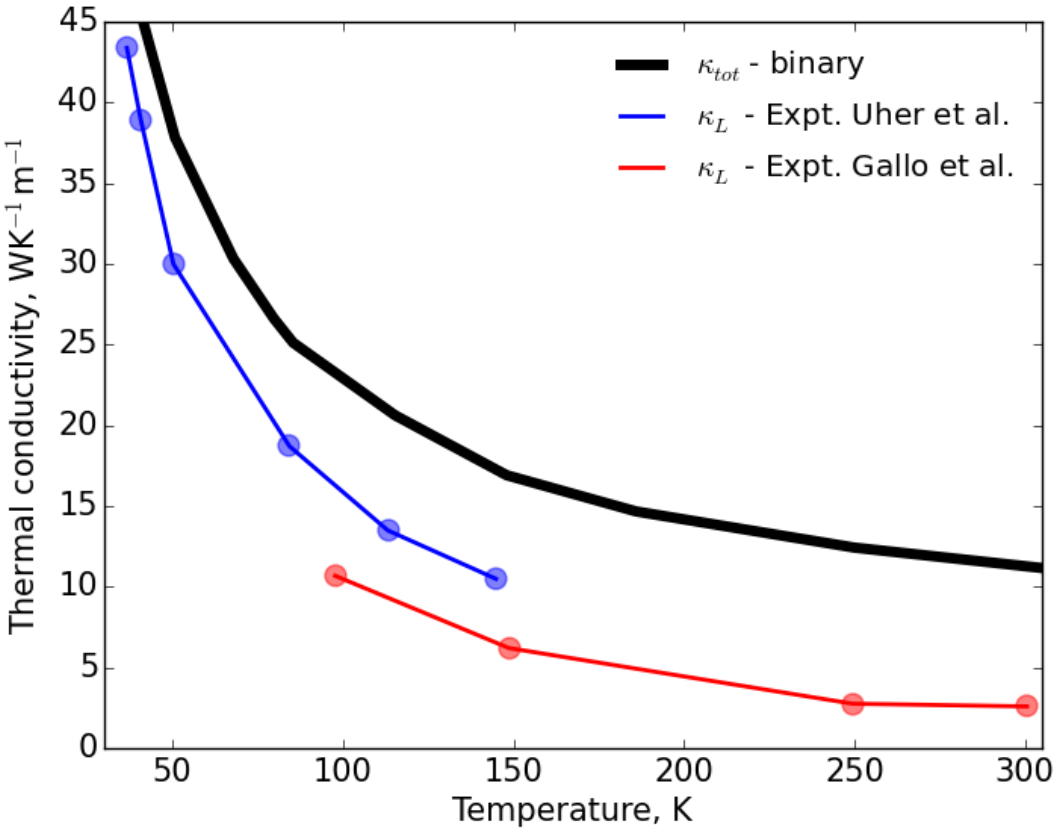

Figure 2.8: Lattice thermal conductivity in the binary direction estimated in the experiment of C. Gallo [8] (red curve) and measured by C. Uher [16] with the magnetic field method (blue curve). The total thermal conductivity from Ref. [14] is also shown (thick black solid curve).

2.4.5 Previous *ab initio* calculations of the lattice thermal conductivity.

The first attempt to calculate the lattice thermal conductivity of bismuth in the limited range of temperatures 50-300 K has been done and published in 2014 by S. Lee *et al.* from Massachusetts Institute of Technology (MIT). The authors used an iterative approach (see Section 1.4.2) to solve the BTE and a real space approach to compute the phonon-phonon matrix elements (see Section 1.5.2). In Chapter 3 I will also compare the results of my calculations with those of S. Lee.

2.4.6 Scattering mechanisms contributing to the lattice thermal conductivity.

Bismuth is an excellent substance for modeling of the lattice thermal conductivity and for the study of thermal transport regimes. In contrast to other materials, bismuth has only one single isotope and, thus, high quality (high purity) Bi single crystals are available for experiments [87]. The electron-phonon scattering does not expect to significantly contribute to the lattice thermal conductivity at high temperatures due to the low concetration of charge carriers (10^{18} cm^{-3}) [14]. For instance, in Si the increase of carrier concentration up to 3 orders (from 10^{15} to 10^{18} cm^{-3}) results in the 2.8% decrease of the lattice thermal conductivity only [95]. Thus, in the most of the temperature range, thermal transport is determined by the competition between two major mechanisms: phonon-phonon scattering and phonon scattering by boundaries.

2.4.7 Second sound

In Chapter 1, I have shown that the violation of empirical Fourier's law results in the heat propagation in form of a damped temperature wave instead of a propagation with the diffusion equation described by Fourier's law 1.4. This temperature wave is called second sound. In Section 1.1.3, I have also discussed the capability of my formalism to predict the conditions necessary for the propagation of second sound in materials.

Due to its isotopic purity and high degree of chemical and physical perfection, bismuth is one of the materials where second sound has been observed experimentally [42]. In Fig. 2.9 one can see the detected signal of heat pulse propagating along the bisectrix direction over a distance of $l = 9.06$ mm. At the lowest temperatures T < 2.1 K there are three distinct peaks attributed to the ballistic propagation of three acoustic (one longitudinal and two transverse, fast and slow) phonon modes. Then, in the interval of temperatures 3 K $< T < 3.5$ K the damped second-sound mode consisting of a thermodynamic mixture of all three modes is registered by the detector [42]. With further increase of temperature, the pulse is broadened and delayed in arrival revealing the diffusion regime of propagation. The transition to the diffusive regime is related to the apparent role of resistive Umklapp processes that are activated with the increase of temperature.

The analogous behavior of heat pulse propagation has also been observed in the trigonal direction where the second sound is detected, for 2.1 K $< T < 3.5$ K [42].

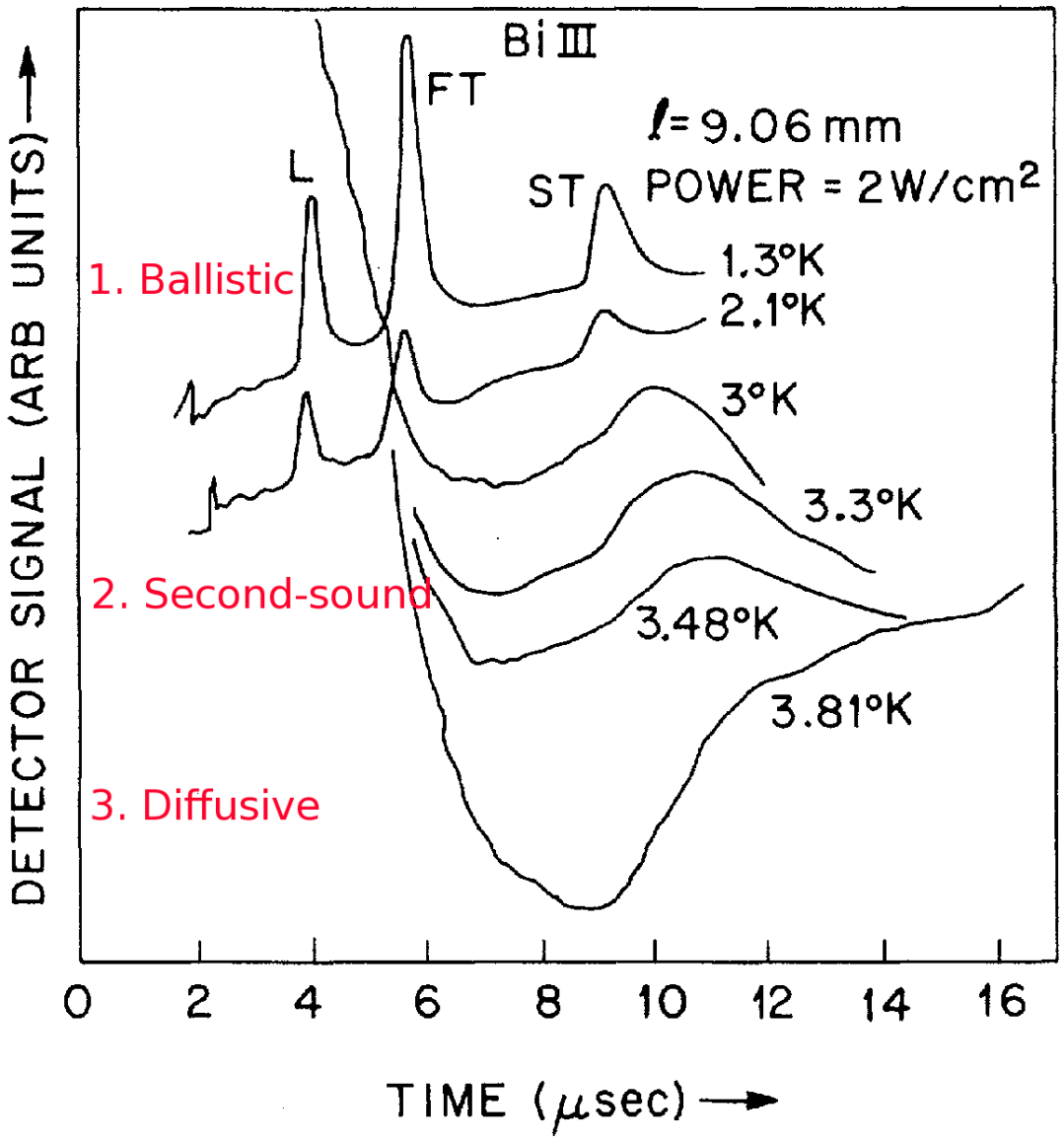

Figure 2.9: Heat pulse propagation in Bi along the bisectrix axis over a distance of $l = 9.06$ mm. The three different propagation regimes have been observed. First, the ballistic propagation of three acoustic (longitudinal L, fast transverse FT and slow transverse ST) modes is clearly identified at the two lowest temperatures $T = 1.3$ K and $T = 2.1$ K. Then, a wave-like propagation pulse corresponding to second-sound is detected at temperatures between 3 K $< T <$ 3.5 K. Finally, the heat pulse begins to diffuse at highest temperature T = 3.81 K. The figure has been extracted from Ref. [42].

2.5 Thermoelectric properties of bismuth nanostructures and thin films.

Since the works of L. D. Hicks and M. S. Dresselhaus, nanostructuring is known to be a promising route to enhance the thermoelectric properties of materials [17, 18]. First, nanostructuring on the scale of a few tens of nanometers, with the aim of opening a confinement-induced energy-gap [17, 18, 96], allows to break the electron-hole symmetry around the Fermi level and, thus, leads to the increase of the density of states [15]. As a result, the increase of the Seebeck coefficient S by several orders of magnitude in nanowires has been observed [96, 97].

Moreover, nanostructuring is known to reduce the lattice thermal conductivity by limiting the longest phonon mean free paths. This effect has been intensively studied in relatively simple materials such as Si [98, 99, 95, 100, 101, 102] and SiGe alloys [99, 103], but systematic studies are scarce in bismuth. A quasi-suppression of the thermal conductivity has been found in bismuth nanowires, but its origin is still debated [15]. Measurements made on thin films [19, 20, 21] and nanowires [22, 15, 23, 24, 25, 26] have yielded widely scattered values, preventing a deep understanding of the mechanisms at play in nanostructures [15]. Thus, a theoretical determination of the nanostructuring effect on the lattice thermal conductivity of bismuth has become mandatory and this is one of the objectives of this thesis.

2.6 Details of the calculations for the thermal conductivity of Bi.

In this Section I provide the technical details of my thermal transport calculations. In my work, phonon frequencies and group velocities have been computed within the density functional perturbation theory (DFPT) [70] on a 6×6×6 **q**-point grid in the Brillouin zone (BZ) centered at Γ. State-of-the-art calculations of the third-order anharmonic constants have been performed on a 4×4×4 **q**-point grid in the Brillouin zone which amounts to 95 irreducible ($\mathbf{q}_1$,$\mathbf{q}_2$,$\mathbf{q}_3$) phonon-triplets [6], where $\mathbf{q}_i$, i=1,3 are phonon wavevectors, and with $\mathbf{q}_1 = \mathbf{q}_2 \pm \mathbf{q}_3 + \mathbf{G}$. $\mathbf{G}$ is a vector of the reciprocal lattice, and both Normal and Umklapp processes have been taken into account exactly in the Boltzmann equation. Then, the third-order anharmonic constants were Fourier-interpolated on the 28×28×28 denser grid necessary for converged integrations in Eq. 1.46. The convergence has been checked at T = 5 K and T = 300 K. In the Boltzmann Transport Equation, the lattice thermal conductivity was accurately converged on a 28×28×28 **q**-point grid in the Brillouin zone with a Gaussian broadening of the detailed balance condition [5] taken to be $\sigma = 1$ cm^{-1}.

When I started my PhD work, progresses had already been achieved in the modeling of bismuth, to interpret photoemission data in photoexcited bismuth [1, 3]. A pseudopotential with $5d^{10}$ semi-core states included as valence states was used. However, phonon calculations were hardly feasible with this pseudopotential, which included 15 electrons in total. Thus, I decided to develop a new pseudopotential with $5d^{10}$ electronic states frozen

in core, and only 5 electrons in the valence. I took the 15 electron pseudopotential as a reference.

The details of my pseudopotental, equilibrium lattice parameters and electronic band structure are reported in Appendix A.

2.7 Conclusions.

Bismuth is an important material in the history of thermoelectricity. For many years it has been used as a foreground n-type material for thermocouples. This is due to its large Seebeck coefficient and low thermal conductivity. However, the thermoelectric efficiency of bismuth is limited by the presence of two types of charge carriers, electrons and holes, at the same time in approximately equal and low concentrations, which is not advantageous for the electrical conductivity and results in the additional bipolar contribution to the thermal conductivity. Thus, the attention of scientists nowadays is mainly focused on bismuth-based compounds, Bi_2Te_3 and Bi-Sb alloy, that inherit and even enhance the outstanding properties of bismuth and allow to overcome its drawbacks.

On the other hand, pure bismuth is a good thermal insulating material due to its low thermal conductivity. However, despite extensive studies, there are still many open questions concerning its thermal transport properties. In particular, the determination of dominant mechanisms governing thermal conduction at different temperatures and the magnitude of the lattice contribution to thermal conductivity remains unclear due to the complexity and limitations of experimental methods. Moreover, the systematic studies of the nanostructuring effect, which is known to suppress thermal conductivity resulting in the enhancement of thermoelectric and thermal insulating properties of material, are scarce in bismuth.

The answers to these questions will be given in Part II of the manuscript which is devoted to my results of *ab initio* simulations of thermal transport in bismuth as well as to the discussion of possible routes to reduce it. The methods I use, *ab initio* plus the Boltzmann Transport Equation, enables me not just to calculate the macroscopic quantities such as the lattice thermal conductivity but also to analyze the specific processes contributing to heat transport on microscopic level, as will be shown in Chapter 6.

Part II

Theoretical results

Chapter 3

Thermal conductivity of bismuth from first principles calculations

Introduction

A study of thermal conductivity is extremely important for a variety of technological applications like thermoelectric energy conversion and thermal management of electronics. However, most of the methods to compute the lattice thermal conductivity rely on theoretical models like the Callaway [104], Klemens [105, 106] or Herring models [107] which contain empirical fitting parameters. This limitation has motivated the development of numerical methods based on first principles and molecular dynamics that can predict the lattice thermal conductivity from the atomic structure, without any adjustable parameters and with accuracy greater than models relying on *ad hoc* parameters [62].

Thermal properties of bismuth are extremely interesting because of its low thermal conductivity. Bismuth is an excellent model substance for the study of thermoelectricity because its high Seebeck coefficient [14]. Moreover, bismuth-based compound Bi_2Te_3 is a typical thermoelectric materials used in industrial applications for mobile refrigerators [76].

In this chapter I will present the results of modeling of thermal properties of bismuth based on the Boltzmann transport equation (BTE) for the phonon system, coupled to fully *ab initio* data. These advanced techniques enable me to study the behavior of the lattice thermal conductivity over a wide range of temperatures, from ultra-low T up to the melting point. In addition, the analysis of the processes governing thermal conduction in bismuth on the microscopic level brings insights into the origin of the small value of thermal conductivity.

The chapter is organized as follows. In Section 3.1, I will describe vibrational properties of bismuth by means of *ab initio* calculations. I will demonstrate the crucial role of spin-orbit coupling (SOC) to obtain a correct phonon dispersion relation for acoustic phonons. In Section 3.2, I will discuss the role of acoustic-optical phonon interaction (AOPI) and I will present a model to modify the optical part of the dispersion to accurately describe the AOPI. In Section 3.3, I will present the results of calculation of the lattice thermal conductivity and I will show how they changed if the corrected AOPI is

taken into account. In Section 3.4, I will perform a detailed analysis of the heat transfer mechanisms in bismuth.

3.1 Vibrational properties of bismuth.

Phonons are quanta of the lattice vibrational field which play a crucial role in heat transport in materials [27]. In general, the lattice conduction of heat is a dominant mechanism in non-metals like semiconductors and insulators when an electronic gap is open. Moreover, it is also important in semimetals when the gap is zero but the density of electronic states at the Fermi level is small [6]. Thus a deep understanding of vibrational properties in materials is mandatory for an accurate description of their thermal properties.

As we have seen in the previous chapters, in the harmonic approximation, phonons are treated as independent quasiparticles. In this case their properties are entirely unaffected by the presence of other phonons. Each single phonon is characterized by the wave vector $\mathbf{q}$, polarization index j and energy $\hbar\omega_{\mathbf{q}j}$. The relationship between the phonon frequency $\omega_{\mathbf{q}j}$ (or phonon energy $\hbar\omega_{\mathbf{q}j}$) and the wave vector $\mathbf{q}$ is called a dispersion law. It is unique for every material and could be obtained experimentally from, for instance, inelastic neutron and inelastic X-ray scattering experiments on single crystals [27, 66, 108] or theoretically from *ab initio* calculations using either the frozen phonon method [109, 110] or the density-functional perturbation theory (DFPT) [70].

3.1.1 Phonon dispersion.

Bismuth possesses an A7 rhombohedral structure similar to other group-V semimetals such as As and Sb. There are two atoms per primitive unit cell which results in six phonon branches [111]. The three lowest branches are conventionally called acoustic. In the limit of small wave vector $\mathbf{q}$ (or long wavelength λ) these modes correspond to the propagation of usual sound waves traveling through the crystal. The three highest phonon branches, in turn, are called optical since they can interact either directly or indirectly with light [66]. In contrast with the acoustic branches, they always have non-zero frequencies at the Brillouin zone center.

In Fig. 3.1 I show the calculated phonon dispersion (black solid lines) of Bi along some high-symmetry directions obtained within the DFPT approach with the LDA norm-conserving pseudopotential developed in this work (see Section 2.6). The details of the pseudopotential generation, parameters of phonon dispersion calculation and the comparison of electronic band structure and phonon dispersion obtained with LDA and GGA exchange-correlation functionals are given in Appendix A. Another theoretical phonon dispersion found in the literature [56] (red dashed line) as well as experimental data from inelastic neutron scattering experiments (green circles [112] and blue circles [113]) are also shown in Fig. 3.1 for comparison. One can see that the acoustic branches of obtained phonon dispersion are in extremely good agreement with the existing experimental data and with the previous calculations.

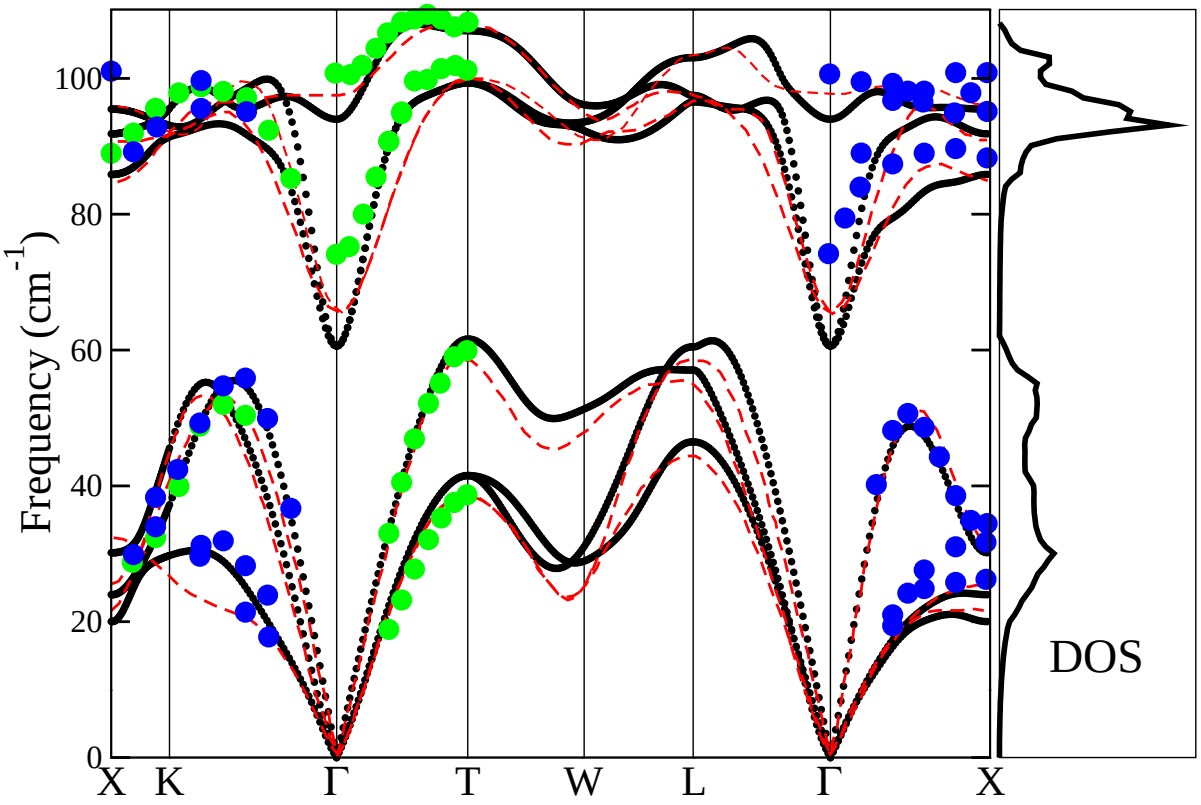

Figure 3.1: DFT-LDA calculated phonon dispersion in bismuth including spin-orbit coupling (black solid line, left panel) and the corresponding density of states (right panel). Previous theoretical results (also including spin-orbit interaction) are reproduced after Lee *et al.* [56] (red dashed line). Experimental data extracted from Ref. [112] (green circles) and Ref. [113] (blue circles).

The three-fold degeneracy which exists in the cubic structure is lifted in the rhombohedral bismuth by the Peierls distortion resulting in a two-fold degenerate E_g mode (displacement perpendicular to the trigonal axis) plus a one-fold A_{1g} mode (displacement parallel to the trigonal axis) [114]. The Γ-T direction in the Brillouin zone corresponds to the direction along the trigonal axis in the real space and preserves the trigonal symmetry. The trigonal symmetry imposes the degeneracy of the transverse optical and acoustic modes along Γ-T.

Another important direction in the Brillouin zone is Γ-K-X, which corresponds to the binary direction in the real space. The eigenvectors of the modes in this direction have two distinct symmetries: they are either symmetric (3^{rd}, 4^{th} and 5^{th} branches) or antisymmetric (1^{st}, 2^{nd} and 6^{th} branches) under a twofold rotation about the binary axis [115]. The branches are well separated near the zone center but show a significant mixing close to the zone boundary. For example, the highest longitudinal acoustic mode first crosses with the fast transverse mode near K point in the Γ-K direction and then becomes the lowest branch when approaching X point.

3.1.2 Acoustic phonons.

As has already been mentioned, in the limit of small wave vector **q** the acoustic branches of the spectrum correspond to the ordinary elastic sound waves propagating through the solid. The acoustic branches are linear in this region with the slope equal to the speed of sound propagating along the given direction. The obtained sound velocities for longitudinal and transverse modes in both trigonal and binary directions are shown in Table 3.2. The sound velocities observed in experiment [116] are also indicated in the Table. The difference between the experiment and theoretical values is small which validates an accurate description of the acoustic branches. In the following TAs and TAf label the transverse acoustic branches having slow and fast sound velocities respectively.

Alternatively, vibrational properties in the elastic region have been described with the second-order elastic constants. By definition the elastic constants are the coefficients of proportionality between the imposed strain and induced physical stress in the crystal. I used an *ElaStic 1.0* package [117] interfaced with *Quantum ESPRESSO* [118] to calculate the energy and stress values of the distorted structures (see Appendix A for details). The six independent Voigt second-order elastic constants obtained in bismuth are given in Table 3.1 as well as the experimental values obtained with the pulse echo technique [116, 119]. Theoretical elastic constants agree reasonably well with the experiment of Eckstein [116]. The greatest difference of 43.1% and 40.3% is observed for the smallest constants C_{14} and C_{44} respectively. The sound velocities can also be obtained from the elastic constants using the relations described in Ref. [120]. As it is shown in Table 3.2, the resulting sound velocities fit well to the velocities obtained from the slopes of the phonon branches near the zone center and the corresponding experimental values from Ref. [116].

However, phonon dispersion shown in the left panel of Fig. 3.1 does not provide the information about the distribution of phonons over the energy states. This information can be obtained with the vibrational density of states (DOS) which gives the number of

C_{ii} (GPa)	DFT-LDA	Ref. [116], 300 K	Ref. [116], 4.2 K	Ref. [119]
C_{11}	69.7±0.3	63.5 (9.7%)	68.7 (1.5%)	62.9 (10.8%)
C_{12}	25.3±0.2	24.7 (2.4%)	-	35.0 (27.7%)
C_{13}	26.6±0.2	24.5 (8.6%)	-	21.1 (26.1%)
C_{14}	4.8±0.5	7.23 (33.6%)	8.44 (43.1%)	4.23 (13.5%)
C_{33}	43.3±0.2	38.1 (13.6%)	40.6 (6.6%)	44.0 (1.6%)
C_{44}	7.7±0.8	11.3 (31.9%)	12.9 (40.3%)	10.8 (28.7%)

Table 3.1: Second-order elastic constants of bismuth. My calculation (DFT-LDA) is done with the ElaStic Package [117] and corresponds to zero temperature. Experimental values have been obtained by Eckstein *et al.*, Ref. [116], and Bridgeman, Ref. [119]. The percentage of error is given in parenthesis, $\frac{C_{th}-C_{exp}}{C_{exp}}$, with theoretical elastic constant C_{th} and experimental value C_{exp}.

Propagation along the binary axis				
v_i (m/sec)	Th., elastic constants	Th., slope	Expt, Ref. [116]	Mode
v_1	2624±11	2460±10	2540±22	Longitudinal (LA)
v_2	1528±225	1610±350	1550±9	Fast shear (TAf)
v_3	786±115	924±176	850±4	Slow shear (TAs)

Propagation along the trigonal axis				
v_i (m/sec)	Th., elastic constants	Th., slope	Expt, Ref. [116]	Mode
v_4	2068±10	2050±10	1972±15	Longitudinal (LA)
v_5	872±90	1271±278	1074±11	Degen. shear (TAs/TAf)

Table 3.2: Velocities of sound propagating along the binary axis (top panel) and along the trigonal axis (bottom panel). Theoretical values were obtained from the second-order elastic constants from Table 3.1 (second column) and from the slopes of acoustic phonons in vicinity of Γ point. Experimental results of Ref. [116] are given in the third column.

states per interval of energy that are occupied. It is shown in the right panel of Fig. 3.1. One can see that in the vicinity of the zone center the number of occupied phonon states is small comparing with the rest of the Brillouin zone for both acoustic and optical modes. The acoustic branches are filled almost uniformly from 20 cm^{-1} to 60 cm^{-1}, while the optical phonons have a pronounced peak in DOS about 93 cm^{-1}.

3.1.3 Stability.

Phonons in bismuth are extremely sensible to external deformations such as strain. Such deformations lead to instability in acoustic phonon branches in vicinity of the Brillouin zone center Γ and thus to "imaginary" phonon frequencies in this region signifying about the phase transition. Indeed, recent transport [121], thermodynamic [122] and magnetoresistance [123] studies show that bismuth loses its three-fold symmetry at low temperatures and high magnetic field. Among the possible origins of this phase transition is a field-induced lattice distortion (magnetostrictive strain) by magnetic field that is driven by electron-phonon coupling [90, 124, 125]. Lowering symmetry in this case allows to get rid of the costly electronic degeneracy, which may be reduced thanks to lattice distortion [90, 124].

3.1.4 The effect of spin-orbit coupling on phonon dispersion.

All results discussed so far were obtained with the electronic Hamiltonian and resulting ground state energy accounting for the relativistic spin-orbit coupling effect (SOC). This effect has been shown to play a crucial role in the description of the electronic properties of bismuth [1, 4]. In particular, the account of spin-orbit interaction changes the electronic structure from metallic to semimetallic and the latter agrees with experiment [4]. Thus the SOC should also change vibrational properties such as phonon dispersion since they are determined by the second-order derivative of the ground state energy with respect to the atomic displacements. Indeed, in Fig. 3.2 one can see the two phonon spectra: one including the spin-orbit coupling (black solid lines) and another without it (red solid lines). The latter has steeper acoustic branches near Γ. Moreover, both acoustic and optical branches are lifted upward comparing with the SOC calculation. Thus, the theoretical results without SOC disagree with the experimental data. Vibrational density of states for the SOC and noSOC cases are shown in the left panel of Fig. 3.2. The effect of SOC interaction on DOS is similar to the one on the phonon dispersion. In particular, the plateau in the region of acoustic phonons is shifted upwards on about 5 cm^{-1}. The DOS of optical phonons is also lifted up and smeared.

In conclusion, we have seen that *ab initio* calculations describe the acoustic part of the phonon dispersion of bismuth remarkably well. The account of the spin-orbit coupling interaction is shown to play a crucial role on vibrational properties of Bi.

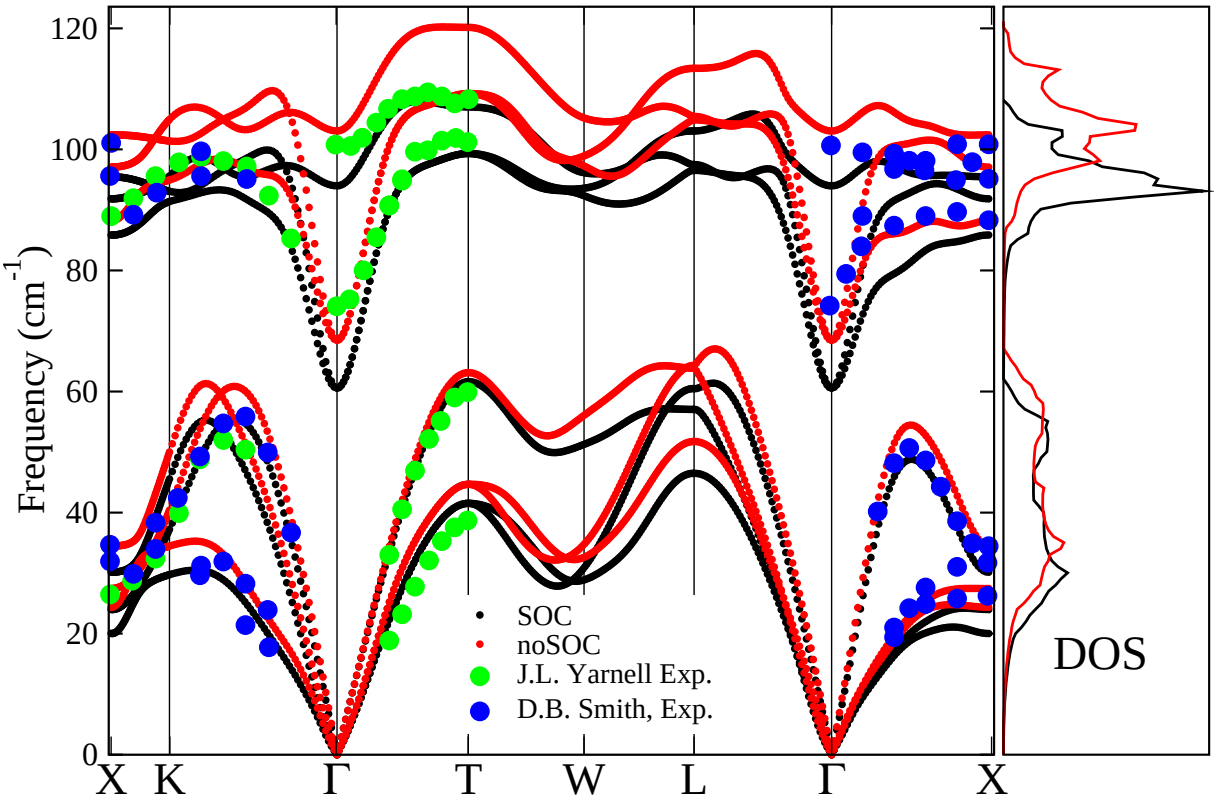

Figure 3.2: Left panel: DFT-LDA calculated phonon dispersion in bismuth including spin-orbit coupling (black solid lines) and without spin-orbit coupling (red solid lines). Experimental data extracted from [112] (green circles) and [113] (blue circles). Right panel: the corresponding density of states.

3.2 The role of optical phonons: AOPI.

3.2.1 Optical phonons.

In the previous section, I have discussed vibrational properties of Bi focusing mainly on the acoustic part of the phonon dispersion and on the quantities that could be derived from it such as sound velocities. Now I consider the optical modes represented by the three highest branches in Fig. 3.1. These branches are almost flat in most of the Brillouin zone except the region near the zone center. This flat behavior results in the small group velocities of the optical phonons. Contrastingly, near the zone center transverse optical modes are very steep and fall down in a deep minimum. However, as one can see from the right panel of Fig. 3.1 the density of states of these modes is small in this region. The maximum frequency of optical phonons in Bi appears not at Γ point but at $\mathbf{q}$ near the zone boundary in contrast with other materials such as Si, Ge or GaAs. A similar behavior has been observed for the longitudinal optical (LO) branch in diamond resulting from the sufficiently large interatomic force constants between second-nearest neighbors giving rise to the overbending [126].

3.2.2 Indirect phonon gap.

The acoustic and optical branches are well separated at each point of the Brillouin zone. To describe the relative position of optical phonon branches with respect to the acoustic modes, I define the *indirect phonon gap* Δ as the difference between the minimum of the transverse optical (TO) mode ω_{TO} at Γ and the maximum of a longitudinal acoustic (LA) branch ω_{LA} at T point

$$\Delta = \omega_{TO}(\Gamma) - \omega_{LA}(T) \tag{3.1}$$

In my calculation this indirect phonon gap is absent[1] and a small intersection of about 1 cm^{-1} is observed instead. As we have already seen, the acoustic branches match well with the experimental data, and the difference in $\omega_{LA}(T)$ lies within a small error bar of about 2 cm^{-1}. However, the experimental value of $\omega_{TO}(\Gamma)$ lies considerably higher of about 12 cm^{-1} than the one found in my calculation and it results in the opening of a phonon gap Δ. The positions of the minimum of the TO mode $\omega_{TO}(\Gamma)$, the maximum of the LA mode $\omega_{LA}(T)$ and the gap value Δ found in this work, in previous theoretical calculations [111, 56] and in experiment [112], are given in Table 3.3. To the best of my knowledge, in most of the DFT calculations [111, 56], including my calculations with both LDA and GGA exchange-correlation potentials, the optical frequencies at Γ are underestimated and lie much lower than the experimental value $\omega_{TO}^{min} = 72 - 74$ cm^{-1} [127, 112]. The only exception is the calculation of Murray *et al.* [115] in which Bi has been treated as a semiconductor and a considerably higher value $\omega_{TO} = 79$ cm^{-1} has been found. As we will see further an accurate position of $\omega_{TO}(\Gamma)$ is important to describe the allowed interaction processes between the acoustic and optical phonons in Bi.

[1] Only a part of the Brillouin zone along some high symmetry directions shown in Fig. 3.1 has been investigated, but not all the Brillouin zone.

Calculation	$\omega_{TO}(\Gamma)$, cm^{-1}	$\omega_{LA}(T)$, cm^{-1}	Δ, cm^{-1}
ab initio SOC (DFT-LDA)	60.4	61.5	-1.1
ab initio SOC (DFT-LDA) + rigid shift	73.0	61.5	11.5
ab initio noSOC (DFT-LDA)	68.1	62.9	5.2
ab initio SOC (DFT-GGA)	67.3	47.7	19.6
Lee *et al* [56] (DFT-LDA)	65.5	58.4	7.1
Gonze *et al* [111] (DFT-LDA)	65.4	58.7	6.7
Murray *et al* [115] (DFT-LDA)	79.0	58.5	20.5
Experiment [112]	74.0	59.7	14.3
Experiment [127]	72.0	-	-

Table 3.3: Phonon frequencies of the transverse optical phonons at Γ, longitudinal acoustic phonons at T and indirect gap between them defined in Eq. 3.1.

3.2.3 Optical phonons as an efficient scattering channel.

As we have just seen the main discrepancy between my theoretical phonon dispersion and experiment is a profoundly deep minimum in frequencies of the transverse optical phonons in the vicinity of Γ. However, optical phonons in general are known to contribute less than acoustic modes in the transport of heat in materials [27]. This is because of their flat behavior in most of the Brillouin zone that results in small group velocities. In bismuth the optical branches are steep only in the vicinity of the zone center, but this region contributes little to the lattice thermal conductivity because of the small DOS.

Nevertheless, as I will show further the optical phonons in bismuth provide an efficient scattering channel for acoustic phonons. The quantity which describes the allowed interaction processes between the phonons based on the energy and momentum conservation laws is called the joint density of states (JDOS). In this work I consider interaction processes in which only three phonons are involved. I define the JDOS as

$$JDOS(\omega) = \int d\omega_{\nu_1} \sum_{\nu_2,\nu_3} \left[\delta(\omega_{\nu_1} + \omega_{\nu_2} - \omega_{\nu_3}) + \delta(\omega_{\nu_1} - \omega_{\nu_2} - \omega_{\nu_3})\right] \delta(\omega - \omega_{\nu_1}) \qquad (3.2)$$

where index ν_i condensates phonon vector q_i and mode index j_i for all three interacting phonons $i = 1, 3$. The first delta function $\delta(\omega_{\nu_1} + \omega_{\nu_2} - \omega_{\nu_3})$ describes the coalescence (collision) between two phonons and a creation of one single outcoming phonon. The second delta function $\delta(\omega_{\nu_1} - \omega_{\nu_2} - \omega_{\nu_3})$ describes a spontaneous decay (fission) of a phonon into two outcoming phonons. Wavevectors of the interacting phonons must satisfy the momentum conservation rule i.e. $\mathbf{q_1} \pm \mathbf{q_2} = \mathbf{q_3} + \mathbf{G}$ where $\mathbf{G}$ is a vector of a reciprocal lattice and plus/minus correspond to coalescence/decay. The JDOS defined in Eq. 3.2 allows to analyze the relative importance of different interaction processes between phonons if their polarization indices are specified.

In the left panel of Fig. 3.3, I show the phonon dispersion which is the same as the one in Fig 3.1. I draw the optical branches obtained from my *ab initio* calculations with the black dashed lines. To estimate the effect of the absence of phonon gap in my *ab initio* calculations on the phonon lifetimes, I open the phonon gap by rigidly shifting the

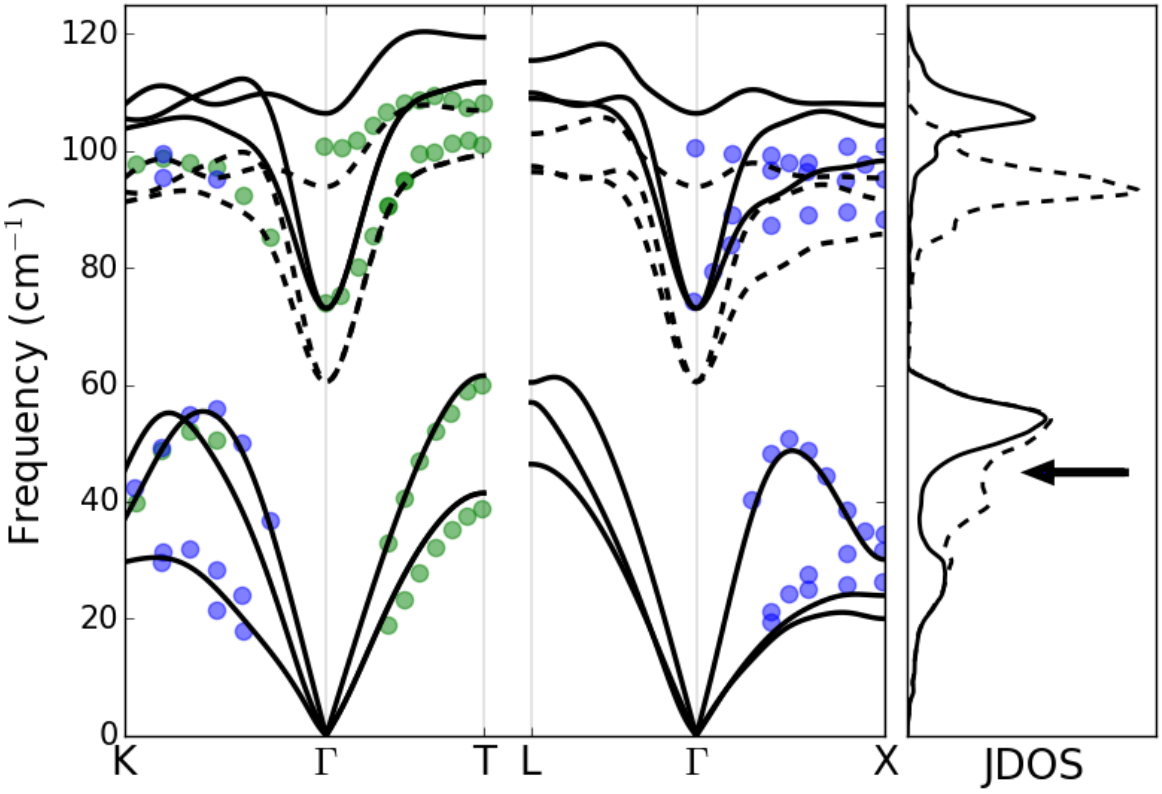

Figure 3.3: Right panel: phonon dispersion of Bi obtained from *ab initio* calculation. Left panel: the corresponding joint density of states.

optical branches upwards (black solid lines) to match the experimental frequency of the TO modes at the Γ point while the acoustic branches remain the same. In the right panel of Fig. 3.3, I show the joint density of states as a function of frequency of incoming phonon. As one can see, the lift of optical phonons considerably reduces the JDOS between 30 and 50 cm^{-1} since the acoustic phonons in this region have not enough energy after the coalescence to reach even the lowest optical branches. Thus an appropriate position of the lowest phonon frequency of the TO mode $\omega_{TO}(\Gamma)$ is important, as it provides a realistic description of the acoustic-optical phonon interaction (AOPI) in bismuth. The peak in the JDOS of optical phonons is also reduced and shifted upwards. However, as has already been mentioned earlier, the optical branches in the rest of the Brillouin zone are not important for the thermal transport since they have low group velocities.

To conclude, in this section I have shown that, although overall optical dispersion is well reproduced, the TO phonons at Γ obtained from *ab initio* calculations lie considerably lower than in experiment. It results in the closure of the indirect phonon gap Δ and causes an enhanced acoustic-optical phonon interaction. To resolve this inconsistency I have shifted rigidly the optical part of the phonon dispersion upwards and got a reduced JDOS of acoustic phonons. In the next section I will show how this change in the JDOS affects the thermal transport properties in Bi.

3.3 Thermal conductivity calculation and analysis: *ab initio* results.

In this section I will present the results of the thermal conductivity calculation in the framework of the theory described earlier in Chapter 1. I will show that the enhanced acoustic optical phonon interaction results in lower values of the lattice thermal conductivity. I will compare results obtained within the single mode approximation and the ones from the full solution of the Boltzmann transport equation.

3.3.1 The effect of AOPI on the lattice thermal conductivity.

The lattice thermal conductivity describes the ability of a material to propagate the heat by means of lattice vibrations. It strongly depends on the quantities derived from the phonon dispersion such as phonon frequencies, group velocities and the JDOS. In the previous section we have seen that the latter is considerably overestimated in my *ab initio* calculations because of the low position of the TO modes near the zone center comparing with the experimental data. To correct this drawback, I rigidly shifted optical phonons upwards to match the value of $\omega_{TO}(\Gamma)$ and obtain a realistic interaction between acoustic and optical modes (AOPI). In the following I will assign the results done with the shifted optical phonons as a reference.

In Fig. 3.4, I show the temperature variation of the lattice thermal conductivity κ_L calculated by exactly solving the Boltzmann transport equation with the modified phonon dispersion (black solid line). As one can see the values of the thermal conductivity are superior to the ones obtained with the pristine *ab initio* dispersion (black dashed line). It

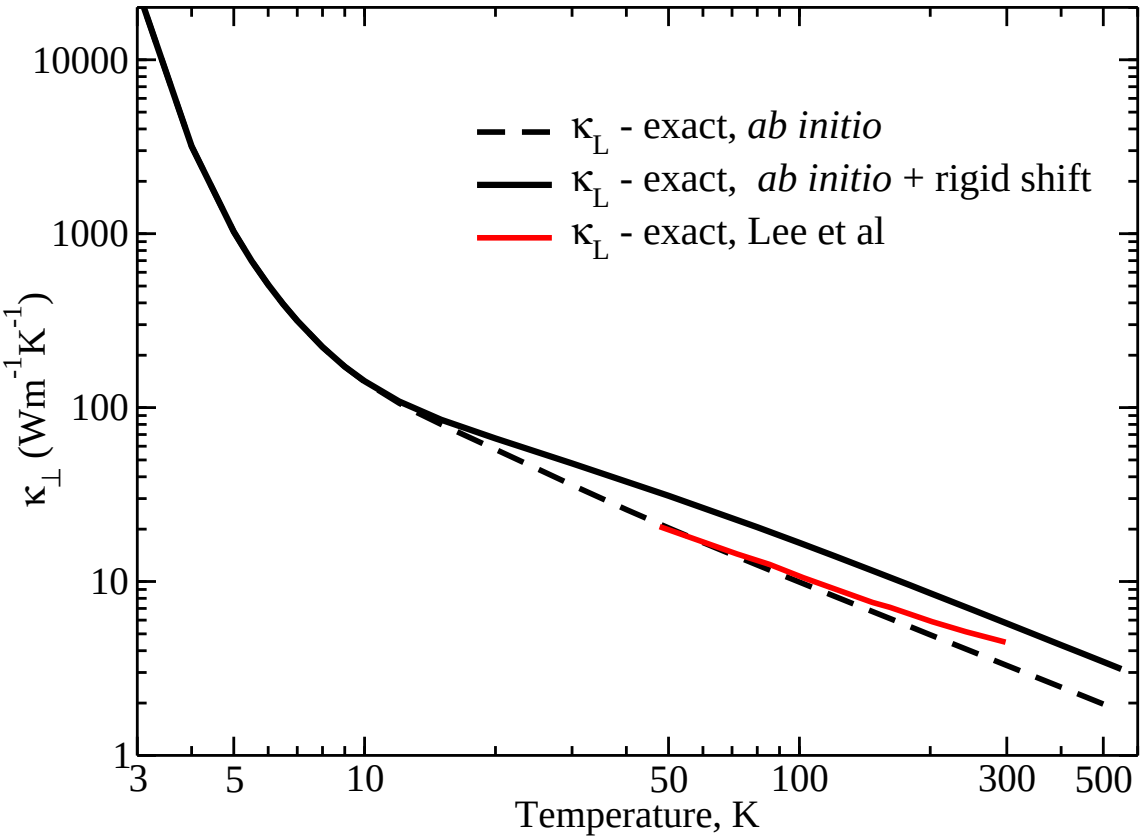

Figure 3.4: Temperature variation of the thermal conductivity in the binary direction. Black solid line - calculation with *ab initio* phonon dispersion with rigid shift of optical phonons. Black dashed line - calculation with *ab initio* phonon dispersion resulting in the enhanced AOPI. Red solid line - calculation of Lee *et al.* [56] with phonon dispersion shown in red dashed lines in Fig. 3.1.

is explained by the fact that the latter dispersion provides an enhanced AOPI that results in the lower phonon relaxation time and thus lower thermal conductivity.

At low temperatures the acoustic phonon modes of high energy (mainly LA) are not populated and hence the interaction processes involving optical phonons are not important. As a result, the two curves coincide. Another theoretical lattice thermal conductivity obtained by Lee *et al* [56] is also shown in Fig. 3.4 (red solid lines)[2]. Since the phonon gap in their calculation is underestimated (see red dashed lines in Fig. 3.1 and Table 3.3), κ_L exhibits a behavior similar to the one with the enhanced AOPI in my calculations.

As one can see thermal conductivity in bismuth noticeably variates with temperature. First, it increases as T^{-1} with decreasing of temperature down to 10 K. Then in the absence of scattering other than phonon-phonon interaction thermal conductivity turns to the exponential growth below 10 K. This behavior is directly due to the decrease of anharmonic phonon decay as the temperature decreases. In this case the lattice vibrations act as a set of harmonic oscillators and the lattice conductivity tends towards infinity.

3.3.2 Exact solution versus SMA

The results of the calculation of the lattice thermal conductivity discussed so far were obtained by exactly solving the BTE. Both variational and iterative methods reviewed in Chapter 1 yield the same results in my calculation. Another method to solve the BTE is the single mode relaxation time approximation (SMRTA or SMA). In Fig. 3.5, I show the difference in the lattice thermal conductivity obtained from the exact solution (black solid line) and from the SMA (blue dashed-dotted line). As one can see, the SMA remains a good approximation at high temperatures when the repopulation processes are not very important. However, at low temperatures the heat is carried not by single phonons but by the collective excitations and the repopulation of the phonon states must be taken into account to get a correct value of the lattice thermal conductivity as discussed in Section 1.4. This is possible only by exactly solving the BTE. Indeed, at T $<$ 10 K the exact solution results in significantly higher values of the lattice thermal conductivity comparing with SMA.

In Table 3.4, I summarized the values of the lattice thermal conductivity in the binary and trigonal direction obtained from the exact solution and from the SMA. We see that it ranges from 3.2 W(K.m)$^{-1}$/2.5 W(K.m)$^{-1}$ near the melting temperature[3], to 5.8 W(K.m)$^{-1}$/4.5 W(K.m)$^{-1}$ at ambient temperature in the binary/trigonal direction respectively. It reaches 31.1 W(K.m)$^{-1}$/25.0 W(K.m)$^{-1}$ at 50 K, and 142 W(K.m)$^{-1}$/103 W(K.m)$^{-1}$ at 10 K, and then gains more than four orders of magnitude between 10 K and 2 K when the boundary scattering is not introduced.

In conclusion, in this section I have discussed the temperature variation of the lattice thermal conductivity in Bi. I have shown that the SMA is a good approximation for κ_L at high temperatures when the heat is carried by the individual phonons. However, at

[2]Harmonic and anharmonic force constants were calculated with the real space approach (see 1.5.2). The Boltzmann Transport Equation was numerically solved with the iterative approach (see 1.4.2).

[3]Near the melting temperature, the quasi-harmonic approximation (QHA) must be used to accurately describe the lattice thermal conductivity. This approximation accounts for the volume dependent thermal effects such as thermal expansion.

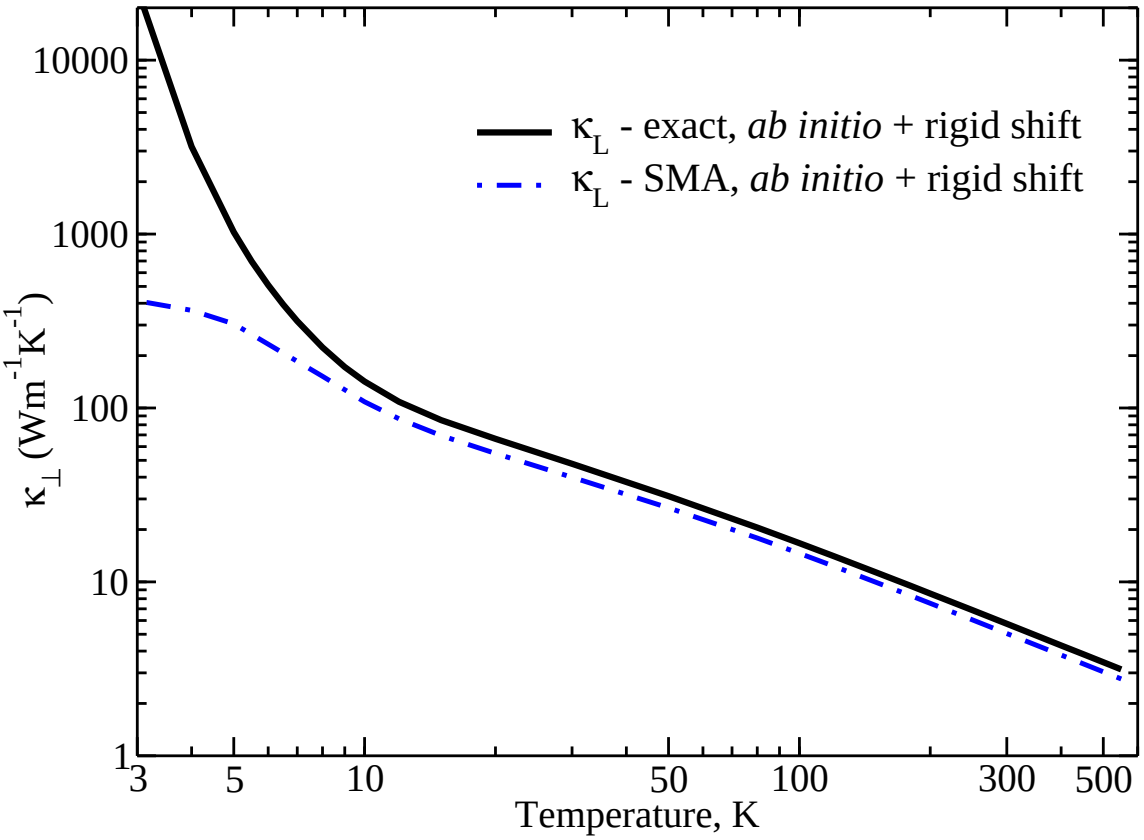

Figure 3.5: Temperature variation of thermal conductivity in the binary direction obtained from *ab initio* phonon dispersion with the rigidly shifted upward optical phonons. Black solid line - exact solution of the BTE. Blue dashed-dotted line - the single mode relaxation time approximation (SMA).

binary		
T, K	κ_L^{full}	κ_L^{SMA}
300	5.8	5.1
200	8.6	7.5
100	16.7	14.6
50	31.1	26.7
20	66.5	54.8
10	142	108

trigonal		
T, K	κ_L^{full}	κ_L^{SMA}
300	4.5	3.9
200	6.8	5.8
100	13.3	11.3
50	25.0	20.8
20	53.0	42.8
10	103	80.0

Table 3.4: The lattice thermal conductivity found in my calculations at different temperatures obtained from full solution of the BTE, κ_L^{full}, and from the SMA in both binary and trigonal directions.

low temperatures the exact solution of the BTE is mandatory since the SMA does not account for the repopulation effects. Moreover, I have demonstrated that the acoustic-optical phonon interaction plays a crucial role in the determination of the magnitude of the lattice thermal conductivity in Bi in a wide temperature range. In the next section I will discuss the basic heat transfer mechanisms in bismuth and I will show what are the phonons that carry heat in this material.

3.4 Phonon heat transfer mechanisms in bismuth.

In the previous section, I have determined the values of the lattice thermal conductivity as a function of temperature. In my calculation I have included only the intrinsic source of scattering due to the phonon-phonon interaction. To provide a realistic interaction between acoustic and optical phonons, I have shifted the optical branches upwards. It leads to the considerable reduction of the JDOS of acoustic phonons. However, because of this rigid shift, the resulting optical branches now lie higher than in experiment in most of the BZ except the region near the zone center Γ. In this section, I will demonstrate that the optical phonons carry only a small portion of heat comparing with the acoustic modes. Thus their prime role is to produce a scattering channel for the acoustic phonons but not to contribute to the transport of heat.

In Figure 3.6, I show the phonon mode contributions to the lattice thermal conductivity in the binary direction as a function of temperature. As one can see, the acoustic phonons carry most of the heat in Bi. The contribution of optical branches to κ_L is only about 16% of the total vibrational part at $T = 300$ K. This result is explained by the flat behavior of optical branches in most of the BZ that leads to the low group velocities c_ν and thus to low contribution to thermal conductivity ($\kappa_L \sim c_\nu^2$ in RTA). Then the optical contribution monotonously decreases with the decrease of temperature and entirely vanishes at $T \approx 20$ K since the highest vibrational energies are no longer populated.

As shown in Figure 3.6, at high temperatures most of the heat is carried by the high energy acoustic modes such as TAf (red solid line) and LA (green solid line) phonons while the lowest TAs branch (blue solid line) has the smallest contribution. At $T = 300$

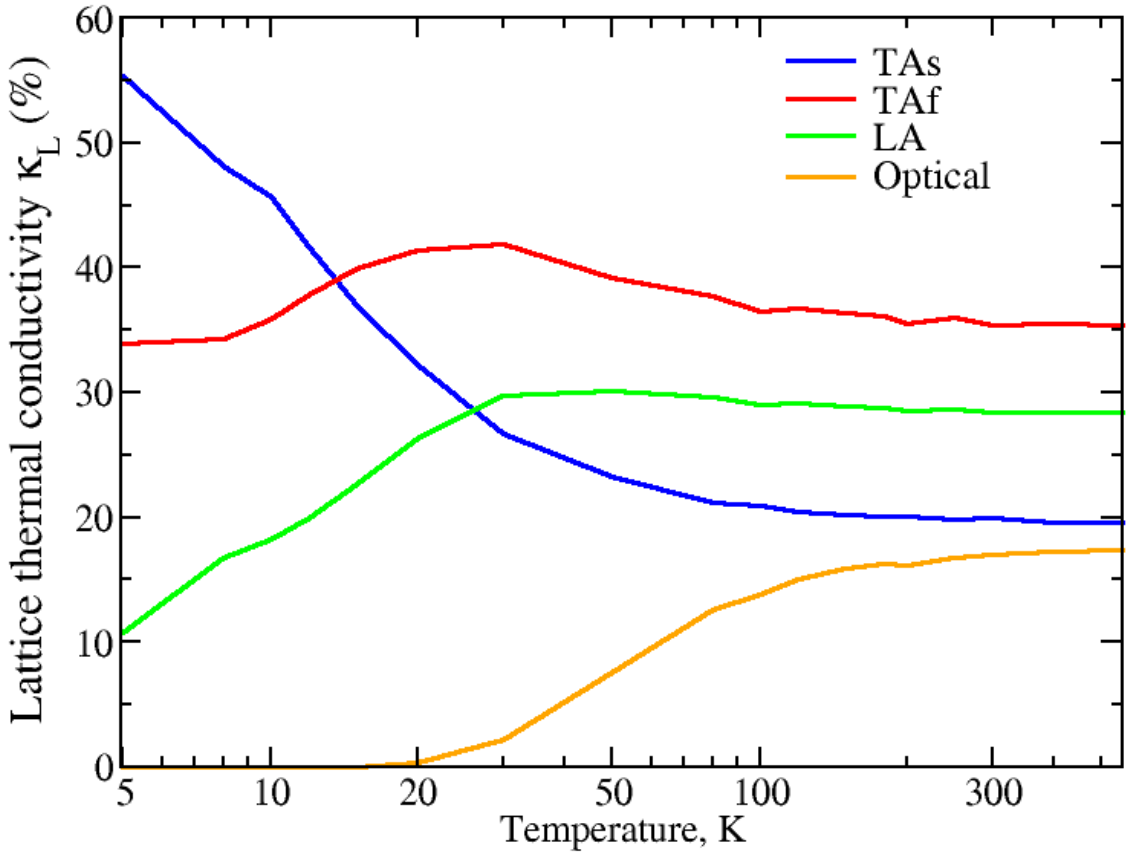

Figure 3.6: The contributions due to the 1st acoustic (TAs, blue line), 2nd acoustic (TAf, red line), 3rd acoustic (LA, green line) and optical (TO and LO, orange line) modes to the vibrational part of the thermal conductivity. TAs and TAf phonon modes are defined in Table 3.2 and in Section 3.1.2.

K, for instance, the LA modes are responsible for about 28%, TAf for about 35% and TAs for only about 20% of the total lattice thermal conductivity. While the temperature decreases, the high energy phonons become less populated and thus less important. The contribution of the lowest TAs mode, in turn, grows and becomes greater than the one of the LA phonons at $T \approx 20$ K. Finally, at low temperatures $T \leq 15$ K the TAs modes give more than 40% of the total lattice thermal conductivity.

3.4.1 Distribution in the Brillouin zone.

To understand how κ_L is distributed in the BZ, I analyze the lattice thermal conductivity calculated from the iterative solution of the BTE as a function of the modulus of the wavevector of the initial phonon $|\mathbf{q}|$. I define the quantity $\kappa_L(|\mathbf{q}|)$ as

$$\kappa_L(|\mathbf{q}|) = \int_{BZ} \kappa_L^{\mathbf{q_i}} \delta(|\mathbf{q}| - |\mathbf{q_i}|) d|\mathbf{q_i}| \tag{3.3}$$

where $\kappa_L^{\mathbf{q_i}}$ is the lattice thermal conductivity contribution from the given $\mathbf{q_i}$ point in the Brillouin zone defined in equation 1.46. The total lattice thermal conductivity can be restored from $\kappa_L(|\mathbf{q}|)$ by integrating over $|\mathbf{q}|$

$$\kappa_L = \int_0^{max(|\mathbf{q}|)} \kappa_L(|\mathbf{q}|) d|\mathbf{q}| \tag{3.4}$$

I choose two temperatures $T = 300$ K and $T = 5$ K where the behavior of the lattice thermal conductivity is found to be qualitatively different. In Fig. 3.7, I show $\kappa_L(|\mathbf{q}|)$ (black solid lines) for $T = 300$ K (top panels) and for $T = 5$ K (bottom panels) in binary (left panels) and trigonal (right panels) directions. At high temperature I find that the lattice thermal conductivity, in both binary and trigonal directions, is due to phonons with $\mathbf{q}$-vectors all over Brillouin zone, and not only due to the phonons near zone center. This is somewhat surprising, as one expects the main contribution to the lattice thermal conductivity to come from the region near the zone center where the group velocities are high and the mean-free paths are long. This behavior can be understood, if one remembers that $\kappa_L(|\mathbf{q}|)$ implicitly contains the density of $\mathbf{q}$-states ($\mathbf{q}$-DOS) of the initial phonon that is defined as

$$DOS(|\mathbf{q}|) = \int_{BZ} \delta(|\mathbf{q}| - |\mathbf{q_i}|) d|\mathbf{q_i}| \tag{3.5}$$

The $\mathbf{q}$-DOS is shown in the insert of Fig. 3.7. It depends only on the form of the BZ and shows a parabolic dependence on $|\mathbf{q}|$ away from the boundaries of the BZ. At high temperatures, when all phonon branches are populated, the difference in group velocities and in phonon lifetimes is insufficient to overcome the difference in $\mathbf{q}$-DOS in the Brillouin zone. Thus, the region around Γ gives a relatively small contribution to the thermal conductivity.

Contrastingly, at small temperatures the major contribution to $\kappa_L(|\mathbf{q}|)$ starts to drift towards the small $|\mathbf{q}|$ since most of the high-energy phonon states are not populated anymore due to the small thermal energy $k_B T$. The only active states are now located

near the zone center Γ and the lattice thermal conductivity $\kappa_L(|\mathbf{q}|)$ has a pronounced peak at $|\mathbf{q}| \approx 0.15 \times \frac{2\pi}{a_0}$ at 5 K for both directions.

In Figure 3.7, I also display the contributions of the three acoustic branches (blue, red and green solid lines). At T = 300 K the contribution of the highest LA branch (green solid line) has a clear maximum at $|\mathbf{q}| \approx 0.2 \times \frac{2\pi}{a_0}$ while the contributions of the lowest TA (blue and red solid lines) branches show the behavior similar to that of the $|\mathbf{q}|$-dependent phonon DOS. At$T = 5$ K the biggest contribution comes from the TAs mode (blue solid line) which is spread in the region of $|\mathbf{q}| = 0.1 - 0.4 \times \frac{2\pi}{a_0}$. The LA contribution is small and is localized near $|\mathbf{q}| = 0.05 \times \frac{2\pi}{a_0}$.

In conclusion, in this section I have discussed the mechanisms of the heat transport in bismuth due to the separate phonon modes. I have shown that optical phonons carry only a small fraction of heat but participate in the scattering of the acoustic phonons. I have analyzed the lattice thermal conductivity distributed over the Brillouin zone at high and low temperatures. I have shown that at ambient temperature the heat is carried by high energy LA and TA phonons. The distribution of heat carrying phonons is found to be almost uniform over the BZ and follows the behavior of the $\mathbf{q}$-DOS. At low temperatures the biggest contribution comes from the lowest TAs mode and all heat carrying phonons are localized in the region of small wave vectors.

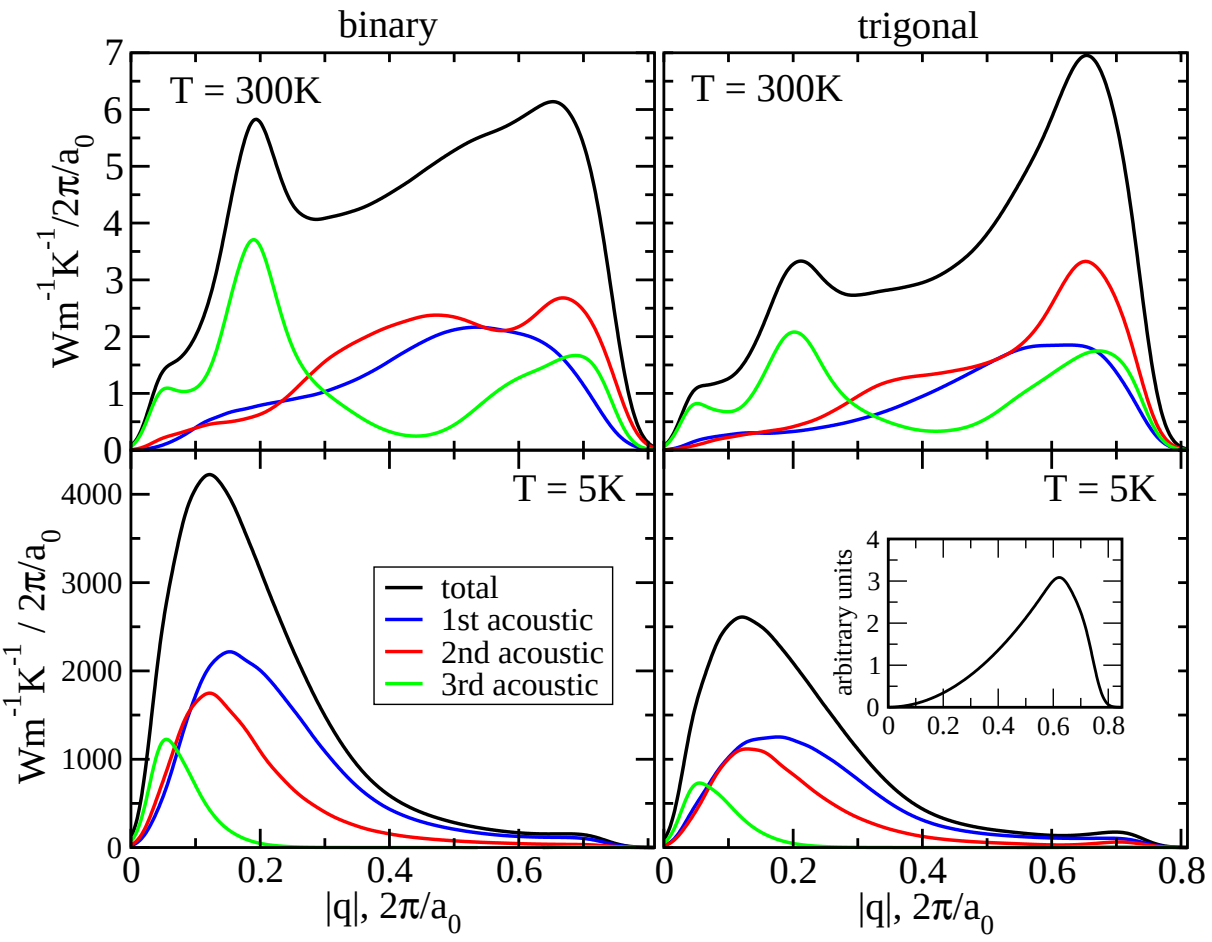

Figure 3.7: Lattice thermal conductivity as a function of the absolute value of the phonon vector of incoming phonon q in the binary (left) and trigonal (right) directions at 300K (top) and 5K (bottom). Black solid line - the total lattice thermal conductivity. Blue - 1^{st} acoustic branch (TAs). Red - 2^{nd} acoustic branch (TAf). Green - 3^{rd} acoustic branch (LA). Insert panel: the density of **q**-phonon states.

3.5 Summary and outlook

This chapter is devoted to the the lattice thermal conduction in bismuth which is defined by the individual lattice vibrations as well as by the interaction between them. First, I have discussed vibrational properties of bismuth obtained from first principles calculations. I have shown that an accurate account of spin-orbit coupling (SOC) is necessary to get a correct phonon dispersion of acoustic modes. However, the optical phonon branches lie considerably lower than in experiment providing an efficient extra-channel of scattering for the acoustic phonons after the coalescence.

To overcome this drawback, I have applied a model to modify an optical part of phonon dispersion by shifting them upward to match the frequency of optical transverse modes at Γ to the experimental value. I have shown that this shift leads to the reduction of the joint-density of states for the acoustic phonons in the frequency region between 30 and 50 cm^{-1}. Then I have presented the results of the calculation of the lattice thermal conductivity with *ab initio* phonon dispersion as well as with the shifted optical branches. I have demonstrated that the acoustic-optical phonon interaction defined by the phonon gap between acoustic and optical phonons allows to modulate the value of the lattice thermal conductivity. With respect to available theoretical literature and, in particular, with respect to Ref. [25], my calculations brought a deeper understanding of the microscopic processes determining the lattice thermal conductivity in bismuth, and also in materials in general.

Finally, I have shown that the acoustic phonons carry most of the heat in bismuth at all temperatures. At high temperatures, when all phonon modes are populated, the heat carrying phonons are almost uniformly distributed over the Brillouin zone except the region near the zone center where the contribution to the lattice thermal conductivity is found to be small. This behavior has been explained by the dominant role of $\mathbf{q}$-DOS. Contrastingly, at low temperatures only the low-energy phonons are populated and and the heat is carrying by the carriers localized near the zone center Γ.

In the next Chapter, my results will be compared with the available experimental data.

Chapter 4

Thermal conductivity of bismuth: comparison with experiment

Introduction

Bismuth is a semimetal and in contrast to other materials like pure metals and insulators, where heat is transferred solely by charge carriers and phonons respectively, there are several types of carriers that contribute to thermal conduction at the same time [14] (see Section 2.4). Thus to understand thermal transport in Bi and to evaluate the relative role of different types of carriers in different temperature regions, one must separate their contributions. Experimentally, this is a quite challenging task. Uher *et al.* [16] were able to measure a contribution to thermal conductivity due to the charge carriers in the binary direction up to T $\approx$ 150 K by applying a very strong magnetic field. However, this method has a serious limitation on the temperature range. Alternatively, Gallo *et al.* [8] evaluated the non-lattice part by implying Wiedmann-Franz law and by using an analytical expression for the binary ("electron-hole") contribution. In both works the lattice contribution has been found as a difference between the measured total thermal conductivity and obtained charge carrier contribution to thermal conductivity. However, estimations of the lattice part of thermal conductivity given in experimental works [16, 8] do not agree with each other, nor with the recent theoretical calculation [56]. In this Chapter I will show that my theoretical calculations presented in Chapter 3 are able to resolve the uncertainty on the absolute value of the lattice thermal conductivity at high temperatures in bulk Bi and, moreover, are able to explain the anisotropy in thermal conductivity.

The Chapter is organized as follows. In Section 4.1, I will recall the experimental methods to separate the lattice and non-lattice contributions to thermal conductivity in Bi. Then in Section 4.2, I will compare the theoretical thermal conductivity obtained in my calculations with the available experimental data. Then, I will estimate the contribution to thermal conductivity due to the charge carriers in the trigonal direction where it has not been measured, and I will discuss the anisotropy of thermal conductivity. Furthermore, in Section 4.3, I will discuss the Casimir model to simulate the effect of boundary scattering. I will show that an account for boundary scattering leads to finite values of thermal

conductivity at low temperatures in contrast with the divergent behavior observed when only intrinsic phonon-phonon scattering is taken into account in my calculations.

4.1 Transport mechanisms in bismuth.

The accurate measurements of the thermal conductivity of bulk materials have become a routine nowadays [48]. There are many satisfactory experimental techniques such as, for example, the steady-state technique [128], the 3ω technique [129], and the thermal diffusivity measurement [130]. However, these methods do not provide information about the carriers that transfer heat in the material to which they are applied. This information is extremely important for the case of intrinsic semiconductors and semimetals when charge carriers and phonons contribute to thermal conductivity together. In this Section I recall some facts about the determination of the lattice thermal conductivity already discussed in detail in Chapter 2.

Bismuth belongs to group V elements and shares with As and Sb the semimetallic nature. Total thermal conductivity of Bi κ can be expressed as a sum of two terms $\kappa = \kappa_L + \kappa_E$, where κ_L is the lattice thermal conductivity and κ_E is the charge carrier (non-lattice thermal conductivity. The latter accounts for all contributions from the charge carriers such as unipolar contributions due to the electrons (κ_e) and holes (κ_h) alone, and a bipolar contribution (κ_{e-h}) that describes the transfer of the "heat of formation" of electron-hole pairs which diffuse from the hot region to the cold one [131].

Gallo *et al.* [8] were the first authors who derived a model to estimate the charge carrier contribution to thermal conductivity in bismuth from the experimentally measured electrical conductivities σ_i and partial Seebeck coefficient S_i, where for holes $i = h$ and electrons $i = e$. This model employs the empirical Wiedmann-Franz law $\kappa_i = L_i \sigma_i T$ for the unipolar contributions. However, the Lorenz numbers L_i for semimetals are not known. To estimate them the authors relied on the model derived for semiconductors assuming a quadratic dispersion law and scattering of the current carriers by acoustical phonons. As has been shown in Ref. [91], violation of the former assumption leads to the overestimation of the electronic thermal conductivity. Thus another more precise method is mandatory.

Another experimental method to separate the contributions is based on the effect of a strong magnetic field on the thermal conductivity. It relies only minimally on an accurate theoretical description of the electronic properties of bismuth [16] and thus allows to correct the result of Ref. [8]. In this approach the non-lattice thermal conductivity has been expressed in terms of galvanomagnetic and thermomagnetic tensors that can be obtained from the mobilities and partial Seebeck coefficients measured in experiment. However, this approach has a strong limitation requiring $\mu_i B_i \gg 1$, where μ_i is the mobility of a carrier and B_i is the magnetic field in the i-th direction. The mobility of charge carriers in Bi goes down with the increase of temperature, and thus stronger magnetic fields are required. In Ref. [16] the analytical expression for κ_E have been determined only in the binary direction and the measurements were performed up to T $\approx$ 150 K. The resulting lattice thermal conductivity has been found as a difference between the total thermal conductivity and its indirectly measured electronic contribution.

In the next section, I will refer to the result of Uher with strong magnetic field as to the experimental reference. However, I will also compare with the experimental values of Gallo.

Ab initio calculations provide an appealing route to determine the heat transport mechanisms in bismuth by revealing the relative role of charge carriers and phonons in the total thermal conductivity. In the next section I will compare my theoretical lattice thermal conductivity presented earlier in Chapter 3 with the available experimental data in the binary direction. Above all, I will also predict the lattice and charge carrier thermal conductivity in the trigonal direction where the experimental data are missing.

4.2 Thermal conductivity at high temperatures

In this section, I study the lattice thermal conductivity in a temperature range in which scattering by sample boundaries is not important. In Section 4.3, I will study the effect of sample boundaries at low temperatures.

In Chapter 3, I have shown that the magnitude of the calculated lattice thermal conductivity in bismuth is modulated by the indirect phonon gap Δ. If the phonon gap is closed, as in the case of my *ab initio* calculations, or is too small, as in the calculations of Lee *et al* [56], the interaction between acoustic and optical phonons is enhanced and phonon lifetimes are shortened. To overcome this problem, I have shifted optical phonons upwards to match the frequency of transverse optical modes at Γ and thus open a phonon gap Δ. In this case, low energy acoustic phonons are not able anymore to reach the high energy optical phonons after a coalescence process, which results in longer lifetimes of acoustic phonons and higher values of the lattice thermal conductivity.

4.2.1 Lattice thermal conductivity.

In Fig. 4.1, I show the theoretical lattice thermal conductivity in the binary direction as a function of temperature as well as the experimental data of Uher *et al* [16] (green squares). As one can see, the calculation with shifted optical phonons (black solid line) describing a realistic AOPI shows an extremely good agreement with experiment of Uher *et al* [16]. For example, the lattice thermal conductivity at T = 50 K and T = 140 K are found to be 31 $Wm^{-1}K^{-1}$ and 11.5 $Wm^{-1}K^{-1}$ in my calculations respectively that is comparing with values of 30 $Wm^{-1}K^{-1}$ and 10.5 $Wm^{-1}K^{-1}$ obtained in experiment by Uher. Contrastingly, my calculation with *ab initio* phonon dispersion (black dashed line) and the calculation of Lee *et al* [56] (red dashed dotted line) predict much lower values of the lattice thermal conductivity due to the enhanced AOPI.

The data of Gallo *et al* [8] provide the lowest values of the lattice thermal conductivity among the all available data. For instance, at ambient temperature Gallo *et al.* found 1.7 and 0.9 $Wm^{-1}K^{-1}$ in the binary and trigonal directions respectively. These values are considerably lower than my results 5.8 and 4.5 $Wm^{-1}K^{-1}$ with the realistic AOPI as well as my *ab initio* results, 3.1 and 2.4 $Wm^{-1}K^{-1}$, and the results of Lee, 4.4 and 3.9 $Wm^{-1}K^{-1}$. However, as has been discussed earlier in Section 4.1, the estimation of Gallo

heavily rely on the electronic structure of bismuth that is approximated by parabolic band structure and found to be inexact in their model [91].

4.2.2 Non-lattice (charge carrier) thermal conductivity.

To evaluate the non-lattice (charge carrier) contribution I subtract the theoretical lattice thermal conductivity from the experimentally measured total thermal conductivity. The resulting differences in the binary and trigonal directions are shown in Fig. 4.2(a) and Fig. 4.2(b) respectively. In both directions the electronic contribution is found to be constant if the lattice part is calculated from phonon dispersion with shifted optical branches (black solid lines). In the binary direction the electronic contribution is found to be about 6 $Wm^{-1}K^{-1}$ that matches remarkably well with the experimental data of Ref. [14] (green circles) and Ref. [91] (green triangles) obtained from the high magnetic field experiments. In the trigonal direction there is no experimental data and I predict the electronic thermal conductivity to be equal to 3 $Wm^{-1}K^{-1}$. At low temperatures $T < 50$ K the estimated electronic contribution goes up that could result from an additional source of scattering that is not taken into account in my calculations. Indeed, the phonon drag effect caused by the strong electron-phonon interaction has been determined to play an important role on the magnitude of Seebeck coefficient at low temperatures [14, 87]. Thus the electron-phonon scattering might play an important role in thermal transport as well. If the lattice thermal conductivity is obtained from the *ab initio* phonon dispersion, the electronic contribution (black dashed line) is not constant anymore and monotonously grows with the decrease of temperature in both directions.

4.2.3 Relative contributions of the charge carriers and of the lattice.

To summarize the relative role of the lattice and charge carrier contributions in the thermal transport in bismuth, I display in Fig. 4.3(a) and Fig. 4.3(b) the bar diagrams of the contributions to the thermal conductivity at several temperatures in the binary and trigonal directions respectively. The non-lattice part (blue bars) becomes less important at low temperatures. It gives only about 17% of the total thermal conductivity at $T = 50$ K, comparing with 49% at ambient temperature in the binary direction. In the trigonal direction, the non-lattice part contributes less than in the binary direction. For instance, it gives 14% instead of 17% at $T = 50$ K, and 43% instead of 49% at $T = 300$ K.

4.2.4 Anisotropy ratio.

So far, I have presented the results of the calculations of the lattice thermal conductivity in two main directions: in the trigonal direction and in the binary direction which is perpendicular to the trigonal axis. Now I define the anisotropy ratio of thermal conductivities in bismuth as $\frac{\kappa_\perp}{\kappa_\parallel}$ where $\kappa_\perp$ is the thermal conductivity in the binary direction and $\kappa_\parallel$ is the thermal conductivity in the trigonal direction.

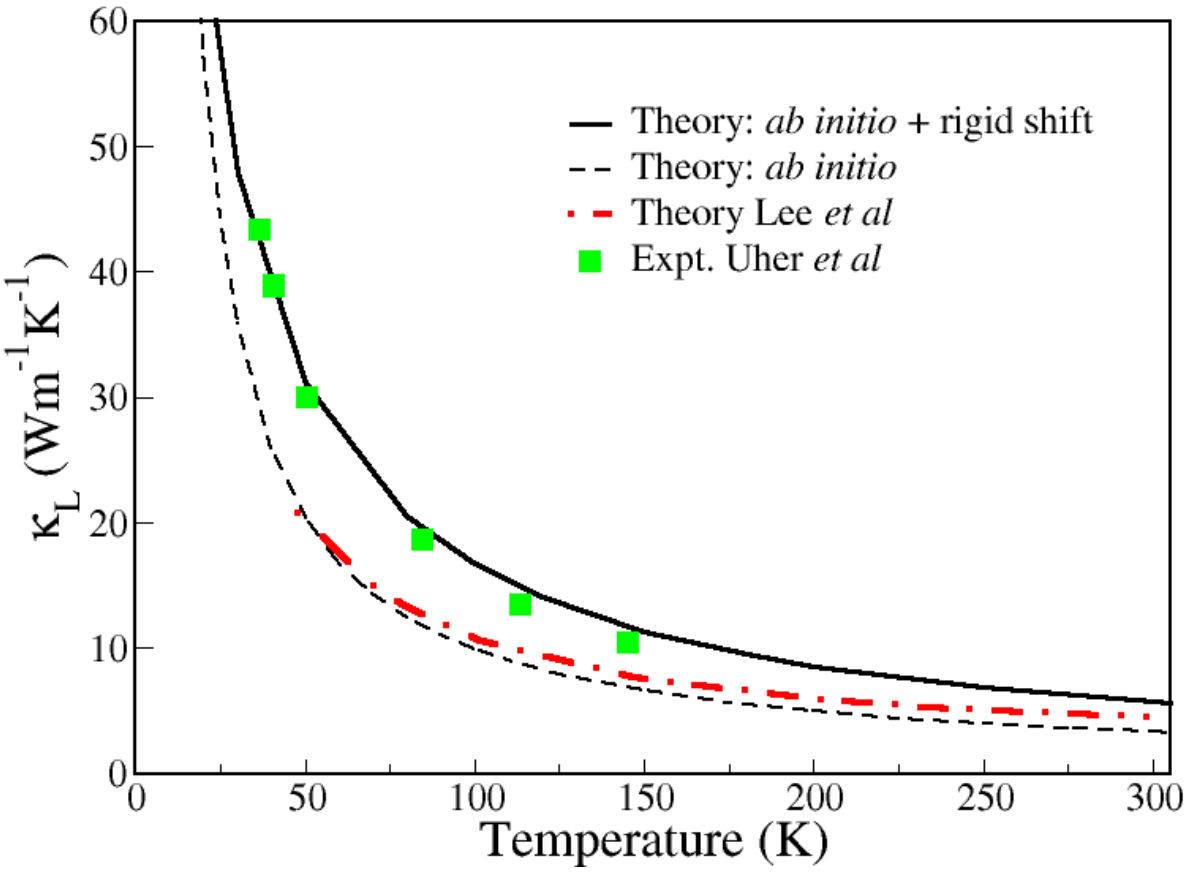

Figure 4.1: The lattice thermal conductivity of bismuth in the binary direction as a function of temperature. Black solid line - calculation with the experimentally observed AOPI. Black dashed line - calculation with *ab initio* phonon dispersion. Red dashed dotted line - calculation of Lee *et al* [56]. Green squares - experimental results of Uher *et al* [16].

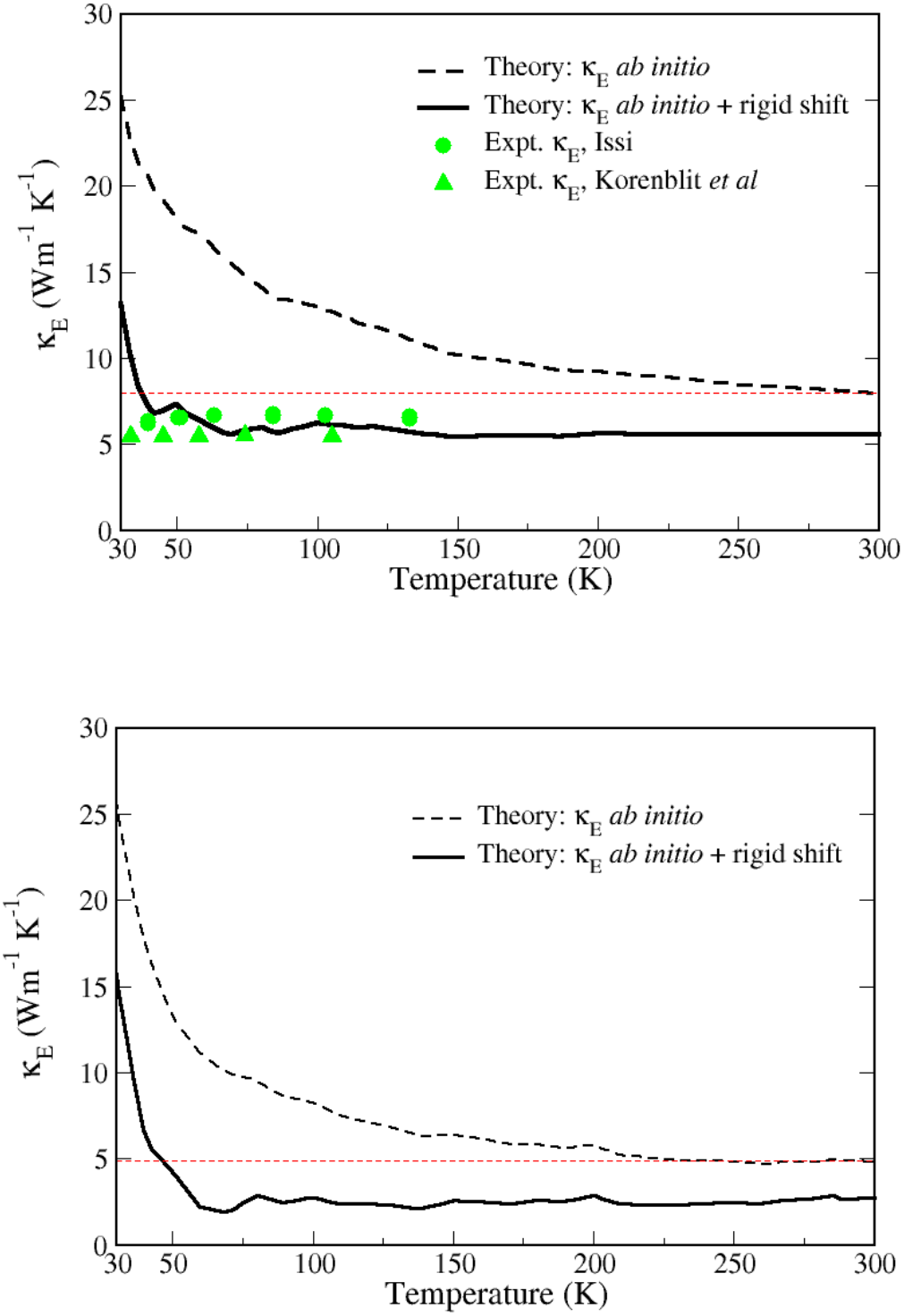

Figure 4.2: Evaluated non-lattice (charge carrier) thermal conductivity in the binary (top panel) and trigonal (bottom panel) directions found as a difference between the measured total thermal conductivity and my theoretical lattice thermal conductivity. Black solid line - calculation with rigidly shifted upwards optical phonons, Black dashed line - calculation with *ab initio* phonon dispersion. Green circles and squares are the experimental data of Ref. [14] and Ref. [91] respectively. Red dashed line shows the value of the non-lattice thermal conductivity at T = 300 K with calculated with *ab initio* phonon dispersion.

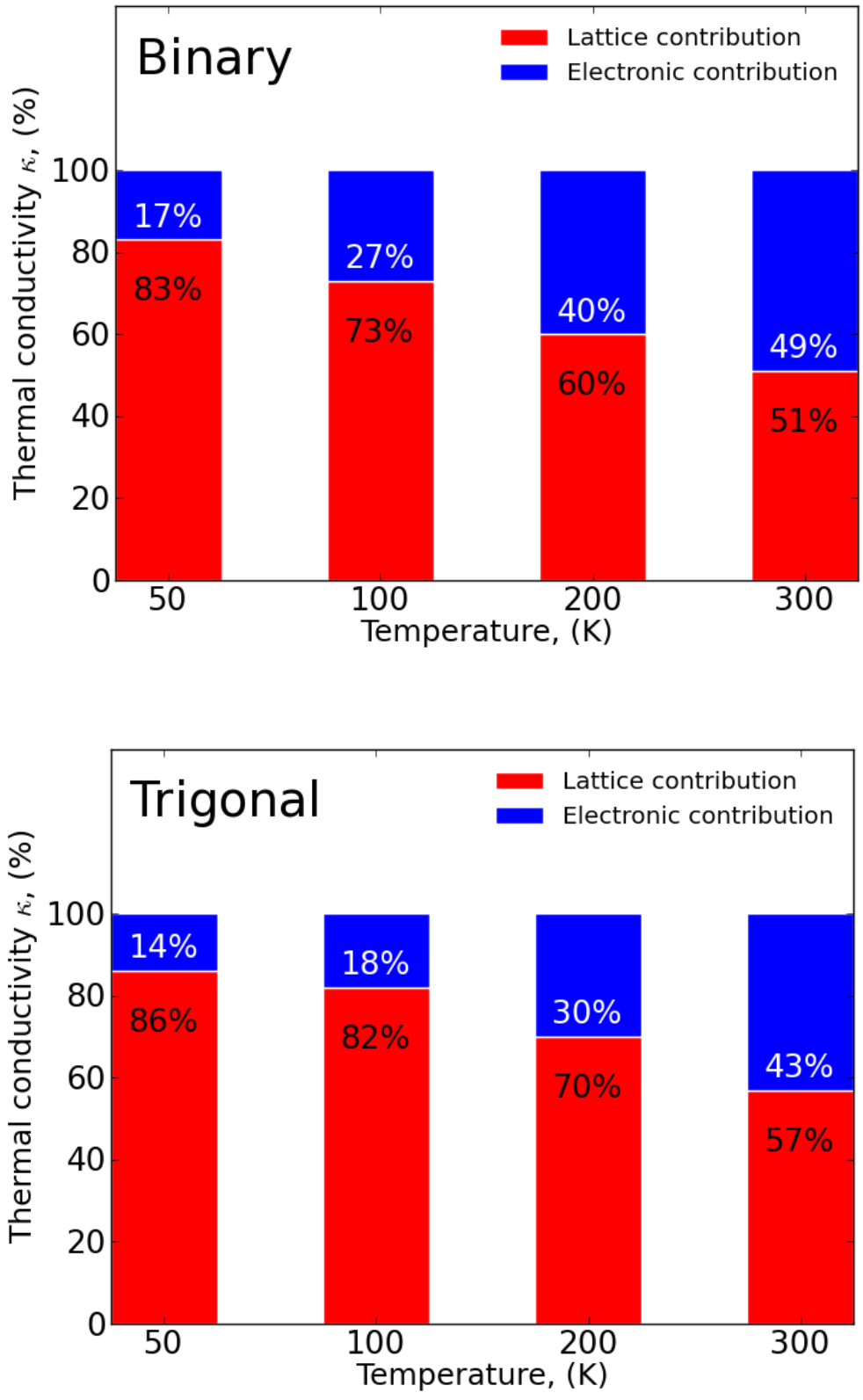

Figure 4.3: Relative contributions of the lattice vibrations (red bars) and of the charge carriers (blue bars) to thermal conductivity of bismuth in the binary (top panel) and trigonal (bottom panel) directions

.

In Fig. 4.4, I show the anisotropy ratio of the **lattice** thermal conductivities obtained in my calculation (black solid line). As one can see, it is constant at T > 20 K and equal to about 1.3. This anisotropy ratio is defined mainly by the acoustic phonons and, thus, does not depend on the shift of optical phonons. The experimental ratio of **total** thermal conductivities (green dashed line) includes the contributions from both the lattice vibrations and the charge carriers. In the region T < 100 K, the black solid curve and the green dashed curve coincide, indicating that the anisotropy ratio is defined only by the lattice part, as expected. The relative role of the charge carrier contribution is negligible in this region.

As we have already seen, the anisotropy ratio of the charge carrier contribution amounts to 2, and play a more and more important role as temperature increases. Thus, we conclude that the anisotropy ratio of the total thermal conductivity increases, while the lattice one stays constant.

Another theoretical results of Lee *et al* [56] (red dashed dotted line) is also displayed for comparison. However, it is considerably lower even in the region of low temperatures where the lattice part strongly dominates.

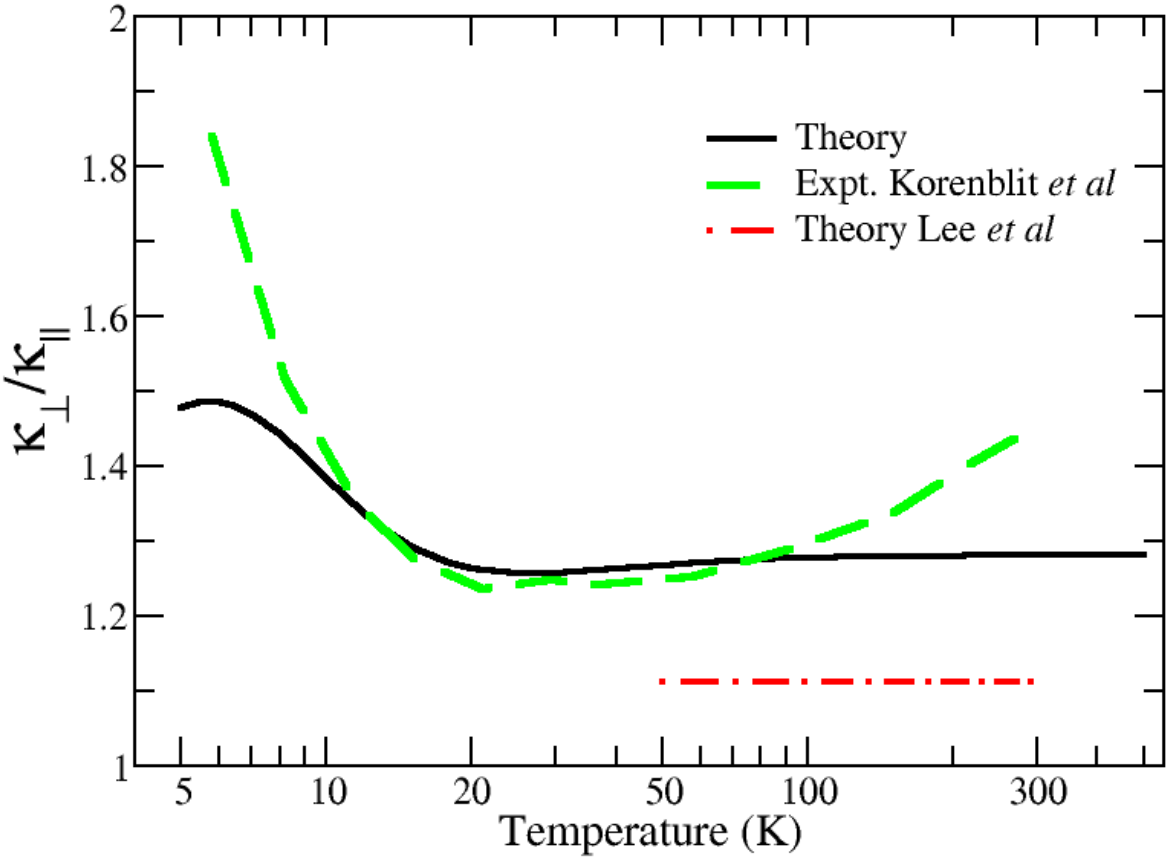

Figure 4.4: Anisotropy of the thermal conductivity defined as the ratio $\frac{\kappa_\perp}{\kappa_\parallel}$ of thermal conductivity in the binary direction $\kappa_\perp$ and $\kappa_\parallel$ thermal conductivity in the trigonal direction. Black solid line - the theoretical lattice thermal conductivity anisotropy found in my calculations. Red dashed-dotted line - the theoretical lattice thermal conductivity anisotropy from Lee *et al.* [56]. Green dashed line - experimental total thermal conductivity anisotropy from Ref. [91].

4.3 Boundary scattering at low temperatures.

In Section 4.2, I have shown that the results of the calculation of the lattice thermal conductivity agree remarkably well with experiment if the realistic acoustic-optical phonon interaction is taken into account. Moreover, I have analyzed the relative role of heat carriers at different temperatures and their role in the anisotropic ratio of thermal conductivities.

However, we have seen in Chapter 3 that the calculated thermal conductivity increases rapidly with the decrease of temperature, tending to infinity at ultra-low temperatures. This divergent behavior is explained by the increase of the phonon mean free path that is an average distance traveled by phonon before being scattered. So far the only source

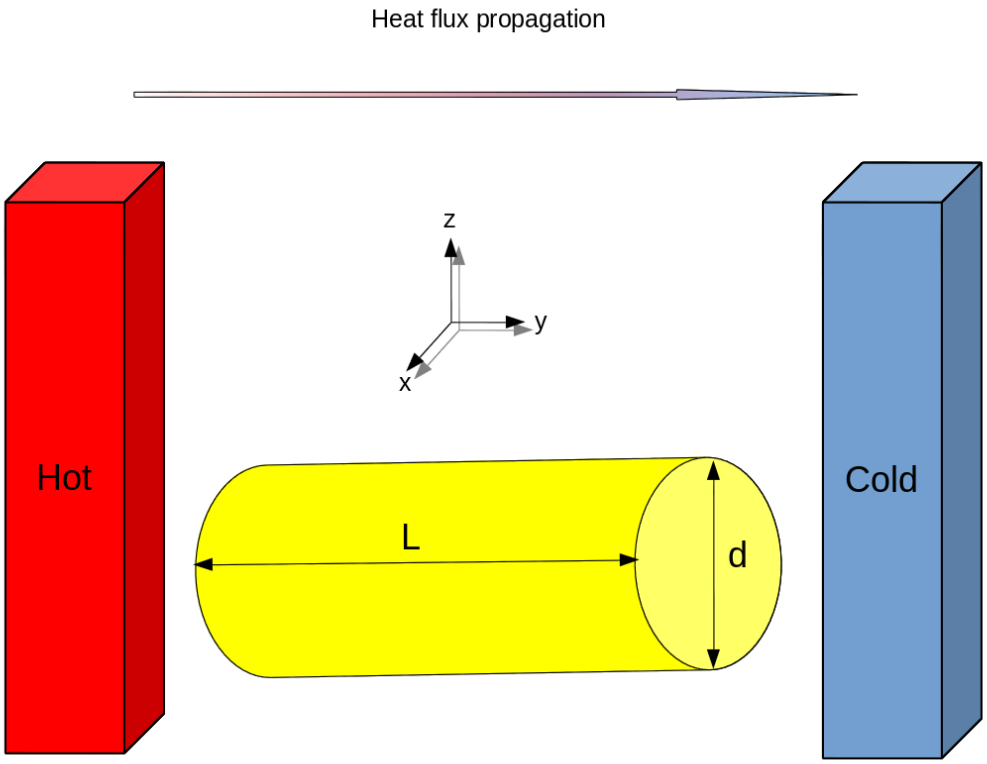

Figure 4.5: Schematic illustration of the geometry of the macroscopic wire of length L and of circular cross-section with diameter d in experiment and in my calculations. Heat propagates in the y direction and the phonon transport is limited in the x and z directions.

of scattering in the calculations was an intrinsic phonon-phonon scattering. But the real experimental samples always have a finite size and the sample boundaries must limit the diffusive propagation of phonons. Thus an additional external source of scattering of phonons from sample boundaries must be included along with the internal phonon-phonon scattering to prevent the divergence of the lattice thermal conductivity in my calculations and describe thermal transport at ultra-low temperatures.

4.3.1 Definition and implementation of the Casimir scattering cross-section.

As we have already discussed in Section 1.2.3, boundary scattering of phonons could be included in the calculation by means of Casimir model [27]. This model gives an analytical expression for the probability of reflection of phonon from the boundary

$$P_{\nu}^{be} = \frac{\left|\mathbf{c}_{\nu}^{b}\right|}{L^{Cas}F} n_{\nu}^{0}(n_{\nu}^{0}+1) \tag{4.1}$$

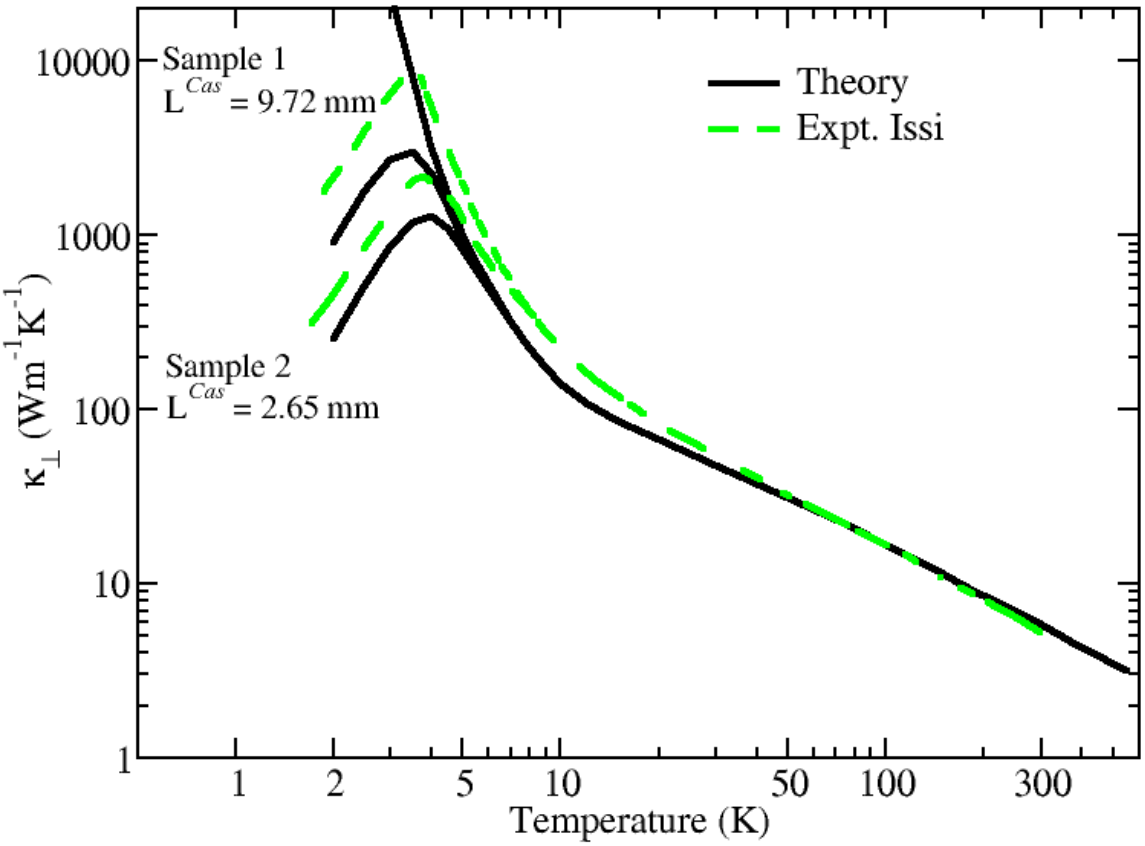

Figure 4.6: Temperature dependence of the lattice thermal conductivity in the binary direction for a single crystal without and with millimeter-sized boundary effects. Black solid lines: the result with no Casimir's scattering rate, or with $L^{Cas} = 2.65$ mm and 9.72 mm. Green dashed lines: lattice thermal conductivity found as a difference between measured total thermal conductivity (from Ref. [14] for sample 1 of a rectangular cross-section 8.8×8.6 mm^2 or from Ref. [91] for sample 2 of diameter $d = 2.65$ mm) and the electronic thermal contribution of 6 W(K.m)$^{-1}$ as determined earlier.

where n^0_ν is the equilibrium Bose-Einstein distribution for the phonon mode ν, L^{Cas} is the Casimir length, describing the shortest sample dimension, F characterizes the sample roughness [27] and is taken to be 0.5 in all further calculations [132, 133, 5], $|\mathbf{c}^b_\nu|$ depends on the phonon group velocity $\mathbf{c}_\nu$ in the direction(s) in which the phonon transport is limited by the sample boundary, and, thus, is defined by the sample geometry.

Most of the experiments have been carried out on macroscopic wires with either circular or rectangular cross-sections. The illustration of the sample geometry with circular cross-section is shown in Fig. 4.5. Heat propagates along the chosen direction which has the length L (oriented along y axis on the figure) that is much longer than two other directions (oriented along x and z axis on the figure) of length d. In this geometry the heat transport is limited in the directions perpendicular to the propagation direction (i.e. in x and z directions on the figure) and thus $|\mathbf{c}^b_\nu| = \sqrt{(c^x_\nu)^2 + (c^z_\nu)^2}$. The Casimir length L^{Cas} is equal to the diameter d of the sample in case of circular cross section and $L^{Cas} = 2\sqrt{\frac{d_1 d_2}{\pi}}$ in case of rectangular cross-section with sides d_1 and d_2. I have implemented in the program the model for the wires and thin films.

4.3.2 Results with Casimir's scattering cross-section.

In Fig. 4.6 I show the calculated lattice thermal conductivity (LTC) in the binary direction as a function of temperature (black solid curves). To compare with the experimental data, I extract the electronic thermal conductivity of 6 $\mathrm{Wm^{-1}K^{-1}}$ found earlier from the measured total thermal conductivity from Refs. [14, 91] (green dashed curves). The first experimental sample has a rectangular cross-section of 8.8×8.6 $\mathrm{mm^2}$ [14] and the second one has a circular cross-section of $d = 2.65$ mm [91]. I determine Casimir's lengths to be $L^{Cas} = 9.72$ mm and $L^{Cas} = 2.65$ mm respectively (see paragraph above). One can see that the account for boundary scattering makes the lattice thermal conductivity to be finite in contrast to the asymptotically-infinitely large values in the absence of boundary scattering. Moreover, the theoretical curves now well reproduce the experimental behavior of the thermal conductivity and, in particular, the positions of the thermal conductivity maxima at about T = 4 K. Further decrease of temperature leads to the decrease of thermal conductivity with a decay low in $\mathrm{T^3}$, showing the dominant role of the scattering of phonons by the boundaries.

4.4 Summary and outlook

This Chapter is devoted to the comparison of the calculated lattice thermal conductivity presented earlier in Chapter 4 with the available experimental data. My *ab initio* calculation and a previous calculation of Lee *et al.* [56] provide a considerably lower value of the lattice thermal conductivity. I have demonstrated that the lattice thermal conductivity in the binary direction obtained with the account for realistic acoustic-optical phonon interaction (AOPI) shows an excellent agreement with the experiment of Uher *et al.* [16]. Above all, I have predicted the lattice thermal conductivity in the trigonal direction where it has not been measured.

Then I have evaluated the non-lattice (charge carrier) thermal conductivity as a difference between the measured total thermal conductivity and my theoretical results. I have found that it is constant as a function of temperature at $T > 20$ K and equal to 6 $\mathrm{Wm^{-1}K^{-1}}$ in the binary direction and to 3 $\mathrm{Wm^{-1}K^{-1}}$ in the trigonal direction. I have discussed the anisotropy of the thermal conductivity and I have shown that it is determined by the lattice contribution in the region of low temperatures where it dominates. At high temperatures the electronic contribution is comparable with the lattice one and contributes to the anisotropy as well. Above all, I have predicted the charge carrier thermal conductivity in the trigonal direction.

Finally, I have discussed the Casimir model of boundary scattering. I have shown that the account for boundary scattering in macro-samples leads to finite values of the lattice thermal conductivity at ultra-low temperatures in contrast with the divergent values in the presence of phonon-phonon scattering only. I have demonstrated that the Casimir model enables me to describe accurately the position of the thermal conductivity maximum as well as temperature behavior of thermal conductivity down to T = 2 K.

Chapter 5

Thermal conductivity reduction.

Introduction.

The enhancement of thermal insulation properties of materials is one of the ways to increase their thermoelectric efficiency. It requires the reduction of thermal conductivity which governs the heat transport. However, the theoretical investigation of the lattice thermal conductivity in such a complicated material as Bi, even in the bulk case, is a quite challenging task and an accurate description of the scattering between optical and acoustic phonons is necessary. As we have seen in the previous chapters, the latter allows me to reproduce the experimental values and opens the way to study the possible routes of thermal conductivity reduction in Bi. That is the aim of this chapter.

The chapter is organized as follows. First, in Section 5.1, I discuss the effect of acoustic-optical phonon interaction (AOPI) and its possible realization in photoexcited bismuth. I show how the magnitude of the lattice thermal conductivity is modulated with the rigid shift of optical phonons. Second, in Section 5.2, I discuss some of the existing approaches to study the effect of nanostructuring which is a well known way to reduce the lattice thermal conductivity. I show that by means of the Casimir model, one can study nanostructures of different geometries. I compare the results of my calculations with experiments on polycrystalline thin films as well as polycrystalline and single crystal nanowires. Finally, in Section 5.7, I predict the reduction of the thermal conductivity in semimetallic and semiconducting thin films and polycrystalline bismuth for different thicknesses and grain sizes respectively.

5.1 Enhancing the acoustic-optical phonon interaction.

In the previous chapters we have seen that an appropriate position of TO phonon branches at Γ is mandatory for an accurate description of the lattice thermal conductivity in Bi. This results in a realistic estimation of the interaction between the acoustic and optical modes (AOPI) comparing with the pure *ab initio* calculation where this interaction is overestimated due to the softening of the optical phonons.

Experimentally, the modulation of the strength of the AOPI defined by the indirect phonon gap between the LA branch at T point and the TO branch at Γ has been achieved by photoexcitation of bismuth in ultra-fast pump-probe experiments [134]. The effect of photoexcitation on the phonon dispersion of Bi has been studied by Murray *et al* [115] by means of the constrained DFT approach in which the valence and conduction bands are filled independently of each other using Fermi-Dirac distributions. Two chemical potentials are determined by requiring the correct total number of electrons within each set of bands separately and Bi has been treated as semiconductor [115]. The resulting dispersions for 0% (equilibrium, orange solid curve) and 1% (magenta dashed curve) fraction of the valence electrons excited to the conduction bands are shown in Fig. 5.1 as well as my theoretical dispersion with the shifted optical branches (black solid lines) and the existing experimental data for phonons in not excited Bi (green crosses and pluses). One can see that photoexcitation has a negligible effect on acoustic phonons which match well with the DFT results. In the equilibrium state, the transverse optical modes at Γ obtained with the constrained DFT approach lie at a frequency about of 79 cm^{-1} that is even higher then the experimental value (see also Table 3.3). In the photoexcited state, the frequencies of optical phonons are reduced almost uniformly over the Brillouin zone by about 8.5 cm^{-1} downward. Thus the rigid shift discussed earlier can be regarded as the photoexcitation of Bi.

The softening of the optical modes may result from two main factors: from the reduction of bond strength when electrons move out of their bonding state and from the change in the equilibrium value of the internal parameter u which describes the atomic positions along the trigonal axis [115] (see Appendix A for details of the atomic structure of Bi). In the latter case u tends to 0.5 which corresponds to the cubic phase and the optical modes must tend toward their corresponding acoustic modes, as the system moves from a two atom unit cell to a single atom unit cell system. The change in the equilibrium value of u has been found to be the dominating factor on the softening of the TO modes [115].

In Fig. 5.2(a), I show the lattice thermal conductivity as a function of the shifting frequency ω_{shift} of optical phonons at T = 100 K (green solid line), 200 K (blue solid line) and 300 K(black solid line). Its zero value corresponds to the experimental position of the TO mode at the zone center. The positive and negative shifting frequencies are attributed to the upward and downward shifts respectively. One can see a monotonous decrease in thermal conductivity with the frequency shift at all temperatures. *Ab initio* values are marked with black dashed-dotted line and lie considerably lower than the experimental values as I have already discussed in the previous chapter. The corresponding reduction factors with respect to $\omega_{shift} = 0$ are shown in Fig. 5.2(b). The shift down to 8.5 cm^{-1} caused by excitation of 1% valence electrons to conduction band [115] leads to the decrease of the lattice thermal conductivity by about 1.4 times. The reduction factor is found to grow almost linearly with the shifting frequency ω_{shift}.

The AOPI turns out to be the reason of thermal conductivity reduction in many materials. For example, the strong anharmonic coupling between the ferroelectric transverse optic mode and the longitudinal acoustic modes results in extremely low thermal conductivity in PbTe [135]. In relaxor ferroelectrics the anharmonic interaction between TA and TO modes leads to the "waterfall" effect when optical phonons become over-damped and

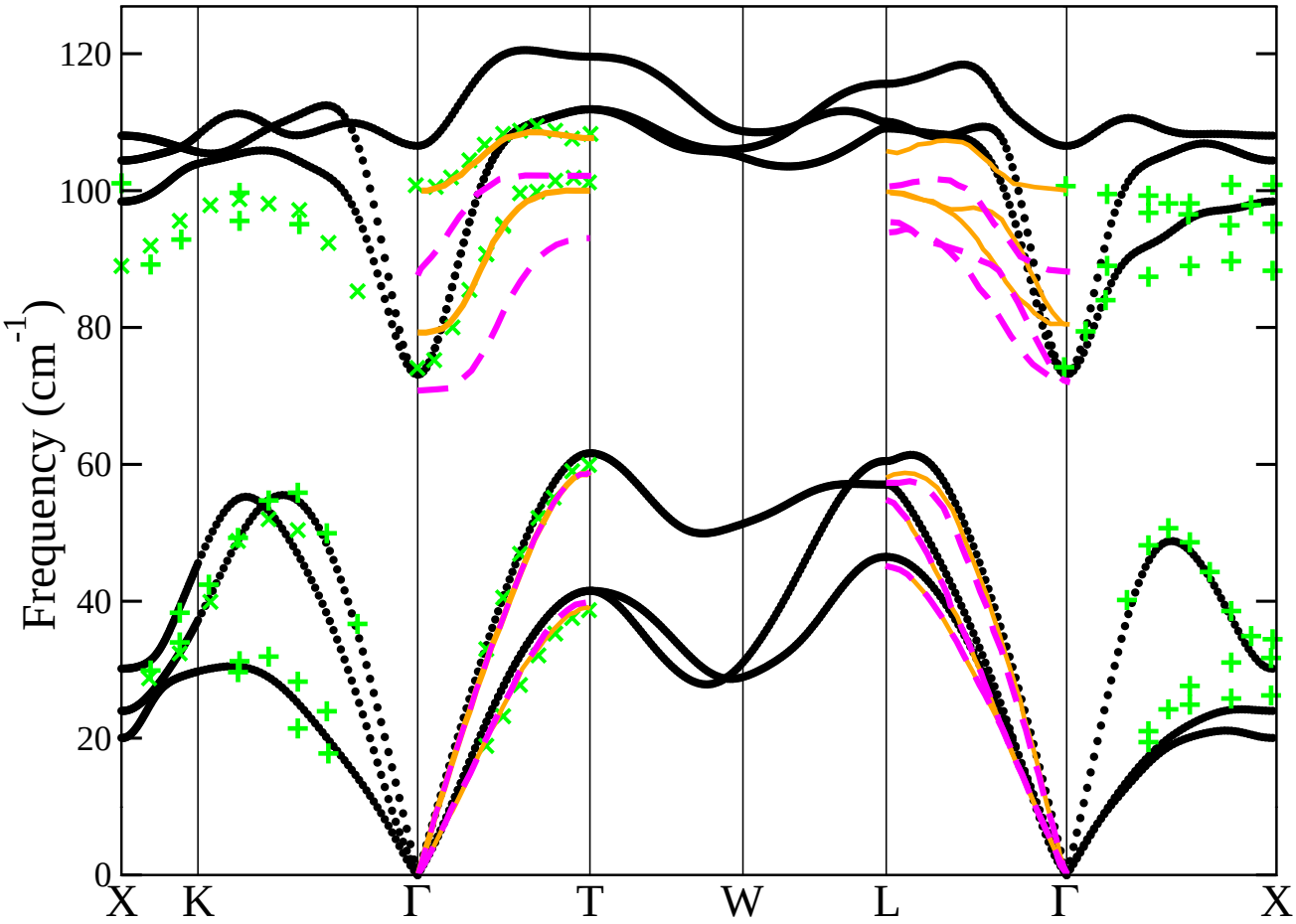

Figure 5.1: Theoretical phonon dispersion with upwardly shifted optical branches to match the frequency of the TO mode at the zone center Γ (black solid lines) and the ones obtained by Murray *et al.* [115] by means of the constrained DFT calculations with 0% (orange solid curve) and 1% (magenta dashed curve) fraction of the valence electrons excited to the conduction bands. Experimental data extracted from [112] (green pluses) and [113] (green crosses)

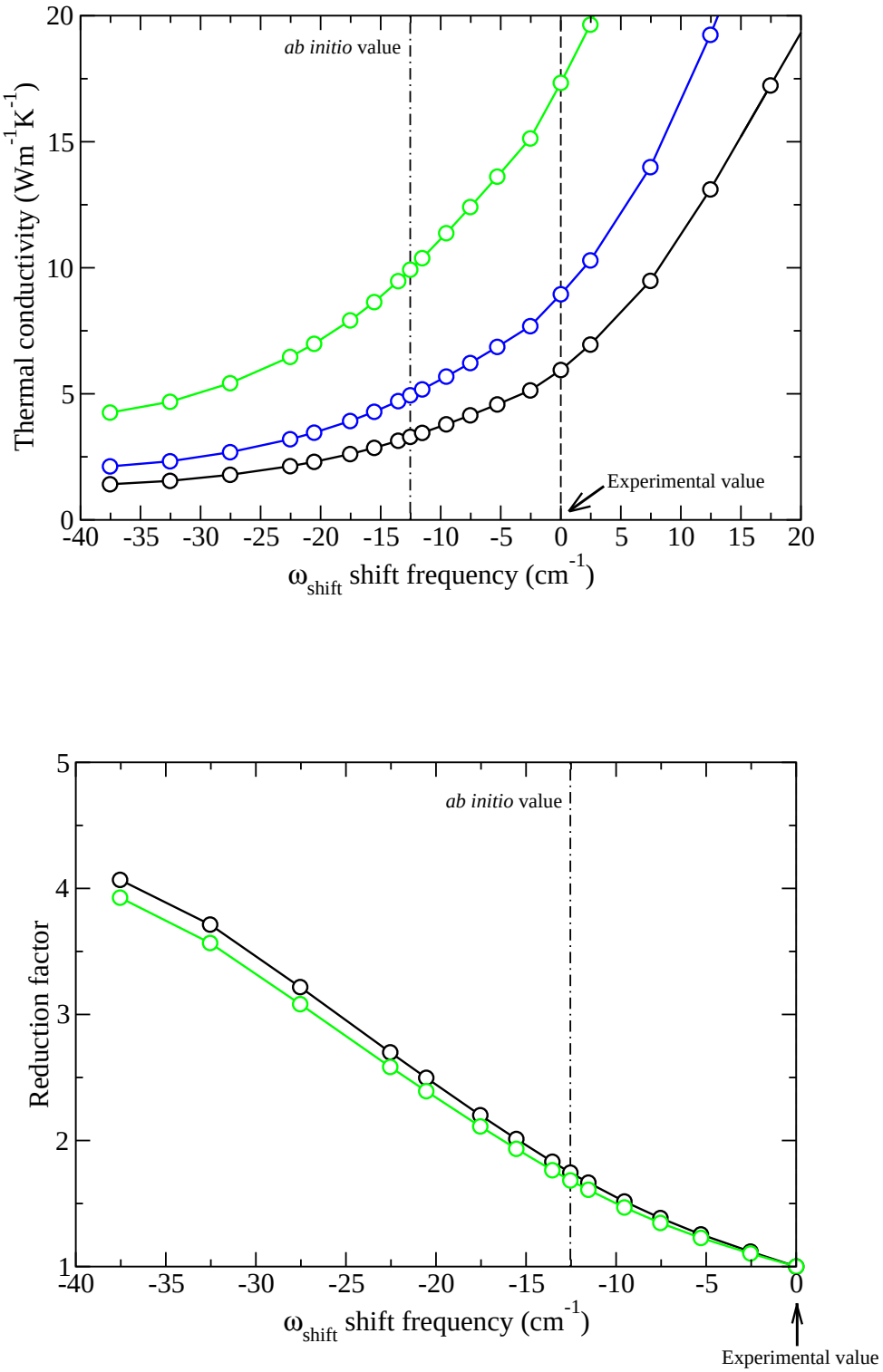

Figure 5.2: Top panel: The lattice thermal conductivity κ_L as a function of the shift frequency ω_{shift} of optical phonons at T = 100 K (green solid line), 200 K (blue solid line) and 300 K (black solid line). Bottom panel: The reduction factor caused by the downward shift of the optical branches ω_{shift} at T = 100 K (green solid line), 200 K and 300 K (black solid line) which are matched to each other. *Ab initio* value of ω_{shift} is marked with thin black dashed-dotted line. Experimental value is set to $\omega_{shift} = 0$.

seem to fall into the acoustic branch resulting in glass-like thermal conductivity [136]. Moreover, in inclusion compounds the acoustic-optical coupling may lead to the resonances between the acoustic modes of the host material and localized modes of the inclusion which leads to enhanced scattering called resonant scattering [48]. In general, this mechanism could be important in any systems with low-lying optical phonon modes and potentially it provides an efficient way of the thermal conductivity reduction [48].

As I have shown in this section, the AOPI could be the way to reduce the lattice thermal conductivity in bismuth. To the best of my knowledge, for the moment no experimental route but photoexcitation was found to soften the optical phonons in bulk Bi. However, the excitation by laser is hard to implement in a thermoelectric device since it has to be constantly maintained. Thus, the result of this section should enoughbe regarded as a theoretical concept.

5.2 Interface scattering.

Interface scattering is a well-known and effective mechanism of the thermal conductivity reduction in materials [137, 138, 139]. It provides the way to improve the thermal insulation properties that is extremely important for thermal management applications. The enhancement of the interface scattering could be achieved by reducing the dimensionality of the material in 1, 2 or 3 directions like in thin films, nanowires and spherical dots. Other nanostructures of various geometries have also been investigated [22], by using a polycrystalline material where the phonons encounter small polycrystalline grains [27, 140] or by nanoparticle inclusions embedded in alloy [141, 142]. On the other hand, the nanostructuring leads to the enhancement of the Seebeck coefficient S and consequently of the power factor $S^2\sigma$, through the modification of the density of states for electrons and holes [17, 18], especially through the decrease of the symmetry of electrons and holes on either side of the Fermi level [12] (see also Section 2.3.2). The simultaneous reduction of the thermal conductivity and the increase of S will result in the significant enhancement of the overall figure of merit ZT necessary to improve the thermoelectric efficiency of the materials [143, 144, 145, 146, 102].

Bulk bismuth has the lowest thermal conductivity among all metals except mercury [15]. The Seebeck coefficient is also large in Bi. However, it is not considered as a good thermoelectric material because of the semimetal band structure which leads to a small electrical conductivity. The interest in Bi as a thermoelectric material was renewed when theoretical and experimental investigations of size effects on the transport properties of Bi and Bi-based nanostructures predicted an enhancement in ZT for one-dimensional systems such as nanowires [147]. The physical mechanisms that result in the superior thermoelectric performance of low-dimensional materials are the increase in the Seebeck coefficient S and the simultaneous reduction of the lattice thermal conductivity [22]. Indeed, in Bi the confinement effect leads to a semimetal-to-semiconductor transition [15, 96, 97] and favors an increase of the thermopower coefficient [15], by several orders of magnitude for instance in a 15-nm-sized Bi composite [96, 97]. The detailed investigation of the thermal conductivity reduction in Bi nanostructures is thus of high practical interest. It will complement the existing studies of the electronic transport

properties of Bi and will give an additional piece of information necessary to evaluate the thermoelectric figure of merit.

In the following sections, I describe the approach I use to study the lattice thermal conductivity of nanostructures. I compare my theoretical calculations with the existing experimental data to show the predictive capability of the method. Finally, I predict the lattice thermal conductivity reduction and the possible overall effect on ZT.

5.3 Method: Casimir's approach *versus* accumulated approach.

5.3.1 Accumulated approach.

The typical approach used in the literature to evaluate the effect of size reduction is an *a posteriori* analysis [148, 149]. It consists in the analysis of the lattice thermal conductivity as an accumulated function of the mean free paths of individual phonons. This approach could be used either in single mode approximation (SMA) or in combination with the iterative solution of the BTE (see Section 1.4.2) when all ingredients to obtain the lattice thermal conductivity defined in (see Eq. 1.46)

$$\kappa_L = -\frac{\hbar}{N_{\mathbf{q}} V k_B T} \sum_{\nu} n_{\nu}^0 (n_{\nu}^0 + 1) c_{\nu}^{heat} \omega_{\nu} f_{\nu} \tag{5.1}$$

are known. Here, the key ingredient, f_ν, is the deviation of the phonon population with respect to the equilibrium distribution n_ν^0 under the influence of the scattering terms, namely the phonon-phonon interaction and the boundary scattering.

Mathematically, to obtain an accumulated lattice thermal conductivity of fixed nanostructure size d one keeps the phonon distribution of bulk material and cancels the phonon contributions to the lattice thermal conductivity when the phonon mean free path Λ is larger than d [148, 149]. The lattice thermal conductivity of Eq (5.1) then becomes

$$\kappa_L(d) = \int_0^d dx \kappa_L(x) \delta(\Lambda - x) \tag{5.2}$$

The described accumulated approach may be valid for the nanostructure analysis only if the mean free paths in nanostructure remain the same as in the bulk. However, the thermal conductivity is a collective property and the change of extrinsic sources of scattering does not merely scale down the largest mean free paths but it also affects all the distribution at once [52]. Thus another approach directly accounting for the redistribution of the phonon mean free paths must be used to correctly describe the lattice thermal conductivity in nanostructures.

5.3.2 Casimir's approach.

To accurately account for the scattering due to the sample boundaries I used the Casimir model [150] with the scattering rate for a phonon ν (see Section 1.2.3)

$$P_{\nu}^{be} = \frac{\left|\mathbf{c}_{\nu}^{b}\right|}{L^{Cas}F} n_{\nu}^{0}(n_{\nu}^{0}+1) \tag{5.3}$$

It has already been used in Section 4.3 to successfully describe the behavior of the lattice thermal conductivity in the finite samples of macroscopic sizes at low temperatures. In particular, boundary scattering has been shown to lead to finite values of the lattice thermal conductivity in contrast with the divergent values in infinite samples. The temperature dependence of the lattice thermal conductivity and the position of its maximum were also described remarkably well validating the correctness of the model on the macroscopic scale.

Boundary scattering depends on the geometry of the sample and on the roughness of the surface. The latter is defined by the specular parameter F which is set to 0.5 everywhere in our calculations to be consistent with the previous theoretical works [132, 133, 5]. The geometry of the sample defines the directions in which the phonon transport is limited by the sample boundary and thus $\left|\mathbf{c}_{\nu}^{b}\right|$ in the formula of the Casimir scattering rate (5.3). It depends on the sample orientation in space with respect to the direction in which the heat flux is measured.

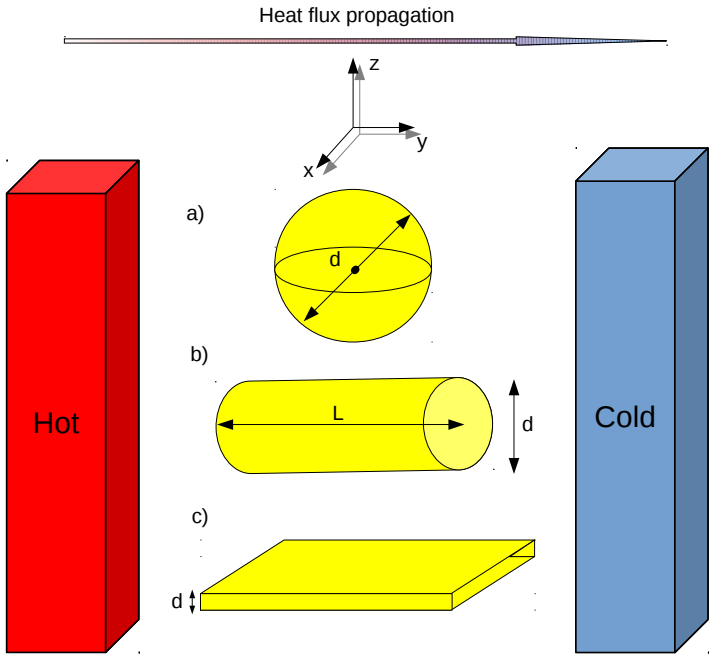

Figure 5.3: Illustration of different sample geometries: a) spherical grains, b) cylindrical wire and c) thin film.

Method	Accumulated approach		Casimir's scattering
T (K)	Lee *et al.*. [56]	This work	This work
Binary direction			
10	-	3380	10400
20	-	526	1430
50	120	148	410
100	55	69	190
200	26	34	90
300	17	22	60
Trigonal direction			
10	-	2240	5467
20	-	412	760
50	87	126	160
100	40	59	68
200	19	29	32
300	13	19	21

Table 5.1: Bi: maximum value of the heat carrier mean-free path Λ (nm) which provides a contribution of 50% to the bulk lattice thermal conductivity in the binary and trigonal directions.

5.3.3 Casimir's approach: geometry.

In contrast to the usual accumulated approach, the Casimir model allows to study the different sample geometries such as thin films, wires, spherical nanoparticles (Fig. 5.3 (c), (b) and (a) respectively). For the sake of generality, in Fig. 5.3, I use Cartesian coordinates, and the heat flux is measured in y direction. In this case we have:

- $\left|\mathbf{c}_\nu^b\right| = |c_\nu^z|$ for the **thin film** geometry,
- $\left|\mathbf{c}_\nu^b\right| = \sqrt{(c_\nu^x)^2 + (c_\nu^z)^2}$ for the **nanowire** geometry,
- $\left|\mathbf{c}_\nu^b\right| = \sqrt{(c_\nu^x)^2 + (c_\nu^y)^2 + (c_\nu^z)^2}$ for the **spherical-grain** geometry.

Here, c_ν^x, c_ν^y, c_ν^z are Cartesian components of the phonon group velocity $\mathbf{c}_\nu$ and $L^{Cas} = d$ is the smallest dimension in which the reduction occurs.

5.3.4 Comparison between Casimir's approach and the accumulated approach.

When applied to bismuth, results obtained with eq. (5.2) and with the full iterative solution of the BTE exceed the ones found in the work of Ref. [56] (columns 1 and 2 in Table 5.1). The difference is explained by the softened optical modes near Γ in the

calculations of Ref. [56] (i.e. enhanced AOPI). It results in an effective scattering channel of the acoustic phonons and smaller phonon relaxation times. The phonon mean free paths and the lattice thermal conductivity are reduced accordingly.

In Figure 5.4, I show that the two approaches yield very different results for the nanostructure lattice thermal conductivity. Indeed, the accumulated approach (Fig. 5.4, empty squares and circles) yields an overestimation of the lattice thermal conductivity in the nanostructures by a factor of 1.6 for a 100 nm nanostructure, and by a factor of 2.0 for a 50 nm nanostructure at ambient temperatures, with respect to the exact solution of the Boltzmann Transport Equation. At low temperature $T = 10$ K, on the contrary, the lattice thermal conductivity is underestimated by the *a posteriori* analysis, by more than one order of magnitude for 100 nm and 50 nm nanostructures.

Turning to the nanostructure size predicted by the two approaches which would yield a 50% reduction of the lattice thermal conductivity, we find that nanostructure sizes obtained with the accumulated approach (column 2 in Table 5.1) are about three times smaller than those predicted using Casimir's scattering rate (column 3 in Table 5.1), at all temperatures. This shows that there is a strong redistribution of the phonon mean free paths when the effect of sample boundaries is taken into account.

5.3.5 Modeling of grain boundaries: polycrystalline samples.

Sample boundaries are the only interface-related source of scattering in *single-crystalline* objects. However, often the experiments are carried out on samples having *polycrystalline* nature. Such samples are composed of a number of smaller crystals or crystallites of different orientations. The presence of grain boundaries introduces an additional source of scattering, which I assume to be independent on others. Thus, for the polycrystalline structures two independent scattering rates of Eq. 5.3 corresponding to the geometry of spherical grain and of the sample under consideration must explicitly be taken into account at the same time. The scattering rates include the extrinsic length L^{Cas}_{grain} for grains and L^{Cas}_{sample} for sample geometry corresponding to the average grain size and minimum dimension of the sample respectively.

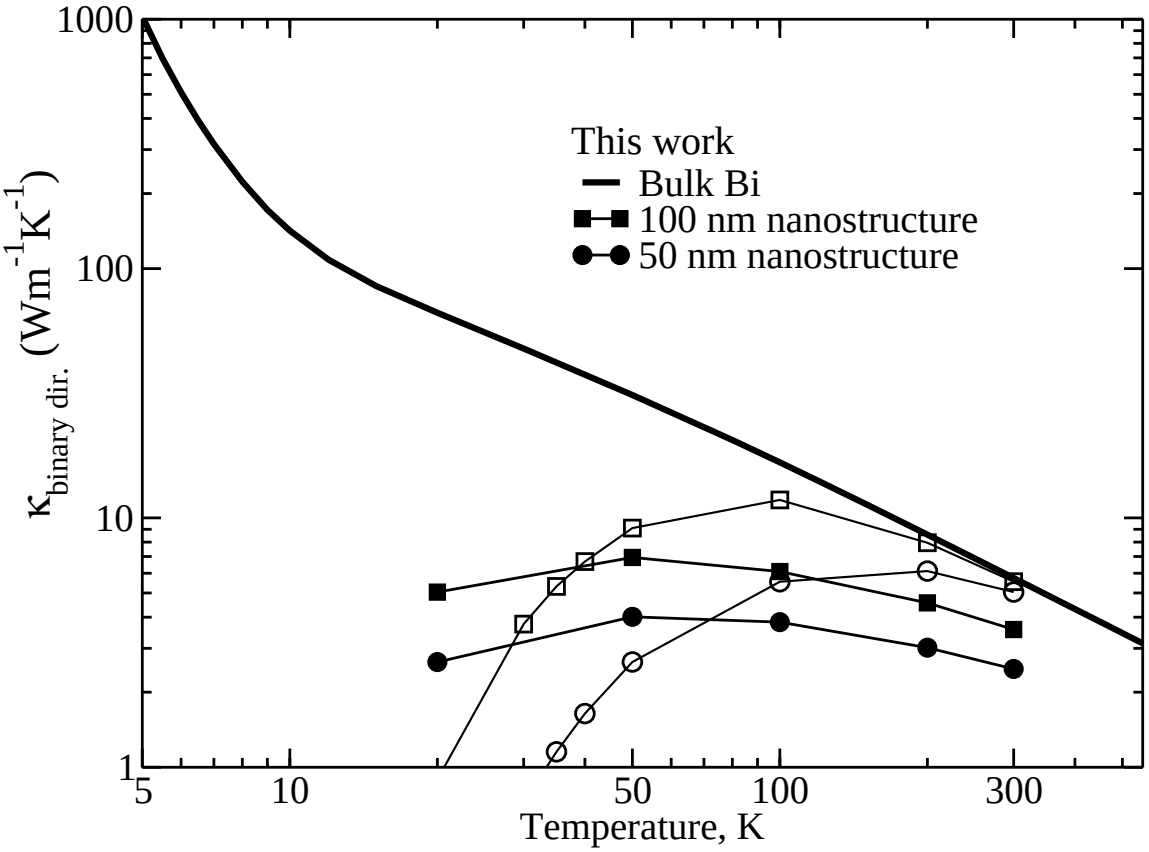

Figure 5.4: Temperature dependence of the lattice thermal conductivity (LTC) in the binary direction of Bi (black solid line). The results for the exact solution of bulk bismuth and for polycrystalline nanostructures with grain sizes of 100 nm (filled squares) and 50 nm (filled disks). The results obtained with the accumulated approach in this work are given for a 100-nm nanostructure (empty squares) and for a 50-nm nanostructure (empty disks).

5.4 Comparison with experiments on polycrystalline thin films.

Bismuth is built of pucked bilayers of atoms perpendicular to the rhombohedral [111] direction (trigonal axis) in which each atom is covalently bonded to its three nearest neighbors. The inter-bilayer bonding is much weaker than the one inside the bilayers. This makes possible to cleave Bi crystals along the [111] direction [114].

However, the exfoliation of bismuth layer (like in graphene or Bi_2Te_3) has never been achieved experimentally. The growth of Bi single crystalline thin films even in [111] is also a quite challenging task and the properties of thin films close to the bulk were obtained only in recent experiments [151, 152]. Unfortunately, no measurements of thermal conductivity in such samples has ever been done. In contrast, most of the experimental studies have been performed on *polycrystalline* or nanoporous thin films [19, 153, 20, 21].

To show a predictive power on the nanoscale of the method I use, I compare the calculated thermal conductivity of polycrystalline thin films with the measurements performed by Volklein and coauthors [19, 153]. First, I note that the nanostructuring effect in polycrystalline samples is characterized by both film thickness d, and average grain size G which I model with the spherical grain geometry (see Section 5.3.3). Thus, in my calculation I take into account scattering from both thin film boundaries and polycrystalline grains at the same time. The resulting thermal conductivity (black solid lines) at T = 100 K, 200 K and 300 K as well as the experimental data of Ref. [19] (red diamonds) are shown in Fig. 5.5. Thin film thickness and average grain size are not independent and have been found to be $G(d) \sim log(d)$ in experiment [19] (see Fig. 5.6(a)). For clarity, I show in Fig. 5.5 the dependence of thermal conductivity on film thickness (bottom abscissa) and on average grain size (top abscissa). As one can see the results show a remarkable agreement with experiments of Ref. [19]. For very thin films, the average grain size has been found to be much larger than the film thickness and thus sample boundaries is a dominating extrinsic source of scattering. Contrastingly, for film thicknesses larger than 200 nm, an average grain size is inferior to the film thickness and the scattering from polycrystalline grains is more important than the scattering from the sample boundaries.

In Fig. 5.5, the available experimental data of Ref. [20] are also shown (empty squares). In Ref. [20], the average grain size was found to be approximately equal to the film thickness, *i.e.* it was found to be larger than that of Ref. [19] for most samples. Although my calculated lattice thermal conductivity lies between the two experimental data sets for 200 K and 300 K, the best agreement is clearly found for the more recent work [19], the most probable cause being the effect of the film-substrate, as pointed out in Ref. [19].

The fact that the theoretical lattice thermal conductivities are close to the experimental total thermal conductivities is consistent with the marked semiconducting temperature-dependent behavior seen in the film electrical resistivity [19]. In Fig. 5.7(a), I show the electrical resistivity of thin films measured in the same experiment [19] and the one measured in bulk bismuth (black solid curve) [8]. Indeed, one can see that the electrical conductivity drops from 3 to 6 times at ambient temperature and from 20 to 25 times at T = 100 K for the samples studied in the experiment [19]. This results in a significant reduction of the charge carrier component of the thermal conductivity which has

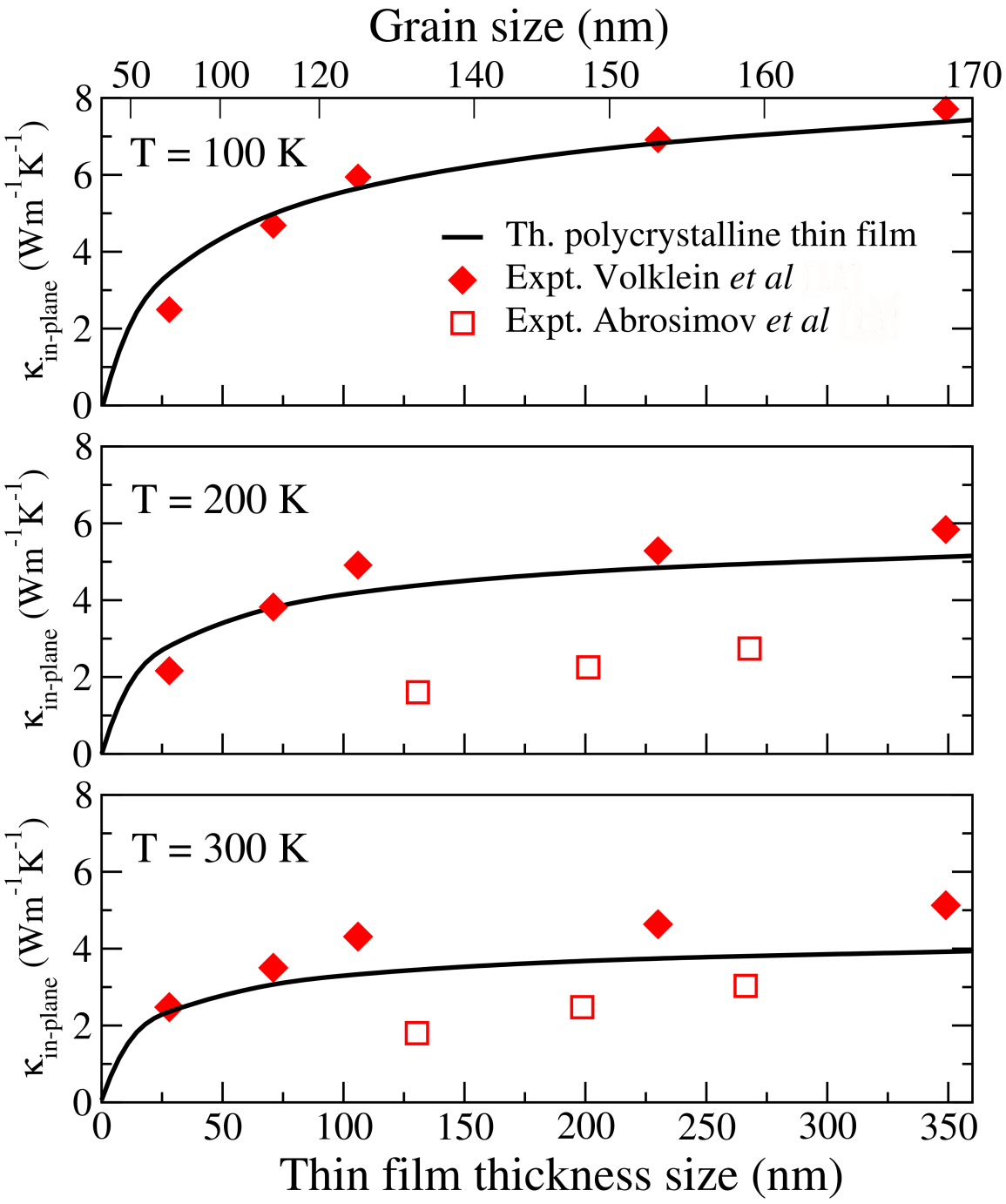

Figure 5.5: Lattice thermal conductivity in the binary direction (solid lines) as a function of the thin-film thickness (nm) (bottom abscissa axis) or of the grain size (top abscissa axis, data from [19]) at 100 K, 200 K and 300 K (resp. top, center and bottom panels). Red filled diamonds: expt. total thermal conductivity κ_{TOT} from Ref. [19]. Empty red squares: expt. κ_{TOT} from Ref. [20].

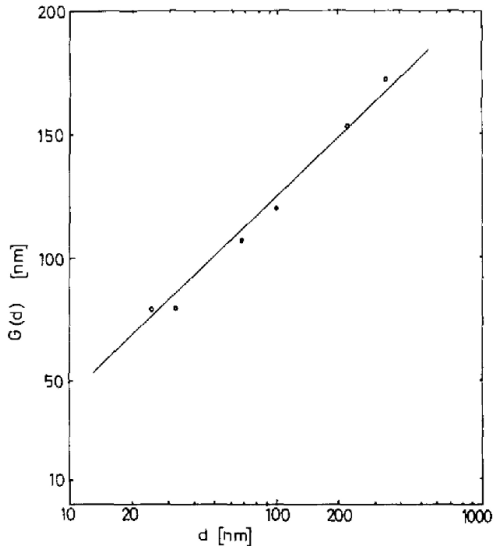

Figure 5.6: Dependence of grain size $G(d)$ ("mean grain diameter") of bismuth films on the thickness d found in experiment [19, 153]. Extracted from Ref. [153].

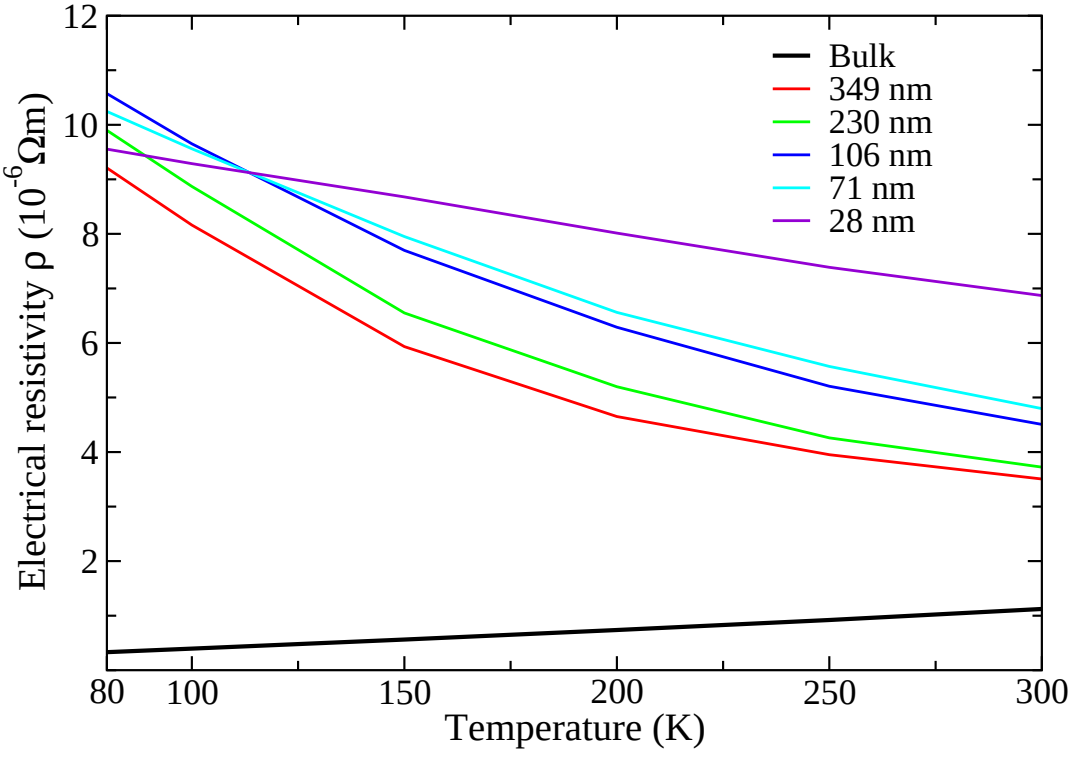

Figure 5.7: Electrical resistivity of Bi thin films measured in the experiments of Ref [19, 153] (red, blue, green, cyan and violet solid curves) and the one measured in bulk Bi [8] (black solid curve).

been found to be constant and equal to about 6 $Wm^{-1}K^{-1}$ in bulk bismuth in the binary direction (see Section 4.2.2).

5.5 Comparison with experiments on nanowires.

5.5.1 Calculations on monocrystalline nanowires.

A quasi-suppression of the thermal conductivity has also been found in bismuth nanowires, but its origin is still debated [15]. Measurements made on nanowires [15, 22, 23, 24, 25, 26], most of which are semiconducting, have yielded widely scattered values. In Fig. 5.8, I show the calculated thermal conductivity for single crystal nanowires (black solid line) which monotonically goes down when the diameter decreases. As one can see, for the nanowire diameters greater than about 200 nm, the curve lies between the experimental data. While for the nanostructures of small size, Casimir's model overestimates the lattice thermal conductivity of nanowire. The extremely scattered character of the experimental data available in literature suggests the presence of unidentified sample-dependent scattering mechanisms in Bi [15], or a problem of contacts in the experiments.

From the experimental point of view, the fabrication and the measurement of the thermal conductivity in single-crystalline nanowires are quite challenging. Synthesized nanowires are often coated with the surrounding oxide shells which might introduce an additional effect on the thermal conductivity. Moreover, the effects of template on which nanowire has been synthesized and of strain in case of suspended nanowire must accurately be taken into account.

Similar problems were recently reported on single-crystalline silicon nanowires [154] where extremely low value of thermal conductivity had been observed. The measured thermal conductivity is one order of magnitude lower than predicted by the diffuse boundary limit of Casimir's theory [100]. The explicit consideration of surface roughness on the atomic level, allowed to obtain lower values of the thermal conductivity than with the Casimir model but a significant disagreement with the experiment was still observed [100, 155]. In other words, available theoretical studies suggest a profound modification of the nanowire atomic structure such as surface oxidation, roughness, and core defects in Si [102, 100, 101].

My calculations show that the same conclusion can be drawn for Bi nanowires. This is surprising with respect to the good agreement with bulk values and with polycrystalline films. Contamination by an oxidation of bulk bismuth has been seen in the experiment of electron energy loss spectroscopy (EELS) [156], in which a peak at 29 eV has been attributed to Bi_2O_3. However, the experiment performed on thin films did not reveal their oxidation.

Thus, the complete understanding of the thermal conductivity in nanowires in general is still lacking. Further studies to resolve the existing discrepancy between theory and experiment would be of great interest and form one of the perspectives of this PhD.

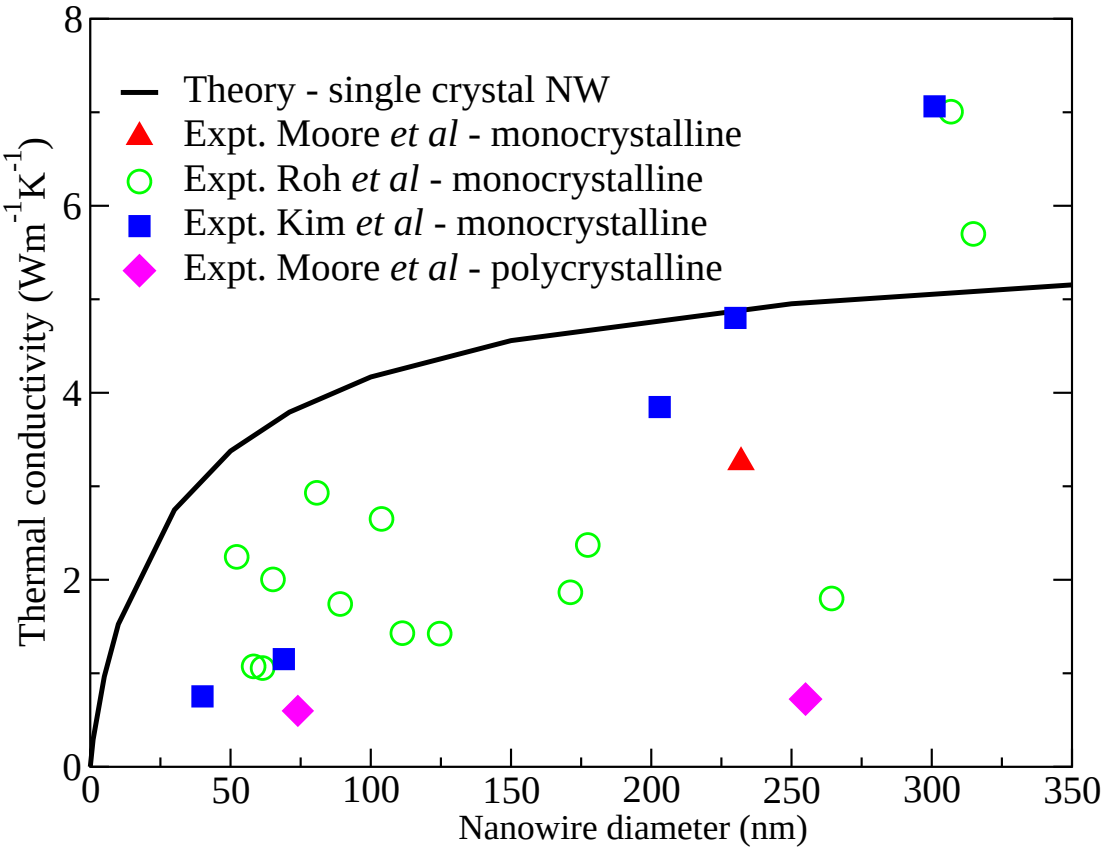

Figure 5.8: Calculated thermal conductivity of single crystalline nanowire grown in the binary direction as a function of the nanowire diameter (black solid line). Experimental data of Ref. [23] (empty green circles), Ref. [26] (blue squares) and Ref. [15] (red triangles) are also indicated.

5.5.2 Calculations on polycrystalline nanowires.

Now let us turn to the polycrystalline nanowires. First, I note that the thermal conductivity measured in polycrystalline nanowires is lower than in single crystal samples and provide a lower band for the thermal conductivity (magenta diamonds on Fig. 5.8). For instance, for the nanowires of $d = 74$ nm and $d = 255$ nm it is $\kappa = 0.60$ $\mathrm{Wm^{-1}K^{-1}}$ and $\kappa = 0.72$ $\mathrm{Wm^{-1}K^{-1}}$ respectively [15]. To describe the experiment of Ref. [15], in analogy with polycrystalline thin films, I introduce two sources of boundary scattering simultaneously *i.e.* the scattering from nanowire boundaries and from grain boundaries. In Fig. 5.9, I show the lattice thermal conductivity for the fixed nanowire diameter given in experiments a function of the grain size (green and black solid lines). The experimental values are displayed with dashed lines. An average grain size has not been identified in experiment of Ref. [15]. I find that the theoretical lattice thermal conductivity matches with the measured one if the grain sizes are 7.5 nm and 5.7 nm for the nanowires with diameters 74 nm and 255 nm respectively.

These values, however, must be taken with extreme caution given the lack of understanding of the case of monocrystalline nanowires reported in the previous section 5.5.1. The scattering by boundaries in Casimir's model is smaller than the one found in experiments. In my calculations for polycrystalline nanowires, a smaller grain size in the scattering by grain boundaries may compensate the smaller value of the scattering by boundaries in nanowires with Casimir's model.

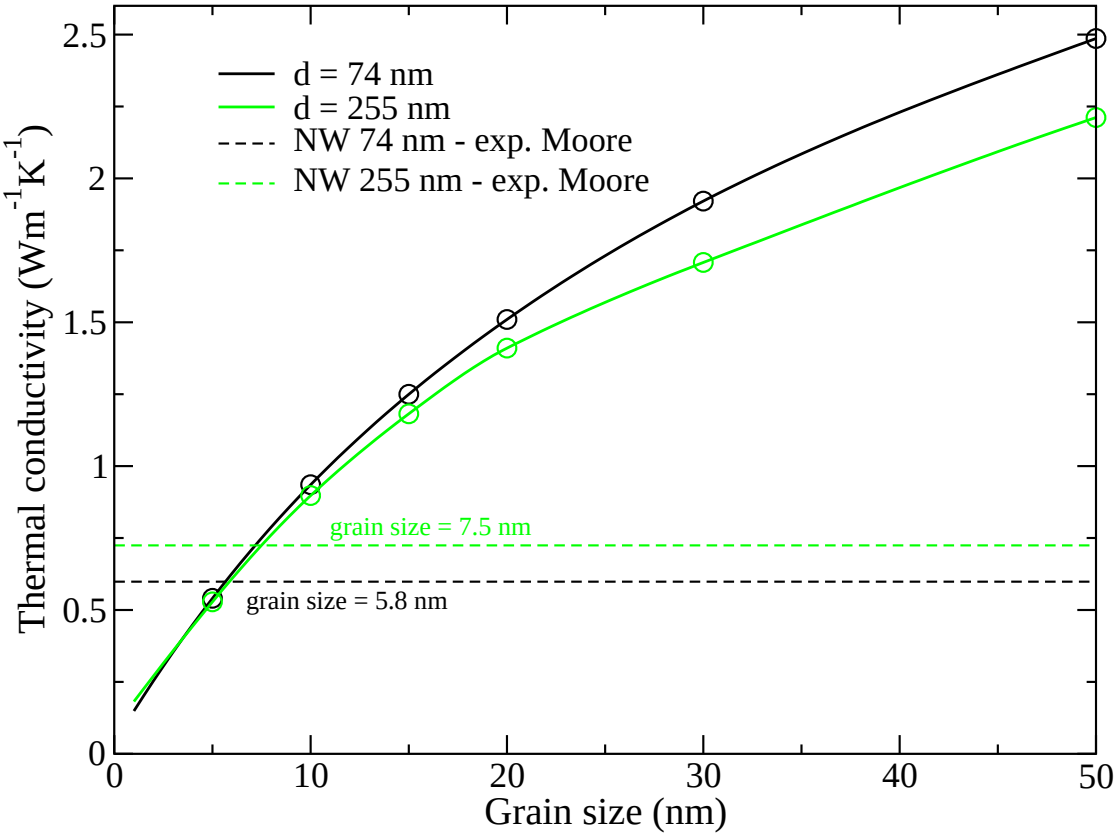

Figure 5.9: Calculated thermal conductivity of polycrystalline nanowires in the binary direction of $d = 74$ nm (black solid curve) and $d = 255$ nm (green solid curve) as a function of the grain size. Experimental thermal conductivities for $d = 74$ nm (black dashed line) and $d = 255$ nm (green dashed line) are shown.

5.6 Effect of geometry on the thermal conductivity of nanostructures.

In the previous sections I have shown a predictive capability of the Casimir model for the available experimental data on thin films. Most of the studied samples possess a polycrystalline nature and the simultaneous account of sample boundaries and grains is crucial to describe the experiment.

Now I consider the *single-crystalline* bismuth nanostructures to see the effect of the geometry on the lattice thermal conductivity. In Fig. 5.10, I show the calculated lattice thermal conductivity for thin films (solid lines), nanowires (dotted lines) and spherical nanograins (dashed lines) at T = 100 K (bottom panel), T = 200 K (medium panel) and 300 K (top panel). I include only one extrinsic source of scattering due to the sample boundary. I take the Casimir length L^{Cas} to be equal to the smallest dimension of the sample. In agreement with previous studies [157, 158], I find that the sample geometry plays an important role in the reduction of the lattice thermal conductivity. The largest heat transport reduction is found for the spherical geometry, and the smallest one for monocrystalline thin films. The results are analogous at all temperatures.

This result could be easily understood if the precise meaning of $\left|\mathbf{c}_\nu^b\right|$ in Eq. (5.3) for each of the geometries is considered. Indeed, as has already been explained in Sec. 5.3, $\left|\mathbf{c}_\nu^b\right| = |c_\nu^z|$ for the thin film geometry, $\left|\mathbf{c}_\nu^b\right| = \sqrt{(c_\nu^x)^2 + (c_\nu^z)^2}$ for the nanowire geometry, and $\left|\mathbf{c}_\nu^b\right| = \sqrt{(c_\nu^x)^2 + (c_\nu^y)^2 + (c_\nu^z)^2)}$ for the spherical-grain geometry. This leads to an obvious relation $\sqrt{(c_\nu^x)^2 + (c_\nu^y)^2 + (c_\nu^z)^2} > \sqrt{(c_\nu^x)^2 + (c_\nu^z)^2} > \sqrt{(c_\nu^z)^2}$ and thus to the inequality for the scattering rates $S_\nu^{grain} > S_\nu^{wire} > S_\nu^{film}$ which is inversely proportional the lattice thermal conductivity in Fig. 5.10. Therefore, the thermal conductivity of the spherical grain is always lower than the one of thin film.

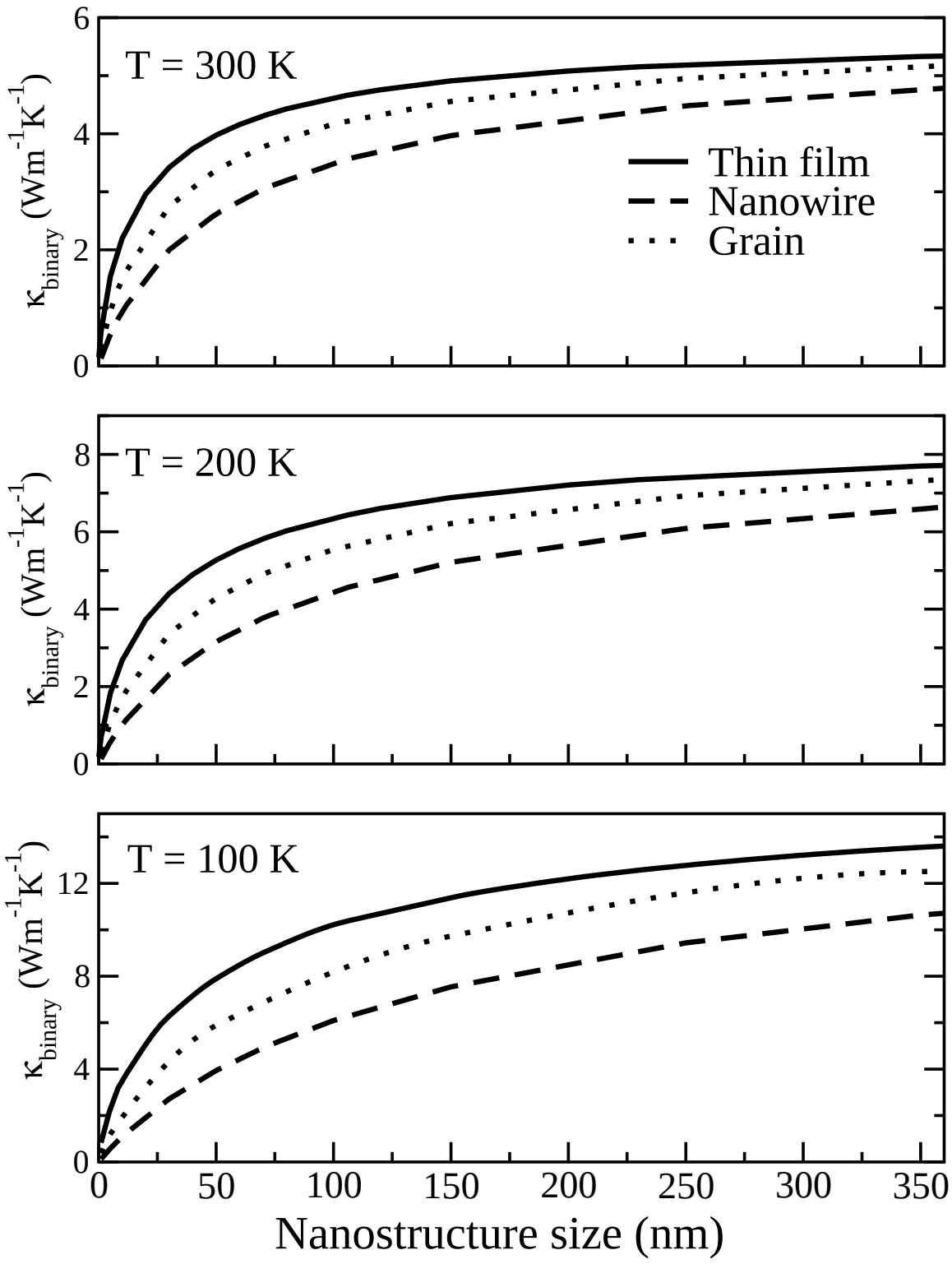

Figure 5.10: Lattice thermal conductivity (LTC) for different geometries of bismuth nanostructures. Solid lines: LTC in the binary direction for monocrystalline thin films as a function of the film thickness. Dotted lines: LTC along the binary axis of monocrystalline nanowires. Dashed lines: spherical grain.

5.7 Reduction factor.

5.7.1 Reduction factor for thin films and spherical grains.

To rationalize the effect of nanostructuring on the lattice thermal conductivity in Bi, I define the reduction factor $R(T) = \frac{\kappa_L^{bulk}(T)}{\kappa_L^{nano}(T)}$, where κ_L^{bulk} is the thermal conductivity of bulk bismuth, κ_L^{nano} is the thermal conductivity of nanostructure. In Fig. 5.11, I show the reduction factor for spherical nanograins (dashed curves) and thin films (solid curves) for a number of temperatures. This figure provides an abacus for the thermal management, that can be employed to deduce the reduction factor for a given nanostructure size or, alternatively, to choose the nanostructure size to obtain a desired reduction of the heat transport.

In Fig. 5.11, we can see that the spherical grain geometry is beneficial comparing with thin film, as has already been pointed out in Sec. 5.6. Indeed, to obtain the same reduction factor one needs a grain size greater than the one of thin film. In cases where only thermal properties matter and electronic conductivity is not so important, the control of grain sizes in polycrystalline films turns out to provide the best strategy for the control of heat transport reduction in bismuth. For instance, for a target reduction factor equal to two, the grain size should be smaller than 62 nm at 300 K, 95 nm at 200 K and 188 nm at 300 K (dashed lines).

5.7.2 Reduction factor for semimetallic and semiconducting thin films.

The synthesis of thin films is facilitated by the atomic structure of bismuth. However, the fabrication of very high quality semimetallic single-crystalline films became possible only recently [151]. The electronic properties of single-crystalline thin-films are much improved with respect to polycrystalline samples, making thin-films a possible alternative for thermoelectric applications. In Fig. 5.12, I show the reduction factor for the semiconducting thin films (thin solid curves) and for the metallic thin films (dashed dotted curves) as a function of nanostructure size and temperature[1]. For the latter case I redefine the reduction factor as $\hat{R}(T) = \frac{\kappa_L^{bulk}+\kappa_E^{bulk}}{\kappa_L^{nano}+\kappa_E^{bulk}}$, where κ_E^{bulk} is the contribution due to the charge carriers in the bulk that has been found to be constant with temperature variation and equal to $\kappa_E^{bulk} = 6$ $\mathrm{Wm^{-1}K^{-1}}$ in the binary direction. One can see that because of the presence of the charge carrier contribution the reduction is smaller in the case of metallic thin films. For a target reduction by factor of two, the film thickness should be smaller than 4 nm at 300 K, 12 nm at 200 K and 40 nm at 100 K. Instead, nanostructure sizes of 19 nm at 300 K, 27 nm at 200 K and 60 nm at 100 K are found to be necessary in case of semiconducting thin films.

[1] I assume that harmonic and anharmonic force constants of Bi in semiconducting state remain the same as in semimetallic state. Calculation of phonon dispersion of semiconducting bismuth has been done in Ref. [115] and show no difference in acoustic part of phonon dispersion that brings the main contribution to the lattice thermal conductivity of Bi.

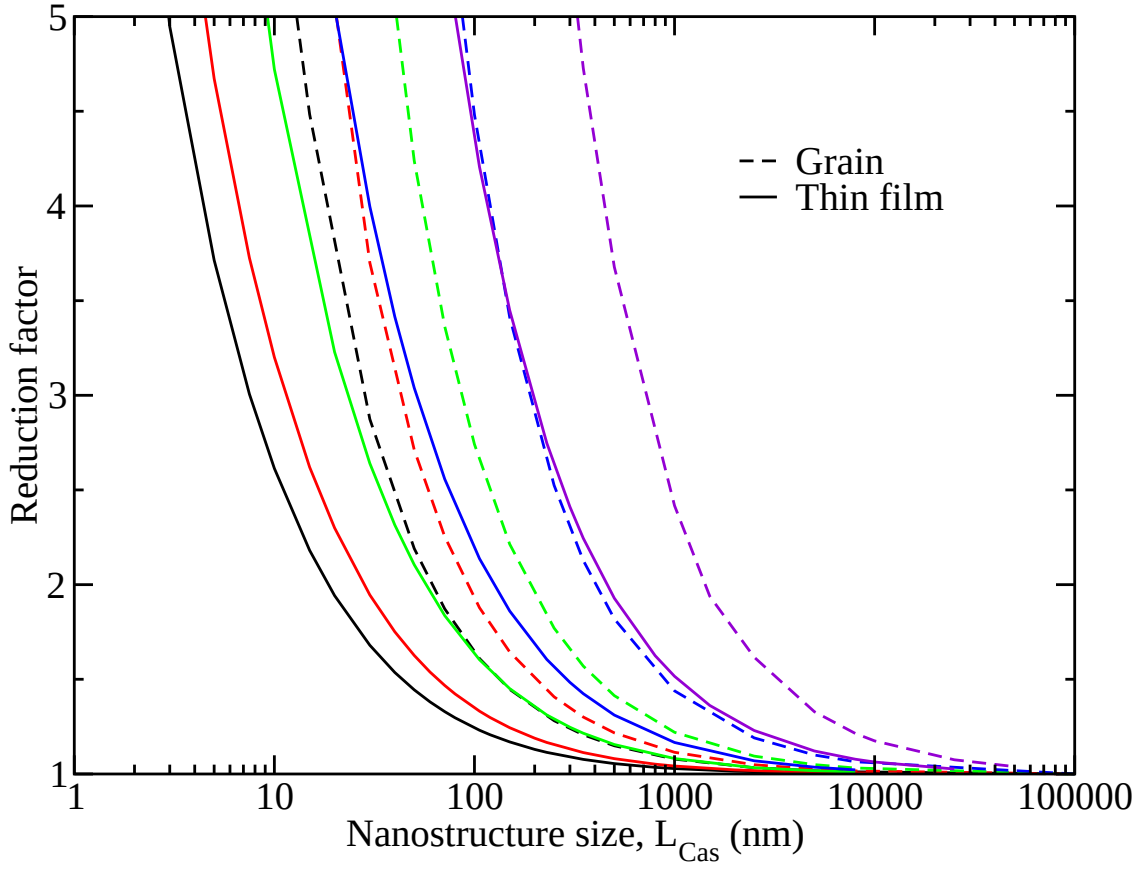

Figure 5.11: Nanostructuring-reduced lattice thermal conductivity (LTC). Abacus of the reduction factor as a function of the nanostructure size and temperature, at 300 K (black), 200 K (red), 100 K (green), 50 K (blue), 20 K (violet). Solid lines: single-crystalline thin-films, LTC along the binary direction; Dashed lines: spherical grain-geometry.

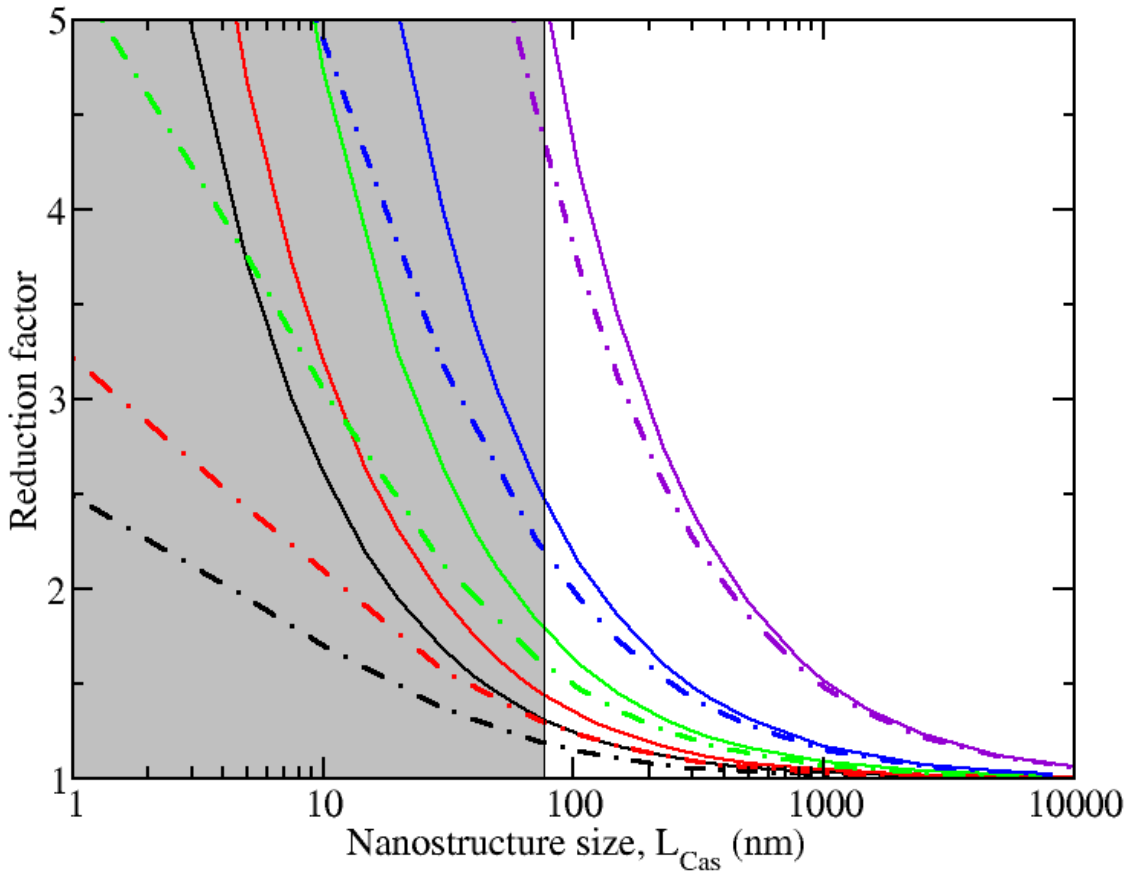

Figure 5.12: Nanostructuring-reduced total thermal conductivity (LTC) for semiconducting (solid curves) and semimetallic (dashed-dotted curves)thin films. The reduction factor as a function of the nanostructure size and temperature, at 300 K (black), 200 K (red), 100 K (green), 50 K (blue), 20 K (violet). The shaded area delimits the 76 nm size, where the contribution from charge carriers vanishes due to the semimetal-to-semiconductor transition in Bi thin films [151].

In Bi thin films with the thicknesses of the several tens of nanometers the semimetal-to-semiconductor transition will occur [159]. The semiconducting region is shaded in Fig. 5.12 by grey color. The best semimetallic Bi thin films fabricated so far had thichness of 76 nm [151]. For this thickness, the reduction factor amounts only to 1.2 at 300 K, 1.3 at 200 K and 1.6 at 100 K. The electrical conductivity σ is higher for the metallic thin films than for the semiconducting ones. However, the drop of the electrical conductivity can be compensated by the increase of the Seebeck coefficient S due to the breaking of the electron-hole symmetry near the Fermi level in semiconducting Bi. Thus, providing a strong thermal conductivity reduction, an experimental and theoretical investigation of the power factor $P_F = S^2\sigma$ in semiconducting single-crystalline thin-films would be of great interest for thermoelectric applications.

5.8 Summary and outlook

In this chapter I have studied by means of *ab initio* DFT calculations the possible routes for the lattice thermal conductivity reduction.

First, I have discussed the practical realization of the acoustic-optical coupling in the ultra-fast pump-probe experiments on photoexcited bismuth. I have shown that this interaction may significantly alter the magnitude of the lattice thermal conductivity causing a strong reduction when the optical branches are softened down towards the acoustic modes. However, the thermoelectric application of this phenomenon is hard to achieve since the excitation by laser has to be constantly maintained.

Then I have turned to the study of nanostructured bismuth. I have explained that the accumulated approach which is often used in the literature to predict the nanostructure size necessary to effectively reduce the lattice thermal conductivity is valid only if the mean-free path distribution in nanostructured bismuth remains the same as in bulk Bi. However, this condition is certainly wrong on the nanoscale. Thus, I have used the Casimir model which allows to accurately take into account the redistribution of the mean free path due to the extrinsic boundary scattering. I have shown that this model allows to study the samples of different geometries such as thin films, nanowires and spherical grains and of both polycrystalline and single crystal nature. I have shown the predictive capability of the method by precisely describing the experiments in the polycrystalline thin films and comparing with the existing thermal conductivity data in nanowires. Finally, I have predicted the effect of size reduction on the lattice thermal conductivity, and I have estimated the effect of size reduction in thin films and semiconducting polycrystalline bismuth providing an abacus for the thermal management and thermoelectric applications as well as for future experiments.

One of the perspectives of this work is to understand the discrepancy between Casimir's model and the experiment in single crystalline nanowires.

Chapter 6

Phonon-phonon interaction in Bi

Introduction.

Phonon-phonon interaction manifests itself in a wealth of temperature-induced physical phenomena like melting or thermal transport, or in the observation of phonon linewidths with spectroscopy techniques like infrared absorption and Raman scattering. As anharmonic coupling limits the mean free paths of heat-carrying phonons, phonon lifetimes are directly related to thermal conductivity of materials, whereas understanding the mechanisms of heat transfer is crucial to design specific materials with new thermal properties [48, 62]. That is the reason why, in the past few years, the mechanisms governing phonon lifetimes have attracted renewed attention, both from the experimental [160, 161, 162, 163, 164, 165, 166] and theoretical point of view [167, 168].

Moreover, recent developments in time-resolved spectroscopy offer the possibility of imaging electronic states after a photo-excitation, with the potential activation of (optical) coherent phonons in the photoexcited excited state [169]. These studies raise the question of the interaction between coherent phonons in the excited states [170], and also the evolution of the phonon-phonon interaction in presence of the free carriers promoted in the conduction band [169].

Bismuth is a material widely studied with femtosecond spectroscopy [170, 171, 172, 134, 173], where optical phonons are of primary interest, with the ultimate aim of exerting an optical control of lattice displacements and manipulating interatomic separations [174]. But acoustic phonons and their anharmonic interaction is also of wide interest, as bismuth, with its low thermal conductivity is a candidate for thermal management and thermoelectric energy conversion. At the same time, the subject of phonon-phonon coupling in bismuth has been little addressed in literature, to the best of my knowledge. It is, however, of great interest, as the identification of the main scattering channels governing the lifetimes could shed light on the above-mentioned phenomena.

The Chapter is organized as follows. In Section 6.1, I will discuss the anharmonic properties of phonon modes in bismuth along some high-symmetry directions in the Brillouin zone. Then, Sections 6.2 and 6.3 are devoted to the detailed analysis of the three-phonon scattering processes contributing to the anharmonicity of acoustic phonons and to the role of acoustic-optical phonon interaction (AOPI). In Section 6.4, I discuss the sound attenu-

ation in bismuth that can be used in future experiments to obtain information about the anharmonicity of acoustic phonons. In Sections 6.5 and 6.6, I turn to the detailed study of the major three-phonon scattering processes contributing to anharmonic broadening of optical phonons as well as the effect of AOPI on it. Finally, in Section 6.7, I will study the anharmonic matrix elements and I will examine the applicability of the long-wave approximation (LWA) which is often used in the literature.

6.1 Anharmonic properties of bismuth.

6.1.1 Introduction.

So far I have been focused on the study of thermal conductivity of bulk bismuth and its nanostructures that is a macroscopic quantity which describes the ability of a material to conduct heat. I have shown that a large portion of heat in bismuth is carried by lattice vibrations, that becomes the sole mechanism for heat transfer at low temperatures. However, phonons do not pass freely from the hot end of sample to the cold one to transmit heat when the temperature gradient is established. On the contrary, on their way phonons undergo many collisions with other phonons and different extrinsic obstacles such as sample boundaries and defects. These collisions limit the propagation of heat, confine phonon lifetimes and mean-free paths, and thus contribute to the thermal resistance in a material. Thus, a direct insight into phonon scattering processes, defining the lattice thermal conductivity on the microscopic level, is extremely important to understand the heat conduction in materials. In this Chapter, I will discuss only three-phonon scattering processes that, as we have already seen in Chapter 4, are sufficient to explain thermal conductivity behavior with respect to experiment.

6.1.2 Anharmonicity.

In Section 1.3.2 we have seen that the anharmonic broadening $\Gamma_{\mathbf{q}j}$ of a particular phonon $|\mathbf{q}, j\rangle$ of wave vector $\mathbf{q}$ and mode index j is inversely proportional to its lifetime $\tau_{\mathbf{q}j}$. It is defined as the total probabilities of phonon-phonon interaction, calculated *via* Fermi's Golden Rule [66]:

$$\tau_{\mathbf{q}j}^{-1} = \frac{\Gamma_{\mathbf{q}j}}{\hbar} = \frac{\pi}{\hbar^2 N_{\mathbf{q}}} \sum_{\mathbf{q}'j',j''} \frac{\left|V^{(3)}(\mathbf{q}j, \mathbf{q}'j', \mathbf{q}''j'')\right|^2}{\omega_{\mathbf{q}j}\omega_{\mathbf{q}'j'}\omega_{\mathbf{q}''j''}} \times$$

$$\times [2(n^0_{\mathbf{q}'j'} - n^0_{\mathbf{q}''j''})\delta(\hbar\omega_{\mathbf{q}j} + \hbar\omega_{\mathbf{q}'j'} - \hbar\omega_{\mathbf{q}''j''}) +$$

$$+ (1 + n^0_{\mathbf{q}'j'} + n^0_{\mathbf{q}''j''})\delta(\hbar\omega_{\mathbf{q}j} - \hbar\omega_{\mathbf{q}'j'} - \hbar\omega_{\mathbf{q}''j''})] \tag{6.1}$$

where $V^{(3)}$ are the matrix elements for three-phonon interaction processes defined in Eq. 1.26. The broadening $\Gamma_{\mathbf{q}j}$ includes all possible scattering processes in which this particular incoming phonon $|\mathbf{q}, j\rangle$ is involved. Specifically, there are coalescence and decay processes that are schematically illustrated in Figs. 1.1 (a) and (b).

In case of coalescence, two incoming phonons, $|\mathbf{q}, j\rangle$ and $|\mathbf{q}', j'\rangle$, interact to create a final $|\mathbf{q}'', j''\rangle$ phonon (Fig. 1.1 a).

$$|\mathbf{q}, j\rangle + |\mathbf{q}', j'\rangle \rightarrow |\mathbf{q}'', j''\rangle \tag{6.2}$$

This process must obey the energy conservation law

$$\hbar\omega_{\mathbf{q}j} + \hbar\omega_{\mathbf{q}'j'} = \hbar\omega_{\mathbf{q}''j''} \tag{6.3}$$

and the momentum conservation rule

$$\mathbf{q} + \mathbf{q}' = \mathbf{q}'' + \mathbf{G} \tag{6.4}$$

These conservation rules are explicitly accounted for in the first Dirac delta function in Eq. 6.1.

The second type of processes is a spontaneous decay of $|\mathbf{q}, j\rangle$ phonon with creation of two outcoming phonons $|\mathbf{q}', j'\rangle$ and $|\mathbf{q}'', j''\rangle$(Fig. 1.1 b).

$$|\mathbf{q}, j\rangle \rightarrow |\mathbf{q}', j'\rangle + |\mathbf{q}'', j''\rangle \tag{6.5}$$

Similarly to coalescence, it obeys the energy conservation rule

$$\hbar\omega_{\mathbf{q}j} = \hbar\omega_{\mathbf{q}'j'} + \hbar\omega_{\mathbf{q}''j''} \tag{6.6}$$

and the momentum conservation rule

$$\mathbf{q} = \mathbf{q}' + \mathbf{q}'' + \mathbf{G} \tag{6.7}$$

These conservation rules are explicitly accounted for in the second Dirac delta function in Eq. 6.1.

Together, the two delta functions in Eq. 6.1 define the joint-density of states (JDOS) describing all allowed scattering processes between three phonons, as it has already been discussed in Section 3.2.3. The anharmonic broadenings depend on temperature through the Bose-Einstein distribution functions, $n^0_{\mathbf{q}'j'}$ and $n^0_{\mathbf{q}''j''}$, that are included as prefactors of delta functions. The three-phonon matrix elements in equation 6.1, in turn, play a role in weighting the various contributions of the allowed phonon-phonon scattering processes in the phonon linewidth.

6.1.3 Anharmonic broadening along high symmetry directions in the Brillouin zone at T = 300 K.

To study anharmonicity in bismuth, I present in Fig. 6.1 the anharmonic broadening $\Gamma_{\mathbf{q}j}$ of an incoming phonon mode $|\mathbf{q}, j\rangle$ at T = 300 K along some high symmetry directions in the Brillouin zone. At ambient temperature all phonon modes are occupied since the maximum phonon frequency ω^{max}_{LO} corresponds to a frequency of about 170 K only[1]. In the top panel of Fig. 6.1, the anharmonic broadening for each of six branches is put on top of phonon dispersion and is increased by 4 times for the illustrative purpose. The

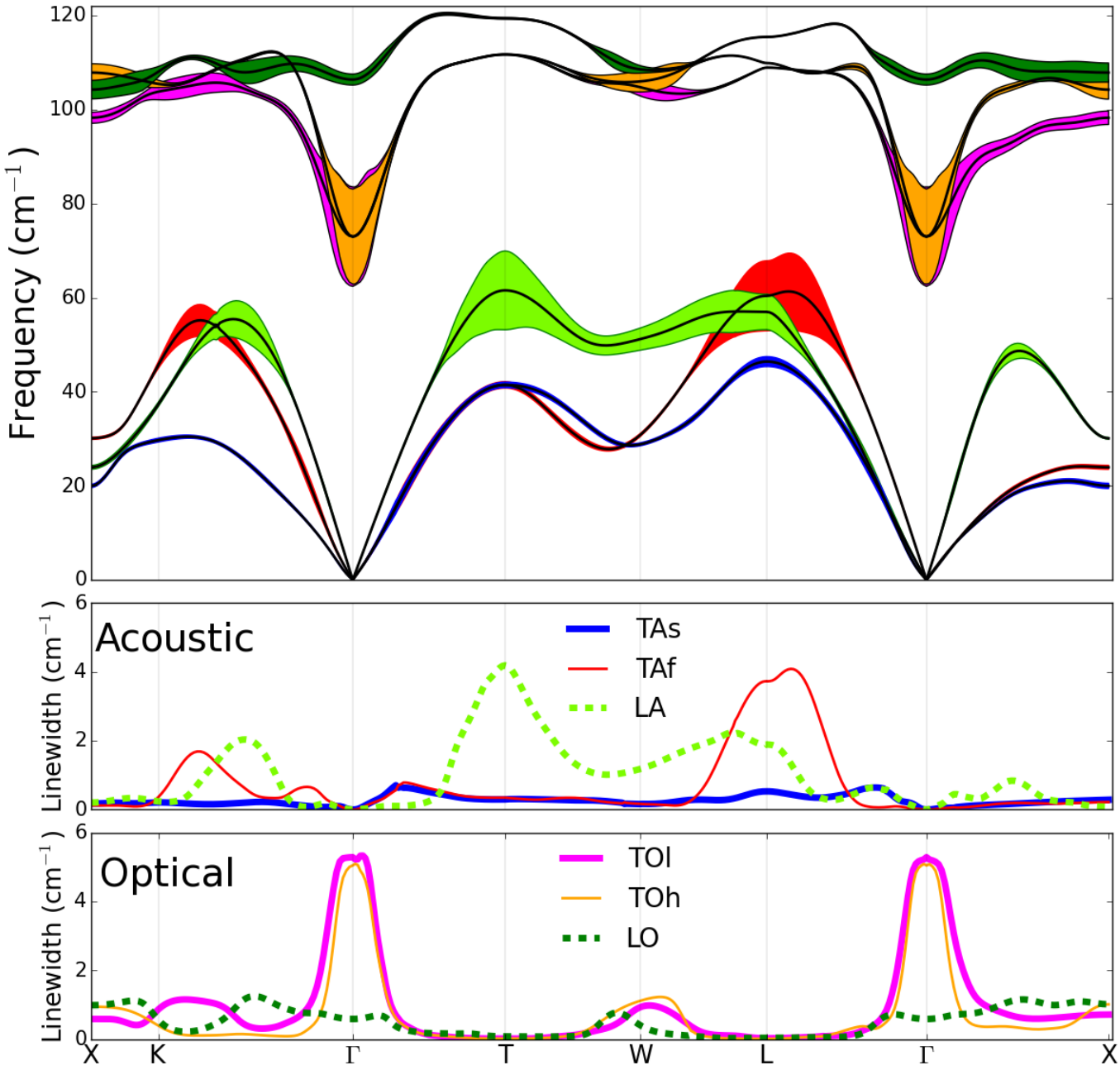

Figure 6.1: Top panel: phonon dispersion of bismuth along some high symmetry directions with anharmonic broadening $\Gamma_{\mathbf{q}j}$ at $T = 300$ K on top of them. Broadening is increased by 4 times for the illustrative purpose. Thick solid blue - **TAs** acoustic branch, thin solid red - **TAf** acoustic branch, thick dashed green - **LA** acoustic branch, thick solid magenta - **TOl** optical branch, thin solid orange - **TOh** optical branch and thick dashed dark green - **LO** optical branch. Middle panel: not scaled anharmonic broadening for acoustic branches only. Bottom panel: not scaled anharmonic broadening for optical branches only. K-Γ is one of the in-plane binary directions and Γ-T is the trigonal direction. **TAs** and **TAf** are defined in Section 3.1.2, as having the smallest (slow) and highest (fast) sound velocities among the transverse acoustic modes. **TOl** and **TOh** are defined as the transverse optical modes having the lowest and highest frequences near Γ.

anharmonic broadenings in real scale are shown on the medium panel for acoustic branches and on the bottom panel for optical phonons.

One can see in Fig. 6.1 that the smallest broadenings $\Gamma_{\mathbf{q}j}$ for acoustic phonons are found near the Brillouin zone center Γ. They result in the longest phonon lifetimes $\tau_{\mathbf{q}j} = \frac{\hbar}{\Gamma_{\mathbf{q}j}}$ and, consequently, the longest mean-free paths $\lambda_{\mathbf{q}j} = |c_{\mathbf{q}j}|\tau_{\mathbf{q}j}$ of phonons in this region. Then, the broadenings grow rapidly with the modulus of the $\mathbf{q}$ vector revealing an active role of acoustic phonons from the zone boundaries in the phonon-phonon interaction in bismuth and, thus, leading to short lifetimes for these phonons. For example, the lifetimes due to phonon-phonon interaction change from about 10 ns to 105 ps for the transverse acoustic (TAs and TAf are degenerated in this direction) modes in the Γ-T direction, and from 25 ns to 8 ps for the longitudinal acoustic (LA) mode in the same direction. The highest branches (LA phonons in the Γ - K, Γ - T and Γ - X directions and TAf phonons in the Γ - L direction) have the smallest broadening among all of the acoustic branches near the zone center, and, on the contrary, the maximum one near the zone boundaries. The values of phonon lifetimes of acoustic phonons at some high-symmetry points of the Brillouin zone are summarized in the top part of Table 6.1. The shortest lifetimes are determined to be $\tau = 8.0$ ps at T point (LA branch), $\tau = 9.0$ ps at L point (TAf mode), $\tau = 17.7$ ps at L point (LA mode) and $\tau = 28.3$ ps at W point (LA branch). At other high-symmetry points considered in this work the lifetimes are found to be of the order of a few hundreds of ps (see Table 6.1).

In the bottom panel of Fig. 6.1, I show the anharmonic broadening of optical phonon modes. In bismuth there are two transverse modes and I denote TOl and TOh as lower and higher transverse optical mode near the Brillouin zone center. As one can see, the transverse optical phonons have the largest broadening in the vicinity of the Brillouin zone center, reaching the value of 5.15 cm^{-1} at Γ. It is explained by the fact that these phonons have the lowest energies among all optical phonons that facilitates their interaction with acoustic modes. In Chapter 5 we have also seen that the acoustic-optical phonon interaction (AOPI) can be even strengthened in photoexcited bismuth, because the optical branches are softened in the excited state, while the acoustic branches remain the same as in non-excited bismuth. The obtained phonon lifetime of the TO phonon at Γ is $\tau = 6.5$ ps (table 6.1) is in excellent agreement with the value found in Raman experiments $\tau = 6.4$ ps [176] and $\tau = 6.2$ ps [175][2]. This fact demonstrates the dominant role of phonon-phonon interaction for TO phonons at Γ. Contrastingly, the LO phonon lifetime is much longer, $\tau = 57.9$ ps, than the experimental values $\tau = 10.1$ ps [176] and $\tau = 6.3$ ps [175]. This fact shows a dominant role of electron-phonon scattering governing the lifetime of LO phonon that is not included in my calculation. The values of phonon lifetimes of optical phonons at some high-symmetry points of the Brillouin zone are summarized in the bottom part of Table 6.1.

[1]Not all the Brillouin zone is studied. The maximum frequency ω_{LO}^{max} is determined only for the directions displayed in Fig. 6.1.

[2]In Raman experiments of Refs. [175, 176] the anharmonic broadening has been measured. The obtained values are $\Gamma_{TO} = 5.2$ cm^{-1} and $\Gamma_{LO} = 3.3$ cm^{-1} in Ref. [176] and $\Gamma_{TO} = 5.4$ cm^{-1} and $\Gamma_{LO} = 5.3$ cm^{-1} in Ref. [175]. In the current section I recalculated the phonon lifetimes from the given values of broadening Γ.

Acoustic branches

	X	K	Γ	T	W	L
TAs	188.5	161.2	-	105.1	200.9	63.1
TAf	163.9	140.7	-	105.1	209.4	9.0
LA	279.8	91.8	-	8.0	28.3	17.7

Optical branches

	X	K	Γ	T	W	L
TOl	56.9	38.5	6.5	1962.1	35.9	1283.4
			6.2 [175]			
			6.4 [176]			
TOh	33.8	85.6	6.5	1962.1	30.0	2674.9
			6.2 [175]			
			6.4 [176]			
LO	35.4	59.8	57.9	417.5	83.0	872.5
			6.3 [175]			
			10.1 [176]			

Table 6.1: Phonon-phonon interaction: relaxation times (ps) at high symmetry points in the Brillouin zone. The lifetimes obtained from the anharmonic broadening for optical phonons at Γ measured in Raman experiments in Bi [175, 176] are also given. See caption of Fig. 6.1 for the definition of TAs, TAf, TOl and TOh.

6.2 The main scattering channels for acoustic phonons.

The intrinsic anharmonic broadening Γ_ν of the heat-carrying phonon mode $|\nu\rangle = |\mathbf{q}, j\rangle$ gathers all possible scattering processes between this particular incoming phonon $|\nu\rangle$ and all other phonons existing in the material. The intensity of scattering determines the thermal resistance, limiting the heat conduction. However, not all of the phonon-phonon scattering processes contribute equally to anharmonicity. Thus, it is important to investigate the major three-phonon scattering processes determining the thermal resistance at the microscopic level.

In this section, I will discuss the role of coalescence and decay processes for incoming acoustic phonons with wavevectors $\mathbf{q}$ in two principle directions: K-Γ (along the binary axis) and Γ-T (along the trigonal axis) at ambient temperature when all phonon states are occupied. In Fig. 6.2 I show the anharmonic broadenings of TAs (bottom panel, thick blue line), TAf (middle panel, thick red line) and LA (top panel, thick green line) phonons that are the same as the ones discussed earlier in Fig. 6.1 in section 6.1.3, and the contributions of some particular anharmonic processes (thin lines).

As one can see in the top panel of Fig. 6.2, the initial LA phonons near the zone boundary, where the broadening is maximal, predominantly decay into TA phonons (thin violet lines). These processes are known as Simons processes [177]. This is in agreement with a theoretical analysis of $Bi_{1-x}Sb_x$ alloys [81] where Simons processes were found to be predominant at all Sb concentrations x. In addition, another important scattering process for LA phonons is their coalescence with LA phonon (from some point in the Brillouin zone[3]) to form an outcoming TO phonon (black thin line). The latter process contributes to anharmonicity mainly in the regions where the LA branch has the highest frequencies among all acoustic phonons.

Near the zone center I find that LA phonons interact particularly with TA modes to form another LA phonon of higher energy (thin orange dashed-dotted line in top panel of Fig. 6.2). This is in contrast to other materials like Si [65], GaAs [65] or TeO_2 [178, 179] where Herring's processes LA + TAs → TAf play a crucial role in the phonon-phonon interaction. However, the original Herring analysis was limited to cubic anharmonicity and low temperatures [180]. Moreover, generally the Herring processes are important only very close to Γ point where the phonon phase space is small [65]. But, as we have already seen in Chapter 3, despite the fact that the phonons near Γ point has a small scattering rate and long relaxation times, they contribute negligibly to the lattice thermal conductivity because of the low density of states in this region (see Section 3.4). Thus they are not important for thermal transport in Bi.

The major processes for TAf phonons are shown on the middle panel of Fig. 6.2. As one can see, in the K-Γ direction the main scattering channels are similar in magnitude to the ones of LA phonons but not at the same $\mathbf{q}$ points. It is expected since LA and TAf branches are very close to each other in this direction (see Fig. 6.1.3). In the Γ-T direction, TAs and TAf transverse modes are degenerate. The TAs phonons have

[3]The analysis is done for the second phonon $\nu' = \{\mathbf{q}', j'\}$ in equation 6.1 defined on a uniform grid in the Brillouin zone. I did not analyze the location in the Brillouin zone of each phonon ν' in the coalescence process.

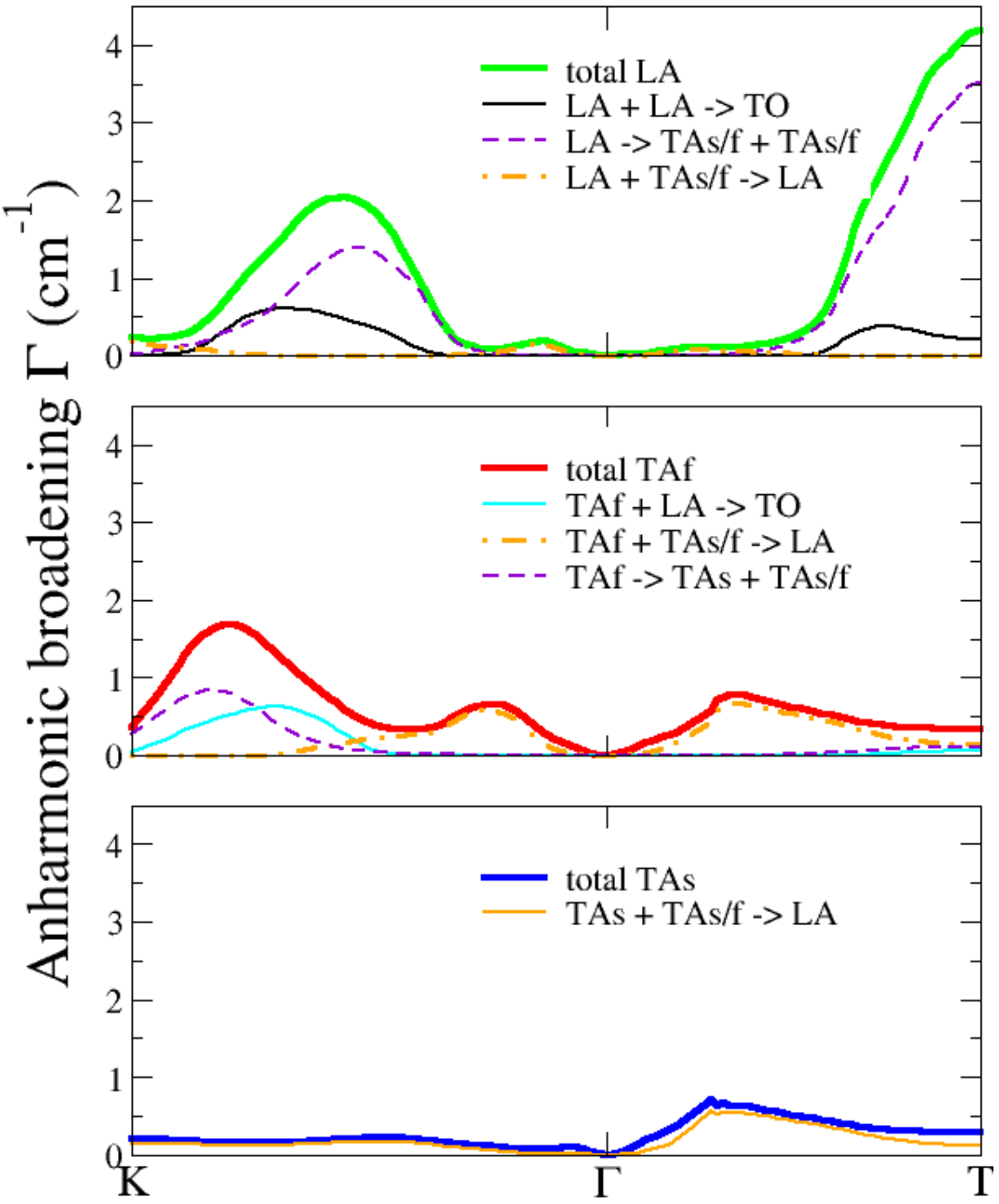

Figure 6.2: The total anharmonic broadening (thick solid lines) and its major contributions due to various coalescence and decay channels for TAs (bottom panel), TAf (middle panel) and LA (top panel) branches of the incoming phonons along the K-Γ (in-plane binary) and Γ-T (out-of-plane trigonal) directions. The particular coalescence and decay processes are marked by thin (solid, dashed and dashed-dotted) color lines as indicated in the legends.

the lowest energy among all phonon branches in bismuth and thus coalescence processes contribute to anharmonic broadening much more than decay processes. Indeed, one can see in the bottom panel of Fig. 6.2 that the dominant scattering process for them is the coalescence with another TAs or TAf mode, resulting in the creation of LA phonons of higher energy.

6.3 Role of acoustic-optical interaction in the anharmonic broadening of acoustic phonons.

In Chapter 3, I have shown that an accurate description of frequencies of TO phonons near Γ point with respect to experiment considerably affects the JDOS of acoustic phonons providing a realistic acoustic-optical phonon interaction (AOPI) and resulting in the values of the lattice thermal conductivity close to the experimental ones. In this section I will show how the AOPI changes the anharmonic broadening of acoustic phonons.

In Fig. 6.3 I show the anharmonic broadening of LA (top panel), TAf (middle panel) and TAs (bottom panel) phonon modes with the realistic AOPI (solid lines) and the *ab initio* AOPI (dashed lines), which is enhanced with respect to the realistic one. For the lowest TAs branch with realistic AOPI, the maximum of the anharmonic broadening is found between Γ and T points, and is equal to 0.7 cm^{-1}. It mainly results from the interaction between the acoustic phonons: TAs + TAf → LA coalescence process. When the optical branches lie lower, like in my *ab initio* calculations and in photoexcited bismuth, the highest broadening is found to be 0.95 cm^{-1} at T point and 1.38 cm^{-1} at L point instead of 0.28 cm^{-1} and 0.51 cm^{-1} respectively when the realistic AOPI is accounted for. At these points TAs phonons have the highest energies in the Brillouin zone, which facilitates their interaction with the softened optical modes.

The *ab initio* description of the two other acoustic phonon branches, TAf and LA, has the same tendency to enlarge the anharmonic broadening in the regions of the Brillouin zone where the branches have the highest energies. For example, a broadband structure in the anharmonic broadening of TAf phonons is enlarged in the X-K-Γ directions with the increase of the maximum peak from 1.7 cm^{-1} to 2.2 cm^{-1}. The broadening of LA phonons is increased from 2.0 cm^{-1} to 2.5 cm^{-1} for the maximum in X-K-Γ directions, from 2.2 cm^{-1} to 2.8 cm^{-1} for the maximum in W-L-Γ directions, and from 0.8 cm^{-1} to 1.2 cm^{-1} for the maximum in the Γ-X direction .

Thus the linewidths of acoustic phonons turn out to be heavily dependent, both in their magnitude and in their **q**-dependence, on an accurate description of the lower TO phonon branch which provides a realistic interaction between acoustic and optical phonons.

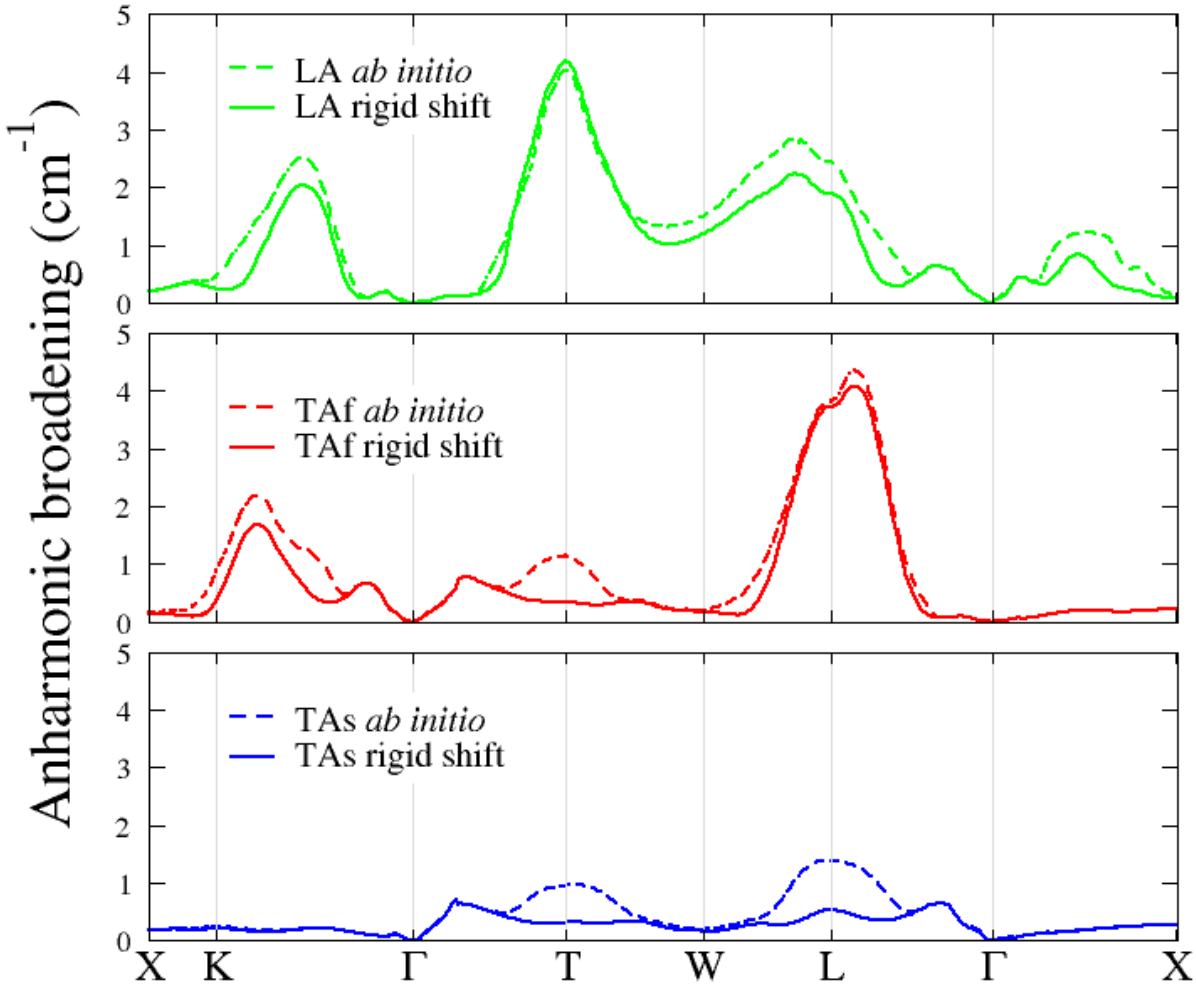

Figure 6.3: Effect of AOPI on the anharmonic broadening of acoustic phonons. Solid lines: with optical phonon branches as shifted in this work. Dashed lines: with the *ab initio* phonon dispersion. Top, center and bottom panel are respectively for longitudinal (LA), second-transverse (TAf) and first-transverse phonons (TAs). K-Γ is one of the in-plane binary directions and Γ-T is the trigonal direction.

6.4 Sound attenuation.

6.4.1 Introduction.

In principle, anharmonic properties of materials can also be studied in picosecond ultrasonic experiments [165, 181]. In these experiments, a laser generates high-frequency light pulses that are then absorbed by a transducer, causing a local stress inside of it. The relaxation of this stress launches strain pulses in the form of an acoustic signal with energy in the THz range. This acoustic signal propagates further in the investigated bulk structure that is put on top of the transducer. By measuring the attenuation of the propagating sound wave, one can get access to information about, for instance, lifetimes of individual phonons experimentally.

The attenuation of sound waves, studied in this Section, should not be confused with second sound, discussed in Sections 1.1.3 and 2.4.7. The former is a mechanical wave describing fluctuations in the density of media while the latter is a temperature wave describing fluctuations in the density of thermal excitations *i.e.* phonons.

The attenuation $\alpha_{\mathbf{q}j}$ of a phonon mode $|\mathbf{q}, j\rangle$ is defined as

$$\alpha_{\mathbf{q}j} = \frac{\Gamma_{\mathbf{q}j}}{2v_{0j}\hbar} \tag{6.8}$$

where v_{0j} is the sound velocity in the propagation direction and $\Gamma_{\mathbf{q}j}$ is the anharmonic broadening due to the scattering of the generated phonon carrying the sound with other phonons from the heat reservoir. However, experimentally it is not easy to transduce the light pulse into an acoustic pulse of well defined energy. Due to the experimental difficulty, most of the studies have been performed in relatively simple bulk structures such as Si, Al or GaAs where the superlattices of Si/Ge, Al/Ag and GaAs/AlAs respectively were used as transducers. However, no attempts to measure the attenuation in such a complex material as bismuth have ever been done and, thus, my *ab initio* calculations provide the data for the future experiments in Bi.

Furthermore, I will study the sound attenuation $\alpha_{\mathbf{q}j}$ of bismuth as a function of its frequency $\omega_{\mathbf{q}j}$. As one can see from eq. 6.8, the sound attenuation depends on frequency only through the anharmonic broadening $\Gamma_{\mathbf{q}j}$, while the sound velocities v_{0j} in the propagation direction remain constant. For the latter, I will use the values obtained from the second-order elastic constants that have already been discussed in Section 3.1.2 in Chapter 3 and that are summarized in Table 3.2.

Furthermore, I will restrict my study to the region $\omega < 40$ cm^{-1}, where the acoustic phonon branches are linear and there is a one-to-one correspondence between the phonon wavevector $\mathbf{q}$ and its energy $\hbar\omega_{\mathbf{q}j}$[4]. The exception is TAs mode in the Γ-K direction where the behavior remains linear for $\omega < 25$ cm^{-1} which defines the restriction range of my study.

[4]In the experiment the energy is fixed and we look at phonon propagation at this fixed energy E_{fix} where there is one solution to $E_{fix} = \hbar\omega_{ph}$. To this end I restrict the frequency range near Γ as, for instance, in the X-K-Γ directions, the equation $E_{fix} = \hbar\omega_{ph}$ has at least two solutions.

6.4.2 Sound attenuation in the trigonal direction.

First, I study the sound attenuation $\alpha_{\mathbf{q}j}$ at T = 300 K in the Γ-T direction in the Brillouin zone, which corresponds to the sound propagation in the trigonal direction.

The two (degenerate) transverse acoustic modes (**TA**) are shown in the top panel of Fig. 6.4. As one can see, the attenuation grows linearly at small frequencies and reaches the maximum value of $\alpha = 12$ μm^{-1} at $\omega \approx 18$ cm^{-1}. Further increase of the frequency ω leads to a linear decrease of the attenuation. This behavior essentially arises from the contribution to the anharmonic broadening due to the coalescence process **TA** + TAf → LA.

Contrastingly, the attenuation of the longitudinal acoustic mode (**LA**), that is shown in the bottom panel of Fig. 6.4, grows as ω^2 up to $\omega = 18$ cm^{-1}. Then, it remains constant, forming a plateau in the region 18 cm^{-1} $< \omega <$ 25 cm^{-1}. At higher frequencies, the sound attenuation continues to grow approximately as $\omega^{5/2}$.

The plateau-like behavior of the attenuation of the LA phonon mode has also been found in GaAs and Si [65]. In these materials it has been associated with the dominant role of the Herring processes LA + TAs → TAf. However, in the case of Bi, the Herring processes are important only in a region of frequencies that is much lower than the plateau region. In contrast, the plateau is formed mainly by two competing scattering processes: **LA** + TAs → LA and **LA** + TAf → LA. The plateau disappears when the decay processes **LA** → TAs + TAs and **LA** → TAs + TAf become dominant, resulting in the increase of $\Gamma_{\mathbf{q}j}$ and, thus, of $\alpha_{\mathbf{q}j}$.

The sound attenuation of the LA mode is much lower than the one of TA modes. It is expected, since the longitudinal phonons always have higher sound velocities than the transverse modes. Moreover, as we have seen in section 6.1.3, the anharmonic broadening of LA phonon close to the BZ center in the Γ-T direction has the smallest value.

6.4.3 Sound attenuation in the binary direction.

Then, I study the attenuation at T = 300 K in the Γ-K direction in the Brillouin zone, which corresponds to the sound wave propagation in the binary direction.

The two (non-degenerate) transverse acoustic modes (TAs and TAf) are shown in the top panel of Fig. 6.5. The slowest transverse mode, **TAs**, first, grows as ω^2 in the small region close to the zone center. Many coalescence processes such as **TAs** + TAs/TAf → TAf/LA contribute to the anharmonic broadening in this region. Then, it varies slowly with frequency at $\omega > 3$ cm^{-1} between 2 μm^{-1} and 4 μm^{-1} reaching the maximum at $\omega = 23$ cm^{-1}. This slow variation is mainly defined by the coalescence process **TAs** + TAs/TAf → LA. The fastest transverse mode, **TAf**, in turn, grows monotonously approximately as ω^2 and then start to slowly decay at $\omega < 23$ cm^{-1}. This behavior is governed by the the coalescence processes **TAf** + TAs/TAf → LA.

The sound attenuation of the longitudinal acoustic mode (**LA**) in the Γ-K direction is shown in the bottom panel of Fig. 6.5. Similar to the Γ-T direction, it grows as ω^2 up to $\omega = 19$ cm^{-1}. However, then, no plateau region is observed in this direction. Contrastingly, the attenuation α decreasing monotonously in the region 19 cm^{-1} $< \omega <$ 32 cm^{-1} and, then, increases rapidly again at $\omega > 32$ cm^{-1}. The absence of plateau is

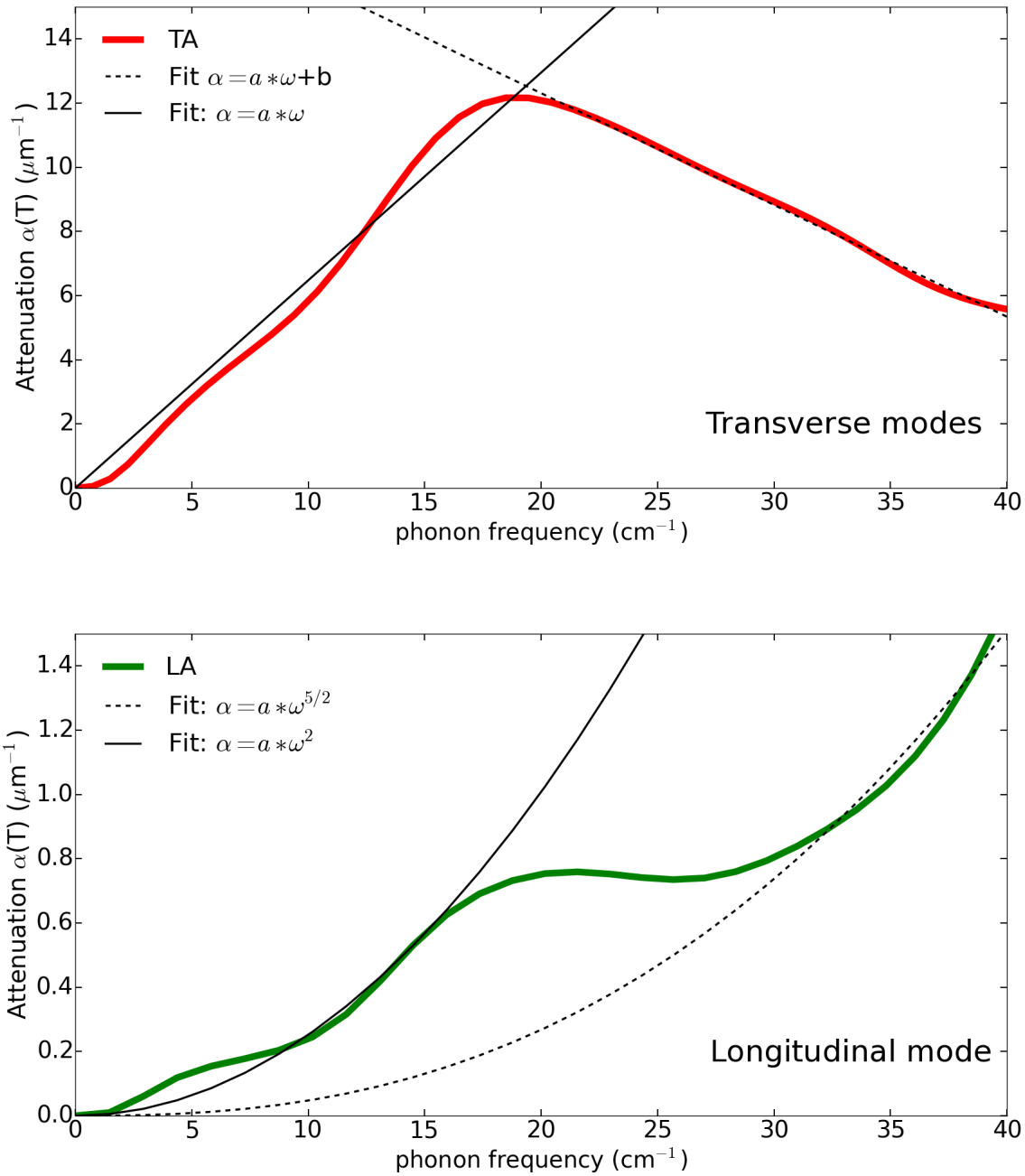

Figure 6.4: The sound attenuation in bismuth in Γ-T direction in the Brillouin zone (trigonal direction) for TA (degenerate) modes (top panel, red thick curve) and LA mode (bottom panel, green thick curve). The fitting curves are also shown on top of the attenuation (black thin solid and dashed curves). The fitting curves are $\alpha = 0.648 \cdot \omega$ and $\alpha = 19.27 - 0.348 \cdot \omega$ for the TA modes and $\alpha = 2.52 \cdot 10^{-3}\omega^2$ and $\alpha = 1.49 \cdot 10^{-3}\omega^{5/2}$ for the LA phonon.

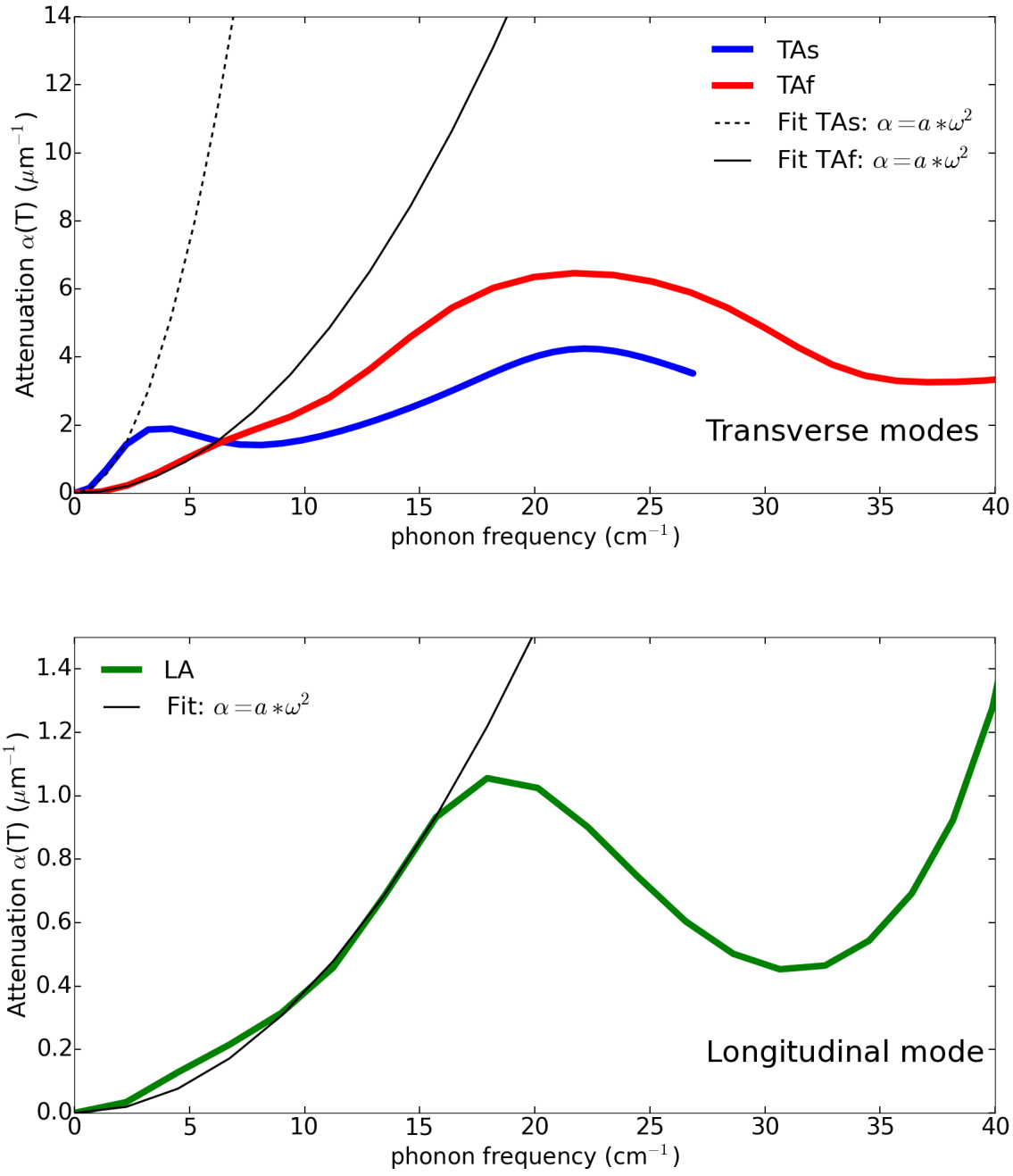

Figure 6.5: The sound attenuation in bismuth in the Γ-K direction in the Brillouin zone (binary direction) for TAs and TAf modes (top panel, red and blue thick curves) and LA mode (bottom panel, green thick curve). The fitting curves are also shown on top of the attenuation (black thin solid and dashed curves). TAs mode on the top panel is shown up to energy $\omega < 25$ cm^{-1} where it has a linear behavior and a one-to-one correspondence with wavevector $\mathbf{q}$. The fitting curves are $\alpha = 0.293 \cdot \omega^2$ for the TAs mode, $\alpha = 3.9 \cdot 10^{-2} \omega^2$ for the TAf mode and $\alpha = 3.8 \cdot 10^{-3} \omega^2$ for the LA mode.

explained by the fact that the dominant contributions to anharmonic broadening from **LA** + TAs → LA and **LA** + TAf → LA processes are more localized in the Γ-K direction than in the Γ-T direction, resulting in a sharp peak but not in the plateau behavior of attenuation.

6.4.4 Conclusion.

In this Section I have analyzed the attenuation of sound waves as a function of its energy in the binary and trigonal directions in bismuth. I have also studied the major phonon-phonon scattering processes determining the attenuation. The predicted values of sound attenuation can be used in future experiments.

6.5 Role of different scattering channels for optical phonons.

So far I have primarily discussed the anharmonic properties of acoustic phonons. These phonons are particularly important for thermal transport since they carry most of the heat in bismuth. However, the relative role of optical phonons in nanostructures is increased since the longest mean free paths of acoustical phonons are severely limited. Moreover, optical phonons are of utmost interest in femtosecond spectroscopy experiment with the aim of optical control of lattice displacements and manipulating interatomic separations [174]. Thus, the understanding of the basic scattering mechanisms determining the anharmonicity of optical phonons become important.

In this section, I will discuss the role of various scattering channels for incoming optical phonons with wavevectors **q** in two principle directions: K-Γ (along the binary axis) and Γ-T (along the trigonal axis) at ambient temperature. In Fig. 6.6, I show the anharmonic broadenings of TOl (bottom panel, thick magenta line), TOh (middle panel, thick orange line) and LO (top panel, thick dark green line) phonons that are the same as the ones discussed earlier in Fig. 6.1 in section 6.1.3 and the contributions of some particular processes anharmonic (thin solid and dashed lines).

The LO phonons have the highest energies among all phonon branches in bismuth. Thus, one can expect to have more decay than coalescence processes. Indeed, the main contribution to anharmonic broadening of LO phonons (top panel of Fig. 6.6) is due to its decay into two acoustic phonons, namely, LO → TAf + LA and LO → LA + LA processes (thin solid cyan line). Moreover, near the T point, LO phonons decay into one high energy TO phonon and one low energy TAs phonon (thin dashed red line).

The major scattering channels of TOl and TOh incoming phonon modes are shown on the middle and in the bottom panels of Fig. 6.6 respectively. As it has already been mentioned in section 6.1, the total anharmonic broadening of TO phonons in the vicinity of the Brillouin zone center is much larger than in the rest of the Brillouin zone. This large broadening results from the low energies of these phonons, comparing with other optical phonons, that facilitates their interaction with the acoustic phonons. The basic scattering channels are found to be the decay into acoustic LA and TA branches (thin

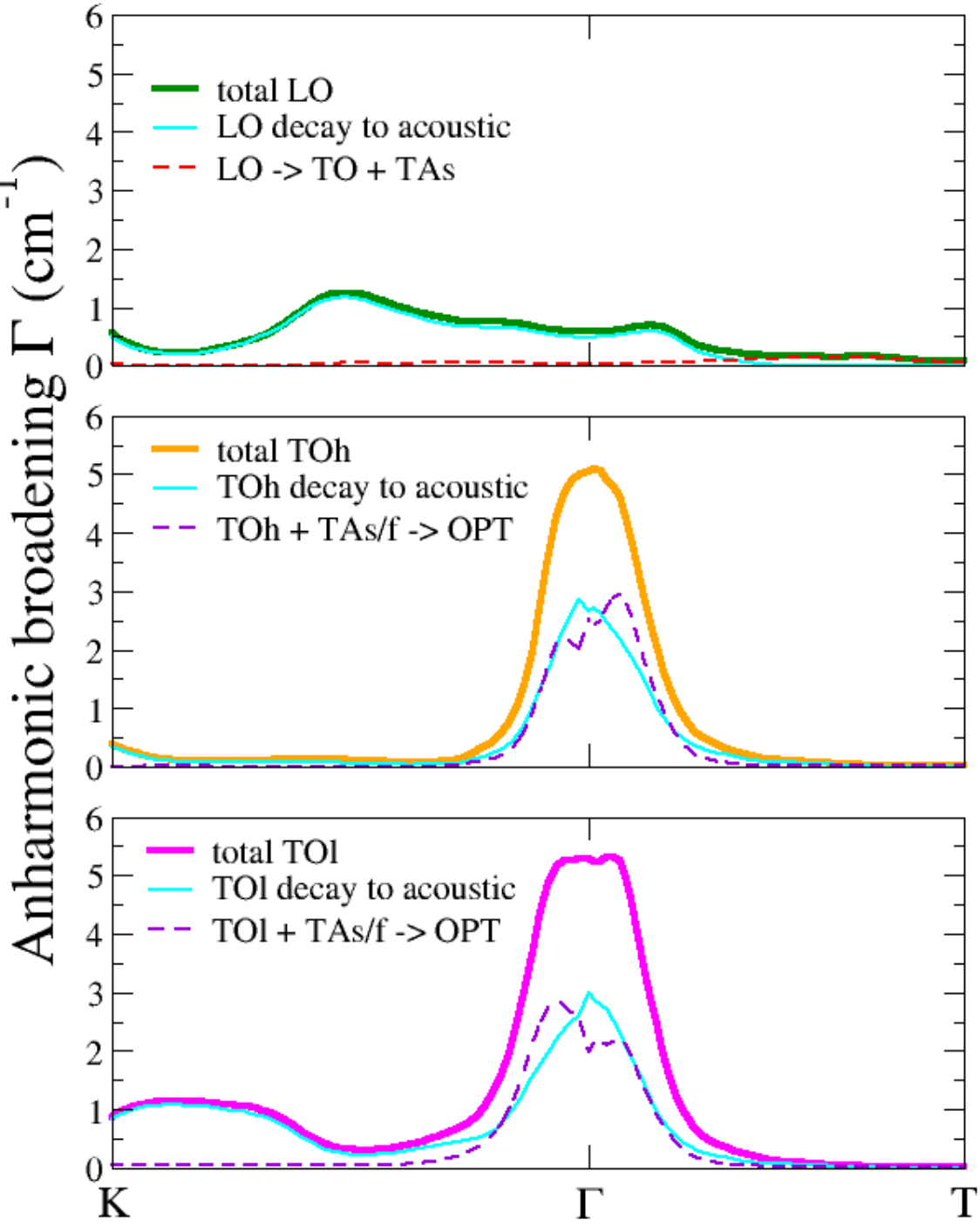

Figure 6.6: The total anharmonic broadening (thick solid lines) and its major contributions due to various scattering channels for TOl (bottom panel), TOh (middle panel) and LO (top panel) branches of the incoming phonons along the K-Γ (in-plane binary) and Γ-T (out-of-plane trigonal) directions. The particular coalescence and decay processes are marked by thin (solid and dashed) color lines as indicated in the legends.

solid cyan lines) and coalescence with TAs or TAf phonon to create an optical phonon of higher energy (thin dashed violet lines).

6.6 Role of acoustic-optical interaction in the anharmonic broadening of optical phonons.

In this section, I discuss the effect of AOPI in the anharmonic broadening of optical phonons in bismuth. In Fig. 6.7, I show the anharmonic broadenings of TOl (bottom panel), TOh (middle panel) and LO (top panel) phonon modes with the realistic AOPI (solid lines) and the *ab initio* AOPI (dashed lines), which is enhanced with respect to the realistic one. One can see that the enhancement of AOPI first of all has a striking effect on anharmonic broadening of TO phonons in the vicinity of Γ point, which is increased from 5.15 cm^{-1} to 12.6 cm^{-1} at Γ point. This effect results from the fact that the low position of optical branches in the *ab initio* facilitates their decay into two acoustic phonons. The optical phonons with the lowest energies are the TO phonons. Thus, these phonons interact with acoustic phonons more intensively than other optical phonons. The LO phonons have a small broadening everywhere in the Brillouin zone. The enhanced AOPI results in a relatively broad band with a maximum of 1.9 cm^{-1} in the T-W direction and in a peak with maximum 1.7 cm^{-1} in the Γ-T direction.

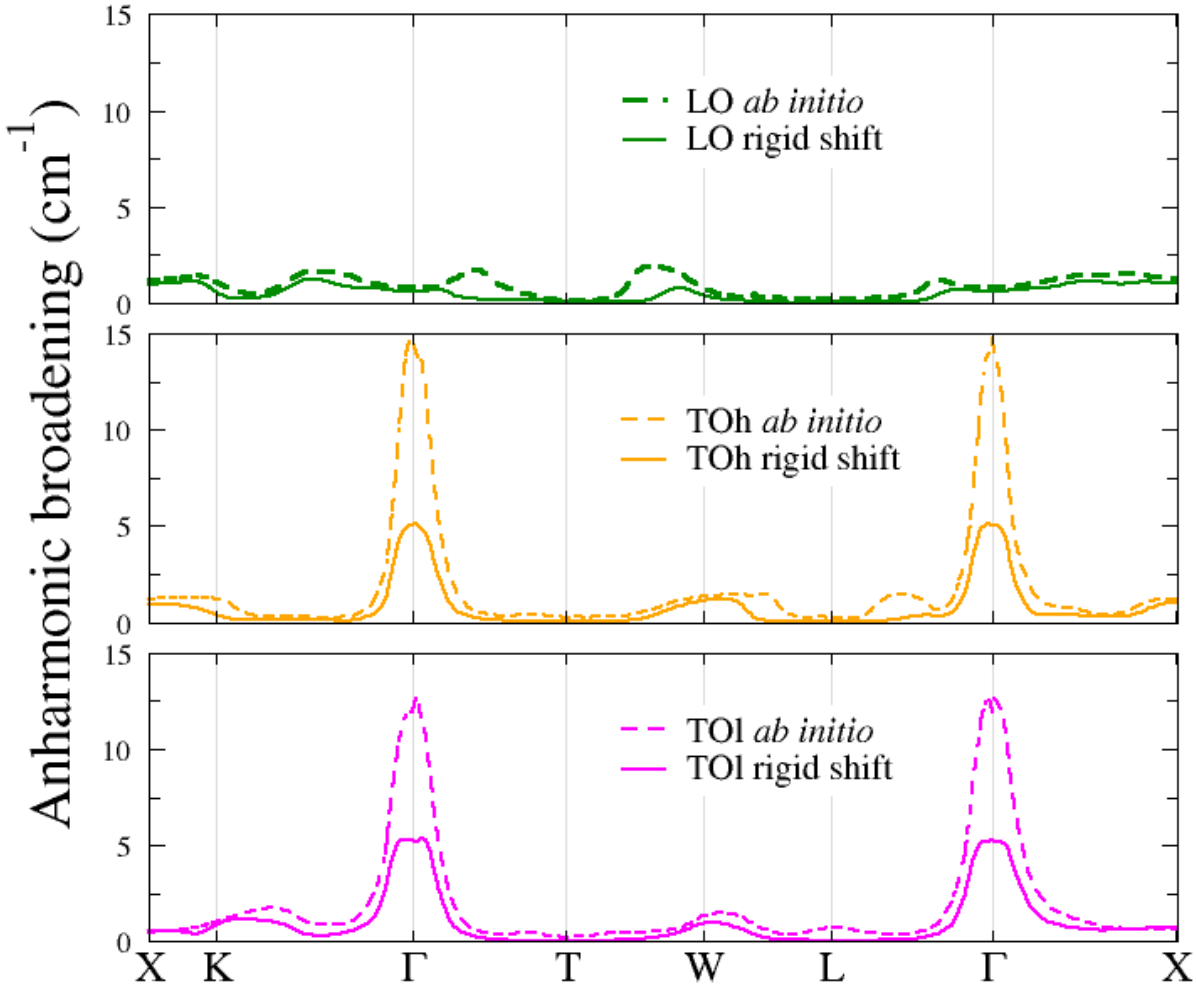

Figure 6.7: Effect of AOPI on the anharmonic broadening of optical phonons. Solid lines: with optical phonon branches as shifted in this work. Dashed lines: with the *ab initio* phonon dispersion. Top, center and bottom panel are respectively for longitudinal (LO), second-transverse (TOh) and first-transverse phonons (TOl).

6.7 Phonon-phonon matrix elements: the validity of the LWA approximation

So far in this chapter I have focused my attention on the study of the anharmonic broadening $\Gamma_{\mathbf{q},j}$ and of the quantities which can be directly derived from it, such as the phonon lifetimes $\tau_{\mathbf{q},j}$ (Sections 6.2 and 6.5) and the sound attenuation $\alpha_{\mathbf{q},j}$ (Section 6.4). The anharmonic broadening, defined in Eq. 6.1, is determined by two major components. The first component, the joint density of states (JDOS) of Eq. 3.2, accounts for the phonon-phonon interaction processes which are allowed by the energy and momentum conservation rules. The JDOS is fully determined by the harmonic properties of crystals *i.e.* one needs to know only phonon frequencies $\omega_{\mathbf{q},j}$ and phonon wave vectors $\mathbf{q}$. In Section 3.2.3, we have seen that the softening of the transverse optical phonon modes at the Γ point leads to the considerable enhancement of the acoustic-optical phonon interaction *via* the JDOS.

The second component is the matrix element(s) of the transition rates in Eqs. 1.24 and 1.24, and more specifically the coefficients $\left|V^{(3)}(\mathbf{q}j,\mathbf{q}'j',\mathbf{q}''j'')\right|$. Their calculation is not an easy task and requires the advance computational method explained in Section 1.5. In this work, I have used a new recently implemented method based on "2n+1" theorem and on *ab initio* calculations to obtain the anharmonic matrix coefficients [6].

To analyze the anharmonic coefficients in Bi, I first define an average squared coefficient as

$$\langle|V^{(3)}|^2\rangle(\mathbf{q}j) = \frac{\pi}{\hbar^2 N_{\mathbf{q}}} \sum_{\mathbf{q}'j',j''} \left|V^{(3)}(\mathbf{q}j,\mathbf{q}'j',\mathbf{q}''j'')\right|^2 \tag{6.9}$$

It depends only on the wave vector $\mathbf{q}$ of the incoming phonon and of its branch index j which includes the acoustic phonon modes j=1,3 and the optical phonon modes j=4,6. This definition is similar to the one of the anharmonic broadening in Eq. 6.1, but without the part containing phonon frequencies (*i.e.* the JDOS and the normalization factor $\frac{1}{\omega_{\mathbf{q}j}\omega_{\mathbf{q}'j'}\omega_{\mathbf{q}''j''}}$).

I calculate the average squared coefficients $\langle|V^{(3)}|^2\rangle(\mathbf{q}j)$ on the uniform grid of $\mathbf{q}$ vectors and I plot the obtained coefficients as a function of the modulus $|\mathbf{q}|$ for each of the acoustic (Fig. 6.8) and optical (Fig. 6.9) branches. Since there are many points $\mathbf{q_i}$ which have the same modulus of wave vector $|\mathbf{q}|$, I also define a mean value as

$$\overline{\langle|V^{(3)}|^2\rangle}(|\mathbf{q}|,j) = \frac{\int_{BZ}\langle|V^{(3)}|^2\rangle(\mathbf{q_i},j)\delta(|\mathbf{q}|-|\mathbf{q_i}|)d|\mathbf{q_i}|}{\int_{BZ}\delta(|\mathbf{q}|-|\mathbf{q_i}|)d|\mathbf{q_i}} \tag{6.10}$$

where the denominator is the density of $\mathbf{q}$-states ($\mathbf{q}$-DOS) discussed in Section 3.4.1. The mean values $\overline{\langle|V^{(3)}|^2\rangle}(|\mathbf{q}|,j)$ are also indicated in Figs. 6.8 and 6.9 by thick cyan solid lines.

As we can see in Fig. 6.8, near the zone center the average coefficients $\langle|V^{(3)}|^2\rangle(\mathbf{q},j)$ of the acoustic phonon modes grow with the increase of the modulus $|\mathbf{q}|$ of the incoming vector. I have fit these coefficients with the quadratic law in the region $|\mathbf{q}| < 0.4$ and obtained an excellent agreement with the mean value $\overline{\langle|V^{(3)}|^2\rangle}$. Such a quadratic dependance on $|\mathbf{q}|$ has been expected from the long-wave approximation (LWA) and, thus, this approximation is validated for the acoustic phonons having small $|\mathbf{q}|$. However, when

$|\mathbf{q}|$ grows further, the values of the average coefficients become scattered while the mean values are essentially constant. The highest value of the average coefficient are found for the highest TAf and LA modes near the zone boundaries.

The average coefficients for optical phonons are shown in Fig. 6.9. One can see, that $\langle|V^{(3)}|^2\rangle(\mathbf{q}, j)$ are more than two orders of magnitude higher for the optical branches than for the acoustic ones. First, the mean values decrease with $|\mathbf{q}|$ quadratically and, similarly to the acoustic phonon, become sufficiently constant at $|\mathbf{q}| > 0.2$.

The mean values $\overline{\langle|V^{(3)}|^2\rangle}(|\mathbf{q}|, j)$ show a universal behavior as a function of $|\mathbf{q}|$: for the acoustic branches they grow parabolically at $|\mathbf{q}| < 0.4$ and then become constant, while for the optical branches they decrease parabolically $|\mathbf{q}| < 0.2$ and then also become constant.

The obtained values of the third-order coefficients can be further used as a simple analytical model for the matrix element and thus avoiding expensive calculations of the anharmonic coefficients.

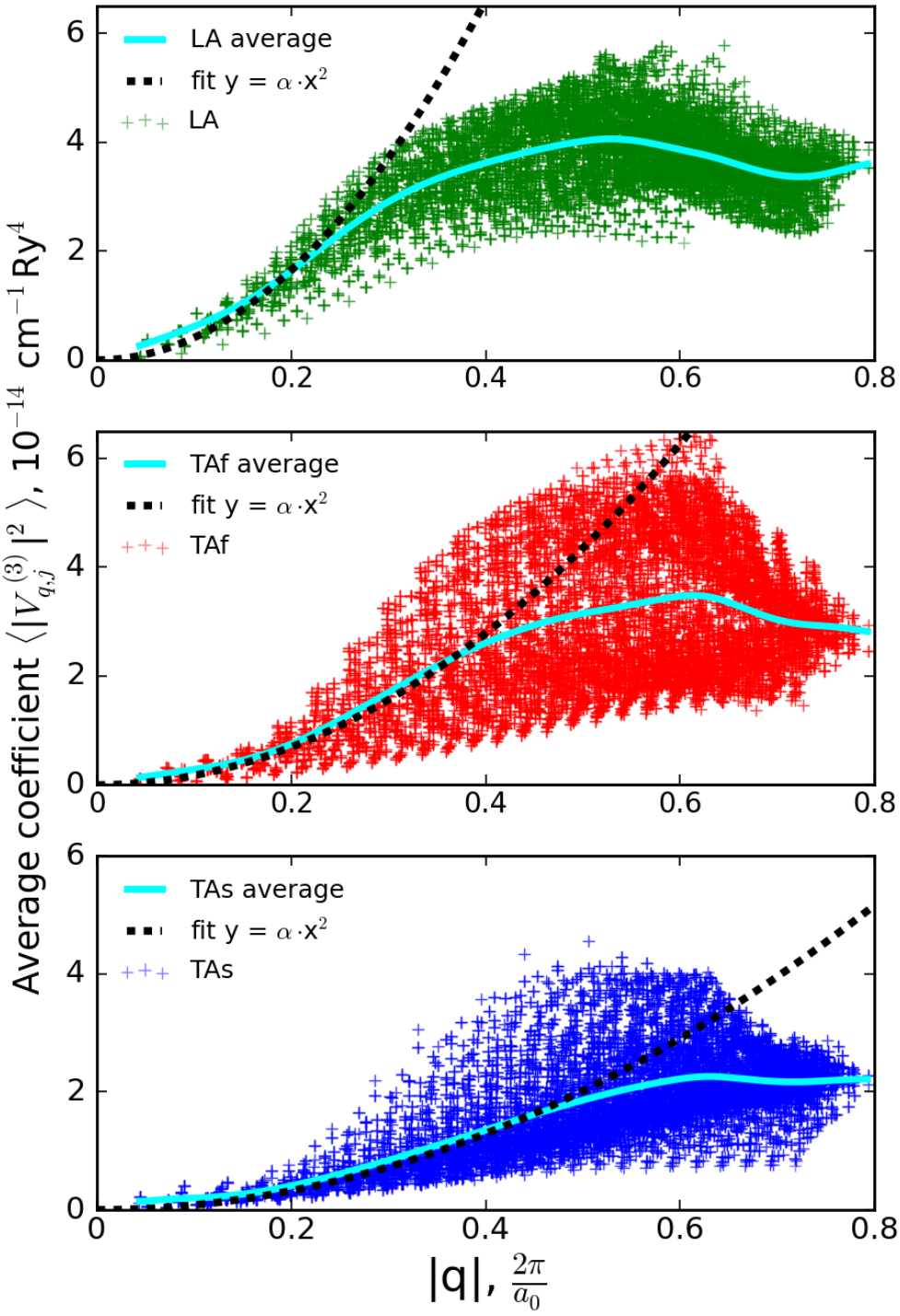

Figure 6.8: Average coefficients $\langle|V^{(3)}|^2\rangle(\mathbf{q}j)$ of acoustic phonon modes as a function of the modulus of the wave vector $|\mathbf{q}|$ of the incoming phonon. Bottom panel: blue crosses - the TAs mode. Middle panel: red crosses - the TAf mode. Top panel: green crosses - the LA mode. The mean values $\overline{\langle|V^{(3)}|^2\rangle}(|\mathbf{q}|, j)$ defined in Eq. 6.10 are shown by thick cyan lines for each phonon mode. The fitting parameters are $\alpha = 8.1 \cdot 10^{-14}$ cm^{-1}Ry^4 $\left(\frac{a_0}{2\pi}\right)^2$ for the TAs mode, $\alpha = 1.7 \cdot 10^{-13}$ cm^{-1}Ry^4 $\left(\frac{a_0}{2\pi}\right)^2$ for the TAf mode and $\alpha = 4.1 \cdot 10^{-13}$ cm^{-1}Ry^4 $\left(\frac{a_0}{2\pi}\right)^2$ for the LA mode.

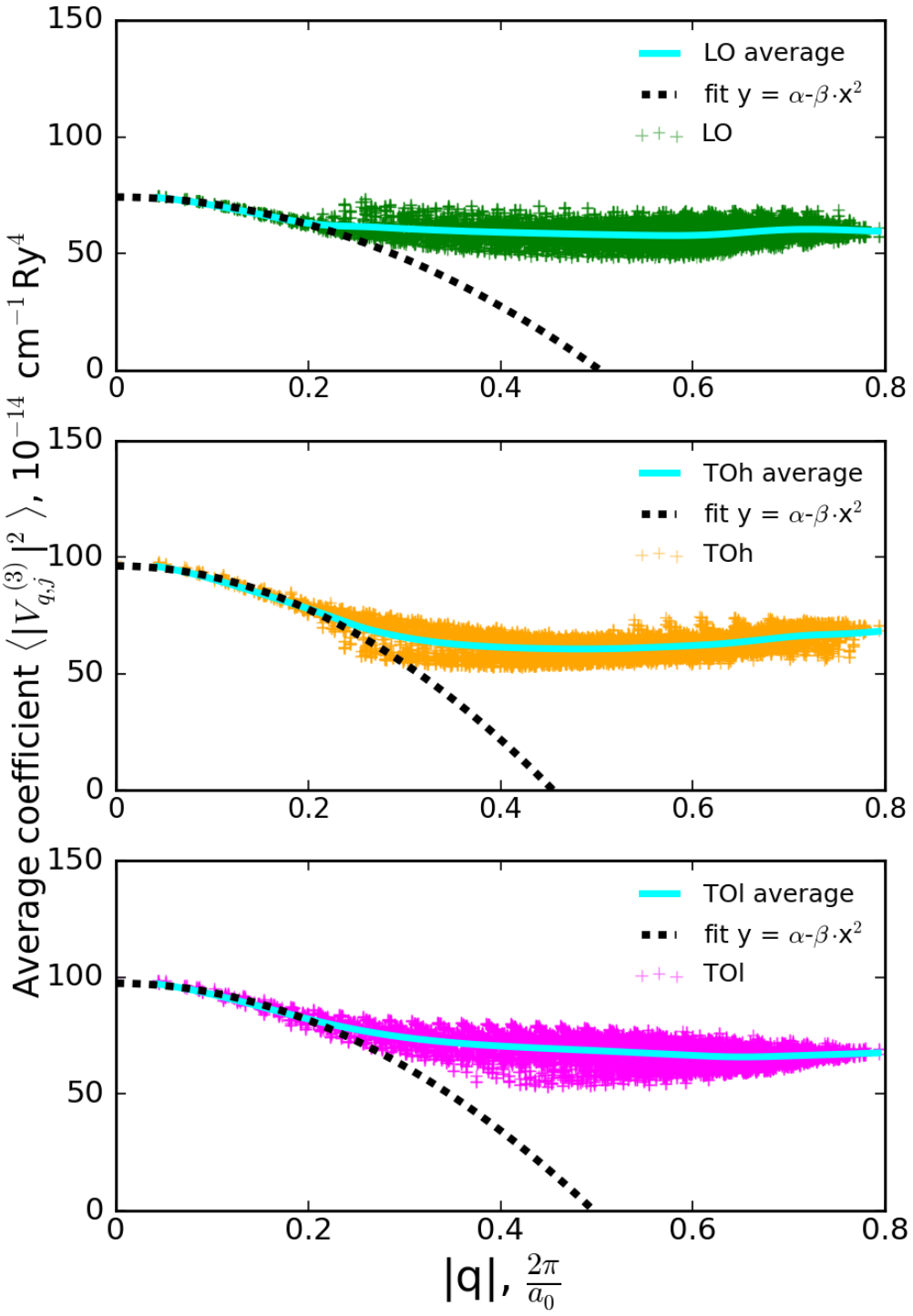

Figure 6.9: Average coefficients $\langle|V^{(3)}|^2\rangle(\mathbf{q}j)$ of optical phonon modes as a function of the modulus of the wave vector $|\mathbf{q}|$ of the incoming phonon. Bottom panel: magenta crosses - the TOl mode. Middle panel: orange crosses - the TOh mode. Top panel: green crosses - the LO mode. The mean values $\overline{\langle|V^{(3)}|^2\rangle}(|\mathbf{q}|, j)$ defined in Eq. 6.10 are shown by thick cyan lines for each phonon mode. The fitting parameters are $\alpha = 9.7 \cdot 10^{-13}$ cm^{-1}Ry^4 $\left(\frac{a_0}{2\pi}\right)^2$ and $\beta = 3.9 \cdot 10^{-12}$ cm^{-1}Ry^4 for the TOl mode, $\alpha = 9.6 \cdot 10^{-13}$ cm^{-1}Ry^4 $\left(\frac{a_0}{2\pi}\right)^2$ and $\beta = 4.6 \cdot 10^{-12}$ cm^{-1}Ry^4 for the TOh mode and $\alpha = 7.4 \cdot 10^{-13}$ cm^{-1}Ry^4 $\left(\frac{a_0}{2\pi}\right)^2$ and $\beta = 2.9 \cdot 10^{-12}$ cm^{-1}Ry^4 for the LO mode.

6.8 Summary and outlook

This Chapter is devoted to the study of phonon-phonon interaction in bismuth and to its anharmonic properties such as anharmonic broadening and phonon lifetime that are governed by this interaction.

First, I have discussed the anharmonic broadening of both acoustic and optical phonon modes at ambient temperature along some high symmetry directions in the Brillouin zone. I have shown that the smallest broadening is observed for the acoustic phonons near the center of the Brillouin zone. The longitudinal modes have the smallest broadening comparing with the transverse modes in the chosen direction. Contrastingly, the acoustic phonons from the zone boundaries and optical phonons in vicinity of Γ point are found to have the largest broadening.

Then, I have analyzed the interaction processes of the incoming phonons in the binary and trigonal directions with arbitrary phonons from all over the Brillouin zone and I have evaluated the contributions of these processes to anharmonic broadening. I have found that the dominant processes for acoustic phonons are the coalescence with another acoustic phonon to create a phonon with higher energy (LA or TO) and the decay of the acoustic phonons near the zone boundary into two TA modes with lower energies. TO modes, in turn, either coalesce with TA phonon to form another optical phonon or decay into two acoustic phonon modes. The highest LO phonons can only decay into the low acoustic modes. The lifetime of TO mode at Γ point is found to be determined by the phonon-phonon interaction solely and matches perfectly with the experimental values obtained from the Raman experiments [175, 176]. However, my value of the lifetime of the LO phonon is much higher than the experimental one. The latter is thus expected to be limited by electron-phonon interaction rather than by phonon-phonon interaction.

I have analyzed the attenuation of sound waves as a function of its energy in the binary and trigonal directions in bismuth. I have also studied the major phonon-phonon scattering processes determining the attenuation. The predicted values of the sound attenuation can be used in future experiments.

I have studied the anharmonic phonon-phonon matrix elements as a function of the modulus of the wavevector $\mathbf{q}$ of incoming phonon. I have examined a long-wave approximation (LWA) for the anharmonic matrix elements. I have found that it gives a good estimation in the region near the zone center and works poorly elsewhere.

I have not discussed the role of anharmonicity on the phonon frequency. Such a calculation requires computation of anharmonic coefficient up to fourth order [51]. This subject is left as a perspective of this work.

General conclusions and perspectives

This thesis has been devoted to the theoretical investigation of the heat conduction in bulk bismuth and to the possible strategies for its reduction such as nanostructuring and photoexcitation. To describe thermal transport, I used a recently developed advanced methods of the solution of the Boltzmann transport equation [5] and of the phonon-phonon matrix elements calculation from first principles [6]. I have also developed my own tools to perform a detailed analysis of the lattice thermal conductivity and of the phonon-phonon interaction. In order to study nanostructuring effect, I have included the Casimir model for a three-dimensional and anisotropic material. I have performed my calculations in a high performance computing environment.

I have studied vibrational properties of bismuth and I have obtained an accurate description of the acoustic part of the phonon dispersion. However, the optical phonon branches near Γ lie considerably lower than in experiments providing an efficient extra-channel of scattering for the acoustic phonons and enhancing the coalescence processes of acoustic phonons into optical ones. Moreover, I have found that optical phonons carry only a small portion of heat in bismuth at all temperatures. Thus, I have applied a model to modify the optical part of the phonon dispersion by shifting them upward to match the frequency of optical transverse modes at Γ to the experimental one. I have shown that this shift leads to the reduction of the joint-density of states for the acoustic phonons and results in the lattice thermal conductivity which is in excellent agreement with the experiments of Uher *et al.* [16]. My *ab initio* calculation without rigid shift agrees with a previous calculation of Lee *et al.* [56] and provides a considerably lower value of the lattice thermal conductivity.

I have calculated the lattice thermal conductivity in the two principal directions, binary and trigonal, in a broad temperature range from 2 K up to melting point temperature 550 K. I have discussed the Casimir model for the scattering of phonons by sample boundaries. I have shown that the account for boundary scattering in macro-samples leads to finite values of the lattice thermal conductivity at ultra-low temperatures in contrast with the divergent values in the presence of phonon-phonon scattering only. I have demonstrated that the Casimir model allows me to describe accurately the position of the thermal conductivity maximum as well as temperature behavior of thermal conductivity down to T = 2 K.

As a byproduct of my calculation, I have evaluated the electronic thermal conductivity as a difference between the measured total thermal conductivity and my theoretical results. I have found that it is constant as a function of temperature and equal to 6 $Wm^{-1}K^{-1}$ in the binary direction and to 3 $Wm^{-1}K^{-1}$ in the trigonal direction. I have

discussed the anisotropy of thermal conductivity and I have shown that it is determined by the lattice contribution in the region of low temperatures where it dominates.

I have discussed the practical realization of the acoustic-optical coupling in the ultrafast pump-probe experiments in photoexcited bismuth. I have shown that this interaction may significantly alter the magnitude of the lattice thermal conductivity causing a strong reduction when the optical branches are softened down towards the acoustic modes.

I have shown that the Casimir model allows to study the samples of different geometries such as thin films, nanowires and spherical grains and of both polycrystalline and single crystal nature. I have shown the predictive capability of the method on the nanoscale by precisely describing the experiments in the polycrystalline thin films and comparing with the existing thermal conductivity data in nanowires. Finally, I have also predicted the effect of size reduction of thermal conductivity in metallic and semiconducting thin films and semiconducting polycrystalline bismuth, providing an abacus for the thermal management and thermoelectric applications as well as for future experiments.

I have studied the anharmonic broadening of both acoustic and optical phonon modes at ambient temperature along some high symmetry directions in the Brillouin zone. I have found that the acoustic phonons from the zone boundaries and optical phonons in the vicinity of Γ have the largest broadening revealing their active role in phonon-phonon interaction in bismuth. Then, I have analyzed the interaction processes of the incoming phonons in the binary and trigonal directions with arbitrary phonons from all over the Brillouin zone and I have evaluated the contributions of these processes to anharmonic broadening. I have shown that the lifetime of TO phonon at Γ is determined by the phonon-phonon interaction solely and matches extremely well with the experimental values obtained from the Raman experiments [175, 176]. I have found that accounting for phonon-phonon interaction is not sufficient to explain the lifetime of LO phonon at Γ which is presumably determined by electron-phonon interaction [169]. I have predicted the attenuation of acoustic phonons which can be used in future experiments. Finally, I have analyzed the anharmonic phonon-phonon matrix elements and validated the long-wave approximation often used in the literature.

Below I list some immediate perspectives of my PhD work.

- *Anharmonic shift of optical E_g mode at* Γ

  In Chapter 3, I have shown that in all DFT calculations of bismuth which have been performed so far, the frequency of the transverse optical (TO) phonon mode at Γ lies considerably lower than in experiment. The possible explanation might be the effect of anharmonic shift which is not taken into account in the phonon dispersion. To calculate the anharmonic shift, one needs to compute a real part of self-energy consisting of tadpole, bubble and loop diagrams [51]. The latter diagram requires the knowledge of fourth-order anharmonic constants.

- *Raman spectrum*

  In general, the calculation of anharmonic shift opens a route to the explanation of Raman spectrum of bismuth [176, 182].

- *Second sound*

  In Chapter 2, I have discussed the violation of Fourier's law resulting in the propagation of heat in form of a damped wave instead of the diffusion mechanism. Second sound has been observed experimentally in bismuth in temperature range 2 K $< T <$3.5 K [42]. The methods I use enable me to study the conditions necessary for the existence of second sound *i.e.* the presence of the hydrodynamic regime of heat flow.

On the long term, I see two main research axes, one of which is not particular to bismuth.

First, the thermal conductivity of monocrystalline nanowires still remains unexplained. This is true in silicon [100, 101] and in bismuth (this work). As we have seen in Section 5.5, experiments in bismuth nanowires provide extremely scattered values of the thermal conductivity (Fig. 5.8). The Casimir model used in this work shows a large thermal conductivity reduction which is, however, not enough large to match the experimental data. Thus, further theoretical and experimental investigations of the thermal conductivity of nanowires are necessary.

On the theoretical side, Casimir's model is limited by the fact that the probability of the scattering of phonons by sample boundaries in Eq. 5.3 has been evaluated with the equilibrium Bose-Einstein phonon distribution. However, in case of strong scattering the role of the out-of-equilibrium distribution function may be important. Another limitation of my formalism is the fact that the different sources of scattering are treated as independent. However, there might be also cases where the two sources of scattering are coupled and the Matthiessen rule is violated [183, 184]. An accurate account for the surface structure effects and roughness might also require more realistic models.

On the experimental side, the production of good electrical and thermal contacts, in particular for nanowires, is challenging and is probably the main source of inaccuracy in experimental data [23, 15]. In the modeling of thermal devices based on silicon, like those performed at Institut d'Électronique Fondamentale (IEF) Université Paris XI, unusually large parameters accounting for the phonon scattering by interfaces must be inserted in the model to reproduce the low experimental values of the lattice thermal conductivity of nanowires. On the other hand, careful transport calculations based on *ab initio* methods have so far been unable to explain the low value of the lattice thermal conductivity in silicon nanowires. As shown in the present manuscript, the same conclusion can be drawn for bismuth. So far, very large atomic modifications in the wires are the main explanations for the low values of the lattice thermal conductivity [100, 101]. Hence, further experimental and theoretical studies are called for.

As a second long-term perspective, the theoretical studies of the electron-related quantities (*i.e.* the power factor $P_F = S^2\sigma$) in bulk bismuth and its nanostructures are of high interest. They will complement the study of the lattice thermal conductivity done in this thesis and enable us to evaluate the full thermoelectric figure of merit ZT. It is especially interesting in view of experiments of Ref. [96, 97] in Bi nanowires where the Seebeck coefficient S has been found to be increased by several orders of magnitude. Moreover, at low temperatures the study of phonon drag effect (see Section 2.3.3) is necessary to explain the high values of the Seebeck coefficient.

Appendix A

Bismuth

A.1 Crystal structure

Bismuth possesses a rhombohedral A7 crystal structure typical for the group V semimetals such as Sb and As. It could be described either by a hexagonal or by a rhombohedral (trigonal) unit cell. In the latter case, the lattice parameters are the rhombohedral edge a_0, the rhombohedral angle α and the internal parameter u, describing atomic positions along the trigonal axis: (u,u,u) and $(-u,-u,-u)$ in crystal coordinates. The rhombohedral unit cell is shown in Fig. A.1. In my calculations after relaxation, I have obtained the following parameters for LDA : $a_0 = 8.820$ a.u., $\alpha = 57.99^0$ and $u = 0.23554$ (in units of a_0) and for GGA $a_0 = 9.270$ a.u., $\alpha = 56.36^0$ and $u = 0.23161$ (in units of a_0). The experimental parameters are $a_0 = 8.9263$ a.u., $\alpha = 57.35^0$ and $u = 0.234$ (in units of a_0)[185].

A.2 Pseudopotential.

Using the `ATOMIC` code integrated in the `QUANTUM ESPRESSO` package, I have generated a full-relativistic norm-conserving pseudopotential of bismuth in a separable form.

Neutral bismuth contains 83 electrons. Its electronic configuration is $[\mathrm{Xe}]4f^{14}5d^{10}6s^26p^3$. However, the chemical properties of materials mainly depend on the valence electrons from the outer shells rather than on the deep core electrons which are hardly influenced by the environment [186]. In my pseudopotential, I have included 5 electrons $6s^26p^3$ in the valence regions and the remaining ones I treat as core electrons.

Often the semi-core $5d^{10}$ are also included in the valence region. It improves the transferability of pseudopotential and its accuracy, but makes the pseudopotential extremely hard from the computational point of view. The norm-conserving pseudopotential with semi-core $5d^{10}$ states in valence had been developed by I. Timrov in our laboratory [4]. It enabled us to achieve an accurate description of electronic of bismuth, as well as to determine the magnitude of the electron-phonon coupling [1, 3]. In this work, I have used the pseudopotential with $5d^{10}$ in valence as the reference one and compared the details of the electronic band structure for both pseudopotentials in Appendix A.3.

All calculations in this work have been performed with pseudopotential including the LDA exchange-correlation functional. The pseudopotential with the same parameters but

with the GGA exchange-correlation functional has also been generated for comparison.

A.3 Comparison of the electronic band structure

The electronic band structure obtained with my pseudopotentials are close to the ones obtained in Iurii Timrov's PhD [4]. The summary of some important energy levels (eV) obtained in this work, in the work of Iurii Timrov [4] and in some experiments is given in Table A.1.

A.4 Comparison of the phonon dispersions with LDA and GGA.

Two phonon dispersions of Bi calculated with LDA and GGA exchange-correlation functionals respectively for a $6 \times 6 \times 6$ uniform grid are shown in Fig. A.2. The spin-orbit-coupling is included in both calculations. As can be seen from Fig. A.2, the acoustic part of the phonon dispersion with GGA shows very low frequencies comparing with experimental data. This is due to the equilibrium lattice paramenters which are much larger for GGA than for LDA (see Section A.1). Phonon dispersion with LDA exchange-correlation potential has been used in this thesis instead.

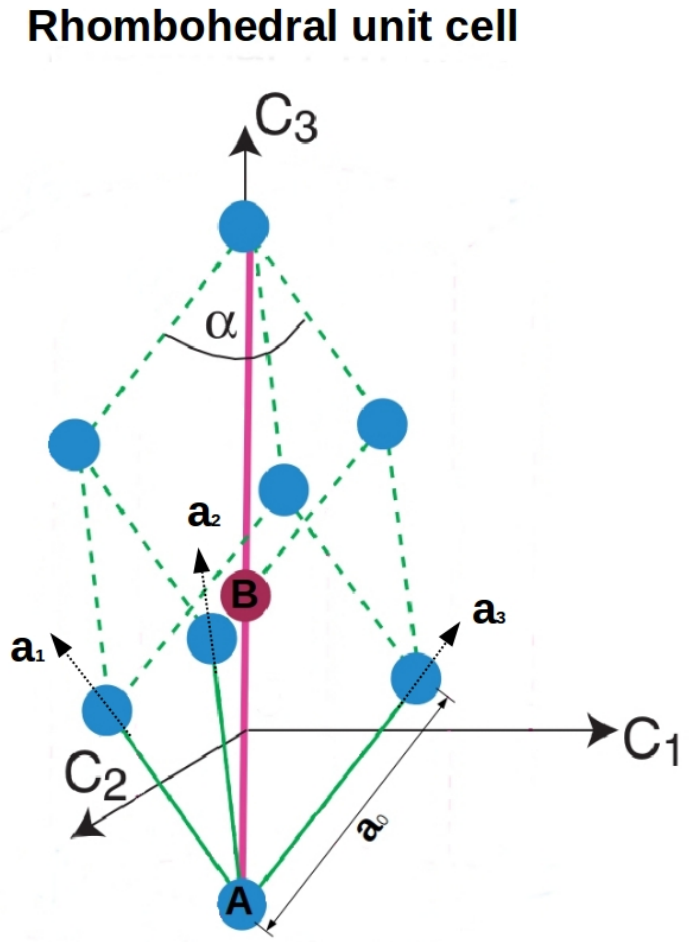

Figure A.1: Crystal structure of bulk bismuth described as a rhombohedral lattice. Two inequivalent atoms in a rhombohedral unit cell with coordinates (-u,-u,-u) and (u,u,u) in crystal coordinates are marked by letters A and B correspondingly. The rhombohedral edge a_0 and angle α are shown. The three cartesian axes are: bisectrix (C_1,y), binary (C_2,x) and trigonal (C_3,z). The three crystal axis are: $\vec{a}_1$, $\vec{a}_2$ and $\vec{a}_3$. Reproduced after Ref. [114].

Band Energy	This work		Theory Ref [1]		Theory (previous works)				Expt.
	LDA	GGA	LDA	GGA	Ref.[a]	Ref.[b]	Ref.[c]	Ref.[d]	
$L_s(3)$	-0.005	-0.035	-0.0148	-0.0959	-0.068	-0.018	-0.0267		-0.0266[e], -0.0276[f]
$L_a(3)$	-0.124	-0.066	-0.1267	-0.1195		-0.28	-0.0403		-0.0416[e], -0.0429[f]
$L_a(3) - L_s(3)$	-0.119	-0.031	-0.112	-0.024		-0.262	-0.014	-0.013	-0.011 – -0.015
$T_{45}^-(1)$	0.079	0.126	0.097	0.092	0.095	0.023	0.011		
$T_6^+(3)$	0.219	0.478	0.217	0.417		0.49	0.381		
$T_6^+(3) - T_{45}^-(1)$	0.140	0.352	0.120	0.326		0.467	0.370		0.18 – 0.41
$T_{45}^-(1) - L_s(3)$	0.084	0.161	0.112	0.188	0.163	0.041	0.038	0.033	0.036 – 0.039
$\Gamma_6^-(1) - \Gamma_6^+(1)$	5.861	4.932	5.65	4.82	5.61	5.73	5.91		4.7 – 5.9
$\Gamma_{45}^+(1) - \Gamma_6^+(3)$	0.151	0.239	0.15	0.25	0.23	0.19	0.31		0.18 – 0.35
$\Gamma_6^-(2) - \Gamma_{45}^+(1)$	1.533	1.125	1.48	1.11		1.72	1.07		0.72 – 0.81
$\Gamma_6^-(2) - \Gamma_6^+(3)$	1.684	1.364	1.62	1.35		1.91	1.37		0.65 – 0.71
$T_6^+(1) - T_6^-(1)$	1.757	2.064	1.72	2.01	1.94	1.88	1.11		1.18 – 1.90
$T_6^+(2) - T_{45}^-(1)$	-1.557	-1.493	-1.60	-1.52	-2.08	-1.30	-1.13		
$T_6^-(3) - T_{45}^-(1)$	0.841	0.996	0.78	0.94		1.09	0.94		0.80 – 0.88
$L_a(1) - L_s(1)$	0.583	0.684	0.57	0.67		0.72	0.36		
$L_a(2) - L_s(3)$	-1.855	-1.876	-1.84	-1.86		-1.97	-1.64		-1.92 – -2.10
$L_s(4) - L_a(3)$	0.801	1.005	0.89	1.00		1.04	0.84		1.05 – 1.15
$L_s(4) - L_s(3)$	0.682	0.974	0.78	0.97		0.78	0.83		

[a] Shick *et al.*, Ref. [187].
[b] Gonze *et al.*, Ref. [189], cited in Ref. [190].
[c] Liu *et al.*, Ref. [192].
[d] Aguilera *et al.*, Ref. [188].
[e] Isaacson *et al.*, Ref. [191].
[f] Smith *et al.*, Ref. [193].

Table A.1: Energy levels (eV) as obtained in this work, in the work of Iurii Timrov [4] and in some experiments specified above.

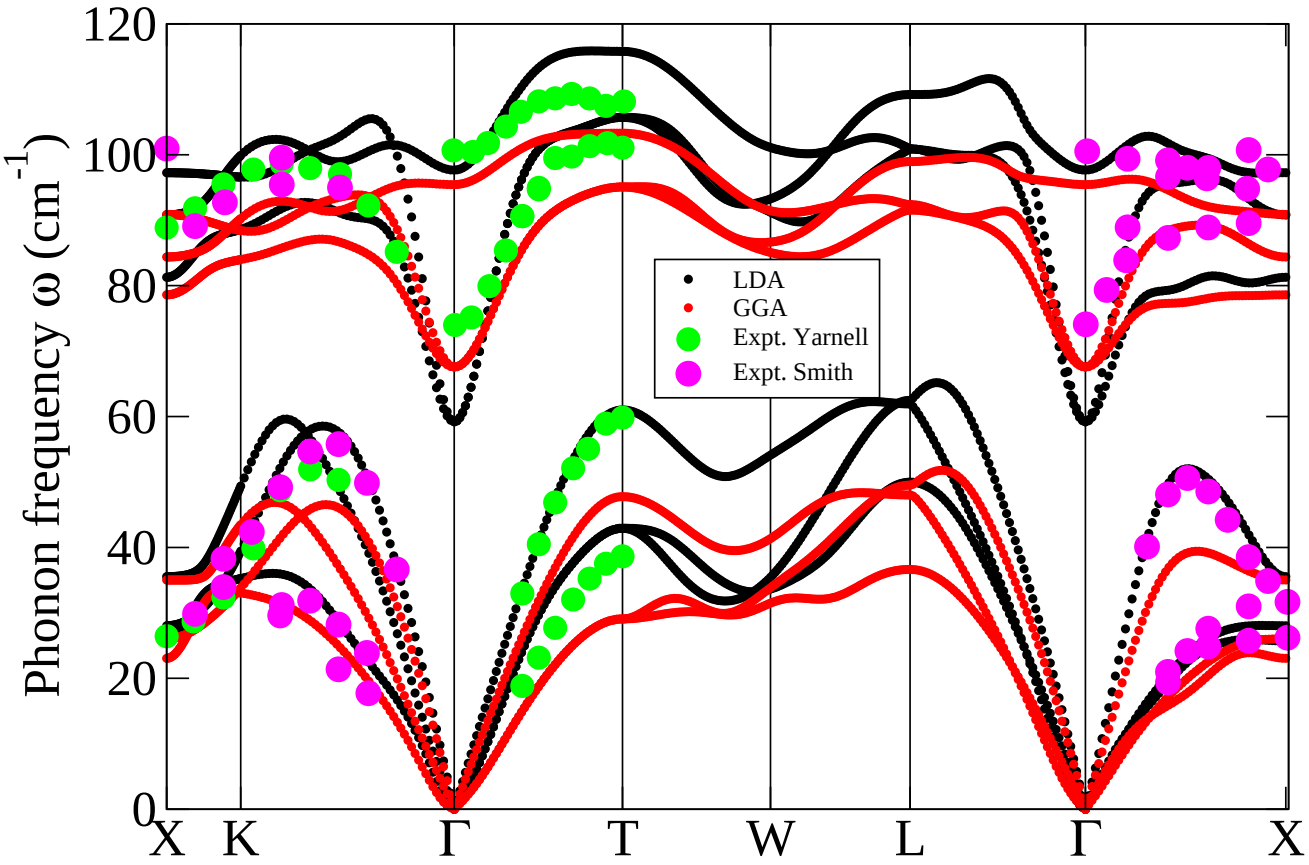

Figure A.2: Phonon dispersions calculated with pseudopotentials developed in this work. Black - calculation within the LDA used in this work. Red - calculation within the GGA. Both calculation are done with accounting for the spin-orbit coupling interaction and with the equilibrium theoretical lattice parameters. Experimental data are also shown (same as in Fig. 3.1).

Bibliography

[1] I. Timrov, T. Kampfrath, J. Faure, N. Vast, C. R. Ast, C. Frischkorn, M. Wolf, P. Gava, and L. Perfetti. Thermalization of photoexcited carriers in bismuth investigated by time-resolved terahertz spectroscopy and *ab initio* calculations. Phys. Rev. B, 85:155139, 2012.

[2] E. Papalazarou, J. Faure, J. Mauchain, M. Marsi, A. Taleb-Ibrahimi, I. Reshetnyak, A. van Roekeghem, I. Timrov, N. Vast, B. Arnaud, and L. Perfetti. Coherent phonon coupling to individual Bloch states in photoexcited bismuth. Phys. Rev. Let., 108:256808, 2012.

[3] J. Faure, J. Mauchain, E. Papalazarou, M. Marsi, D. Boschetto, I. Timrov, N. Vast, Y. Ohtsubo, B. Arnaud, and L. Perfetti. Direct observation of electron thermalization and electron-phonon coupling in photoexcited bismuth. Phys. Rev. B, 88:075120, 2013.

[4] I. Timrov. *Ab initio* study of plasmons and electron-phonon coupling in bismuth: From free-carrier absorption towards a new method for electron energy-loss spectroscopy. PhD thesis, École Polytechnique, France, 2013.

[5] G. Fugallo, M. Lazzeri, L. Paulatto, and F. Mauri. *Ab initio* variational approach for evaluating lattice thermal conductivity. Phys. Rev. B, 88:045430, 2013.

[6] L. Paulatto, F. Mauri, and M. Lazzeri. Anharmonic properties from a generalized third-order *ab initio* approach: Theory and applications to graphite and graphene. Phys. Rev. B, 87:214303, 2013.

[7] M. Markov, J. Sjakste, G. Fugallo, L. Paulatto, M. Lazzeri, F. Mauri, and N. Vast. Nanoscale mechanisms for the reduction of heat transport in bismuth. Phys. Rev. B, 93:064301, 2016.

[8] C. F. Gallo, B. S. Chandrasekhar, and P. H. Sutter. Transport properties of bismuth single crystals. J. Appl. Physics, 34:144, 1963.

[9] C. J. M. Lasance. The Seebeck coefficient. Electronics Cooling, 2006. http://www.electronics-cooling.com/2006/11/the-seebeck-coefficient/.

[10] C. Uher and H. J. Goldsmid. The magneto-Seebeck coefficient of bismuth single crystals. Phys. Stat. Sol. (b), 63:163, 1974.

[11] L. C. Brodie, D. N. Sinha, C. E. Sanford, and J. S. Semura. Bismuth magnetoresistive thermometry for transient temperature measurements in liquid helium. Rev. Sci. Instrum., 52:1697, 1981.

[12] A. Georges. Thermoélectricité : concepts, matériaux et enjeux énergétiques. Note de cours. Collège de France, 2013. http://www.college-de-france.fr/site/antoine-georges/course-2012-2013.htm.

[13] W. Hansch. Temperature dependence of the diffusion thermopower in metals. Phys. Rev. B, 31:3504, 1985.

[14] J.-P. Issi. Low temperature transport properties of the group V semimetals. Aus. J. Phys., 32:585, 1979.

[15] A. L. Moore, M. T. Pettes, F. Zhou, and L. Shi. Thermal conductivity suppression in bismuth nanowires. Journal of Applied Physics, 106:034310, 2009.

[16] C. Uher and H. J. Goldsmid. Separation of the electronic and lattice thermal conductivities in bismuth crystals. Phys. Stat. Sol. (b), 65:765, 1974.

[17] L. D. Hicks and M. S. Dresselhaus. Thermoelectric figure of merit of a one-dimensional conductor. Phys. Rev. B, 47:16631, 1993.

[18] L. D. Hicks and M. S. Dresselhaus. Effect of quantum-well structures on the thermoelectric figure of merit. Phys. Rev. B, 47:12727, 1993.

[19] F. Völklein and E. Kessler. A method for the measurement of thermal conductivity, thermal diffusivity, and other transport coefficients of thin films. Phys. Stat. Sol. (a), 81:585, 1984.

[20] G. Abrosimov. The dimensional effect of the transfer coefficients in oriented films of bismuth grown on polymer substrates. Teplofizika Vysokikh Temperatur, 12:530–536, 1974.

[21] D. W. Song, W.-N. Shen, B. Dunn, C. D. Moore, M. S. Goorsky, T. Radetic, R. Gronsky, and G. Chen. Thermal conductivity of nanoporous bismuth thin films. Applied Physics Letters, 84:1883, 2004.

[22] J. P. Heremans. Low-dimensional thermoelectricity. Acta Phys. Pol. A, 108:609, 2005.

[23] J. W. Roh, K. Hippalgaonkar, J. H. Hal, R. Chen, M. Z. Li, P. Ercius, A. Majumdar, W. Kim, and W. Lee. Observation of anisotropy in thermal conductivity of individual single-crystalline bismuth nanowires. ACS Nano, 5:3954, 2011.

[24] Y. Hasegawa, M. Murata, F. Tsunemi, Y. Saito, K. Shirota, T. Komine, C. Dames, and J.E. Garay. Thermal conductivity of an individual bismuth nanowire covered with a quartz template using a 3-omega technique. J. Elec. Mat., 42:2048, 2013.

[25] S.-Y. Lee, G.-S. Kim, M.-R. Lee, H. Lim, W.-D. Kim, and S.-K. Lee. Thermal conductivity measurements of single-crystalline bismuth nanowires by the four-point-probe 3-omega technique at low temperatures. Nanotechnology, 24:185401, 2013.

[26] J. Kim, S. Lee, Y. M. Brovman, Ph. Kim, and W. Lee. Diameter-dependent thermoelectric figure of merit in single-crystaltine Bi nanowires. Nanoscale, 7:5053, 2015.

[27] J. M. Ziman. Electrons and Phonons: The Theory of Transport Phenomena in Solids. Oxford University Press, Oxford, 1960.

[28] D.M. Rowe. Thermoelectrics handbook: macro to nano. CRC Press, Taylor and Francis Group, Boca Raton, FL, 2006.

[29] H. Alam and S. Ramakrishna. A review on the enhancement of figure of merit from bulk to nano-thermoelectric materials. Nano energy, 2:190, 2012.

[30] S.B. Riffat and Xiaili Ma. Thermoelectrics: a review of present and potential applications. Appl. Therm. Eng., 23:913, 2003.

[31] T. M. Tritt and M. A. Subramanian. Thermoelectric materials, phenomena, and applications: A bird's eye view. MRS Bull., 31:188, 2006.

[32] D.M. Rowe. Thermoelectrics, an environmentally-friendly source of electrical power. Renewable energy, 16:1251, 1999.

[33] A. M. Dehkordi, M. Zebarjadi, J. He, and T. M. Tritt. Thermoelectric power factor: Enhancement mechanisms and strategies for higher performance thermoelectric materials. Mat. Sci. Eng. R, 97:1, 2015.

[34] H. Imai, Y. Shimakawa, and Y. Kubo. Large thermoelectric power factor in TiS_2 crystal with nearly stoichiometric composition. Phys. Rev. B, 64:241104, 2001.

[35] M. Chester. Second sound in solids. Phys. Rev., 5:131, 1963.

[36] P. Vernotte. Les paradoxes de la théorie continue de l'équation de la chaleur. Comptes Rendus Acad. Sci. Paris, 246:3154, 1958.

[37] C. Cattaneo. Sur une forme de l'équation de la chaleur éliminant le paradoxe d'une propagation instantanée. Comptes Rendus Acad. Sci. Paris, 247:431, 1958.

[38] C. Ulbrich. Exact Electric Analogy to the Vernotte Hypothesis. Phys. Rev., 123:2001, 1961.

[39] R. J. Hardy. Phonon Boltzmann Equation and Second Sound in Solids. Phys. Rev. B, 2:1193, 1969.

[40] B. Abdel-Hamid. Modelling non-Fourier heat conduction with periodic thermal oscillation using the finite integral transform. Applied Mathematical Modelling, 23:899, 1999.

[41] D. W. Pohl and V. Irniger. Observation of Second Sound in NaF by Means of Light Scattering. Phys. Rev. Lett., 36:480, 1976.

[42] V. Narayanamurti and R.C. Dynes. Observation of second sound in bismuth. Phys. Rev. Lett., 28:1461, 1972.

[43] C. C. Ackerman, B. Bertman, H. A. Fairbank, and R. A. Guyer. Second sound in solid helium. Phys. Rev. Lett., 16:789, 1966.

[44] A. Cepellotti, G. Fugallo, L. Paulatto, M. Lazzeri, F. Mauri, and N. Marzari. Phonon hydrodynamics in two-dimensional materials. Nature Communications, 6:6400, 2015.

[45] S. Lee, D. Broido, K. Esfarjani, and G. Chen. Hydrodynamic phonon transport in suspended graphene. Nature Communications, 6:6290, 2015.

[46] R. Peierls. On the kinetic theory of thermal conduction in crystals. Ann. Phys., 395:1055, 1929.

[47] V. L. Gurevich. Transport in phonon systems. Elsevier Science Publishers Company Inc., 1986.

[48] T.M. Tritt. Thermal Conductivity – Theory, Properties, and Applications. Kluwar Academic / Plenum Publishers, New York, 2004.

[49] A. A. Maradudin and A. E. Fein. Scattering of neutrons by an anharmonic crystal. Phys. Rev., 128:2589, 1962.

[50] R.A. Cowley. Anharmonic crystals. Rep. Prog. Phys., 31:123, 1968.

[51] M. Calandra, M. Lazzeri, and F. Mauri. Anharmonic and non-adiabatic effects in MgB_2: Implications for the isotope effect and interpretation of Raman spectra. Physica C, 456:38–44, 2007.

[52] G. Fugallo, A. Cepellotti, L. Paulatto, M. Lazzeri, N. Marzari, and F. Mauri. Thermal conductivity of graphene and graphite: collective excitations and mean free paths. Nano Lett., 14:6109, 2014.

[53] G. P. Srivastava, editor. The Physics of Phonons. Adam Hilger, Bristol, 1990.

[54] M. Omini and A. Sparavigna. Heat transport in dielectric solids with diamond structure. Il Nuovo Cimento D, 19:1537, 1997.

[55] M. Omini and A. Sparavigna. Effect of phonon scattering by isotope impurities on the thermal conductivity of dielectric solids. Physica B, 233:230, 1997.

[56] S. Lee, K. Esfarjani, J. Mendoza, M. S. Dresselhaus, and G. Chen. Lattice thermal conductivity in Bi, Sb, and Bi-Sb alloy from first principles. Phys. Rev. B, 89:085206, 2014.

[57] L. Lindsay, D. A. Broido, and T. L. Reinecke. Phonon-isotope scattering and thermal conductivity in materials with a large isotope effect: A first-principles study. Phys. Rev. B, 88:144306, 2013.

[58] T. R. Anthony, W. F. Banholzer, J. F. Fleischer, L. Wei, P. K. Kuo, R. L. Thomas, and R. W. Pryor. Thermal diffusivity of isotopically enriched ^{12}C diamond. Phys. Rev. B, 42:1104, 1990.

[59] S. Chen, Q. Wu, C. Mishra, J. Kang, H. Zhang, K. Cho, W. Cai, A. A. Balandin, and R. S. Ruoff. Thermal conductivity of isotopically modified graphene. Nature Materials, 11:203, 2012.

[60] L. Lindsay, D. A. Broido, and T. L. Reinecke. Thermal conductivity and large isotope effect in GaN from first principles. Phys. Rev. Lett., 109:095901, 2013.

[61] L. Lindsay, D. A. Broido, and T. L. Reinecke. First-principles determination of ultrahigh thermal conductivity of boron arsenide: A competitor for diamond? Phys. Rev. Lett., 111:025901, 2013.

[62] T. Feng and X. Ruan. Prediction of Spectral Phonon Mean Free Path Thermal Conductivity with Applications to Thermoelectrics and Thermal Mamagement: A Review. Journal of Nanomaterials, 2014:206370, 2014.

[63] R. A. Hamilton and J. E. Parrott. Variational calculation of the thermal conductivity of germanium. Phys. Rev., 178:1284, 1969.

[64] A. Berke, A. P. Mayer, and R. K. Wehner. Spontaneous decay of long-wavelength acoustic phonons. J. Phys. C: Solid State Phys, 21:2305–2323, 1988.

[65] R. Legrand. Acoustique - étude et utilisation de nouvelles sources et transducteurs aux longueurs d'onde nanométriques. PhD thesis, Université Pierre et Marie CURIE Paris VI (France), 2014.

[66] M. Born and K. Huang, editors. Dynamical Theory of Crystal Lattices. Oxford University Press, New York, 1954.

[67] W. Li, J. Carrete, N. A. Katcho, and N. Mingo. ShengBTE: a solver of the Boltzmann transport equation for phonons. Comp. Phys. Commun., 185:1747–1758, 2014.

[68] K. Esfarjani and H.T. Stokes. Method to extract anharmonic force constants from first principles calculations. Phys. Rev. B, 77:144112, 2008.

[69] W. Li, L. Lindsay, D. A. Broido, D. A. Stewart, and N. Mingo. Thermal conductivity of bulk and nanowire $Mg_2Si_xSn_{1-x}$ alloys from first principles. Phys. Rev. B, 86:174307, 2012.

[70] S. Baroni, S. de Gironcoli, A. Dal Corso, and P. Giannozzi. Phonons and related crystal properties from density-functional perturbation theory. Rev. Mod. Phys., 73:515, 2001.

[71] T. J. Seebeck. Magnetic polarization of metals and minerals. Abhandlungender Deutschen Akademie der Wissenschafren zu Berlin, 265, 1822-1823.

[72] H. J. Goldsmid. Bismuth – the thermoelectric material of the future? Proc. 25th International Conference on Thermoelectrics, pages 5–10, 2006.

[73] Poh Liong Yong. Pacific 'A' Level Physics Volume 2. EPB Pan Pacific, Singapore, 1994.

[74] H. J. Goldsmid and R. W. Douglas. The use of semiconductors in thermoelectric refrigeration. Brit. J. Appl. Phys., 5:386–390, 1954.

[75] H. J. Goldsmid. XXVII. thermoelectric applications of semiconductors. J. Electronics and Control, 1:218, 1955.

[76] H. J. Goldsmid. Bismuth telluride and its alloys as materials for thermoelectric generation. Materials, 7:2577–2592, 2014.

[77] F. D. Rosi, B. Abeles, and R. V. Jensen. Materials for thermoelectric refrigeration. J. Phys. Chem. Solids, 10:191, 1959.

[78] N. B. Brandt, E. A. Svistova, and M. V. Semenov. Electron transitions in antimony-rich bismuth-antimony alloys in strong magnetic fields. Sov. Phys. JETP, 32:238, 1971.

[79] B. Lenoir, A. Dauscher, M. Cassart, Yu. I. Ravich, and H. Scherrer. Effect of antimony content on the thermoelectric figure of merit of $Bi_{1-x}Sb_x$ alloys. J. Opt. Soc. Am., 55:1072, 1998.

[80] H. J. Goldsmid. Bismuth-Antimony Alloys. Phys. Stat. Sol. (a), 1:7, 1970.

[81] V. D. Kagan and N. A. Redko. Phonon thermal conductivity of bismuth alloys. Zh. Eksp. Teor. Fiz., 100:1205, 1991.

[82] T. Yazaki. Thermal conductivity of bismuth-antimony alloy single crystals. J. Phys. Soc. Jpn., 25:1054, 1968.

[83] G. E. Smith and R. Wolfe. Thermoelectric properties of Bi-Sb alloys. J. Appl. Phys., 33:841, 1962.

[84] H. J. Goldsmid. Introduction to Thermoelectricity. Springer Series in Material Science. Springer, Berlin Heidelberg Dordrecht London New York, 2010.

[85] A. Nikolaeva, T. E. Huber, D. Gitsu, and L. Konopko. Diameter-dependent thermopower of bismuth nanowires. Phys. Rev. B, 77:035422, 2008.

[86] R. Clasen, P. Grosse, A. Krosti, F. Lévy, S.F. Marenkin, W. Richter, N. Ringelstein, R. Schmechel, G. Weiser, H. Werheit, M. Yao, and W. Zdanowicz. Semiconductors: Non-Tetrahedrally Bounded Elements and Binary Compounds I. In O. Madelung, editor, Landolt-Börnstein, volume III/41C. Springer-Verlag, Berlin, 1998.

[87] I. Ya. Korenblit, M. E. Kuznetsov, and S. S. Shalyt. Thermal EMF and thermomagnetic properties of bismuth at low temperatures. Sov. Physics JETP, 29:4, 1969.

[88] J. Boxus and J-P. Issi. Giant negative phonon drag thermopower in pure bismuth. J. Phys. C: Solid State Phys., 10:L397, 1977.

[89] V. D. Kagan, N. A. Red'ko, N. A. Rodionov, V. I. Pol'shin, and O. V. Zotova. Phonon drag thermopower in doped bismuth. Physics of the Solid State, 46:1410–1419, 2004.

[90] A. Collaudin. Tenseur de mobilité et magnétothermoélectricité anisotrope du bismuth. PhD thesis, Université Pierre et Marie CURIE Paris VI (France), 2014.

[91] I. Ya. Korenblit, M. E. Kuznetsov, V. M. Muzhdaba, and S. S. Shalyt. Electron heat conductivity and the Wiedemann-Franz low for Bi. Sov. Physics JETP, 30:1009, 1970.

[92] J.R. Drabble and H. J. Goldsmid. Thermal conduction in semiconductors. Pergamon Press, Oxford, New York, 1961.

[93] C. F. Gallo, R. C. Miller, P. H. Sutter, and R. W. Ure Jr. Bipolar electronic thermal conductivity in semimetals. J. Appl. Physics, 33:3144, 1962.

[94] H. Jin, O. D. Restrepo, N. Antolin, S. R. Boona, W. Windl, R. C. Myers, and J. P. Heremans. Phonon-induced diamagnetic force and its effect on the lattice thermal conductivity. Nature Materials, doi:10.1038/nmat4247, 2015.

[95] B. Liao, B. Qiu, J. Zhou, S. Huberman, K. Esfarjani, and G. Chen. Significant reduction of lattice thermal conductivity by the electron-phonon interaction in silicon with high carrier concentrations: A first-principles study. Phys. Rev. Lett., 114:115901, 2015.

[96] J. P. Heremans, C. M. Thrush, D. T. Morelli, and M. C. Wu. Thermoelectric power of bismuth nanocomposites. Phys. Rev. Lett., 88:216801, 2002.

[97] E. Shapira, A. Holtzman, D. Marchak, and Y. Selzer. Very High Thermopower of Bi Nanowires with Embedded Quantum Point Contacts. Nano Letters, 12:808–812, 2012.

[98] Q. Hao, G. Zhu, G. Joshi, X. Wang, A. Minnich, Z. Ren, and G. Chen. Theoretical studies on the thermoelectric figure of merit of nanograined bulk silicon. Appl. Phys. Lett., 97:063109, 2010.

[99] C. Hua and A. J. Minnich. Importance of frequency-dependent grain boundary scattering in nanocrystalline silicon and silicon–germanium thermoelectrics. Semicond. Sci. Technol., 29:124004, 2014.

[100] J. Carrete, L. J. Gallego, L. M. Varela, and N. Mingo. Surface roughness and thermal conductivity of semiconductor nanowires: Going below the Casimir limit. Phys. Rev. B, 84:075403, 2011.

[101] Y. He and G. Galli. Microscopic origin of the reduced thermal conductivity of silicon nanowires. Phys. Rev. Lett., 108:215901, 2012.

[102] D. G. Cahill, P. V. Braun, G. Chen, D. R. Clarke, S. H Fan, K. E. Goodson, P. Keblinski, W. P. King, G. D. Mahan, A. Majumdar, H. J. Maris, S. R. Phillpot, E. Pop, and L. Shi. Nanoscale thermal transport. II. 2003-2012. Applied Physics Reviews, 1:011305, 2015.

[103] J. Mendoza, K. Esfarjani, and G. Chen. An *ab initio* study of multiple phonon scattering resonances in silicon germanium alloys. J.Appl.Phys., 117:174301, 2015.

[104] J. Callaway. Model for lattice thermal conductivity at low temperatures. Phys. Rev. B, 113:1046, 1959.

[105] P. G. Klemens. The thermal conductivity of dielectric solids at low temperatures (theoretical). Proceedings of the Royal Society A, 208:108–133, 1951.

[106] P. Klemens. in Thermal Conductivity and Lattice Vibrational Modes, edited by F.Seitz and D. Turnbull, Solid State Physics. Academic Press, New York, 1958.

[107] C. Herring. Theory of the thermoelectric power of semiconductors. Phys. Rev., 96:1163, 1954.

[108] G. Dolling, editor. in "Dynamical Properties of Solids" (G. K. Horton and A. A. Maradudin, eds.) Vol.1, p. 541. North-Holland Publ., Amsterdam, 1974.

[109] K. Kunc and R.M. Martin. *Ab initio* force constants of GaAs: A new approach to calculation of phonons and dielectric properties. Phys. Rev. Lett., 48:406, 1982.

[110] M.T. Yin and M.L. Cohen. Theory of lattice-dynamical properties of solids: Application to Si and Ge. Phys. Rev. B, 26:3259, 1982.

[111] L. E. Diaz-Sanchez, A. H. Romero, and X. Gonze. Phonon band structure and interatomic force constants for bismuth: Crucial role of spin-orbit interaction. Phys. Rev. B, 76:104302, 2007.

[112] J. L. Yarnell, J. L. Warren, R. G. Wenzel, and S. H. Koenig. Phonon dispersion curves in bismuth. IBM J. Res. Dev., 8:234, 1964.

[113] D. B. Smith. Los Alamos Report 3773, (unpublished), 1967.

[114] Ph. Hofmann. The surfaces of bismuth: Structural and electronic properties. Progr. Surf. Sci., 81:191, 2006.

[115] E. D. Murray, S. Fahy, D. Prendergast, T. Ogitsu, D. M. Fritz, and D. A. Reis. Phonon dispersion relations and softening in photoexcited bismuth from *first principles*. Phys. Rev. B, 75:184301, 2007.

[116] Y. Eckstein, A. W. Lawson, and D.H. Reneker. Elastic constants of bismuth. J. Appl. Phys., 31:1534, 1960.

[117] R. Golesorkhtabar, P. Pavone, J. Spitaler, P. Puschnig, and C. Draxl. ElaStic: A tool for calculating second-order elastic constants from first principles. Comp. Phys. Comm., 184:1861, 2013.

[118] Paolo Giannozzi, Stefano Baroni, Nicola Bonini, Matteo Calandra, Roberto Car, Carlo Cavazzoni, Davide Ceresoli, Guido L Chiarotti, Matteo Cococcioni, Ismaila Dabo, Andrea Dal Corso, Stefano de Gironcoli, Stefano Fabris, Guido Fratesi, Ralph Gebauer, Uwe Gerstmann, Christos Gougoussis, Anton Kokalj, Michele Lazzeri, Layla Martin-Samos, Nicola Marzari, Francesco Mauri, Riccardo Mazzarello, Stefano Paolini, Alfredo Pasquarello, Lorenzo Paulatto, Carlo Sbraccia, Sandro Scandolo, Gabriele Sclauzero, Ari P. Seitsonen, Alexander Smogunov, Paolo Umari, and Renata M Wentzcovitch. Quantum espresso: a modular and open-source software project for quantum simulations of materials. Journal of Physics: Condensed Matter, 21(39):395502 (19pp), 2009.

[119] P. W. Bridgman. Certain Physical Properties of Single Crystals of Tungsten, Antimony, Bismuth, Tellurium, Cadmium, Zinc, and Tin. Proc. Am. Acad. Sci., 60:305, 1925.

[120] W. P. Mason, editor. Physical acoustics and the properties of solids. D. van Nostrand Company, Inc., Princeton, New Jersey, 1958.

[121] Z. Zhu, A. Collaudin, B. Fauqué, W. Kang, and K. Benhia. Field-induced polarization of Dirac valleys in bismuth. Nat. Phys., 8:89, 2012.

[122] R. Küchler, L. Steinke, R. Daou, M. Brando, K. Behnia, and F. Steglich. Thermodynamic evidence for valley-dependent density of states in bulk bismuth. Nat. Mater., 13:461, 2014.

[123] A. Collaudin, B. Fauqué, Y. Fuseya, W. Kang, and K. Behnia. Angle dependence of the orbital magnetoresistance in bismuth. Phys. Rev. X, 5:021022, 2015.

[124] G. P. Mikitik and Yu. V. Sharlai. Spontaneous symmetry breaking of magnetostriction in metals with multivalley band structure. Phys. Rev. B, 91:075111, 2015.

[125] P. B. Littlewood, B. Mihaila, and R. C. Albers. Electron-phonon coupling in semimetals in a high magnetic field. Phys. Rev. B, 81:144421, 2010.

[126] P. Pavone, K. Karch, O. Schütt W. Windl, D. Strauch, P. Giannozzi, and S. Baroni. *Ab initio* lattice dynamics of diamond. Phys. Rev. B, 48:3156, 1993.

[127] J. Höhne, U Wenning, H. Schulz, and S. Hüfner. Temperature dependence of the k=0 optical phonons of Bi and Sb. Z. Phys. B, 27:297, 1977.

[128] T. C. Harman and J. M. Honig. Thermoelectric and thermomagnetic effects and applications. McGraw-Hill, New York, 1967.

[129] D. G. Cahill. Thermal conductivity measurement from 30 to 750 K: the 3ω method. Rev. Sci. Instrum., 61:802, 2001.

[130] S.E. Gustafsson and E. Karawacki. Transient hot-strip probe for measuring thermal properties of insulating solids and liquids. Rev. Sci. Instrum., 54:744, 1983.

[131] Metals: Electronic transport phenomena, thermal conductivity of pure metals and alloys. In O. Madelung and G. K. White, editors, Landolt-Börnstein, Numerical Data and Functional Relationships in Science and Technology, volume III/15c. Springer-Verlag, Berlin, 1991.

[132] A. Sparavigna. Influence of isotope scattering on the thermal conductivity of diamond. Phys. Rev. B, 65:064305, 2002.

[133] D. A. Broido, L. Lindsay, and A. Ward. Thermal conductivity of diamond under extreme pressure: A first-principles study. Phys. Rev. B, 86:115203, 2012.

[134] D.M. Fritz, D.A. Reis, B. Adams, R.A. Akre, J. Arthur, C. Blome, P.H. Bucksbaum, A.L. Cavalieri, S. Engemann, S. Fahy, R.W. Falcone, P.H. Fuoss, K.J. Gaffney, M.J. George, J. Hajdu, M.P. Hertlein, P.B. Hillyard, M. Horn von Hoegen, M. Kammler, J. Kaspar, R. Kienberger, P. Krejcik, S.H. Lee, A.M. Lindenberg, B. McFarland, D. Meyer, T. Montagne, É.D. Murray, A.J. Nelson, M. Nicoul, R. Pahl, J. Rudati, H. Schlarb, D.P. Siddons, K. Sokolowski-Tinten, Th. Tschentscher, D. von der Linde, and J.B. Hastings. Ultrafast bond softening in bismuth: Mapping a solid's interatomic potential with X-rays. Science, 315:633, 2007.

[135] O. Delaire, J. Ma, K. Marty, A.F. May, M.A. McGuire, M-H. Du, D.J. Singh, A. Podlesnyak, G. Ehlers, M.D. Lumsden, and B.C. Sales. Giant anharmonic phonon scattering in PbTe. Nature Materials, 10:614, 2011.

[136] R. Blinc, editor. Advanced Ferroelectricity. International Series of Monographs on Physics. Oxford University Press, New York, 2011.

[137] H. J. Goldsmid and A. W. Penn. Boundary scattering of phonons in solid solutions. Phys. Lett. A, 27:523, 1968.

[138] N. Savvides and H. J. Goldsmid. Boundary scattering of phonons in fine-grained hot-pressed Ge-Si alloys. I. The dependence of lattice thermal conductivity on grain size and porosity. J. Phys. C, 13:4657, 1980.

[139] J. W. Sharp, S. J. Poon, and H. J. Goldsmid. Boundary scattering and the thermoelectric figure of merit. Phys. Stat. Sol. A, 187:507–516, 2001.

[140] P. G. Klemens. The thermal conductivity of dielectric solids at low temperatures (theoretical). International Journal of Thermophysics, 15:1345, 1994.

[141] N. A. Katcho, N. Mingo, and D. A. Broido. Lattice thermal conductivity of $(Bi_{1-x}Sb_x)_2Te_3$ alloys with embedded nanoparticles. Phys. Rev. B, 85:115208, 2012.

[142] A. Kundu, N. Mingo, D. A. Broido, and D. A. Stewart. Role of light and heavy embedded nanoparticles on the thermal conductivity of SiGe alloys. Phys. Rev. B, 84:125426, 2011.

[143] M. G. Kanatzidis. Nanostructured thermoelectrics: The new paradigm? Chem. Mater., 22:648–659, 2010.

[144] C. J. Vineis, A. Shakouri, A. Majumdar, and M. G. Kanatzidis. Nanostructured thermoelectrics: Big efficiency gains from small features. Adv. Mater., 22:3970–3980, 2010.

[145] D. L. Medlin and G. J. Snyder. Interfaces in bulk thermoelectric materials. Curr. Opin. Colloid Interface Sci., 14:226–235, 2009.

[146] D. G. Cahill, W. K. Ford, K. E. Goodson, G. D. Mahan, A. Majumdar, H. J. Maris, R. Merlin, and S. R. Phillpot. Nanoscale thermal transport. J. Appl. Phys., 93:793, 2003.

[147] Y.-M. Lin, X. Sun, and M. S. Dresselhaus. Theoretical investigation of thermoelectric transport properties of cylindrical Bi nanowires. Phys. Rev. B, 62:4610, 2000.

[148] C. Dames and G. Chen. Handbook of Thermoelectrics: Macro to Nano, edited by D. M. Rowe. CRC Press, Boca Raton, Florida, 2006.

[149] A. S. Henry and G. Chen. Spectral phonon transport properties of silicon based on molecular dynamics simulations and lattice dynamics. J. Comput. Theor. Nanosci., 5:141, 2008.

[150] H. B. G. Casimir. Note on the conduction of heat in crystals. Physica, 5:495, 1938.

[151] M. Rudolph and J. J. Heremans. Electronic and quantum phase coherence properties of bismuth thin films. Appl. Phys. Lett., 100:241601, 2012.

[152] D. L. Partin, J. Heremans, D. T. Morelli, C. M. Thrush, C. H. Olk, and T. A. Perry. Growth and characterization of epitaxial bismuth films. Phys. Rev. B, 38:3818, 1988.

[153] F. Völklein and E. Kessler. Analysis of the lattice thermal conductivity of thin films by means of a modified Mayadas-Shatzkes model: The case of bismuth films. Thin Solid Films, 142:169, 1986.

[154] A.I. Hochbaum, R. Chen, R.D. Delgado, W. Liang, E.C. Garnett, M. Najarian, A. Majumdar, and P. Yang. Enhanced thermoelectric performance of rough silicon nanowires. Nature, 451:163, 2008.

[155] E. B. Ramayya, L. N. Maurer, A. H. Davoody, and I. Knezevic. Thermoelectric properties of ultrathin silicon nanowires. Phys. Rev. B, 86:115328, 2012.

[156] C. Wehenkel and B. Gauthé. Electron energy loss spectra and optical constants of bismuth. Solid State Commun., 15:555, 1974.

[157] A. J. H. McGaughey, E. S. Landry, D. P. Sellan, and C. H. Amon. Size-dependent model for thin film and nanowire thermal conductivity. Appl. Phys. Lett., 99:131904, 2011.

[158] Z. Wang and N. Mingo. Absence of Casimir regime in two-dimensional nanoribbon phonon conduction. Appl. Phys. Lett., 99:101903, 2011.

[159] S. Xiao, D. Wei, and X. Jin. Bi(111) thin film with insulating interior but metallic surfaces. Phys. Rev. Lett., 109:166805, 2012.

[160] D. B. Hondongwa, B. C. Daly, T. B. Norris, B. Yan, J. Yang, and S. Guha. Ultrasonic attenuation in amorphous silicon at 50 and 100 GHz. Phys. Rev. B, 83:121303(R), 2011.

[161] J. Cuffe, O. Ristow, E. Chávez, A. Shchepetov, P-O. Chapuis, F. Alzina, M. Hettich, M. Prunnila, J. Ahopelto, T. Dekorsy, and C. M. Sotomayor Torres. Lifetimes of confined acoustic phonons in ultrathin silicon membranes. Phys. Rev. Lett., 110:095503, 2013.

[162] A. J. Kent, N. M. Stanton, L. J. Challis, and M. Henini. Generation and propagation of monochromatic acoustic phonons in gallium arsenide. Appl. Phys. Lett., 81:3497, 2002.

[163] A. A. Maznev, F. Hofmann, A. Jandl, K. Esfarjani, M. T. Bulsara, E. A. Fitzgerald, G. Chen, and K. A. Nelson. Lifetime of sub-THz coherent acoustic phonons in a GaAs-AlAs superlattice. Appl. Phys. Lett., 102:041901, 2013.

[164] T-M. Liu, S-Z. Sun, C-F. Chang, C-C. Pan, G-T. Chen, J-I. Chyi, V. Gusev, and C-K. Sun. Anharmonic decay of subterahertz coherent acoustic phonons in GaN. Appl. Phys. Lett., 90:041902, 2007.

[165] B. C. Daly, K. Kang, Y. Wang, and D. G. Cahill. Picosecond ultrasonic measurements of attenuation of longitudinal acoustic phonons in silicon. Phys. Rev. B, 80:174112, 2009.

[166] G. Rozas, M. Winter, B. Jusserand, A. Fainstein, B. Perrin, E. Semenova, and A. Lemaître. Lifetime of THz acoustic nanocavity modes. Phys. Rev. Lett., 102:015502, 2009.

[167] J. M. Larkin and A. J. H. McGaughey. Thermal conductivity accumulation in amorphous silica and amorphous silicon. Phys. Rev. B, 89:144303, 2014.

[168] A. Togo, L. Chaput, and I. Tanaka. Distributions of phonon lifetimes in Brillouin zones. Phys. Rev. B, 91:094306, 2015.

[169] K. Ishioka, M. Kitajima, and O.V. Misochko. Temperature dependence of coherent A_{1g} and E_g phonons of bismuth. J. Appl. Phys., 100:093501, 2006.

[170] E.S. Zijlstra, L. L. Tatarinova, and M.E. Garcia. Laser-induced phonon-phonon interactions in bismuth. Phys. Rev. B, 74:220301(R), 2006.

[171] M. Hase, M. Kitajima, S. Nakashima, and K. Mizoguchi. Dynamics of coherent anharmonic phonons in bismuth using high density photoexcitation. Phys. Rev. Lett., 88:067401, 2002.

[172] K. Sokolowski-Tinten, C. Blome, J. Blums, A. Cavalleri, C. Dietrich, A. Tarasevitch, I. Uschmann, E. Förster, M. Kammler, M. Horn von Hoegen, and D. von der Linde. Femtosecond X-ray measurement of coherent lattice vibrations near the Lindemann stability limit. Nature, 422:287, 2003.

[173] S.L. Johnson, P. Beaud, , C.J. Milne, F.S. Krasniqi, E.S. Zijlstra, M.E. Garcia, M. Kaiser, D. Grolimund, R. Abela, and G. Ingold. Nanoscale depth-resolved coherent femtosecond motion in laser-excited bismuth. Phys. Rev. Lett., 100:155501, 2008.

[174] O. V. Misochko. Optical control of coherent and squeezed phonons: major differences and similarities. arXiv preprint arXiv:1304.7485, 2013.

[175] E. Haro-Poniatowski, M. Jouanne, J.F. Morhange, M. Kanehisa, R. Serna, and C.N. Afonso. Size effects investigated by Raman spectroscopy in Bi nanocrystals. Phys. Rev. B, 60:10080, 1999.

[176] H. Olijnyk, S. Nakano, and K. Takemura. First- and second order Raman scattering in Sb and Bi at high pressure. Phys. Status Solidi B, 244:3572, 2007.

[177] S. Simons. On the mutual interaction of parallel phonons. Proc. Phys. Soc., 82:401, 1963.

[178] S. Tamura, A. Sangu, and H. J. Maris. Anharmonic scattering of longitudinal acoustic phonons: Herring processes in tetragonal TeO_2 crystals. Phys. Rev. B, 68:014302, 2003.

[179] E. P. N. Damen, A. F. M. Arts, and H. W. de Wijn. Experimental verification of Herring's theory of anharmonic phonon relaxation: TeO_2. Phys. Rev. B, 59:349, 1999.

[180] C. Herring. Role of low-energy phonons in thermal conduction. Phys. Rev., 95:954, 1954.

[181] J. Y. Duquesne and B. Perrin. Ultrasonic attenuation in a quasicrystal studied by picosecond acoustics as a function of temperature and frequency. Phys. Rev. B, 68:134205, 2003.

[182] J.C. Lannin, J.M. Calleja, and M. Cardona. Second-order Raman scattering in the group-V semimetals: Bi, Sb, and As. Phys. Rev. B, 12:585, 1975.

[183] T. Feng, B. Qiu, and X. Ruan. Coupling between phonon-phonon and phonon-impurity scattering: A critical revisit of the spectral Matthiessen's rule. Phys. Rev. B, 92:235206, 2015.

[184] A. I. Chervanyov. Effects of boundary scattering and optic phonon drag on thermal conductivity of a slab of rectangular cross-section. Phys. Rev. B, 66:214302, 2002.

[185] D. Schiferl and C.S. Barrett. The crystal structure of arsenic at 4.2, 78 and 299 k. J. Appl. Crystallogr., 2:30, 1969.

[186] R.M. Martin, editor. Electronic Structure: Basic Theory and Practical Methods. Cambridge University Press, Cambridge, 2004.

[187] A.B. Shick, J.B. Ketterson, D.L. Novikov, and A.J. Freeman. Electronic structure, phase stability, and semimetal-semiconductor transitions in Bi. Phys. Rev. B, 60:15484, 1999.

[188] I. Aguilera, C. Friedrich, and S. Blugel. Electronic phase transitions of bismuth under strain from relativistic self-consistent GW calculations. Phys. Rev. B, 91:125129, 2015.

[189] X. Gonze, J.-P. Michenaud, and J.-P. Vigneron. *First-principles* study of As, Sb, and Bi electronic properties. Phys. Rev. B, 41:11827, 1990.

[190] J.H. Xu, E.G. Wang, C.S. Ting, and W.P. Su. Tight-binding theory of the electronic structures for rhombohedral semimetals. Phys. Rev. B, 48:17271, 1993.

[191] R.T. Isaacson and G.A. Williams. Alfvén-Wave Propagation in Solid-State Plasmas. III. Quantum Oscillations of the Fermi Surface of Bismuth. Phys. Rev., 185:682, 1969.

[192] Y. Liu and R.E. Allen. Electronic structure of the semimetals Bi and Sb. Phys. Rev. B, 52:1566, 1995.

[193] G. E. Smith, G. A. Baraff, and J. M. Rowell. Effective g factor of electrons and holes in bismuth. Phys. Rev., 135:A1118, 1964.

université PARIS-SACLAY
ÉCOLE DOCTORALE
INTERFACES
Approches Interdisciplinaires : Fondements, Applications et Innovation

Titre : Prédiction de la conductivité thermique et stratégie de réduction du transport de la chaleur dans le bismuth: étude *ab initio*.

Mots clefs : bismuth, théorie de la fonctionnelle de la densité, théorie de perturbation de la fonctionnelle de la densité, phonons, anharmonicité, équation de transport de Boltzmann, modèle de Casimir, transport de la chaleur, conductivité thermique, nanostructures de bismuth, couches minces, nanofils, atténuation du son, calcul haute performance

Résumé : Cette thèse de doctorat porte sur l'étude théorique de la conductivité thermique du réseau dans le bismuth semi-métallique et sur les stratégies pour réduire la conductivité thermique en vue d'applications pour réduire l'échauffement dans les circuits électroniques, et pour la thermoélectricité. J'ai utilisé des méthodes avancées de résolution de l'équation de transport de Boltzmann pour les phonons, et de calcul *ab initio* des éléments de matrice de l'interaction phonon-phonon. J'ai calculé la dépendance en température de la conductivité thermique du réseau dans le matériau en volume en excellent accord avec les rares expériences disponibles. J'ai obtenu une description très précise, à l'échelle microscopique, du transport de la chaleur et j'ai quantifié la contribution des porteurs de charge à la conductivité thermique totale. J'ai démontré que la nano-structuration et la photo-excitation sont des moyens très efficaces dans le bismuth de contrôler la diffusion des phonons qui portent la chaleur, respectivement par interaction avec les bords de l'échantillon, et par interaction phonon-phonon. En contrôlant l'équilibre entre ces deux derniers effets, j'ai prédit de façon exhaustive l'effet de réduction pour différentes températures et tailles de nano-structures, pour des mono- et poly-cristaux, semi-conducteurs ou semi-métalliques. Enfin, j'ai étudié l'élargissement anharmonique des phonons acoustiques et optiques, et j'ai déterminé pour chacun les interactions majeures qui contribuent à l'élargissement. L'atténuation du son a été prédite dans le bismuth pour de futures expériences. L'approximation des grandes longueurs d'ondes [long-wave approximation (LWA)] a été validée pour le bismuth et ses limites ont été déterminées.

Title : Prediction of thermal conductivity and strategies for heat transport reduction in bismuth: an *ab initio* study.

Keywords : bismuth, density functional theory, density functional perturbation theory, phonons, anharmonicity, Boltzmann transport equation, Casimir's model, heat transport, thermal conductivity, Bi nanostructures, thin films, nanowires, sound attenuation, high performance computing.

Abstract : This Ph.D. thesis has been devoted to the theoretical study of the lattice thermal conductivity (LTC) in bismuth and of the possible strategies for its reduction, for applications in thermal management and thermoelectricity. I have employed advanced methods of the solution of the Boltzmann transport equation for the phonon system, and of ab initio calculations of the phonon-phonon interaction matrix elements. I have obtained the temperature dependence of the bulk LTC in excellent agreement with the rare available experiments. A very accurate microscopic description of heat transport has been achieved and the charge-carrier contribution to the total thermal conductivity has been determined. I have demonstrated that nanostructuring and photoexcitation are very efficient routes to control respectively phonon-boundary scattering and phonon-phonon interaction in bismuth. By controlling the interplay between these two scattering processes, I have predicted in an exhaustive way the effect of size reduction for various temperatures and nanostructure shapes, both single- and polycrystalline ones, and both semiconducting and semi metallic. I have studied the anharmonic broadenings of both acoustic and optical modes and determined the major interaction processes contributing to them. Sound attenuation has been predicted in bismuth for future experiments. The long-wave approximation (LWA) has been validated for bismuth and its limitations studied.

Université Paris-Saclay
Espace Technologique / Immeuble Discovery
Route de l'Orme aux Merisiers RD 128 / 91190 Saint-Aubin, France